REPORT DOCUMENTATION PAGE

Public reporting burden for this collection of information is estimated to average 1 hour per response, including the time for reviewing instructions, searching existing data sources, gathering and maintaining the data needed, and completing and reviewing the collection of information. Send comments regarding this burden estimate or any other aspect of this collection of information, including suggestions for reducing this burden, to Washington Headquarters Services, Directorate for Information Operations and Reports, 1215 Jefferson Davis Highway, Suite 1204, Arlington, VA 22202-4302, and to the Office of Management and Budget, Paperwork Reduction Project (0704-0188), Washington, DC 20503.

1. AGENCY USE ONLY (Leave blank)	2. REPORT DATE 28.Jun.00	3. REPORT TYPE AND DATES COVERED THESIS

4. TITLE AND SUBTITLE
DYNAMIC LOADING OF SHALLOW FOUNDATIONS: THEORY VERSUS EXPERIMENT

5. FUNDING NUMBERS

6. AUTHOR(S)
2D LT SLOAN JOEL A

7. PERFORMING ORGANIZATION NAME(S) AND ADDRESS(ES)
UNIVERSITY OF COLORADO AT BOULDER

8. PERFORMING ORGANIZATION REPORT NUMBER

9. SPONSORING/MONITORING AGENCY NAME(S) AND ADDRESS(ES)
THE DEPARTMENT OF THE AIR FORCE
AFIT/CIA, BLDG 125
2950 P STREET
WPAFB OH 45433

10. SPONSORING/MONITORING AGENCY REPORT NUMBER

FY00-225

11. SUPPLEMENTARY NOTES

12a. DISTRIBUTION AVAILABILITY STATEMENT
Unlimited distribution
In Accordance With AFI 35-205/AFIT Sup 1

12b. DISTRIBUTION CODE

13. ABSTRACT (Maximum 200 words)

20000718 031

14. SUBJECT TERMS	15. NUMBER OF PAGES 221
	16. PRICE CODE

17. SECURITY CLASSIFICATION OF REPORT	18. SECURITY CLASSIFICATION OF THIS PAGE	19. SECURITY CLASSIFICATION OF ABSTRACT	20. LIMITATION OF ABSTRACT

DTIC QUALITY INSPECTED 4

Dynamic Loading of Shallow Foundations:

Theory versus Experiment

by

Joel Andrew Sloan

B.S. Civil Engineering, United States Air Force Academy,

1998

A thesis submitted to the

Faculty of the Graduate School of the

University of Colorado in partial fulfillment

of the requirements for the degree of

Masters of Science

Department of Civil, Environmental, and Architectural Engineering

2000

This thesis entitled:
Dynamic Loading of Shallow Foundations:
Theory versus Experiment
written by Joel Andrew Sloan
has been approved for the Department of Civil, Environmental, and
Architectural Engineering

_____

Ronald Y. S. Pak

_____
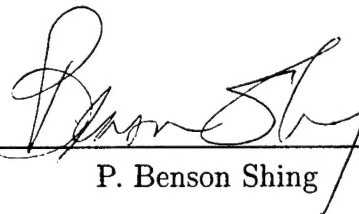
P. Benson Shing

_____

Stein Sture

Date _June 7, 2000_

The final copy of this thesis has been examined by the signatories, and we find
that both the content and the form meet acceptable presentation standards of
scholarly work in the above mentioned discipline.

Sloan, Joel Andrew (M.S. Civil Engineering)

Dynamic Loading of Shallow Foundations:

    Theory versus Experiment

Thesis directed by Professor Ronald Y. S. Pak

In soil-structure interaction problems in soil dynamics, an important subject is the dynamic behavior of embedded foundations. Presented in this thesis is a basic study of the vertical and lateral vibration characteristics of shallow foundations. To obtain a physical understanding of the problem for granular soils, a series of forced vibration tests of square foundations embedded to various depths in sand is performed in a geotechnical centrifuge. A parallel boundary element analysis which can handle nonuniform soil profiles is also used to develop an analytical framework for the problem. By comparing the experimental results with the analytical solution, it is shown that the modeling of the experimental results from vertical vibrations with the homogeneous half-space or square-root half-space theory is directly feasible, while the lateral vibration case requires the use of appropriate Impedance Modification Factors (IMF's) to capture the observed dynamic foundation stiffnesses. Support is also shown for a power law dependence of the embedded foundation equivalent homogeneous shear modulus on the prototype footing half-width and average contact pressure.

Dedication

To my parents Fred and Grace Sloan, whose love and support have made this work possible.

Acknowledgements

I would like to thank my advisor, Professor Ronald Y. S. Pak, for his wisdom and guidance. Thank you for teaching me how to approach experimental research.

I would also like to thank Jeramy Ashlock for teaching me a great deal of what he learned through his research on surface foundations. Thanks also to Satoshi Kurahashi for help with sample preparation.

I am grateful to Professors Benson Shing and Stein Sture for serving on my thesis committee.

Contents

Tables

Table

Figures

Figure

Chapter 1

Introduction

The observed massive destruction of property and loss of life caused by foundation and structural failures in earthquakes have clearly demonstrated the need for improved design methodologies in seismic hazard mitigation. In the last several decades, structural dynamics and soil dynamics analysis in earthquake engineering have seen increasing recognition as an intrinsically coupled problem. Additional impetus to the field of research is also generated by related activities in the design of machine foundations, off-shore structures, and blast-resistant buildings (e.g. Stokoe and Richart [36], Gazetas [8]).

For many applications, soil-structure interaction problems can be simplified by employing a suitably linearized analysis for small to moderate deformation. Using this method, the soil, foundation, and structure can be divided into several substructures which can be analyzed individually. The four basic problems which must be solved are (Luco [23]): (i) free-field ground motion, (ii) scattering field motion, (iii) forced vibration of foundations (radiation problem), and (iv) interfacial mechanics (structural dynamics problem). Among them, the scattering field motion problem and the forced vibration problem are often true three-dimensional continuum mechanics problems (Guzina [13]). Solving the scattering field motion problem yields the foundation input motions which describe the foundation's response to specified incident seismic waves in the absence of any other forces (Mita and Luco [28]). Solving the forced vibration problem leads to the dynamic interfacial compliances which provide the displacement per unit of forced vibration

applied to the foundation as a function of frequency (Dominguez [6]). Reciprocally related to the interfacial compliances are the interfacial impedances which can be obtained by inverting the compliance matrix.

In the study of soil-structure interaction problems, much attention has been given to analytical modeling and experimental testing of surface footings (see Gazetas [8], Guzina [12], Ashlock [1]) due to its fundamental importance. A more challenging and practical case, however, is an embedded foundation. Because of the side contacts and related effects, the dynamic response of embedded foundations must be a function of the embedment depth and the nature of the surrounding soil. Therefore, seeking an understanding of the characteristics of the problem, researchers have taken a variety of approaches to investigating the behavior of embedded foundations on soil. Some have proposed an analytical approach (e.g. Mita and Luco [26], Karabalis and Beskos [20]), while others have conducted experiments on full-scale prototypes (e.g. Novak [29], Stokoe and Richart [36], Crouse et. al. [5]) or centrifuge models (Hushmand [19], Guzina [12]). In this study, a combined analytical and experimental approach will be used to study the vibrations of embedded foundations in cohesionless soils. A boundary element method will be utilized to provide the analytical framework in the form of impedances for a homogeneous half-space and a square-root shear modulus profile, while centrifuge modeling will provide the experimental results for forced vibration of shallowly embedded square foundations on sand. As will be illustrated in the following chapters, the two approaches complement each other well and lead to an overall understanding of the problem which would be difficult to achieve otherwise.

Chapter 2

Embedded Foundation Impedance Functions

2.1 Interfacial Impedance Matrix

One of the most important elements in the substructuring approach to soil-structure interaction problems is the determination of the foundation impedance matrix. Defined in the frequency domain, the interfacial impedances relate forces and moments to the corresponding translations and rotations at a control point on the soil-foundation interface as a function of frequency. With reference to Figure 2.1 which shows a square foundation with base dimensions $2b \times 2b$ embedded to depth h in a soil medium, the control point is often selected to be the point $\mathbf{x}_{ref} = \mathbf{x}_h = (0, 0, h)$ at the base of the foundation. Using such a point as the reference, the motion of the foundation can be defined in the frequency domain by the generalized displacement vector

$$\bar{\mathbf{U}}(\omega) = \left[\bar{U}_x, \bar{U}_y, \bar{U}_z, \bar{\Theta}_x, \bar{\Theta}_y, \bar{\Theta}_z \right]^T \qquad (2.1)$$

where

$$\bar{U}_x = \frac{U_x}{b}, \quad \bar{U}_y = \frac{U_y}{b}, \quad \bar{U}_z = \frac{U_z}{b} \qquad (2.2)$$

are the dimensionless displacements and

$$\bar{\Theta}_x = \Theta_x, \quad \bar{\Theta}_y = \Theta_y, \quad \bar{\Theta}_z = \Theta_z \qquad (2.3)$$

are the dimensionless angular rotations at $\mathbf{x}_h$ where b is the half-width of a square foundation. Likewise, the generalized force vector can be written as

$$\bar{\mathbf{F}}(\omega) = \left[\bar{F}_x, \bar{F}_y, \bar{F}_z, \bar{M}_x, \bar{M}_y, \bar{M}_z \right]^T . \qquad (2.4)$$

where

$$\bar{F}_x = \frac{F_x}{Gb^2}, \quad \bar{F}_y = \frac{F_y}{Gb^2}, \quad \bar{F}_z = \frac{F_z}{Gb^2} \tag{2.5}$$

are the resultant forces and

$$\bar{M}_x = \frac{M_x}{Gb^3}, \quad \bar{M}_y = \frac{M_y}{Gb^3}, \quad \bar{M}_z = \frac{M_z}{Gb^3} \tag{2.6}$$

are the resultant moments at $\mathbf{x}_h$ where G is a chosen reference shear modulus. In terms of these forces and displacements, the interfacial impedance matrix for
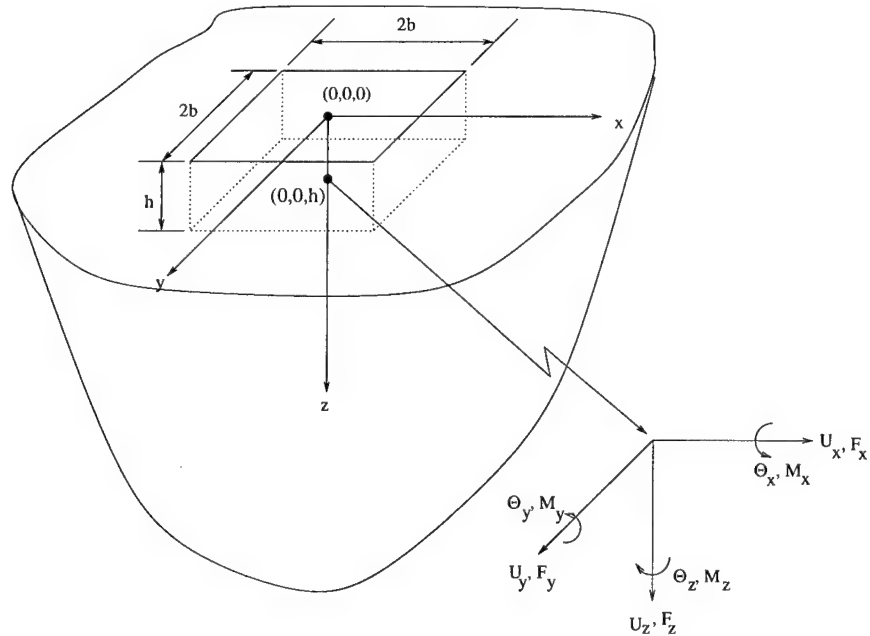
Figure 2.1: Square footing with half-width "b" embedded in soil to depth "h".

a general rectangular foundation at the control point $\mathbf{x}_h$, denoted $\mathbf{K}(\omega)$, can be defined as

$$\bar{\mathbf{F}}(\omega) = \bar{\mathbf{K}}(\omega)\bar{\mathbf{U}}(\omega) \tag{2.7}$$

where the components of $\bar{\mathbf{K}}(\omega)$ are,

$$\bar{\mathbf{K}}(\omega) = \begin{bmatrix} \bar{K}_{hh}^{xx}(\omega) & 0 & 0 & 0 & \bar{K}_{hm}^{xy}(\omega) & 0 \\ 0 & \bar{K}_{hh}^{yy}(\omega) & 0 & \bar{K}_{hm}^{yx}(\omega) & 0 & 0 \\ 0 & 0 & \bar{K}_{vv}(\omega) & 0 & 0 & 0 \\ 0 & \bar{K}_{mh}^{xy}(\omega) & 0 & \bar{K}_{mm}^{xx}(\omega) & 0 & 0 \\ \bar{K}_{mh}^{yx}(\omega) & 0 & 0 & 0 & \bar{K}_{mm}^{yy} & 0 \\ 0 & 0 & 0 & 0 & 0 & \bar{K}_{tt}(\omega) \end{bmatrix}. \tag{2.8}$$

where

$$\bar{K}_{vv}(\omega) = \frac{K_{vv}(\omega)}{Gb}, \quad \bar{K}_{hh}^{kk}(\omega) = \frac{K_{hh}^{kk}(\omega)}{Gb}, \quad \bar{K}_{mm}^{kk}(\omega) = \frac{K_{mm}^{kk}(\omega)}{Gb^3},$$
$$\bar{K}_{mh}^{kj}(\omega) = \frac{K_{mh}^{kj}(\omega)}{Gb^2}, \quad \bar{K}_{hm}^{jk}(\omega) = \frac{K_{hm}^{jk}(\omega)}{Gb^2}, \quad \bar{K}_{tt}(\omega) = \frac{K_{tt}(\omega)}{Gb^3}. \tag{2.9}$$

The eight independent components of the impedance matrix are $\bar{K}_{hh}^{kk}(\omega)$, $\bar{K}_{vv}(\omega)$, $\bar{K}_{mm}^{kk}(\omega)$, $\bar{K}_{hm}^{jk}(\omega) = \bar{K}_{mh}^{kj}(\omega)$ $(j,k=x,y)$, and $\bar{K}_{tt}(\omega)$, which are the horizontal, vertical, rocking, coupling, and torsional stiffness functions respectively. The first subscript in the notation refers to the force or moment being reported while the second subscript refers to the translation or rotation applied. The first superscript refers to the direction of the force or moment and the second superscript refers to the direction of the translation or rotation. For example, $\bar{K}_{mh}^{yx}$ is the moment about the y-axis necessary to ensure a pure horizontal translation in the x-direction.

In the case of a square foundation, further simplifications can be made due to symmetry since the force-displacement relations will be the same in the x- and y-directions. They are

$$\bar{K}_{hh}^{xx}(\omega) = \bar{K}_{hh}^{yy}(\omega) \equiv \bar{K}_{hh}(\omega), \quad \bar{K}_{mm}^{xx}(\omega) = \bar{K}_{mm}^{yy}(\omega) \equiv \bar{K}_{mm}(\omega),$$
$$\bar{K}_{mh}^{yx}(\omega) = -\bar{K}_{mh}^{xy}(\omega) \equiv \bar{K}_{mh}(\omega), \quad \bar{K}_{hm}^{xy}(\omega) = -\bar{K}_{hm}^{yx}(\omega) \equiv \bar{K}_{hm}(\omega), \tag{2.10}$$

where $\bar{K}_{hm}^{jk}(\omega) = \bar{K}_{mh}^{kj}(\omega)$ $(j,k=x,y)$ implies that $\bar{K}_{hm}(\omega) = \bar{K}_{mh}(\omega)$, and the negative sign for the coupling terms occurs due to the alignment of the axis system.

Consequently, there are now only five independent components of the impedance matrix

$$\bar{\mathbf{K}}(\omega) = \begin{bmatrix} \bar{K}_{hh}(\omega) & 0 & 0 & 0 & \bar{K}_{hm}(\omega) & 0 \\ 0 & \bar{K}_{hh}(\omega) & 0 & -\bar{K}_{hm}(\omega) & 0 & 0 \\ 0 & 0 & \bar{K}_{vv}(\omega) & 0 & 0 & 0 \\ 0 & -\bar{K}_{mh}(\omega) & 0 & \bar{K}_{mm}(\omega) & 0 & 0 \\ \bar{K}_{mh}(\omega) & 0 & 0 & 0 & \bar{K}_{mm} & 0 \\ 0 & 0 & 0 & 0 & 0 & \bar{K}_{tt}(\omega) \end{bmatrix}. \quad (2.11)$$

In a similar manner, one can define the 6x6 compliance matrix according to

$$\bar{\mathbf{U}}(\omega) = \bar{\mathbf{C}}(\omega)\bar{\mathbf{F}}(\omega), \quad (2.12)$$

where,

$$\bar{\mathbf{C}}(\omega) = \begin{bmatrix} \bar{C}_{hh}(\omega) & 0 & 0 & 0 & \bar{C}_{hm}(\omega) & 0 \\ 0 & \bar{C}_{hh}(\omega) & 0 & -\bar{C}_{hm}(\omega) & 0 & 0 \\ 0 & 0 & \bar{C}_{vv}(\omega) & 0 & 0 & 0 \\ 0 & -\bar{C}_{mh}(\omega) & 0 & \bar{C}_{mm}(\omega) & 0 & 0 \\ \bar{C}_{mh}(\omega) & 0 & 0 & 0 & \bar{C}_{mm} & 0 \\ 0 & 0 & 0 & 0 & 0 & \bar{C}_{tt}(\omega) \end{bmatrix} \quad (2.13)$$

and

$$\bar{C}_{vv} = GbC_{vv}, \quad \bar{C}_{hh} = GbC_{hh}, \quad \bar{C}_{mm} = Gb^3C_{mm},$$

$$\bar{C}_{mh} = Gb^2C_{mh}, \quad \bar{C}_{hm} = Gb^2C_{hm}, \quad \bar{C}_{tt} = Gb^3C_{tt}. \quad (2.14)$$

To compute the impedances, the simplest method is to consider four displacement boundary value problems: (i) a pure vertical rigid body translation

u_z for computing K_{vv} ($K_{vv} = F_z/u_z$), (ii) a pure horizontal rigid body translation u_x for computing K_{hh} ($K_{hh} = F_x/u_x$) and K_{mh} ($K_{mh} = M_y/u_x$), (iii) a pure rigid rocking rotation Θ_y about the reference point for computing K_{mm} ($K_{mm} = M_y/\Theta_y$) and K_{hm} ($K_{hm} = F_x/\Theta_y$), and (iv) a pure torsional rotation $\Theta_z = 1.0$ about the reference point for computing K_{tt} ($K_{tt} = M_z/\Theta_z$). Some of the methods to compute the impedances analytically will be discussed in the following section.

2.2   Overview of Analytical Methods

There are four major methods which have been used to solve for the embedded foundation impedance matrix which can be categorized as follows: (i) simplified analytical methods, (ii) finite element methods (FEM), (iii) boundary element methods (BEM), and (iv) methods which combine the FEM and BEM.

2.2.1   Simplified Analytical Methods

Simplified analytical methods of finding the impedances for embedded foundations are often based on a modification of results from surface foundations by certain factors which change due to embedment. For instance, Gazetas et. al. [9] proposed an approximate approach in the form of empirical formulas and dimensionless graphs using numerical results from a boundary integral equation method for vertical vibrations of arbitrarily shaped embedded foundations. Gazetas and Tassoulas [10] and Hatzikonstantinou et. al. [18] used the same method to describe horizontal and rocking vibrations respectively. The findings of these three papers ([9], [10], [18]) are summarized by Gazetas in [8]. Gazetas proposes the usage of three coefficients used to modify the surface stiffness which are based on three proposed stiffening effects that embedment has on a foundation. The first effect is based on the fact that soil at greater depths is generally stiffer than soil
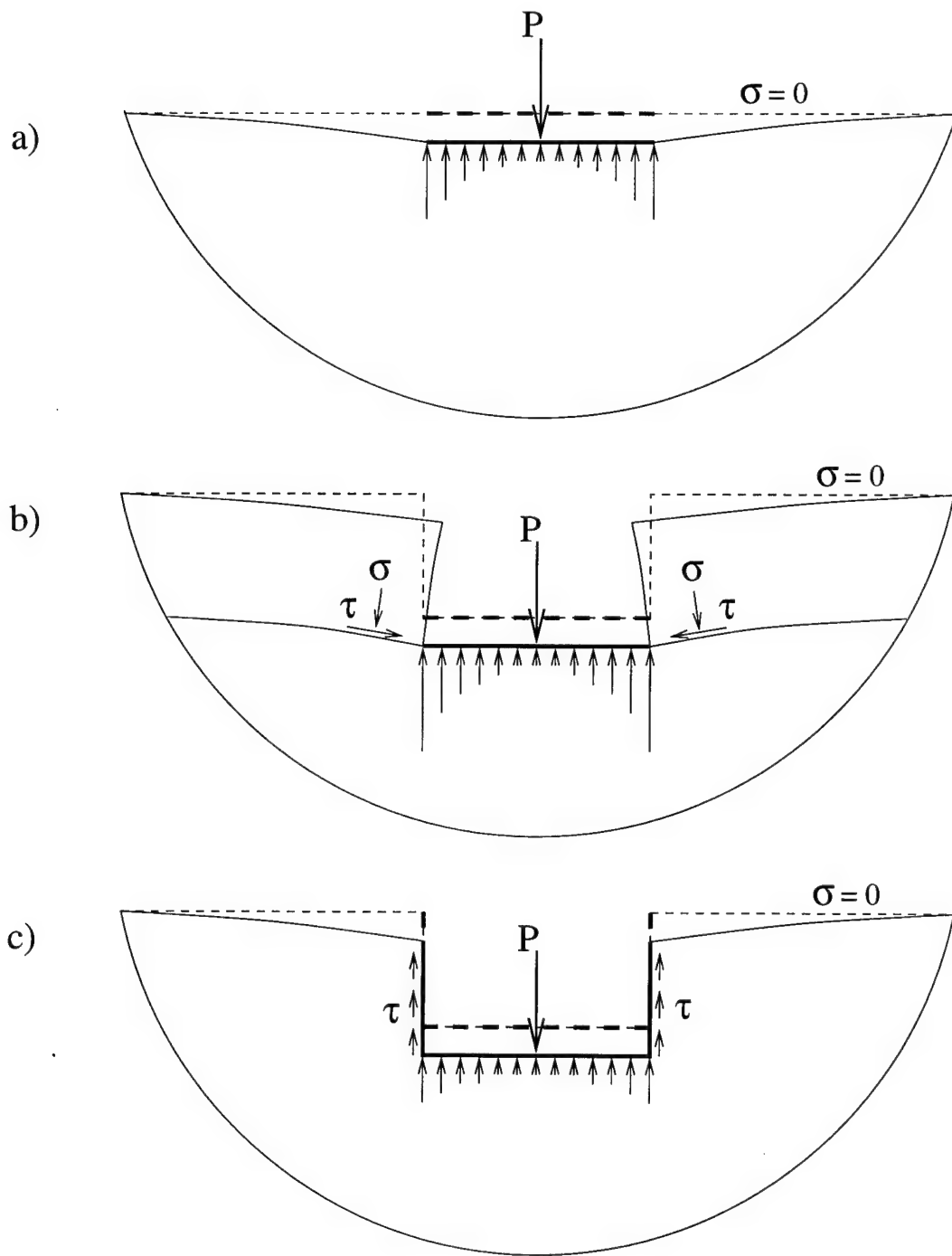
Figure 2.2: Illustration of (a) a surface footing with a stress-free surface, (b) the trench effect, (c) sidewall effects (Gazetas et al [9]).

at the surface. The second effect is called the "trench" effect and is illustrated in Figure 2.2b. The trench effect can best be explained by the fact that a rigid mat will settle less when placed in a trench of a homogeneous half-space than on the surface of a homogeneous half-space. For a surface mat, the soil surface around the rigid mat is free of traction (see Figure 2.2a). However, such tractions are present in the case of embedded foundations due to the normal and shear forces developed in the overlying soil above the rigid mat as in Figure 2.2b. The presence of these forces can provide a push-back effect which resists the motion of the rigid mat. The third effect is called the "sidewall-contact" effect and is shown in Figure 2.2c. When a load is applied to an embedded foundation, the sides of the footing are in contact with the soil and can transfer load to the soil. Thus, one would expect that increasing the embedment depth of a foundation would lead to higher impedances due to the effect of transferring load through the sides of the footing in contact with the soil. This method proposed by Gazetas [8] is one of many simplified analytical methods appearing in the literature. Due to the simplistic uncoupling of the three effects, the method does not have a high reliability as will be shown in Section 2.3.

2.2.2   Finite Element Methods

Although the finite element method is widely used in many areas of engineering for representing finite geometries, difficulties arise when using FEM to represent a semi-infinite medium such as the soil beneath a foundation, since the entire soil region must be discretized. This creates problems in dynamic modeling since some sort of finite artificial boundary must be imposed. The insertion of this boundary often causes errors due to the reflection of waves off of the boundaries and back to the foundation itself. Problems of wave reflections have been partially solved in FEM by means of special nonreflecting boundaries (e.g. Roesset and Et-

touney [34]) and infinite elements (e.g. Medina and Penzien [25]) at an increased computational cost. However, the method of choice for representing infinite or semi-infinite mediums is still the boundary element method.

2.2.3   Boundary Element Methods

The boundary element method has been the most popular for computing the interfacial impedances due to its inherent ability to deal with a semi-infinite medium. Among various half-space models, the homogeneous isotropic case which is fully characterized by elastic parameters G, ν, and ρ, is the most widely used. Solutions for simple inhomogeneous soil profiles have also been developed as in Guzina and Pak [16]. With the use of multi-layered half-space Green's functions, more complicated variations of the soil can also be considered (Guzina and Pak [14], Luco and Wong [24]). Because of the need to discretize only the boundary surface, BEM has a fundamental appeal to researchers and formulations have been developed in both the frequency and time domains. For example, Fukuzawa et al.[37] and Yoshida and Kawase [38] use a frequency-domain boundary element technique to obtain the dynamic response of rectangular foundations embedded in a homogeneous elastic half-space and subjected to both external forces and elastic waves. Karabalis and Beskos [20] employ a time-domain boundary element method for a homogeneous half-space, while Dominguez [6], [7] utilizes a frequency domain boundary element method for a homogeneous half-space.

The most recent development is the work of Pak and Guzina [33]. Using the fundamental boundary integral equation for three-dimensional elastodynamics, the authors implement a version with a rigorous multilayered Green's function representation of the soil medium and design a set of special singular boundary elements to handle the singular tractions caused by sharp foundation edges and three-dimensional corners (see also Guzina [13]). The existence of such singulari-
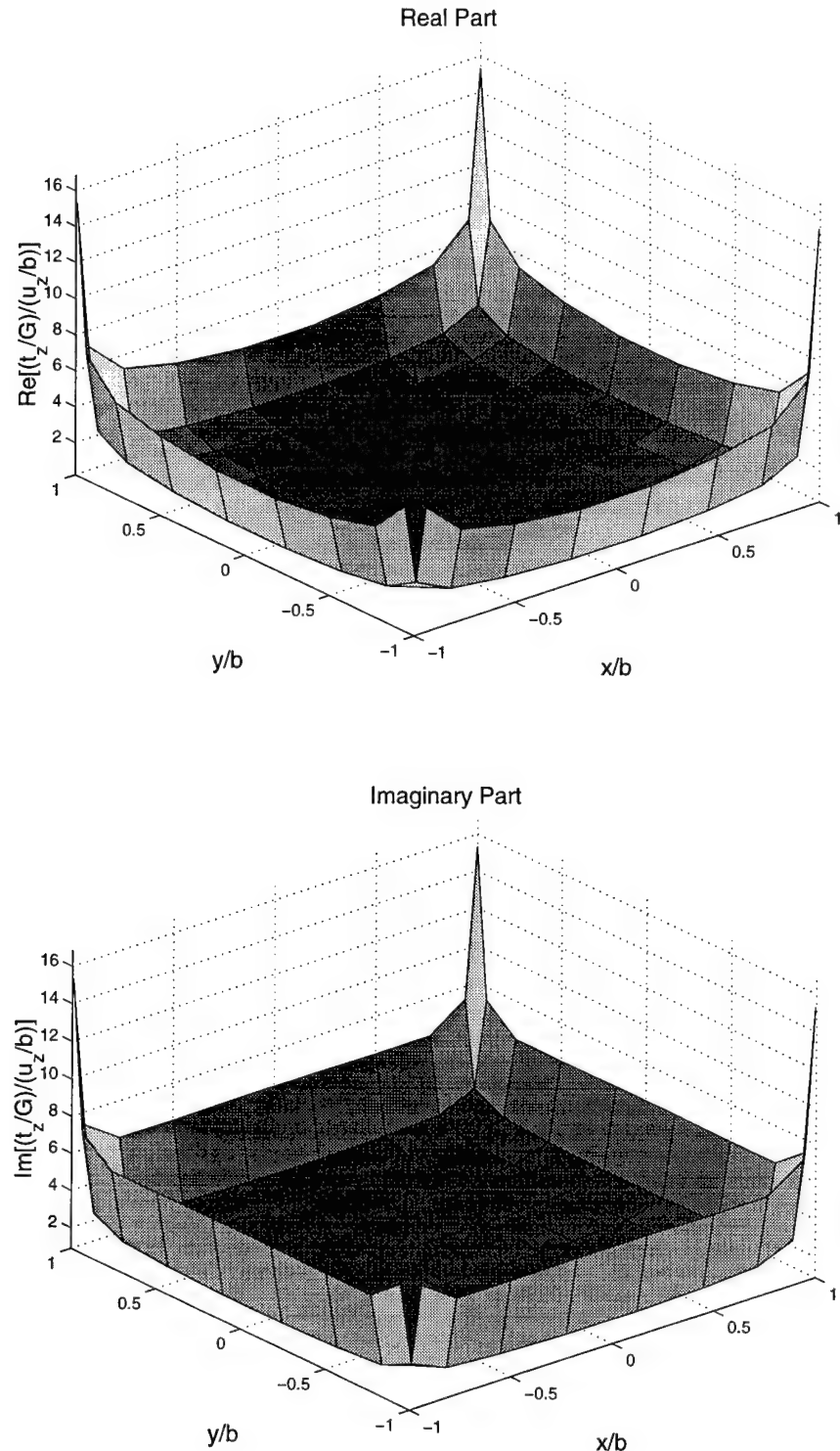
Figure 2.3: Distribution of normal contact tractions t_z corresponding to dynamic stiffness $\bar{K}_{vv}(\bar{\omega} = 1.0)$ for a homogeneous half-space. (Bottom of the rigid foundation, $h/b = 1.0$, $\nu = 0.25$)
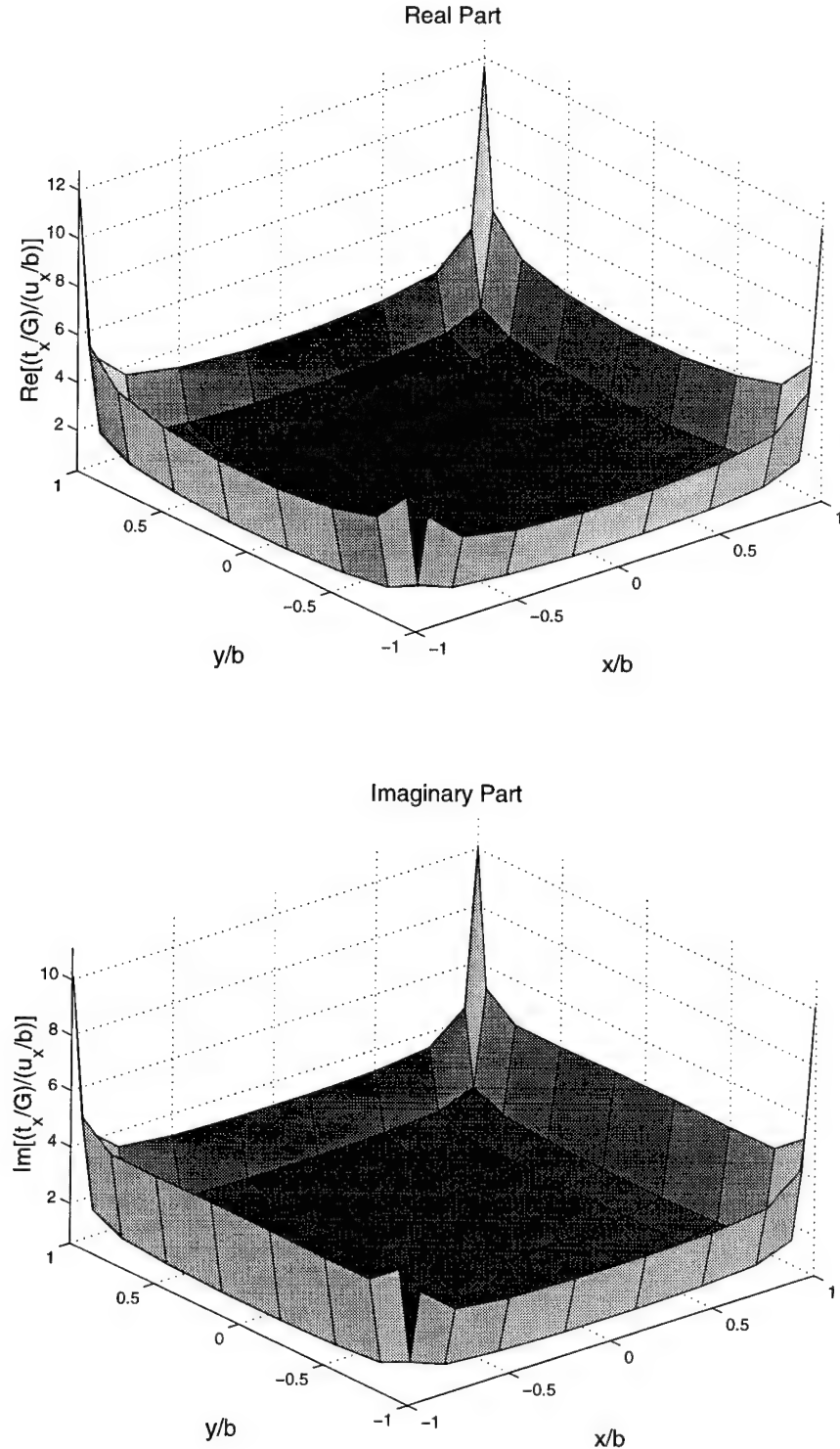
Figure 2.4: Distribution of shear contact tractions t_x corresponding to dynamic stiffness $\bar{K}_{hh}(\bar{\omega} = 1.0)$ for a homogeneous half-space. (Bottom of the rigid foundation, $h/b = 1.0$, $\nu = 0.25$)
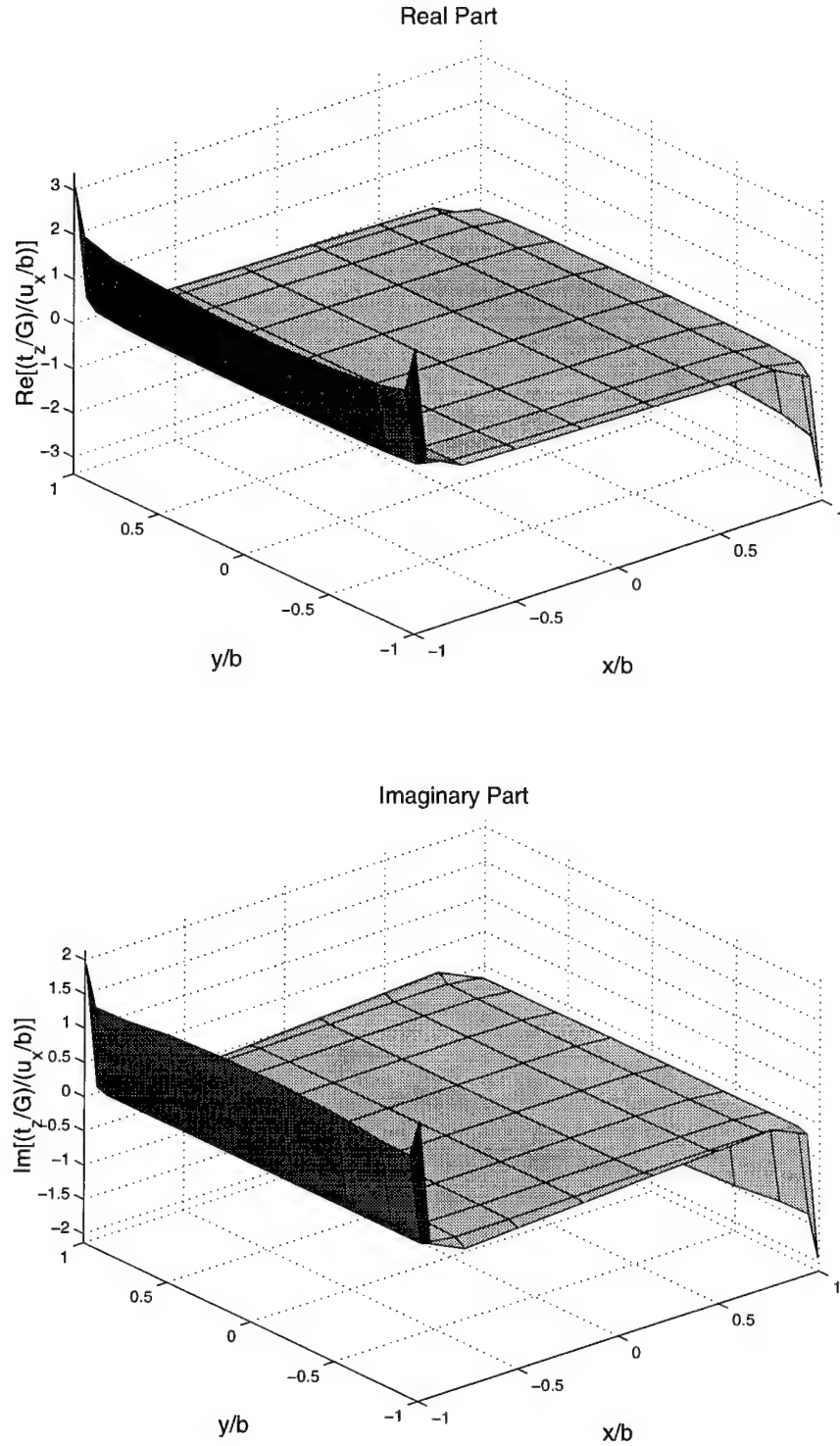
Figure 2.5: Distribution of normal contact tractions t_z corresponding to dynamic stiffness $\bar{K}_{mh}(\bar{\omega} = 1.0)$ for a homogeneous half-space. (Bottom of the rigid foundation, $h/b = 1.0$, $\nu = 0.25$)
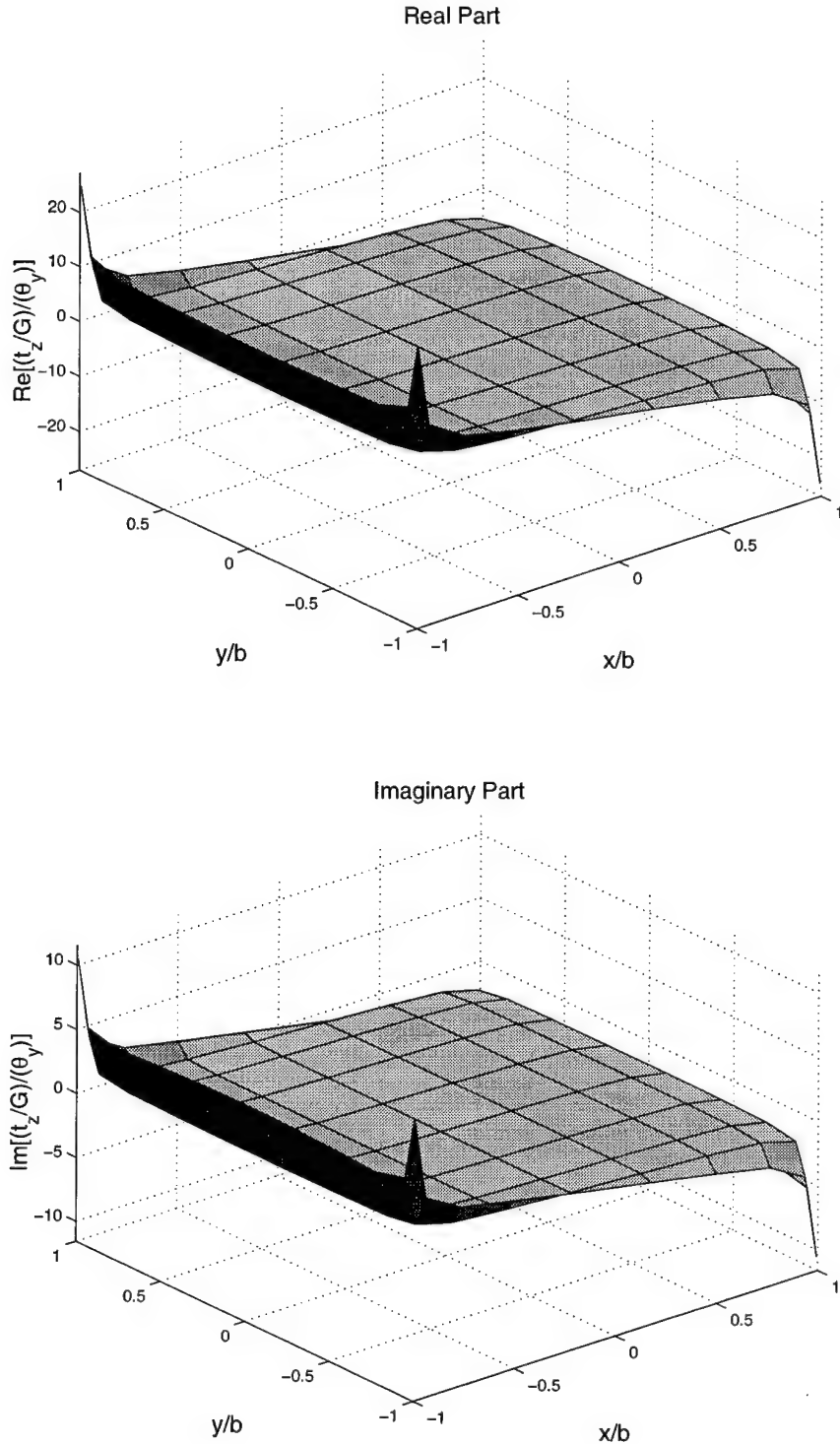
Figure 2.6: Distribution of normal contact tractions t_z corresponding to dynamic stiffness $\bar{K}_{mm}(\bar{\omega} = 1.0)$ for a homogeneous half-space. (Bottom of the rigid foundation, $h/b = 1.0$, $\nu = 0.25$)

Real Part

Imaginary Part
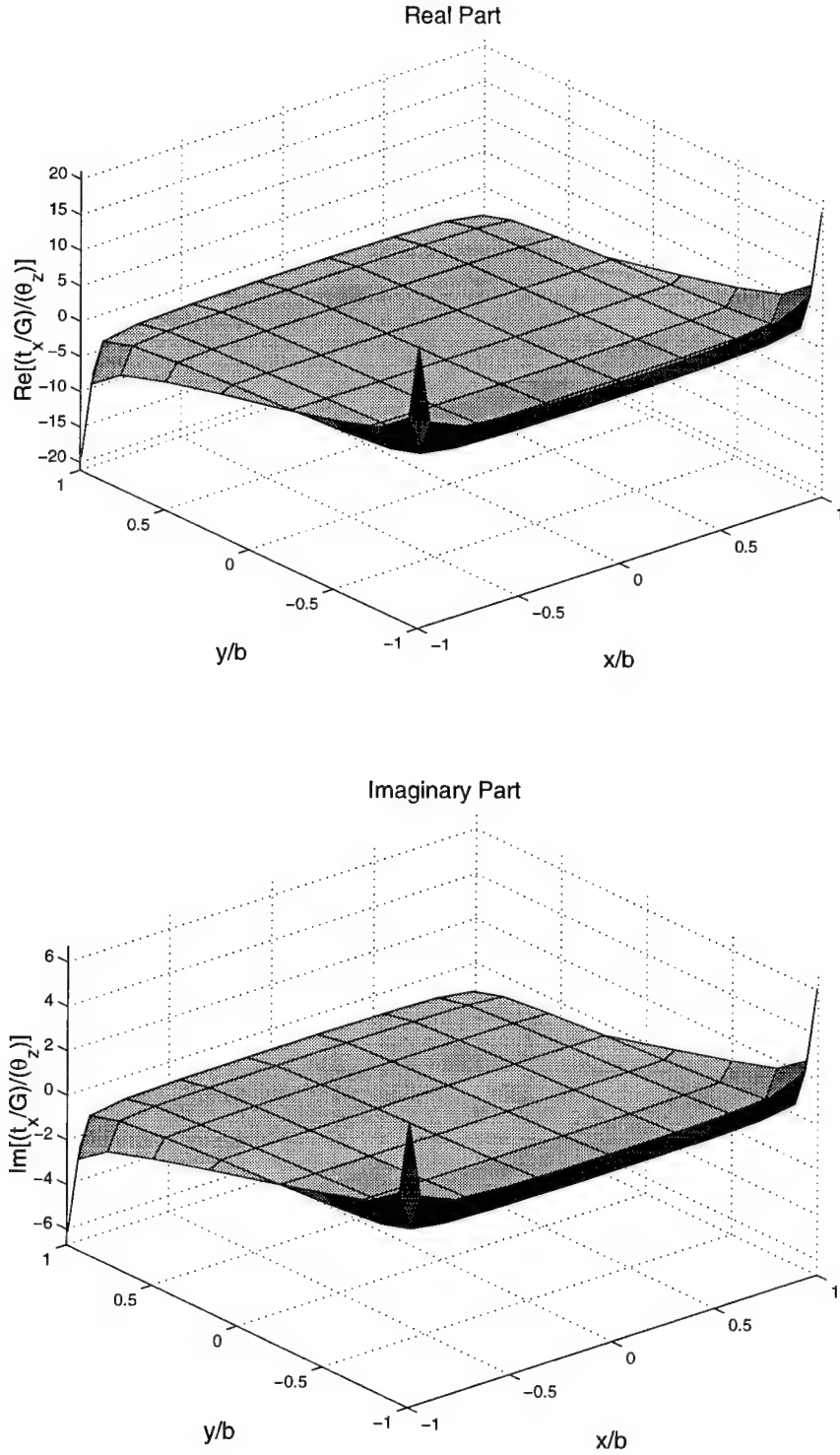
Figure 2.7: Distribution of shear contact tractions t_x corresponding to dynamic stiffness $\bar{K}_{tt}(\bar{\omega} = 1.0)$ for a homogeneous half-space. (Bottom of the rigid foundation, $h/b = 1.0$, $\nu = 0.25$)
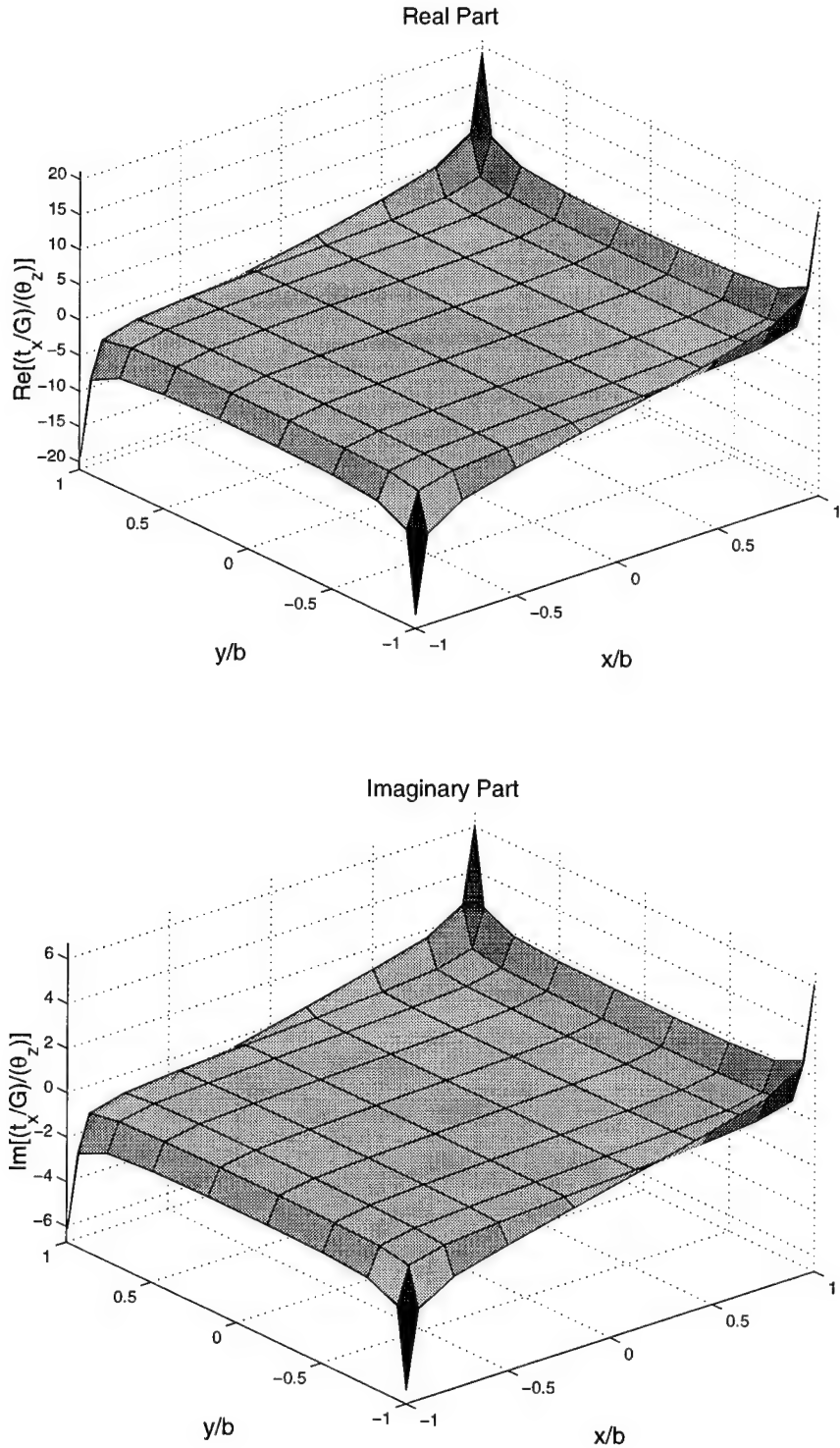
Figure 2.8: Distribution of shear contact tractions t_y corresponding to dynamic stiffness $\bar{K}_{tt}(\bar{\omega} = 1.0)$ for a homogeneous half-space. (Bottom of the rigid foundation, $h/b = 1.0$, $\nu = 0.25$)

Real Part

Imaginary Part
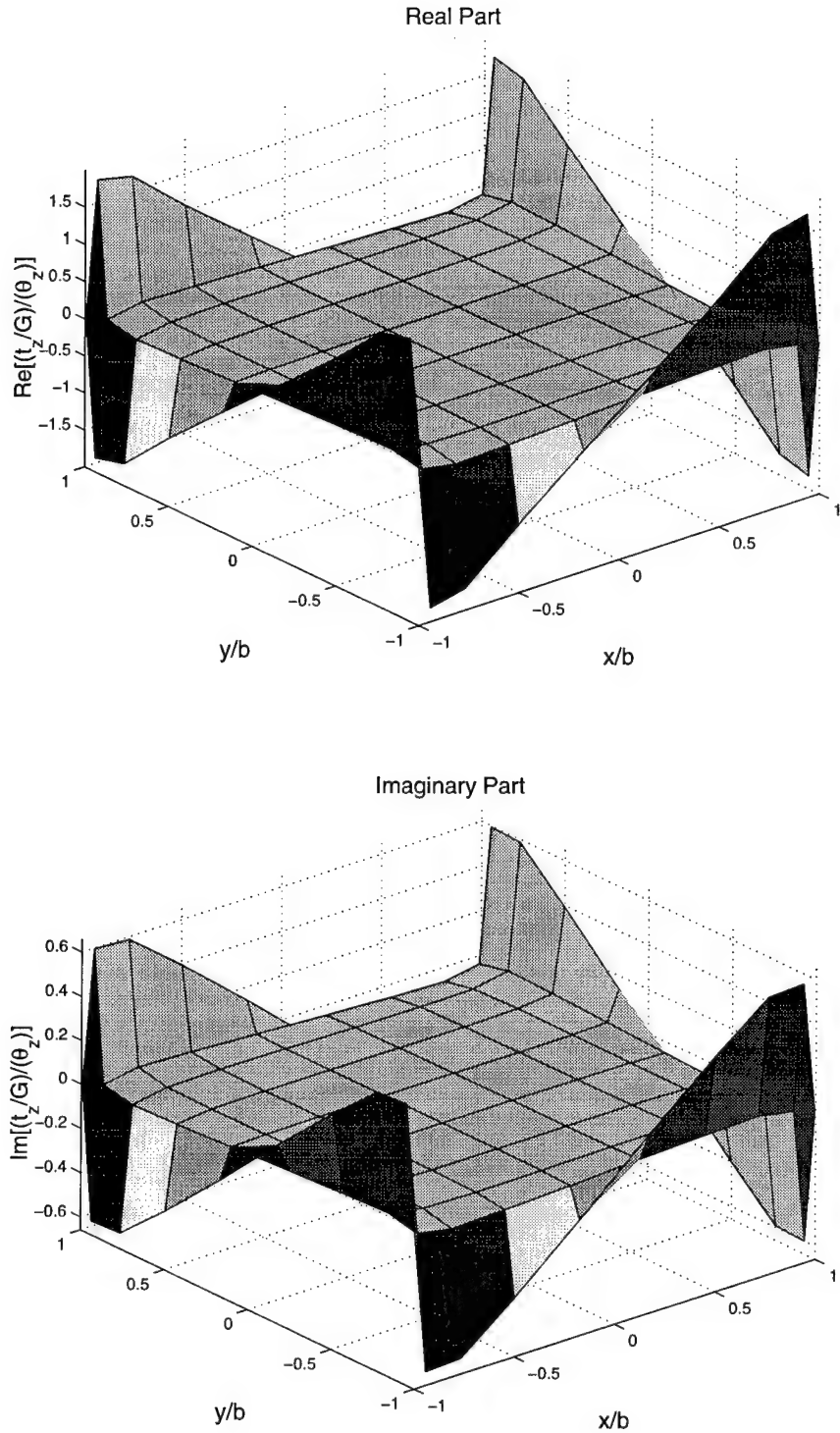
Figure 2.9: Distribution of normal contact tractions t_z corresponding to dynamic stiffness $\bar{K}_{tt}(\bar{\omega} = 1.0)$ for a homogeneous half-space. (Bottom of the rigid foundation, $h/b = 1.0$, $\nu = 0.25$)
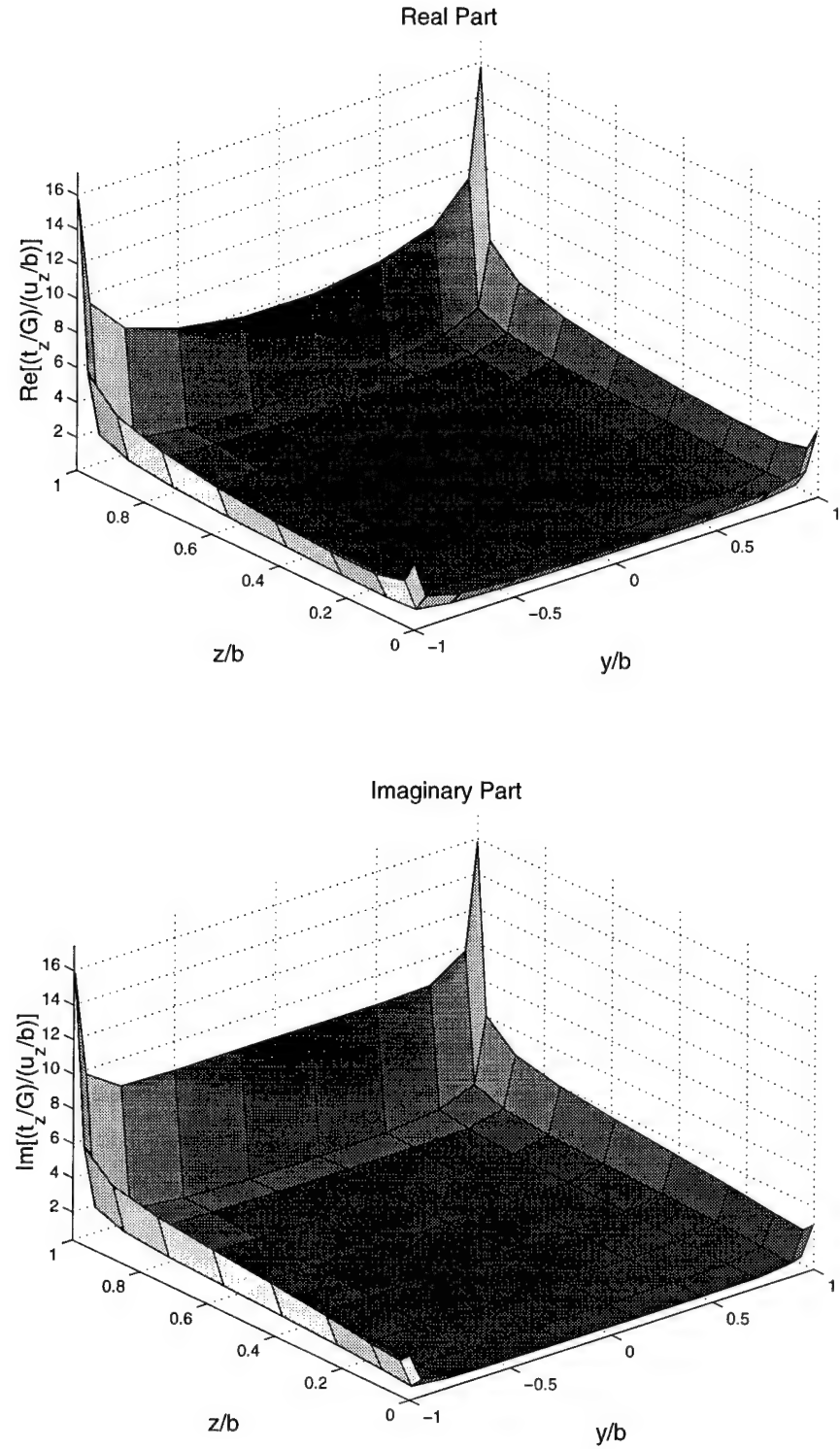
Figure 2.10: Distribution of shear contact tractions t_z corresponding to dynamic stiffness $\bar{K}_{vv}(\bar{\omega} = 1.0)$ for a homogeneous half-space. (X-face of the rigid foundation, $h/b = 1.0$, $\nu = 0.25$)
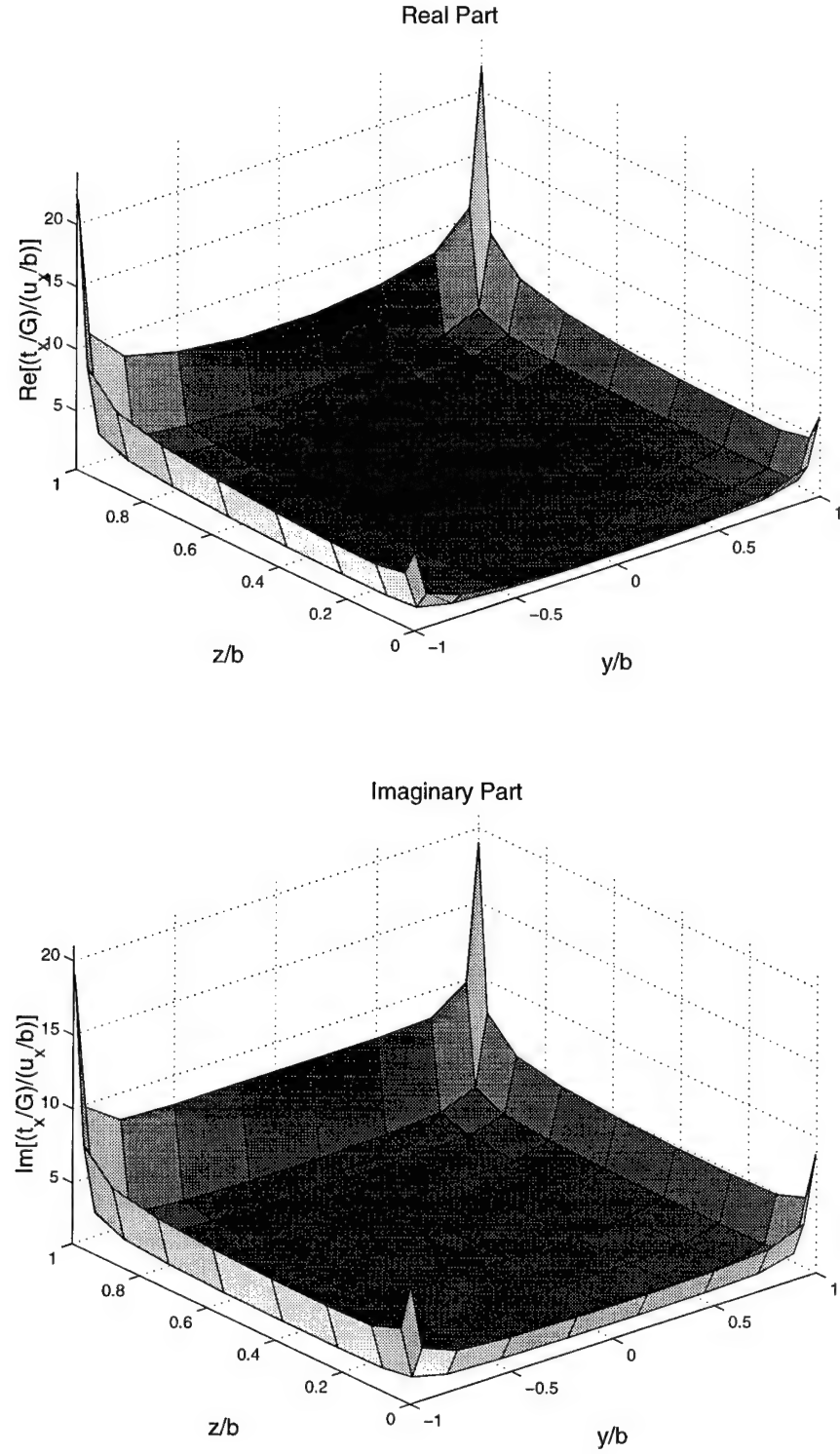
Figure 2.11: Distribution of normal contact tractions t_x corresponding to dynamic stiffness $\bar{K}_{hh}(\bar{\omega} = 1.0)$ for a homogeneous half-space. (X-face of the rigid foundation, $h/b = 1.0$)
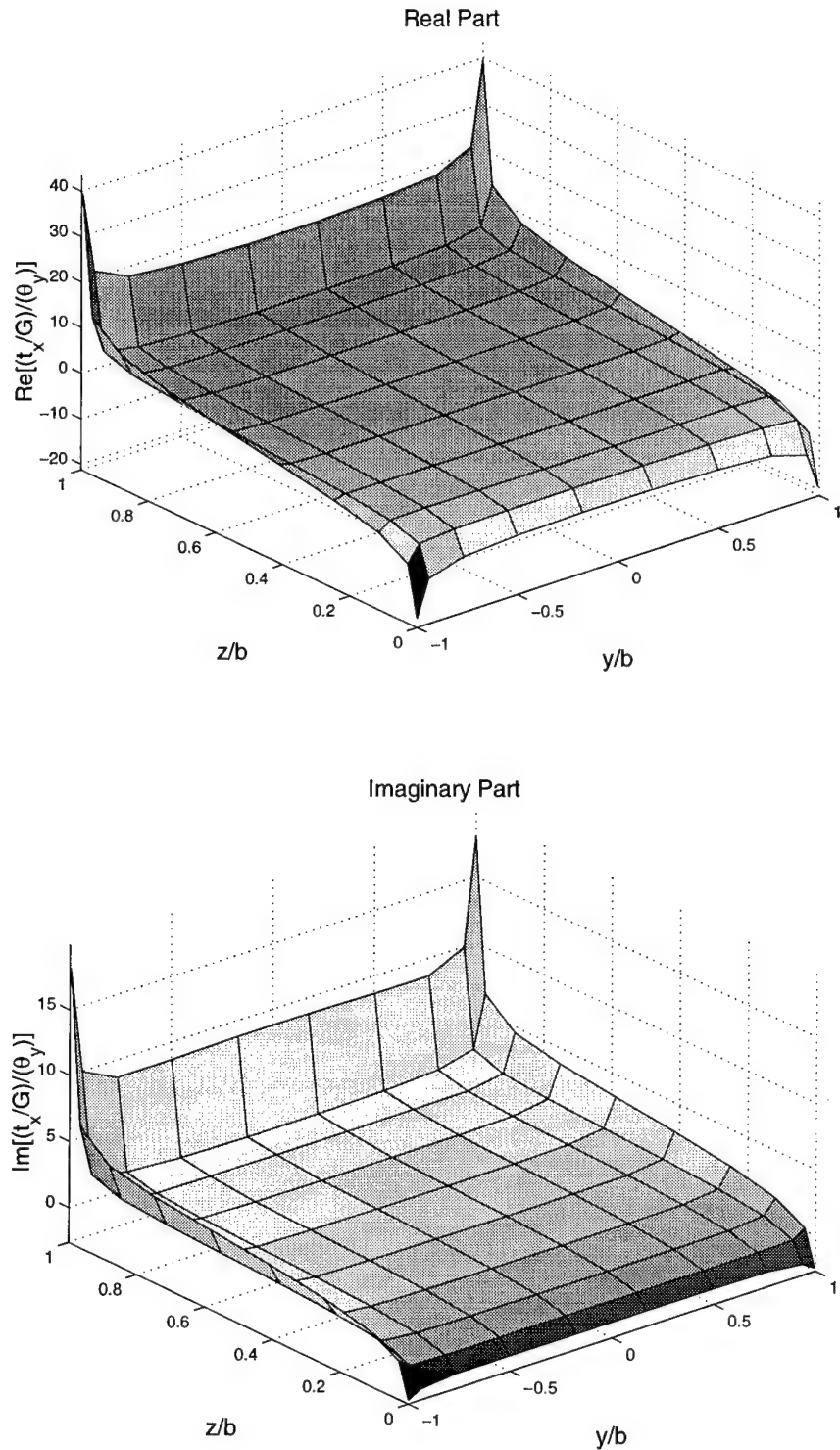
Figure 2.12: Distribution of normal contact tractions t_x corresponding to dynamic stiffness $\bar{K}_{mm}(\bar{\omega} = 1.0)$ for a homogeneous half-space. (X-face of the rigid foundation, $h/b = 1.0$, $\nu = 0.25$)
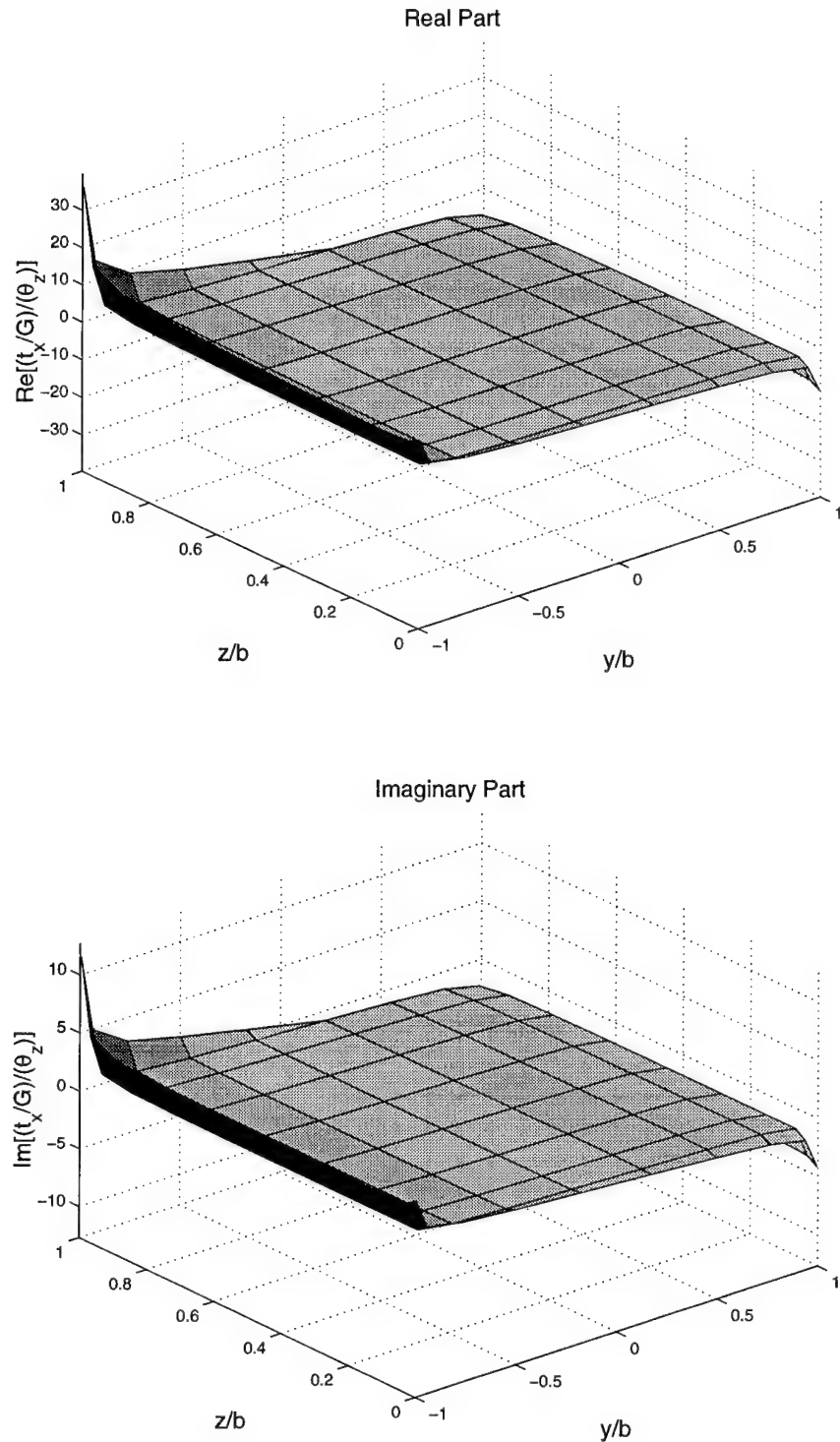
Figure 2.13: Distribution of normal contact tractions t_x corresponding to dynamic stiffness $\bar{K}_{tt}(\bar{\omega} = 1.0)$ for a homogeneous half-space. (X-face of the rigid foundation, $h/b = 1.0$, $\nu = 0.25$)
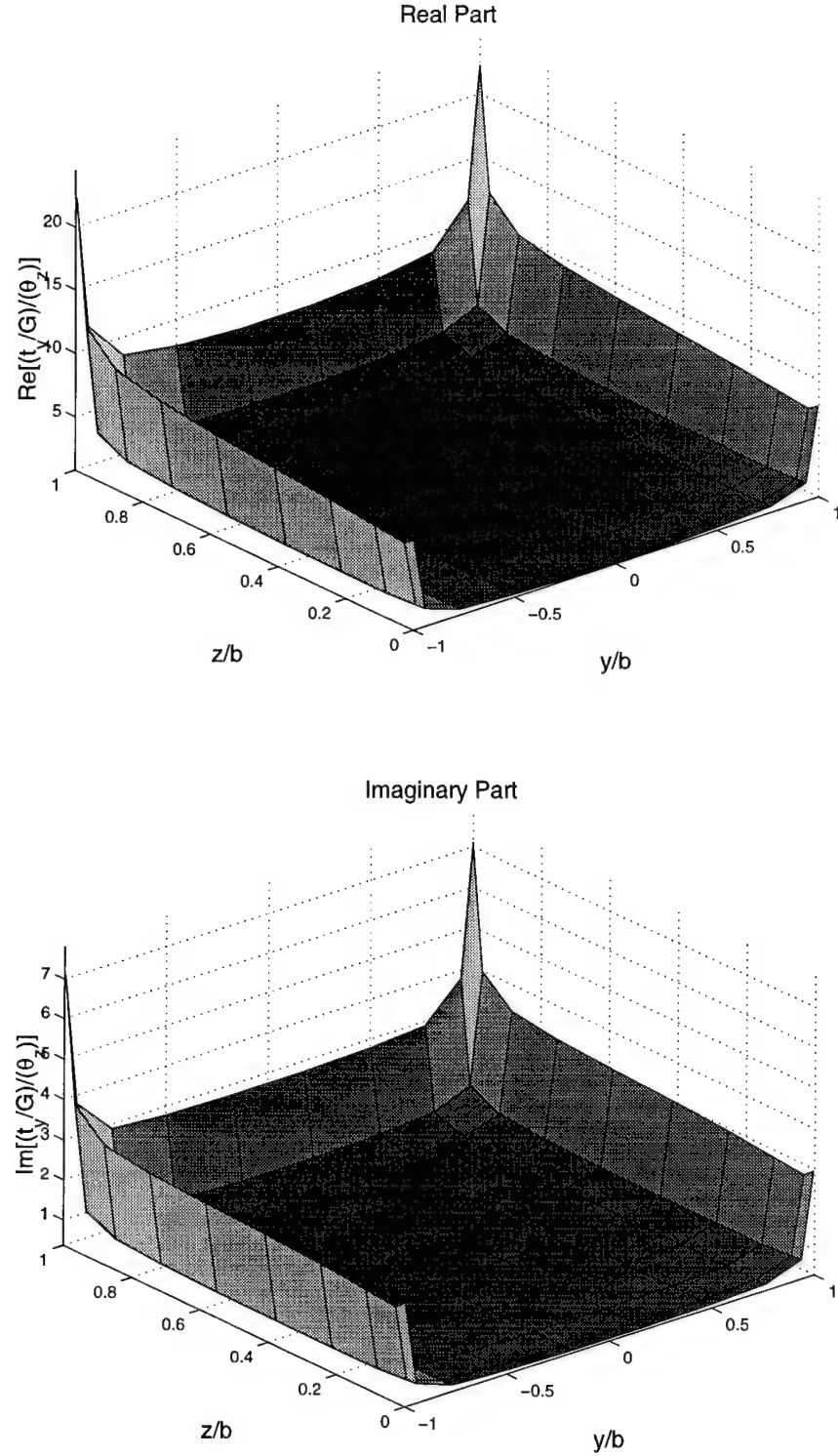
Figure 2.14: Distribution of shear contact tractions t_y corresponding to dynamic stiffness $\bar{K}_{tt}(\bar{\omega} = 1.0)$ for a homogeneous half-space. (X-face of the rigid foundation, $h/b = 1.0$, $\nu = 0.25$)
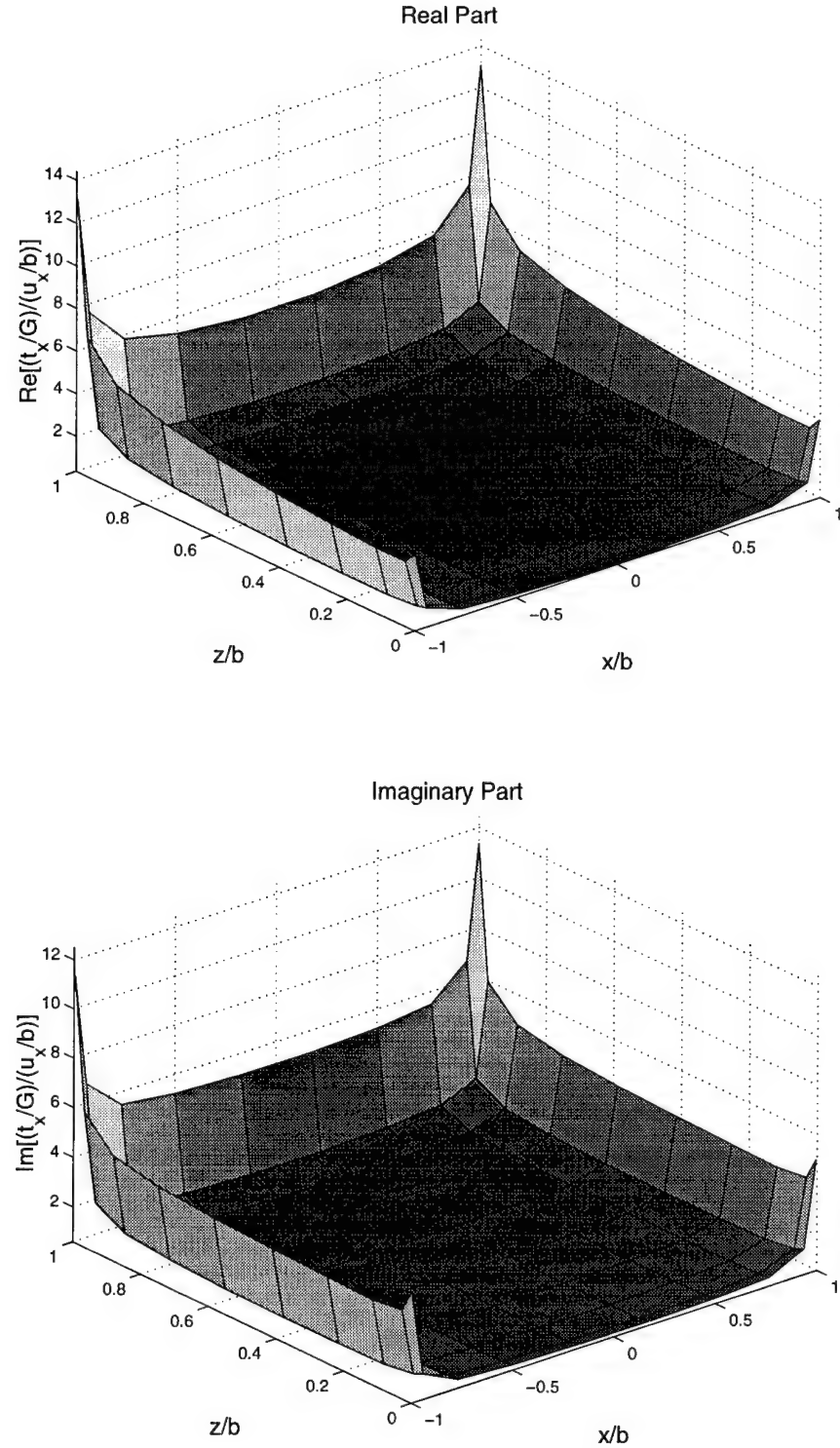
Figure 2.15: Distribution of shear contact tractions t_x corresponding to dynamic stiffness $\bar{K}_{hh}(\bar{\omega} = 1.0)$ for a homogeneous half-space. (Y-face of the rigid foundation, $h/b = 1.0$, $\nu = 0.25$)
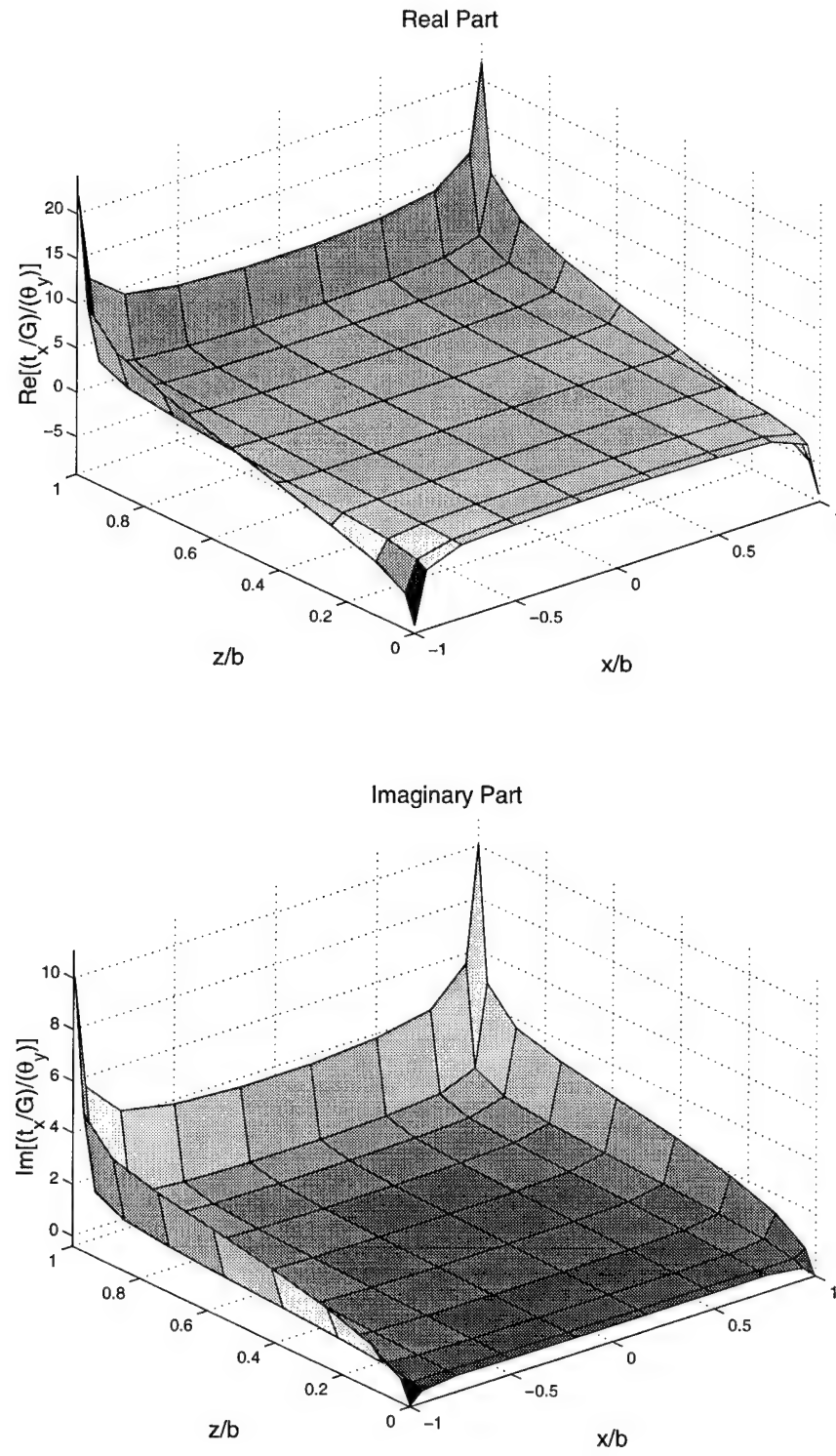
Figure 2.16: Distribution of shear contact tractions t_x corresponding to dynamic stiffness $\bar{K}_{mm}(\bar{\omega} = 1.0)$ for a homogeneous half-space. (Y-face of the rigid foundation, $h/b = 1.0$, $\nu = 0.25$)

ties of the tractions can be seen in Figures 2.3 to 2.16 which show the tractions on each face of a rigid cavity embedded to $h/b = 1.0$ in a homogeneous half-space with a Poisson's ratio of 0.25. The homogeneous half-space Green's function derivation is presented in Pak [30] for an arbitrary, time-harmonic, finite, internal source.

2.2.4   Hybrid Formulations

An interesting approach to computing the components of the interfacial impedance matrix was proposed by Mita and Luco [26] and involves combining finite and boundary element methods. They present a hybrid formulation which utilizes the Green's functions for a half-space continuum in combination with a finite element discretization of the soil excavated for the foundation. Tabulated results for a variety of embedment depths and half-space characteristics are presented in Mita and Luco [28]. Mita and Luco apply an approximate scheme where displacement compatibility between the foundation and the excavated portion of the half-space is imposed away from the soil-foundation interface to avoid the singularities. Additional approximations are made by assuming that the unknown sources are located in the interior of the excavated soil region instead of on the soil-foundation interface. Mita and Luco compare results from their formulation with some of the boundary element results mentioned above ([6], [7], [20], [37], [38]) in a subsequent publication [27].

2.3   Comparison of Results

In the present study, the analysis developed by Pak and Guzina [33] will be employed due to its rigor and generality. To check the degree of accuracy of past approaches, the results for a homogeneous half-space ($\nu = 0.25$) is computed and compared with the approximate approach by Gazetas [8] and the hybrid approach by Mita and Luco [28]. The impedances from Mita and Luco were computed for a

complex Poisson's ratio with a small imaginary component and a real component equal to 0.25, and a shear modulus with an imaginary component in the form $G = G_o(1 + 0.002i)$. One should also note that Gazetas' formula for an arbitrarily shaped footing is not for a specific Poisson's ratio, although in some of the formulas there is a distinction between $\nu > 0.4$ and $\nu < 0.4$. In this case, the formula in Gazetas for $\nu < 0.4$ is used to correspond to the case of $\nu = 0.25$ in the other two approaches.

Figures 2.17 to 2.20 present the impedances obtained by the three approaches for an embedment depth of $h/b = 1.0$ in terms of the spring and dashpot coefficients. The dimensionless impedances $\bar{K}_{ij}$ in Equation (2.9) are related to the spring and dashpot coefficients according to

$$\bar{K}_{vv}(\bar{\omega}) = k_{vv}(\bar{\omega}) + i\bar{\omega}c_{vv}(\bar{\omega}),$$

$$\bar{K}_{hh}(\bar{\omega}) = k_{hh}(\bar{\omega}) + i\bar{\omega}c_{hh}(\bar{\omega}),$$

$$\bar{K}_{mm}(\bar{\omega}) = k_{mm}(\bar{\omega}) + i\bar{\omega}c_{mm}(\bar{\omega}), \tag{2.15}$$

$$\bar{K}_{mh}(\bar{\omega}) = k_{mh}(\bar{\omega}) + i\bar{\omega}c_{mh}(\bar{\omega}),$$

$$\bar{K}_{tt}(\bar{\omega}) = k_{tt}(\bar{\omega}) + i\bar{\omega}c_{tt}(\bar{\omega}),$$

where $k_{ij}(\bar{\omega})$ and $c_{ij}(\bar{\omega})$ are the spring and dashpot coefficients $(i, j = v, h, m, t)$. The dimensionless frequency $\bar{\omega}$ is defined by

$$\bar{\omega} = \frac{\omega b}{C_s}, \tag{2.16}$$

where C_s is the shear wave velocity of the medium. The plots in Figures 2.17 to 2.20 reveal that the rigorous solution employed in this investigation and the result from Mita and Luco are quite close overall. The differences between the two can probably be attributed to the approximate method used by Mita and Luco, where the displacement compatibility between the foundation and the "excavated" portion of the half-space is imposed at a fictitious non-interfacial surface. Guzina [13]

notes that Mita and Luco underestimate the value of the dashpot coefficient in many cases. This can be seen clearly in the plots for c_{hh} and c_{mh}, and for c_{mm} above $\bar{\omega} = 1.0$. The impedances from Gazetas are similar to the other two sets of impedances and may be a good approximation in some cases. However, in general, the resulting dynamic impedances do not capture the true frequency dependent characteristics of the problem. For example, his formula predicts that the spring and dashpot coefficients associated with the rocking and coupling modes in Figures 2.19 and 2.20 to be linear, whereas exact impedances show obvious frequency dependence which is not linear. For k_{vv}, the error in Gazetas' solution increases with frequency and is over 50% at $\bar{\omega} = 2.0$. Likewise, k_{hh} differs by about 13% at $\bar{\omega} = 2.0$, c_{mm} differs by more than 400% at low frequencies, and k_{mh} differs by 80% at $\bar{\omega} = 2.0$. Given the rigor of the current method over the other two approaches, impedances presented in the remainder of this investigation are computed based on the formulation by Pak and Guzina [33].
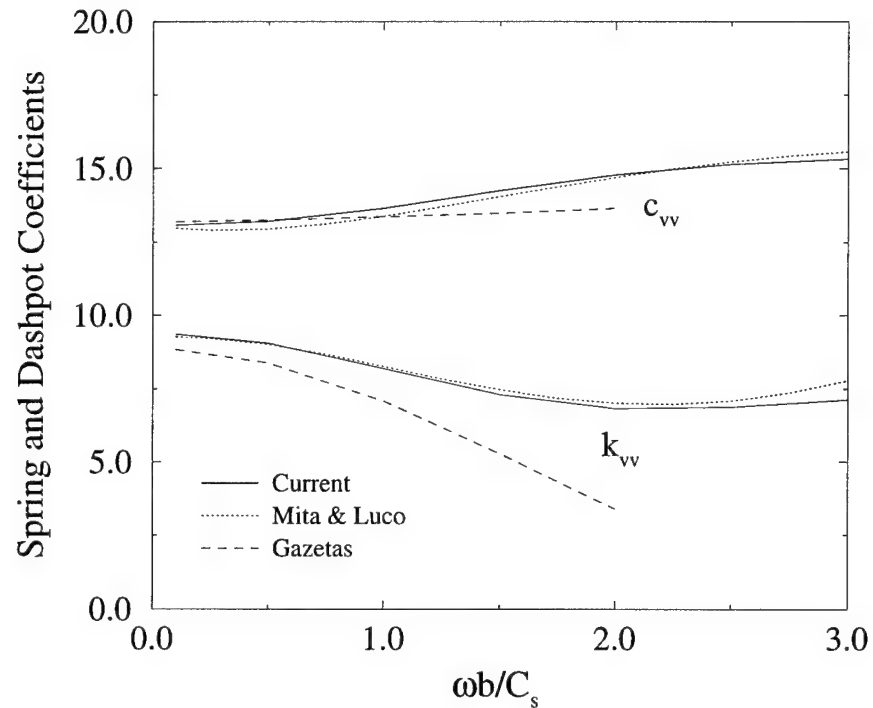
Figure 2.17: Dynamic vertical spring and dashpot coefficients for a rigid embedded square foundation (h/b=1.0).
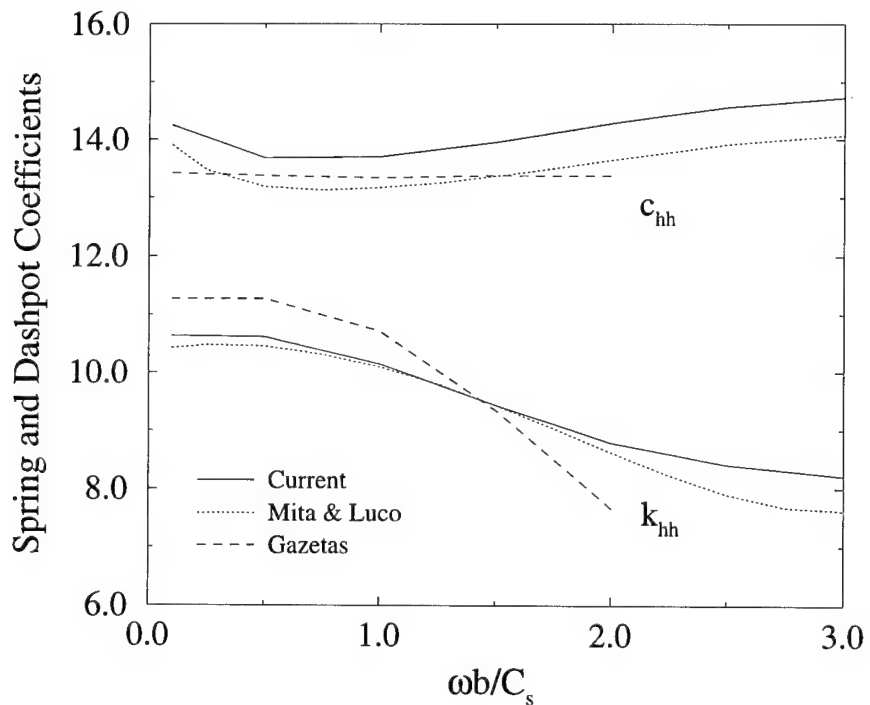
Figure 2.18: Dynamic horizontal spring and dashpot coefficients for a rigid embedded square foundation (h/b=1.0).
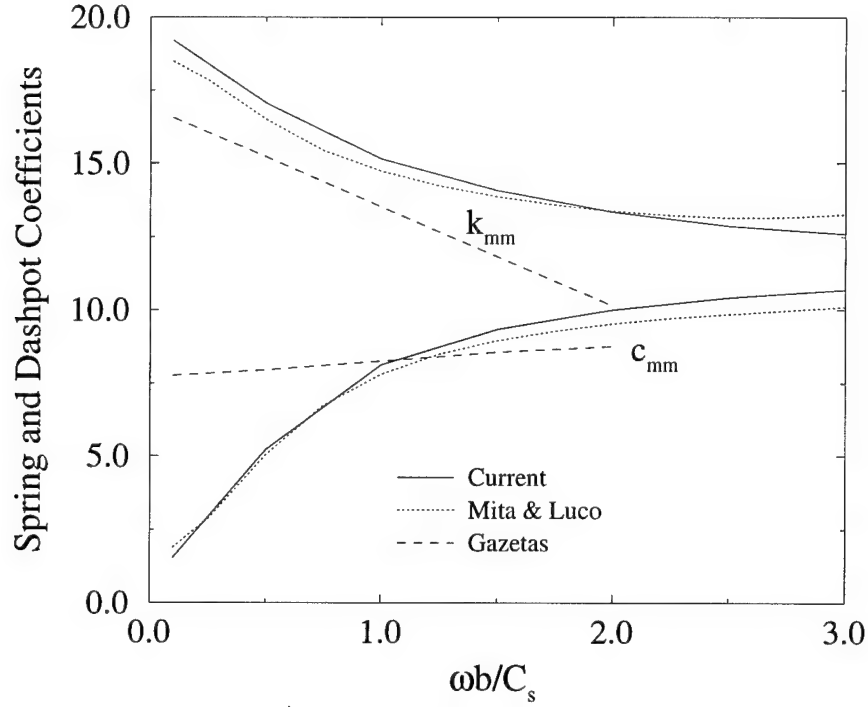
Figure 2.19: Dynamic rocking spring and dashpot coefficients for a rigid embedded square foundation (h/b=1.0).
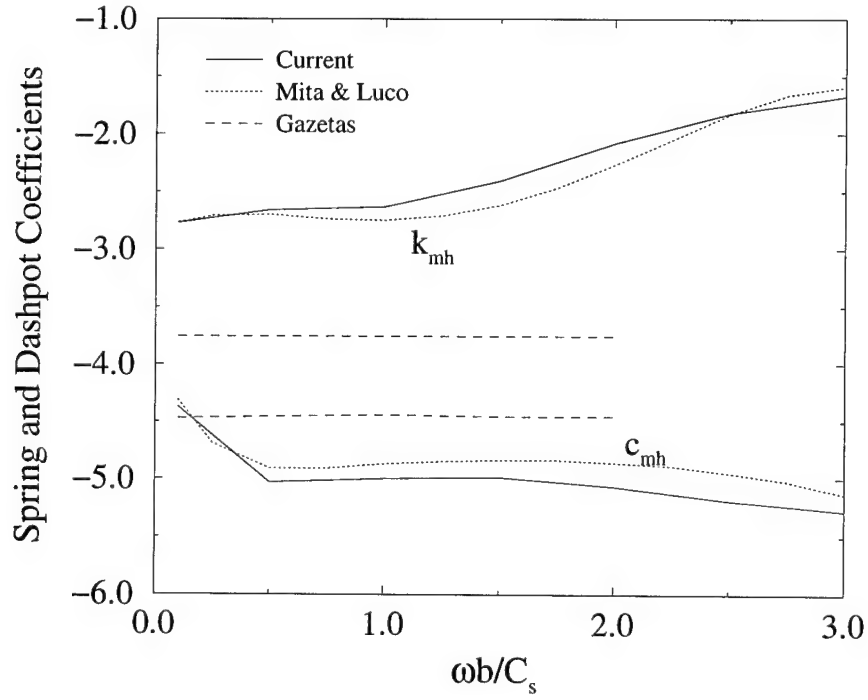
Figure 2.20: Dynamic coupling spring and dashpot coefficients for a rigid embedded square foundation (h/b=1.0).

2.4 Change in Impedance with Depth of Embedment for the Homogeneous Half-Space

As a benchmark reference for the dynamic behavior, Table 2.1 shows the static values of the interfacial impedances for a foundation embedded in a homogeneous half-space with a Poisson's ratio of 0.25 for embedment depths of $h/b = 0.0$ to 4.0 (see also Figures 2.21 to 2.23). Additionally, Figures 2.24 to 2.27 show the dynamic impedances for $\bar{\omega} = 0.0$ to 4.0 for embedment depths of $h/b = 0.0$, $h/b = 1.0$, and $h/b = 2.0$. The dynamic impedances in Figures 2.24 to 2.27 are normalized by the static values for the appropriate embedment depth given in Table 2.1. Even though the focus of this investigation is on vertical and lateral vibrations of embedded foundations, the torsional impedance K_{tt} is also provided in Table 2.1 and Figures 2.22 and 2.28 for completeness.

Figures 2.21, 2.22 and 2.23 reveal that all impedances increase in magnitude with increasing embedment. One can see that $\bar{K}_{vv}$ and $\bar{K}_{hh}$ increase at a more moderate rate for the embedment depths shown than $\bar{K}_{mm}$ and $\bar{K}_{mh}$. One can also see that $\bar{K}_{mh}$ is positive for shallow embedment depths, but is negative for deeper embedments. This phenomenon will be discussed further in Section 2.5.1.

Dynamically, the real parts of the normalized impedances show approximately the same trends throughout the frequency range of interest, regardless of embedment depth, with the primary difference in dynamic impedance with increasing embedment coming as a result of the static impedance given in Table 2.1. The imaginary parts do show an increase with increasing embedment, even when normalized by the static value. This observation has significant practical implication in that an embedded foundation can realize greater radiation damping than a surface footing.

h/b	$\bar{K}_{vv}$	$\bar{K}_{hh}$	$\bar{K}_{mm}$	$\bar{K}_{mh}$	$\bar{K}_{tt}$
0.00	6.39	5.36	5.94	0.68	8.56
0.10	6.85	6.28	7.07	0.50	11.85
0.25	7.36	7.21	8.59	0.17	15.44
0.50	8.09	8.48	11.50	-0.60	20.76
0.75	8.76	9.58	15.05	-1.60	25.79
1.00	9.38	10.59	19.37	-2.81	30.69
1.25	9.97	11.53	24.55	-4.21	35.52
1.50	10.54	12.43	30.75	-5.82	40.30
1.75	11.09	13.28	37.94	-7.56	45.05
2.00	11.63	14.11	46.33	-9.50	49.78
2.25	12.16	14.91	55.94	-11.60	54.49
2.50	12.67	15.69	66.85	-13.85	59.19
2.75	13.17	16.45	79.17	-16.27	63.89
3.00	13.66	17.19	92.91	-18.82	68.58
3.25	14.15	17.92	108.20	-21.54	73.26
3.50	14.62	18.63	125.10	-24.38	77.94
3.75	15.09	19.34	143.70	-27.42	82.62
4.00	15.56	20.03	164.00	-30.55	87.29

Table 2.1: Static impedance vs. depth of embedment for a rigid cavity embedded in a homogeneous half-space with $\mathbf{x}_{ref} = (0, 0, h)$.
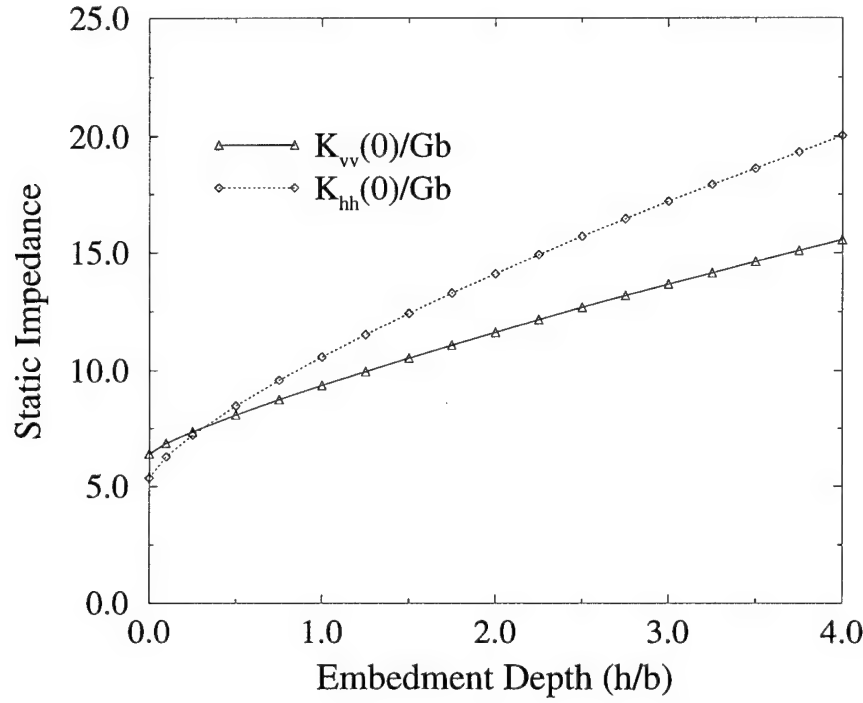
Figure 2.21: Static vertical ($\bar{K}_{vv}$) and horizontal ($\bar{K}_{hh}$) impedance versus embedment depth (h/b).
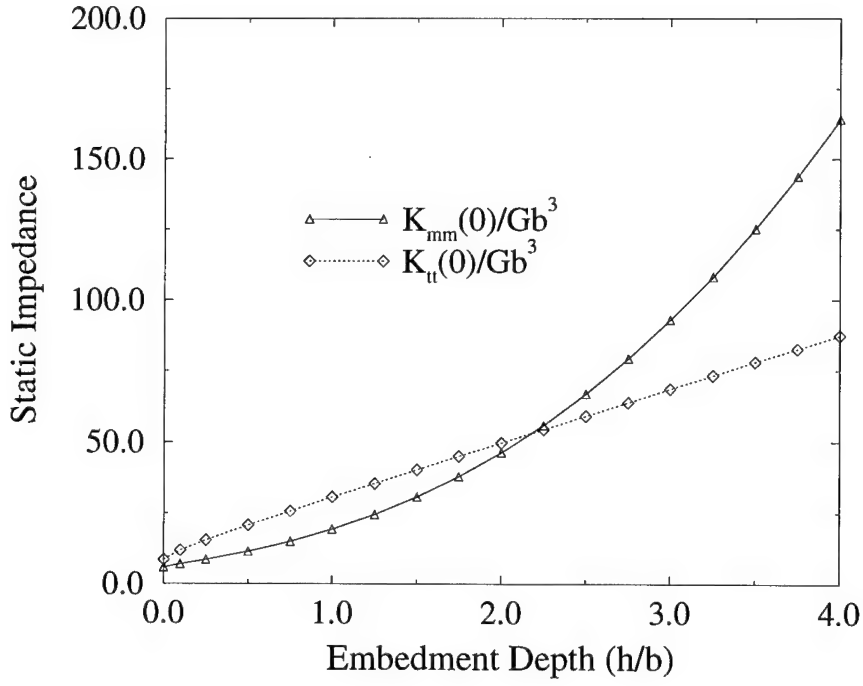
Figure 2.22: Static rocking ($\bar{K}_{mm}$) and torsional ($\bar{K}_{tt}$) impedance versus embedment depth (h/b).
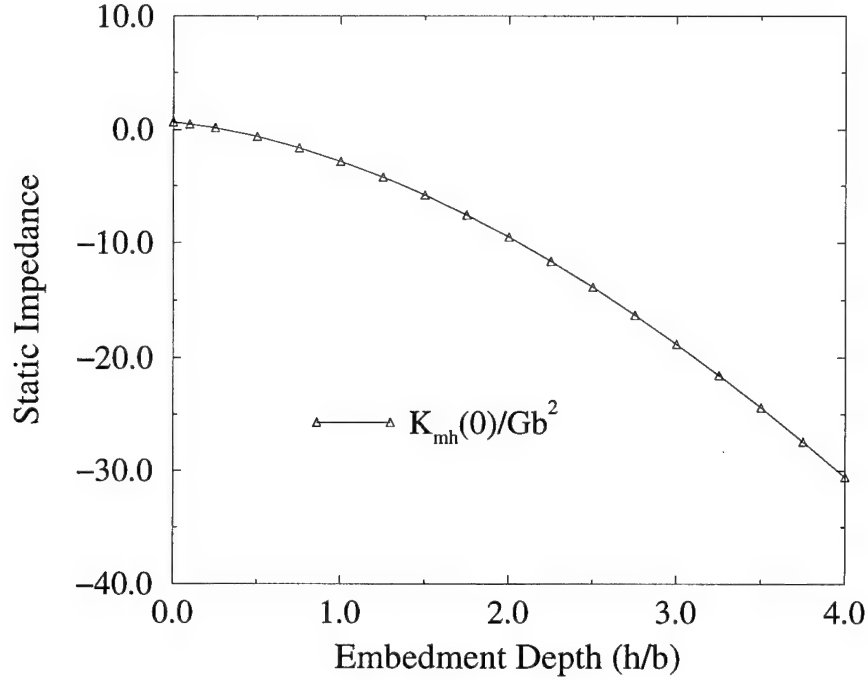
Figure 2.23: Static coupling impedance ($\bar{K}_{mh}$) versus embedment depth (h/b).
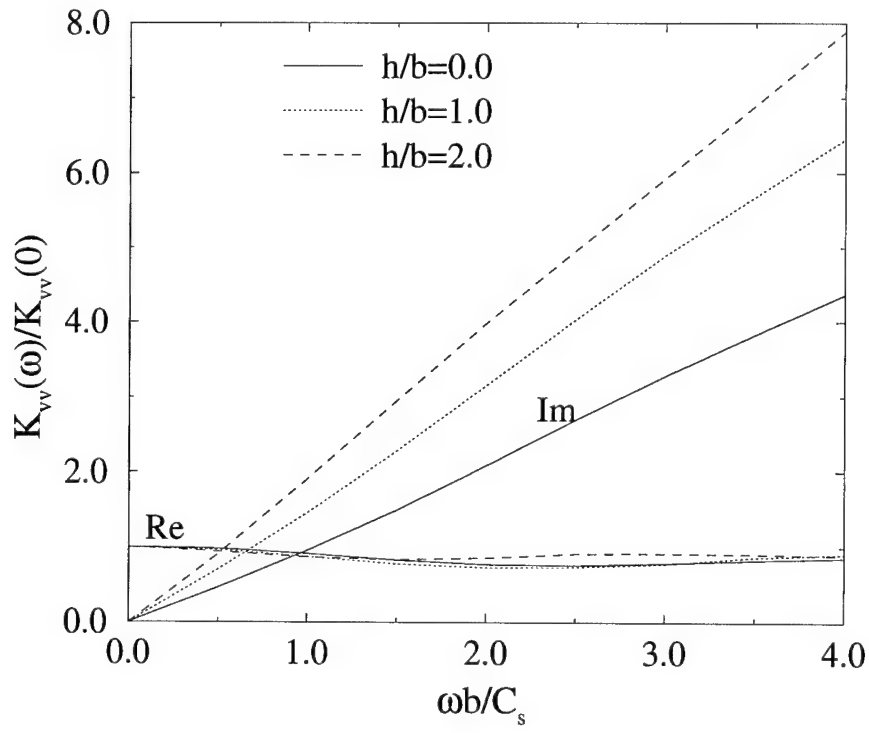
Figure 2.24: Normalized dynamic vertical stiffness ($\bar{K}_{vv}$) for a square foundation embedded in a homogeneous half-space, $\nu = 0.25$.
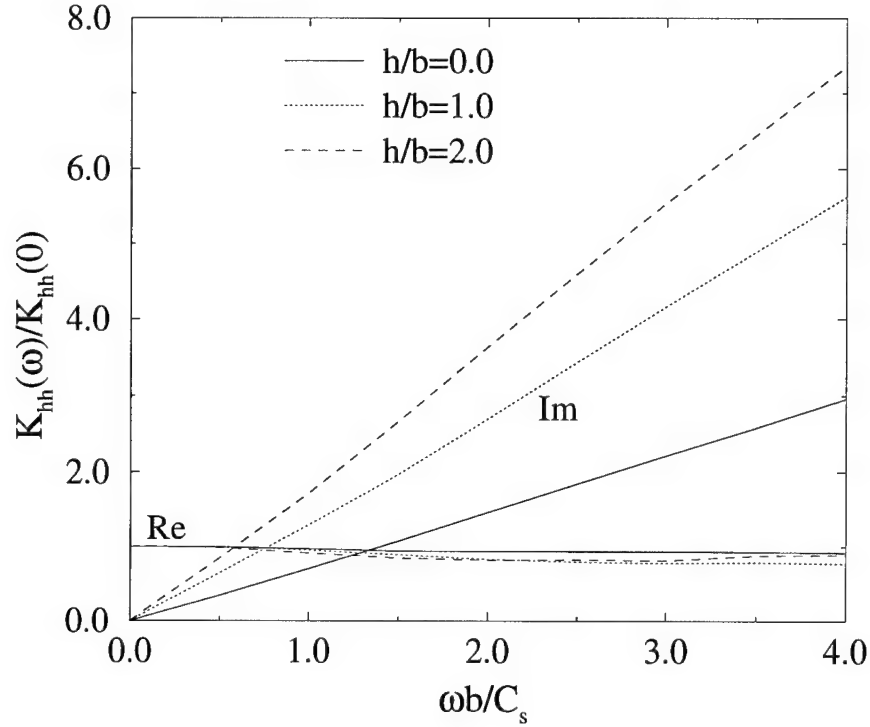
Figure 2.25: Normalized dynamic horizontal stiffness ($\bar{K}_{hh}$) for a square foundation embedded in a homogeneous half-space, $\nu = 0.25$.
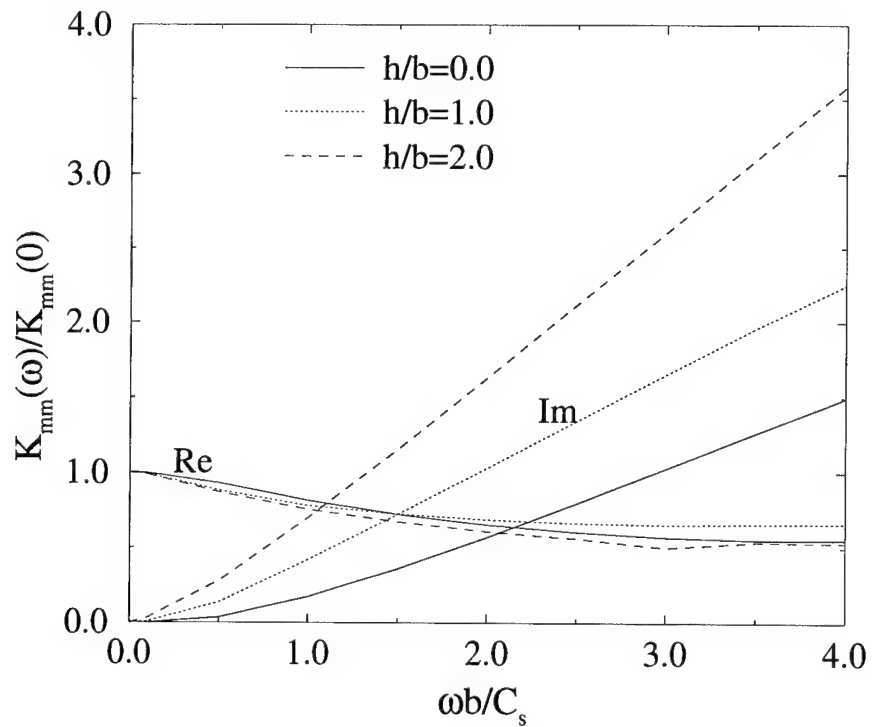
Figure 2.26: Normalized dynamic rocking stiffness ($\bar{K}_{mm}$) for a square foundation embedded in a homogeneous half-space, $\nu = 0.25$.
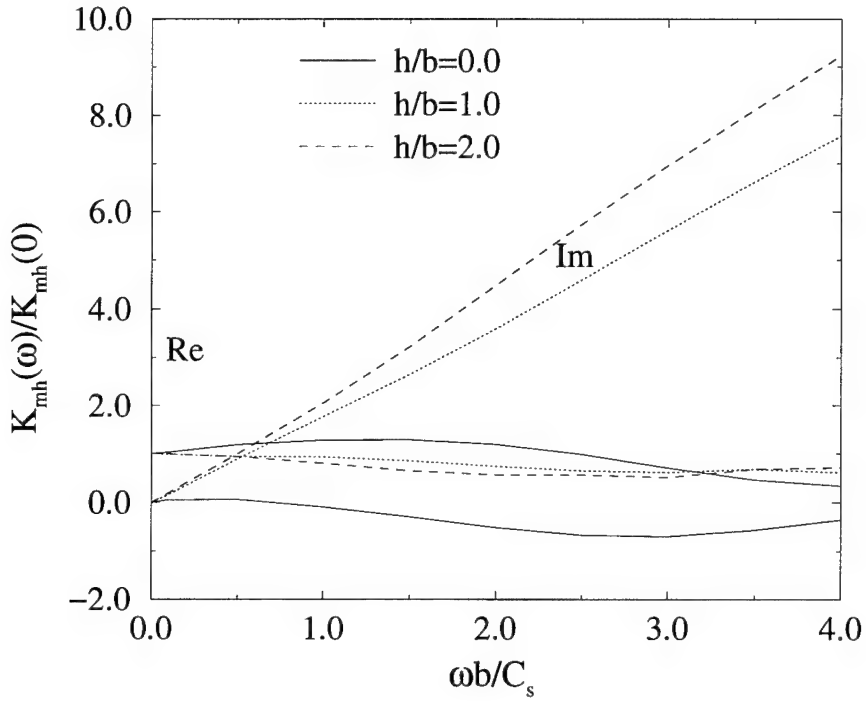
Figure 2.27: Normalized dynamic coupling stiffness ($\bar{K}_{mh}$) for a square foundation embedded in a homogeneous half-space, $\nu = 0.25$.
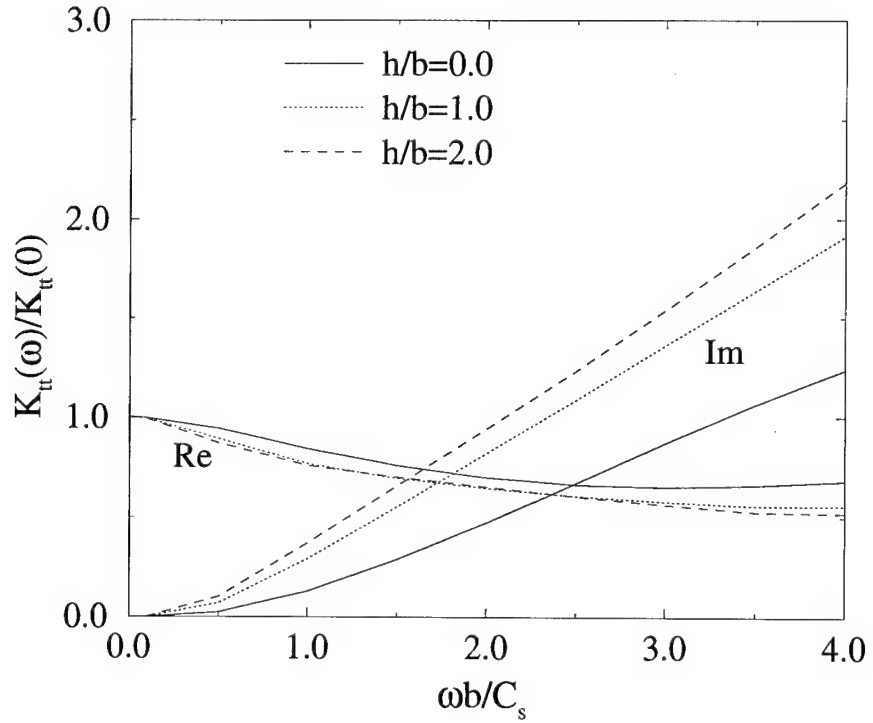
Figure 2.28: Normalized dynamic torsional stiffness ($\bar{K}_{tt}$) for a square foundation embedded in a homogeneous half-space, $\nu = 0.25$.

2.5   Choice of Control Point for Impedance Computation

2.5.1   Sign Change in $\bar{K}_{mh}$

As mentioned in Section 2.4 there is an interesting change of sign of $\bar{K}_{mh}$ and $\bar{K}_{hm}$ as embedment depth increases. To make it easier to visualize this response, it is helpful to make use of the concept of compliances which is more closely related to the manner in which the physical experiments are conducted on a soil-structure system. Recall that one can express the relationship between the displacements and resultant interfacial forces at any control point as,

$$\begin{pmatrix} \bar{U}_x \\ \bar{\Theta}_y \end{pmatrix} = \begin{bmatrix} \bar{C}_{hh} & \bar{C}_{hm} \\ \bar{C}_{mh} & \bar{C}_{mm} \end{bmatrix} \begin{pmatrix} \bar{F}_x \\ \bar{M}_y \end{pmatrix} \tag{2.17}$$

where $\bar{C}_{ij}$ are the foundation compliance functions. In this form, it is important to note that when the impedance coupling terms are negative, then the compliance coupling terms are often positive, and vice versa. Table 2.2 shows the dimensionless static compliances corresponding to the impedances in Table 2.1. If a unit force is applied in the positive x-direction without a corresponding moment, then (2.17) becomes

$$\begin{pmatrix} \bar{U}_x \\ \bar{\Theta}_y \end{pmatrix} = \begin{bmatrix} \bar{C}_{hh} & \bar{C}_{hm} \\ \bar{C}_{mh} & \bar{C}_{mm} \end{bmatrix} \begin{pmatrix} \bar{F}_x \\ 0 \end{pmatrix}, \tag{2.18}$$

which yields the following translation $\bar{U}_x$ and rotation $\bar{\Theta}_y$ per unit force

$$\frac{\bar{U}_x}{\bar{F}_x} = \bar{C}_{hh}, \quad \frac{\bar{\Theta}_y}{\bar{F}_x} = \bar{C}_{mh}. \tag{2.19}$$

For a surface foundation or a foundation with very shallow embedment, $\bar{C}_{mh}$ is negative, indicating that the rotation per unit force $(\bar{\Theta}_y/\bar{F}_x)$ of the footing is clockwise as illustrated in Figure 2.29a. For a square foundation with an embedment depth of $0.5b$ or greater, $\bar{C}_{mh}$ from Table 2.2 for a control point at $(0, 0, h)$ is posi-

h/b	$\bar{C}_{vv}$	$\bar{C}_{hh}$	$\bar{C}_{mm}$	$\bar{C}_{mh}$	$\bar{C}_{tt}$
0.00	0.1565	0.1891	0.1709	-0.0215	0.1168
0.25	0.1359	0.1387	0.1164	-0.0027	0.0648
0.50	0.1236	0.1183	0.0873	0.0062	0.0482
0.75	0.1142	0.1062	0.0677	0.0113	0.0388
1.00	0.1066	0.0982	0.0537	0.0143	0.0326
1.25	0.1003	0.0925	0.0435	0.0159	0.0282
1.50	0.0949	0.0883	0.0357	0.0167	0.0248
1.75	0.0902	0.0849	0.0297	0.0169	0.0222
2.00	0.0860	0.0822	0.0250	0.0169	0.0201
2.25	0.0822	0.0800	0.0213	0.0166	0.0184
2.50	0.0789	0.0780	0.0183	0.0162	0.0169
2.75	0.0759	0.0763	0.0159	0.0157	0.0157
3.00	0.0732	0.0748	0.0138	0.0151	0.0146
3.25	0.0707	0.0734	0.0121	0.0146	0.0137
3.50	0.0684	0.0721	0.0107	0.0140	0.0128
3.75	0.0663	0.0709	0.0095	0.0135	0.0121
4.00	0.0643	0.0697	0.0085	0.0130	0.0115

Table 2.2: Static compliance vs. depth of embedment for a rigid cavity embedded in a homogeneous half-space with $\mathbf{x}_{ref} = (0, 0, h)$.

tive, indicating that the rotation per unit force of the footing is counter-clockwise as illustrated in Figure 2.29.

a) Coupled rotational motion for shallow embedment under horizontal force

b) Coupled rotational motion for deep embedment under horizontal force
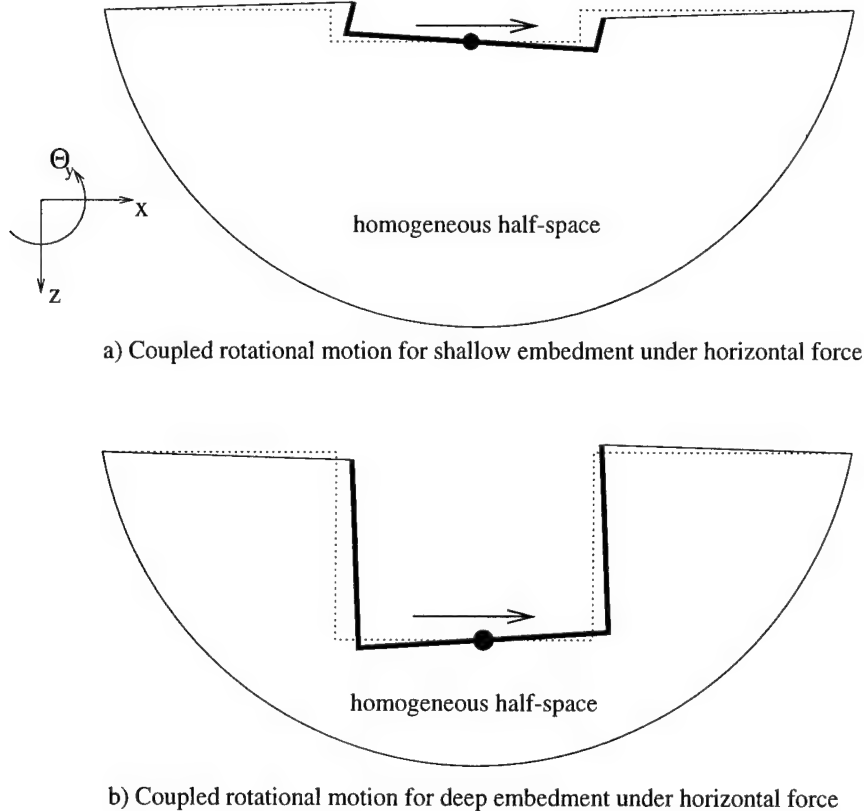
Figure 2.29: Physical implication of $\bar{C}_{mh}$ and $\bar{C}_{hm}$ for (0,0,h).

2.5.2 Relationship Between the Interfacial Impedances at Different Control Points

To further clarify the issue of the sign change in $\bar{K}_{mh}$ with depth, it is useful to examine the corresponding interfacial impedances using a surface location as the control point. Since the impedances are calculated for a rigid massless foundation, they can be easily transferred from one point to another by a rigid-body kinematic transformation. Most of the literature reports the impedances at the point $(0, 0, h)$ of the bottom of the soil-foundation interface. Unlike the case of

a surface foundation, this point will constantly change as a function of embedment depth. Figure 2.30 shows an embedded footing with a reference point located at
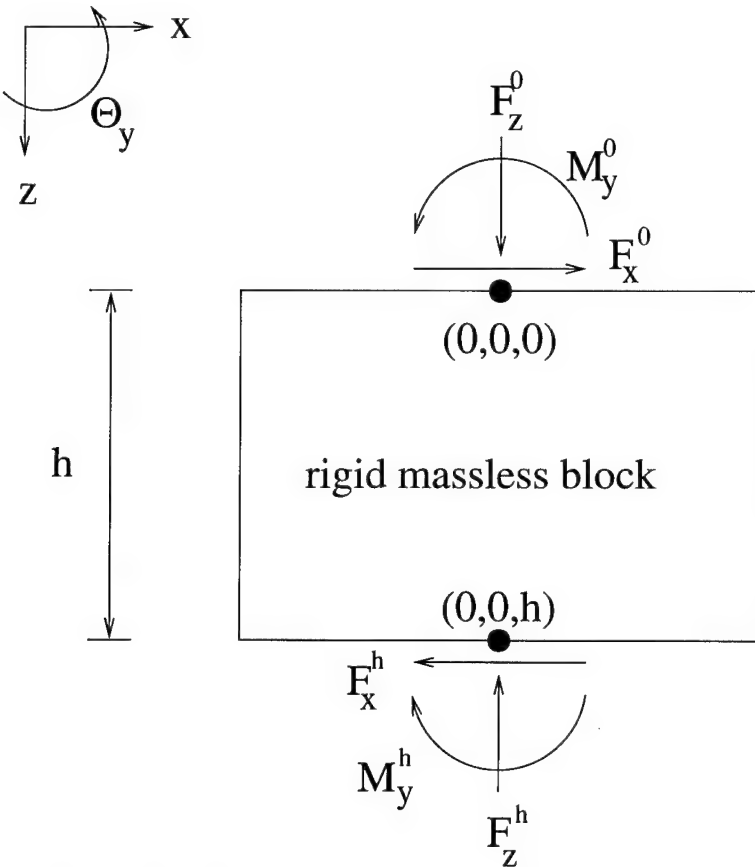
Figure 2.30: Illustration of rigid massless footing.

$\mathbf{0} = (0,0,0)$ on the top and one at $\mathbf{x}_h = (0,0,h)$ at the base. For the former choice, one may denote the resultant forces and displacements as $\mathbf{F}^0 = (F_z^0, F_x^0, M_y^0)^T$ and $\mathbf{U}^0 = (U_z^0, U_x^0, \Theta_z^0)^T$ respectively. For the latter choice of reference location, the resultant forces and displacements are defined as $\mathbf{F}^h = (F_z^h, F_x^h, M_y^h)^T$ and $\mathbf{U}^h = (U_z^h, U_x^h, \Theta_z^h)^T$ respectively. Since the block is massless, it can be shown by

the three equations of motion that

$$\Sigma \bar{F}_z = 0 = \bar{F}_z^0 - \bar{F}_z^h,$$

$$\Sigma \bar{F}_x = 0 = \bar{F}_x^0 - \bar{F}_x^h, \tag{2.20}$$

$$\Sigma \bar{M}_y^{(0,0,0)} = 0 = \bar{M}_y^0 - \bar{M}_y^h - \bar{h}\bar{F}_x^h,$$

where $\bar{h} = \frac{h}{b}$. Additionally, the displacements at the two points can be related according to

$$\bar{U}_z^0 = \bar{U}_z^h,$$

$$\bar{U}_x^0 = \bar{U}_x^h + \bar{h}\bar{\Theta}_y, \tag{2.21}$$

$$\bar{\Theta}_y^0 = \bar{\Theta}_y^h,$$

and the impedance relationships can be written as

$$\bar{\mathbf{F}}^0 = \bar{\mathbf{K}}^0 \bar{\mathbf{U}}^0, \quad \bar{\mathbf{F}}^h = \bar{\mathbf{K}}^h \bar{\mathbf{U}}^h \tag{2.22}$$

where

$$\bar{\mathbf{K}}^0 = \begin{bmatrix} \bar{K}_{vv}^0 & 0 & 0 \\ 0 & \bar{K}_{hh}^0 & \bar{K}_{mh}^0 \\ 0 & \bar{K}_{hm}^0 & \bar{K}_{mm}^0 \end{bmatrix}, \tag{2.23}$$

are the impedances at $\mathbf{0}$ and

$$\bar{\mathbf{K}}^h = \begin{bmatrix} \bar{K}_{vv}^h & 0 & 0 \\ 0 & \bar{K}_{hh}^h & \bar{K}_{mh}^h \\ 0 & \bar{K}_{hm}^h & \bar{K}_{mm}^h \end{bmatrix}, \tag{2.24}$$

are the impedances at $\mathbf{x}_h$. Using Equations 2.20 and 2.21, the impedances at $\mathbf{0}$ are related to the impedances at $\mathbf{x}_h$ according to

$$\bar{\mathbf{K}}^0 = \mathbf{Q}\bar{\mathbf{K}}^h\mathbf{Q}^T \tag{2.25}$$

where

$$\mathbf{Q} = \begin{bmatrix} 1 & 0 & 0 \\ 0 & 1 & 0 \\ 0 & \bar{h} & 1 \end{bmatrix}. \tag{2.26}$$

In a similar manner, the compliances at $\mathbf{0}$ are related to the compliances at $\mathbf{x}_h$ by

$$\bar{\mathbf{C}}^0 = \mathbf{Q}^{-T} \bar{\mathbf{C}}^h \mathbf{Q}^{-1} \tag{2.27}$$

Using (2.25) and (2.26), the impedances can be transferred from $\mathbf{x}_h = (0, 0, h)$ to $\mathbf{0} = (0, 0, 0)$. Likewise, the impedances can be transferred to any vertical point between $\mathbf{x}_h$ and $\mathbf{0}$ by substituting another value for h which is between 0 and h. The impedances at $\mathbf{0}$ are shown in Table 2.3and, for completeness, the compliances are shown in Table 2.4. One can see that the coupling terms $(\bar{K}_{mh}$ and $\bar{K}_{hm})$ are now always positive for different h's when reported at $\mathbf{0}$ since the loading location $\mathbf{0}$ does not change. Physically, this makes the impedances easier to interpret since the magnitudes of the coupling terms at various embedment depths can be examined directly without having to account for the sign change. In an analysis, however, the point $\mathbf{x}_h$ is generally the most convenient location for the impedances since it is located on the soil-foundation interface.

Based on the kinematic relationships in Equations (2.25) and (2.26), Table 2.3 expectedly reveals that $\bar{K}_{vv}^0$, $\bar{K}_{hh}^0$, and $\bar{K}_{tt}^0$ at $\mathbf{0}$ are the same as $\bar{K}_{vv}^h$, $\bar{K}_{hh}^h$, and $\bar{K}_{tt}^h$ at $\mathbf{x}_h$ given in Table 2.1. On the other hand, both $\bar{K}_{mm}^0$ and $\bar{K}_{mh}^0$ are larger than $\bar{K}_{mm}^h$ and $\bar{K}_{mh}^h$.

2.5.3   The Concept of Principal Impedance

Since the coupling terms are positive at $\mathbf{0}$ and negative (for $h/b > 0.3$) at $\mathbf{x}_h$, it is evident that there must be a point lying between $(0, 0, 0)$ and $(0, 0, h)$ where the coupling terms are exactly zero. At such a point, which will be called

h/b	$\bar{K}_{vv}^0$	$\bar{K}_{hh}^0$	$\bar{K}_{mm}^0$	$\bar{K}_{mh}^0$	$\bar{K}_{tt}^0$
0.00	6.39	5.37	5.94	0.68	8.56
0.25	7.36	7.21	9.13	1.97	15.44
0.50	8.09	8.48	13.02	3.64	20.76
0.75	8.76	9.58	18.03	5.58	25.79
1.00	9.38	10.59	24.33	7.78	30.69
1.25	9.97	11.53	32.04	10.20	35.52
1.50	10.54	12.43	41.27	12.83	40.30
1.75	11.09	13.28	52.15	15.68	45.05
2.00	11.63	14.11	64.77	18.72	49.78
2.25	12.16	14.91	79.22	21.95	54.49
2.50	12.67	15.69	95.67	25.38	59.19
2.75	13.17	16.45	114.09	28.97	63.89
3.00	13.66	17.19	134.70	32.75	68.58
3.25	14.15	17.92	157.47	36.70	73.26
3.50	14.62	18.63	182.66	40.83	77.94
3.75	15.09	19.34	210.02	45.11	82.62
4.00	15.56	20.03	240.08	49.57	87.29

Table 2.3: Static impedance vs. depth of embedment for a rigid cavity embedded in a homogeneous half-space with $\mathbf{x}_{ref} = (0, 0, 0)$.

h/b	$\bar{C}^0_{vv}$	$\bar{C}^0_{hh}$	$\bar{C}^0_{mm}$	$\bar{C}^0_{mh}$	$\bar{C}^0_{tt}$
0.00	0.1565	0.1891	0.1709	-0.0215	0.1168
0.25	0.1359	0.1473	0.1164	-0.0318	0.0648
0.50	0.1236	0.1339	0.0873	-0.0374	0.0482
0.75	0.1142	0.1273	0.0677	-0.0394	0.0388
1.00	0.1066	0.1234	0.0537	-0.0394	0.0326
1.25	0.1003	0.1207	0.0435	-0.0384	0.0282
1.50	0.0949	0.1185	0.0357	-0.0368	0.0248
1.75	0.0902	0.1167	0.0297	-0.0351	0.0222
2.00	0.0860	0.1149	0.0250	-0.0332	0.0201
2.25	0.0822	0.1133	0.0213	-0.0314	0.0184
2.50	0.0789	0.1116	0.0183	-0.0296	0.0169
2.75	0.0759	0.1100	0.0159	-0.0279	0.0157
3.00	0.0732	0.1084	0.0138	-0.0263	0.0146
3.25	0.0707	0.1068	0.0121	-0.0249	0.0137
3.50	0.0684	0.1052	0.0107	-0.0235	0.0128
3.75	0.0663	0.1036	0.0095	-0.0222	0.0121
4.00	0.0643	0.1021	0.0085	-0.0211	0.0115

Table 2.4: Static compliance vs. depth of embedment for a rigid cavity embedded in a homogeneous half-space with $\mathbf{x}_{ref} = (0, 0, 0)$.

$\mathbf{x}^* = (0, 0, h^*)$, the impedance matrix becomes diagonal as there is no coupling between the rocking and horizontal vibration modes. For the static case, the location of h^* as a function of embedment depth is shown in Table 2.5. For the dynamic problem, however, the precise location of h^* must be calculated for each frequency point since the impedances vary with frequency. Additionally, only the real part of the coupling terms will be guaranteed to be zero (unless at $\omega = 0.0$ where the imaginary part is always zero) since the depth h^* is a real value and cannot have an imaginary component. This concept is likely to be a useful consideration in the design of physical testing. Its full exploration, however, is beyond the present study.

h/b	0.50	1.00	1.50	2.00	2.50	3.00	3.50	4.00
h^*/b	0.429	0.734	1.032	1.327	1.617	1.905	2.191	2.475

Table 2.5: Location of h^*/b as a function of h/b.

2.6 Load Transfer to the Soil

In the study of embedded foundations, an item of basic interest is how the load is transferred through the sides and the base of the foundation to the soil. For fully bonded contact, the sides of the foundation will carry an increasing amount of the load when compared to the base as the depth of embedment increases. In addition to examining the case where a rigid-body translation or rotation is applied (corresponding to the impedance functions), it is also useful to examine the distribution of forces for the case where a pure force or a pure moment is applied (corresponding to the compliance coefficients). For this purpose, one can define the following eight states which can be invoked at $\mathbf{x}_{ref} = \mathbf{x}_h$ or $\mathbf{x}_{ref} = \mathbf{0}$,

(1) pure rigid body vertical translation

(2) pure rigid body horizontal translation

(3) pure rigid body rotation applied at the reference point about the y-axis

(4) pure rigid body rotation about the z-axis

(5) application of a pure vertical force

(6) application of a pure horizontal force at the reference point

(7) application of a pure moment at the reference about the y-axis

(8) application of a pure torsional moment about the z-axis.

where States 1 through 4 correspond to the impedances, and States 5 through 8 correspond to the compliances. Furthermore, a column vector $\mathcal{S}^j$, $j = 1, 2, \ldots, 8$ for each of the eight states can be defined where the components of the $\mathcal{S}^j$ are

$$\mathcal{S}^j = \left\{ \bar{F}_z^j, \bar{F}_x^j, \bar{M}_y^j, \bar{M}_z^j, \bar{u}_z^j, \bar{u}_x^j, \bar{\Theta}_y^j, \bar{\Theta}_z^j \right\}^T. \tag{2.28}$$

The individual force and displacement conditions are stated fully in Table 2.6, where the dimensionless forces and displacements are defined in Section 2.1 and the $\bar{K}_{ij}$ and $\bar{C}_{ij}$ can be found in Tables 2.1 and 2.2 respectively for $\mathbf{x}_{ref} = (0, 0, h)$. In Table 2.6, the imposed boundary conditions are unit displacements or loads and the $\bar{K}_{ij}$ and $\bar{C}_{ij}$ describe the response under the unit displacement or load. States $\mathcal{S}^1$, $\mathcal{S}^2$, $\mathcal{S}^3$, and $\mathcal{S}^4$ are calculated by the boundary element program as the impedances are computed and states $\mathcal{S}^5$ and $\mathcal{S}^8$ can be calculated directly from $\mathcal{S}^1$ and $\mathcal{S}^4$ since the vertical and torsional cases are uncoupled. States $\mathcal{S}^6$ and $\mathcal{S}^7$ can be calculated by multiplying $\mathcal{S}^2$ and $\mathcal{S}^3$ by two real parameters α and β to form each of the new states according to

$$\mathcal{S}^6 = \alpha^6 \mathcal{S}^2 + \beta^6 \mathcal{S}^3, \quad \mathcal{S}^7 = \alpha^7 \mathcal{S}^2 + \beta^7 \mathcal{S}^3. \tag{2.29}$$

State	$\bar{F}_z^j$	$\bar{F}_x^j$	$\bar{M}_y^j$	$\bar{M}_z^j$	$\bar{U}_z^j$	$\bar{U}_x^j$	$\bar{\Theta}_y^j$	$\bar{\Theta}_z^j$
$\mathcal{S}^1$	$\bar{K}_{vv}$	0.0	0.0	0.0	1.0	0.0	0.0	0.0
$\mathcal{S}^2$	0.0	$\bar{K}_{hh}$	$\bar{K}_{mh}$	0.0	0.0	1.0	0.0	0.0
$\mathcal{S}^3$	0.0	K_{hm}	$\bar{K}_{mm}$	0.0	0.0	0.0	1.0	0.0
$\mathcal{S}^4$	0.0	0.0	0.0	$\bar{K}_{tt}$	0.0	0.0	0.0	1.0
$\mathcal{S}^5$	1.0	0.0	0.0	0.0	$\bar{C}_{vv}$	0.0	0.0	0.0
$\mathcal{S}^6$	0.0	1.0	0.0	0.0	0.0	$\bar{C}_{hh}$	$\bar{C}_{mh}$	0.0
$\mathcal{S}^7$	0.0	0.0	1.0	0.0	0.0	$\bar{C}_{hm}$	$\bar{C}_{mm}$	0.0
$\mathcal{S}^8$	0.0	0.0	0.0	1.0	0.0	0.0	0.0	$\bar{C}_{tt}$

Table 2.6: Force and displacement conditions for $\mathcal{S}^1$ to $\mathcal{S}^8$ at $\mathbf{x}_{ref} = \mathbf{x}_h$ or $\mathbf{x}_{ref} = \mathbf{0}$.

The horizontal/rocking impedance sub-matrix corresponding to $\mathcal{S}^6$ and $\mathcal{S}^7$ can be written as

$$\begin{pmatrix} \bar{F}_x^6 \\ \bar{M}_y^6 \end{pmatrix} = \begin{bmatrix} \bar{F}_x^2 & \bar{F}_x^3 \\ \bar{M}_y^2 & \bar{M}_y^3 \end{bmatrix} \begin{pmatrix} \alpha^6 \\ \beta^6 \end{pmatrix} \tag{2.30}$$

and

$$\begin{pmatrix} \bar{F}_x^7 \\ \bar{M}_y^7 \end{pmatrix} = \begin{bmatrix} \bar{F}_x^2 & \bar{F}_x^3 \\ \bar{M}_y^2 & \bar{M}_y^3 \end{bmatrix} \begin{pmatrix} \alpha^7 \\ \beta^7 \end{pmatrix}. \tag{2.31}$$

The unit forces and moments desired in each case can be substituted into (2.30) and (2.31) which yields

$$\begin{pmatrix} 1 \\ 0 \end{pmatrix} = \begin{bmatrix} \bar{F}_x^2 & \bar{F}_x^3 \\ \bar{M}_y^2 & \bar{M}_y^3 \end{bmatrix} \begin{pmatrix} \alpha^6 \\ \beta^6 \end{pmatrix} \tag{2.32}$$

and

$$\begin{pmatrix} 0 \\ 1 \end{pmatrix} = \begin{bmatrix} \bar{F}_x^2 & \bar{F}_x^3 \\ \bar{M}_y^2 & \bar{M}_y^3 \end{bmatrix} \begin{pmatrix} \alpha^7 \\ \beta^7 \end{pmatrix}. \tag{2.33}$$

Solving for (α^6, β^6) and (α^7, β^7) yields

$$\beta^6 = \frac{1}{\bar{F}_x^3 - \frac{\bar{M}_y^3}{\bar{M}_y^2}\bar{F}_x^2}, \quad \alpha^6 = -\beta^6\frac{\bar{M}_y^3}{\bar{M}_y^2} \tag{2.34}$$

and

$$\beta^7 = \frac{1}{\bar{M}_y^3 - \frac{\bar{F}_x^3}{\bar{F}_x^2}\bar{M}_y^2}, \quad \alpha^7 = -\beta^7\frac{\bar{F}_x^3}{\bar{F}_x^2}. \tag{2.35}$$

Consequently, the forces and moments corresponding to $\mathcal{S}^5$ and $\mathcal{S}^6$ can be calculated quite easily. Additionally, the α and β pair for each new case can be multiplied by the forces on each face of the foundation to get the corresponding forces on each face for the two new cases. Figures 2.31, 2.32, and 2.33 show the distribution of forces between the sides and the base of the footing for both applied translations/rotations and applied forces/moments at both $\mathbf{x}_h = (0, 0, h)$ and $\mathbf{0} = (0, 0, 0)$.

Figure 2.31 shows the contributions of vertical resistance from the base and the sides for the application of a vertical translation $(\bar{U}_z)$. Since the vertical case is not coupled with any other vibration modes, this distribution of forces also corresponds to the response when a vertical force $\bar{F}_z$ is applied. Probably the most important location on the graph is the point at which the two lines cross, indicating the embedment depth at which the sides and base each distribute an equal amount of load to the soil medium. For vertical loading, this embedment depth is approximately $h/b = 0.75$.

Figure 2.32 shows the contributions of horizontal resistance from the base and sides of the footing for three cases of horizontal loading: (i) application of a rigid body horizontal translation $(\bar{U}_x)$, (ii) application of a pure horizontal force $(\bar{F}_x)$ at $\mathbf{x}_h$, and (iii) application of a pure horizontal force $(\bar{F}_x)$ at $\mathbf{0}$. The sides and base transfer an equal distribution of load at an embedment of about $h/b = 0.3$ for rigid translation and the application of a force at $\mathbf{x}_h$, which is relatively

shallow. For a horizontal force applied at $\mathbf{0}$, this depth is even shallower and is approximately $h/b = 0.2$.

Figure 2.33 shows the distribution of the resisting moment for four cases: (i) an application of a rigid body rotation $\bar{\Theta}_y$ about $\mathbf{x}_h$, (ii) application of a pure rotational moment $\bar{M}_y$ about the point $\mathbf{x}_h$, (iii) an application of a rigid body rotation $\bar{\Theta}_y$ about $\mathbf{0}$, and (iv) application of a pure rotational moment $\bar{M}_y$ about the point $\mathbf{0}$. One can see from Figure 2.33 that the base resistance is mobilized more for a rotation or moment applied at $\mathbf{0}$ than for a rotation or moment applied at $\mathbf{x}_h$. For $\mathbf{0}$, the base still provides 30 to 40% of the resistance versus less than 5% at $\mathbf{x}_h$. Additionally, the sides and base each provide 50% of the total resistance at an embedment depth of about 0.3 for applied moment or rotation at $\mathbf{x}_h$, whereas this depth is about 0.7 for a moment or rotation at $\mathbf{0}$.

Figure 2.34 shows the contributions of torsional resistance from the base and the sides of an embedded foundation for the application of a torsional rotation about the z-axis ($\bar{\Theta}_z$). The sides and base share the load equally at a very shallow depth of about $h/b = 0.15$, and the sides provide over 90% of the resistance at $h/b = 4.0$.
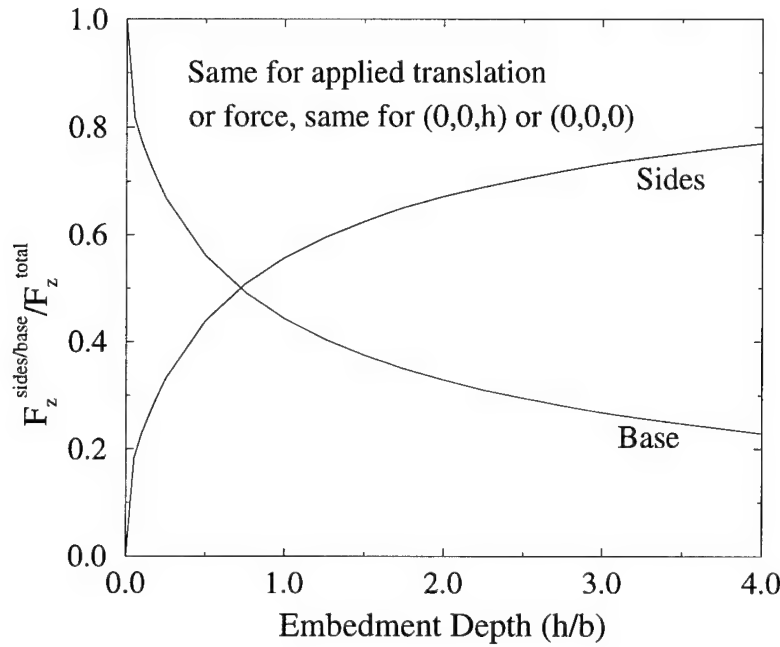
Figure 2.31: Components of vertical resistance vs. embedment depth for the homogeneous half-space.
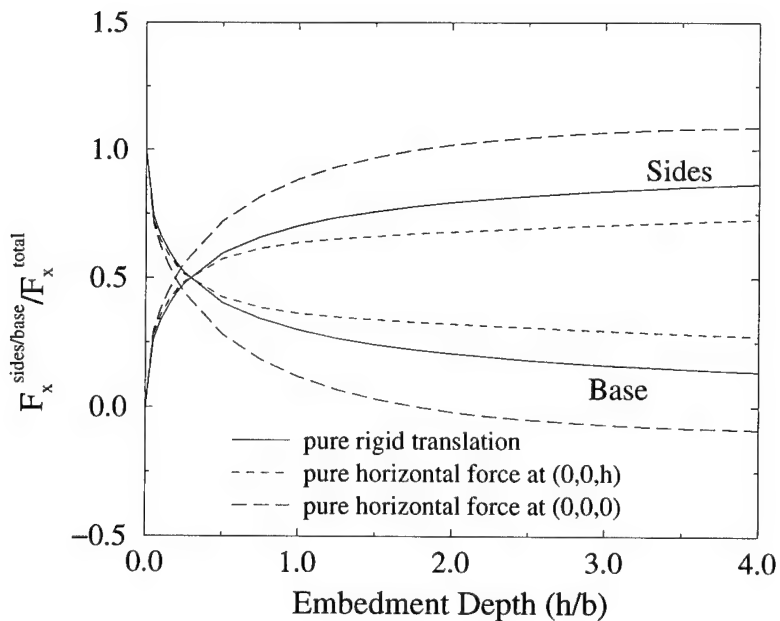
Figure 2.32: Components of horizontal resistance vs. embedment depth for the homogeneous half-space.
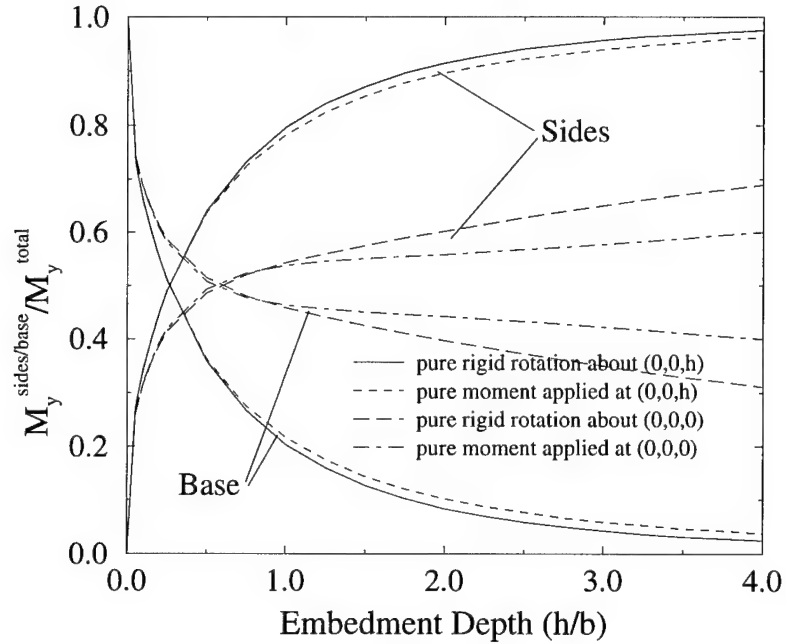
Figure 2.33: Components of rotational resistance vs. embedment depth for the homogeneous half-space.
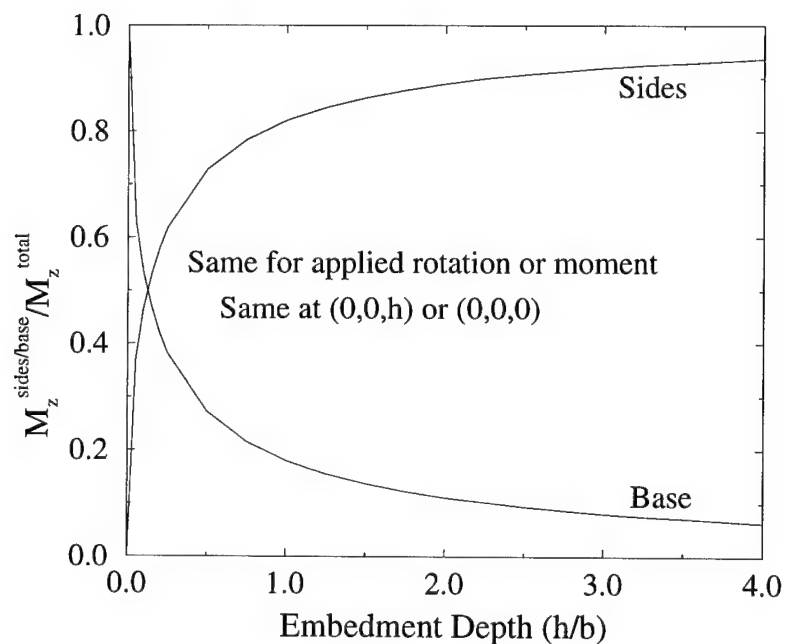
Figure 2.34: Components of torsional resistance vs. embedment depth for the homogeneous half-space.

Chapter 3

Square-Root Shear Modulus Profile Impedances for a Layered Half-Space

3.1   Introduction

While the homogeneous half-space solution is fundamentally important, it may or may not provide an adequate analytical model for analyzing all soil conditions. In the case of a sandy medium, for instance, the applied foundation load and the self weight of the soil will induce a significant spatial dependence on the soil modulus. By virtue of the results from Hardin and Drnevich [17],

$$G_{max} = 1230\frac{(2.973 - e)^2}{(1 + e)}(OCR)^K \bar{\sigma}_o^{1/2}, \qquad (3.1)$$

where e is the void ratio, OCR is the overconsolidation ratio, K is a constant that depends on the plasticity index and is zero for a dry sand, and $\bar{\sigma}_o$ is the mean principal effective stress in psi, the gravity effect alone will produce a square root type of variation in the maximum shear modulus G_{max} even in a soil with uniform density. To model such characteristics, it has been proven to be viable to employ a multi-layered half-space whose piecewise constant shear modulus is taken to vary with depth according to the square root power, i.e.

$$G = G_0 \bar{z}^{1/2}, \qquad (3.2)$$

where $\bar{z} = z/b$ is the normalized depth and b is the half-width of the square footing (Guzina and Pak [14]). This model can be considered as an improvement over the homogeneous profile because it accounts for the variation in the shear modulus

with depth. Figure 3.1b shows the square root variation in shear modulus due to the gravity effects on the soil in the far-field. However, once a foundation is placed onto the ground, there will be local stiffening of the soil due to the presence of the footing as shown in Figure 3.1a. Thus, depending on the level of the footing contact pressure, the square-root profile may still fall short of capturing the complete problem (see Ashlock [1]).
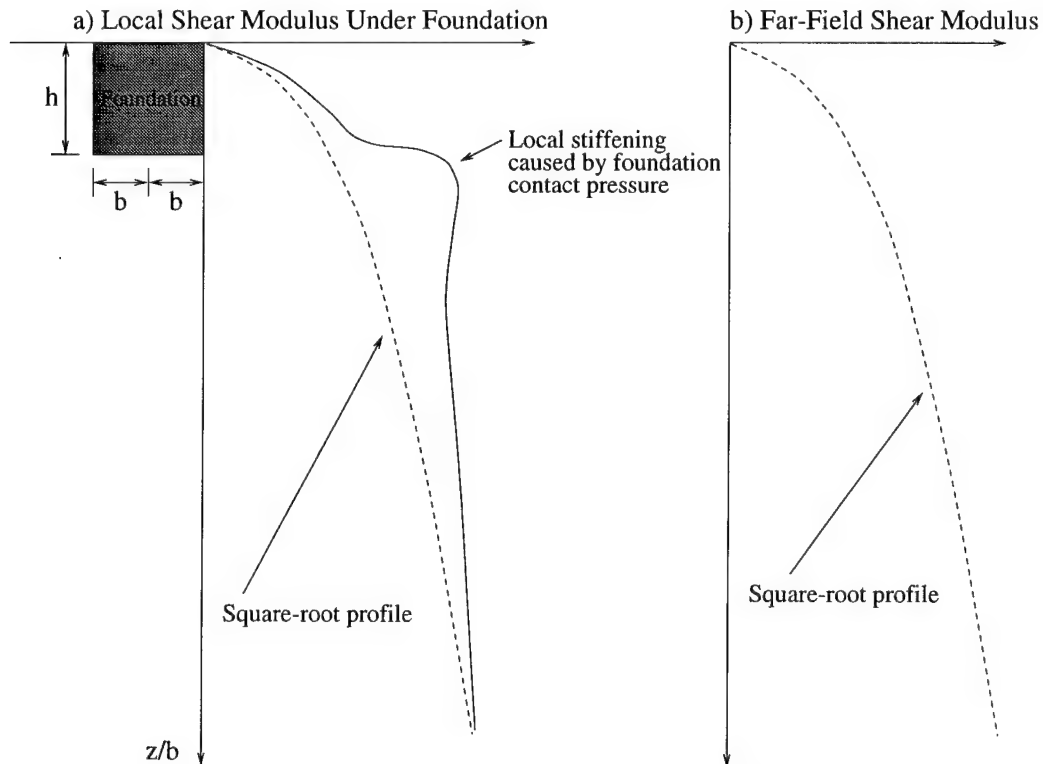
Figure 3.1: Local and far-field variation in shear modulus.

3.2   Defining the Square-Root Shear Modulus Profile

In order to model the square-root shear modulus profile, a half-space can be discretized into piece-wise constant layers, where the shear modulus for a given layer is $G = G_0\sqrt{\hat{z}/b}$, where $\hat{z}$ is the midpoint of the layer. Henceforth, this shear modulus profile will be referred to as a "square-root half-space" or "square-root shear modulus profile." In this approach, the number of layers necessary to

adequately capture the continuous modulus profile is of clear interest. Figure 3.2 shows three shear modulus profiles with 64, 128, and 256 equally spaced layers to $\bar{z} = 16$ (see also Ashlock [1]). For reference, a smooth curve is plotted along with each profile to illustrate the effect of discretization visually.
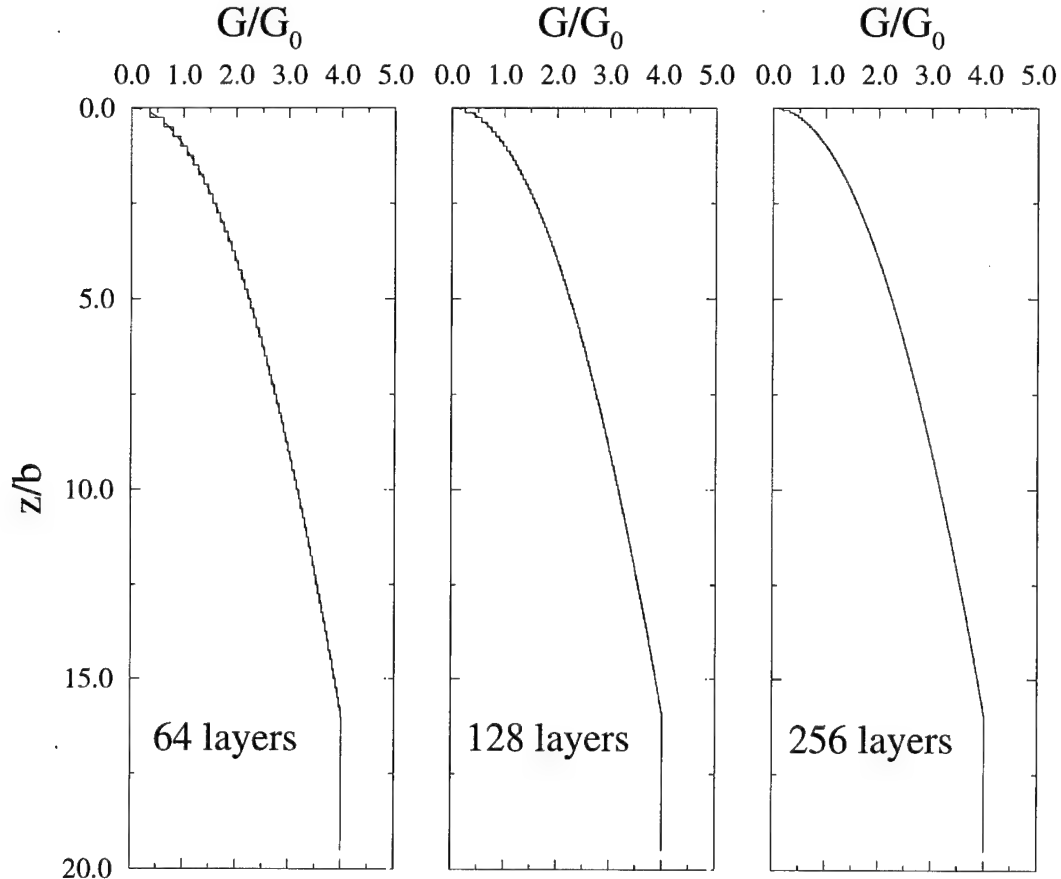
Figure 3.2: Square-root shear modulus profiles overlaying a homogeneous half-space.

As a measure of convergence, impedances were computed at $h/b = 1.0$ for the three different layer profiles shown in Figure 3.2. The result is given in Table 3.1 where the dimensionless impedances for the square-root shear modulus profile are defined as

$$\bar{K}_{vv}(\omega) = \frac{K_{vv}(\omega)}{G_0 b}, \quad \bar{K}_{hh}(\omega) = \frac{K_{hh}(\omega)}{G_0 b}, \quad \bar{K}_{mm}(\omega) = \frac{K_{mm}(\omega)}{G_0 b^3},$$
$$\bar{K}_{mh}(\omega) = \frac{K_{mh}(\omega)}{G_0 b^2}, \quad \bar{K}_{tt}(\omega) = \frac{K_{tt}(\omega)}{G_0 b^3}, \tag{3.3}$$

and G_0 is defined in Equation (3.2). As can be seen from Table 3.1, the impedances are reliably captured by the 64 layer profile, with the possible exception of $\bar{K}_{tt}$. However, this is not the case for the contact tractions. To illustrate the details, the tractions on all faces of the foundation using the 256 layer profile for $\nu = 0.25$ are plotted in Figures 3.3 to 3.16, which correspond to Figures 2.3 to 2.16 for the homogeneous half-space. Figure 3.17 shows an observable difference near $z/b = 1.0$ in the contact tractions for a 64 layer profile for the case corresponding to Figure 3.16 for 256 layers. With its convergence demonstrated at $h/b = 1.0$ in Table 3.1, the 256 layer profile is employed for computing the impedances and contact tractions.

As can be seen from Figures 3.3 to 3.16, the tractions in the square-root half-space solution are all singular along the sharp edges and corners. The singularity along the side faces of the foundation tends to increase as the depth increases, reflecting the increase in shear modulus with depth in the square root profile. Additionally, Figures 3.12, 3.13, 3.14, and 3.16 show some waviness in the real parts of the contact tractions which is not present in the corresponding plots for the homogeneous half-space (see Figures 2.12, 2.13, 2.14, and 2.16). Such waviness most likely illustrates the need to use a finer mesh than the 9×9 mesh for each face of the embedded foundation. However, Table 3.1 illustrates that the impedances have been captured reliably at $h/b = 1.0$ even though there may be some slight variation in the distribution of contact tractions.

Layers	64		128		256	
Stiffness	Real	Imag	Real	Imag	Real	Imag
$\bar{K}_{vv}$	9.72	11.08	9.68	11.05	9.71	11.05
$\bar{K}_{hh}$	9.09	11.52	9.07	11.49	9.09	11.48
$\bar{K}_{mm}$	12.74	4.98	12.63	4.93	12.61	4.89
$\bar{K}_{mh}$	-1.01	-3.36	-0.99	-3.29	-0.95	-3.25
$\bar{K}_{tt}$	17.84	6.97	17.91	6.98	18.12	7.02

Table 3.1: Convergence of the impedances from a square-root shear modulus profile with increasing number of layers for $h/b = 1.0$, $\nu = 0.25$, $\bar{\omega} = 1.0$.
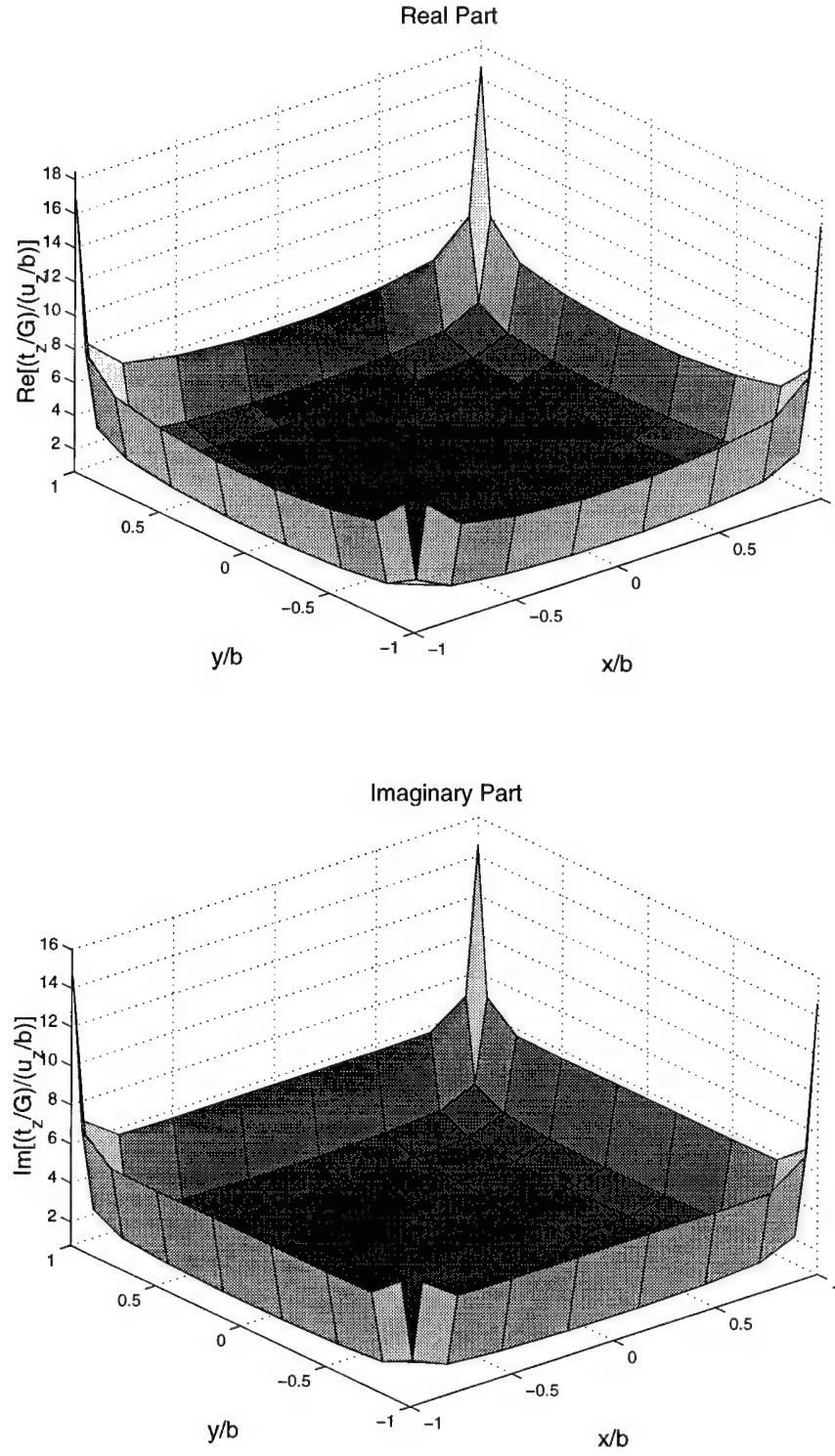
Figure 3.3: Distribution of contact tractions t_z corresponding to dynamic stiffness $K_{vv}(\bar{\omega} = 1.0)$ for the square root profile (256 layers). (Bottom of the rigid foundation, $h/b = 1.0$, $\nu = 0.25$)
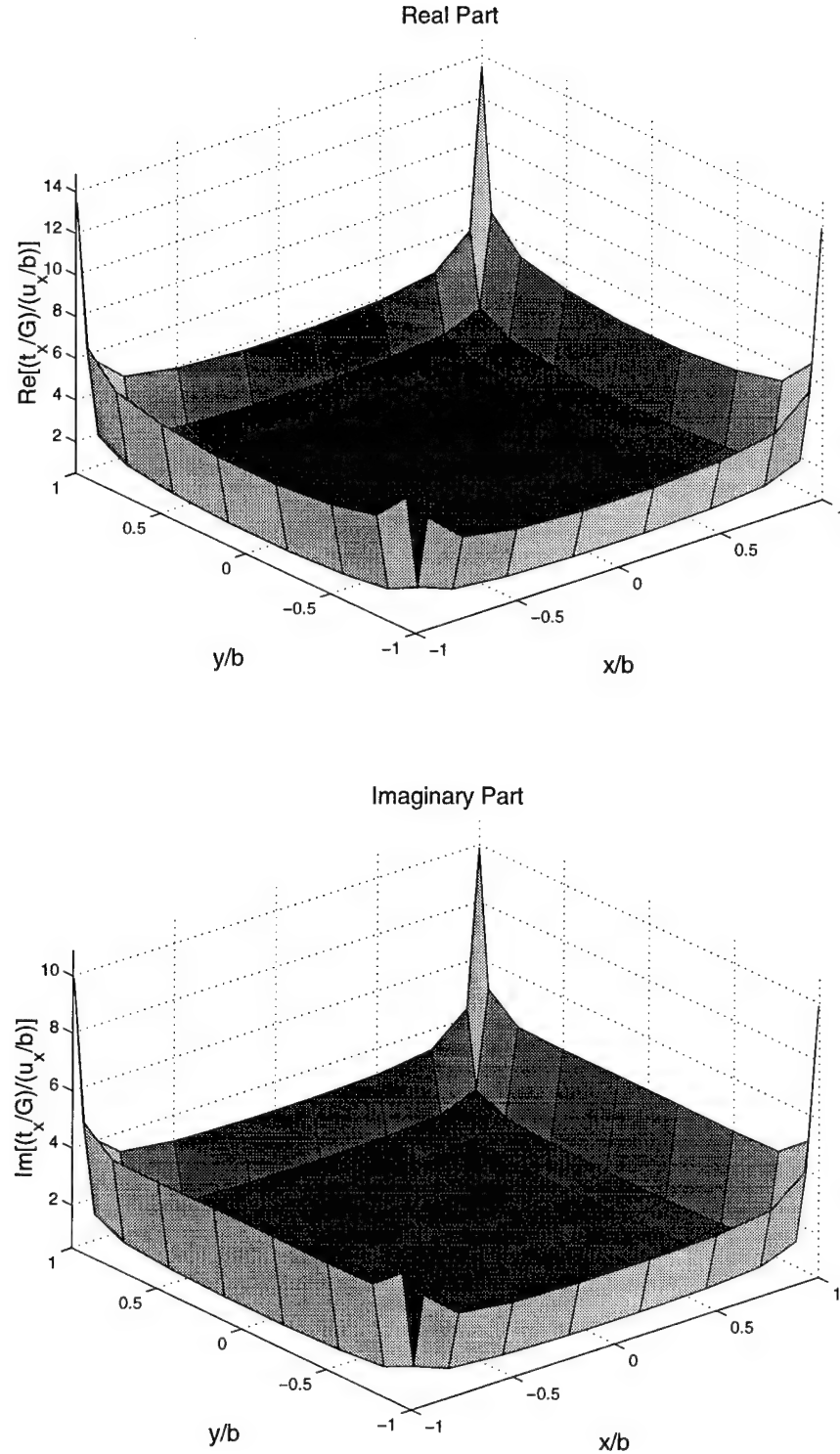
Figure 3.4: Distribution of contact tractions t_x corresponding to dynamic stiffness $K_{hh}(\bar{\omega} = 1.0)$ for the square root profile (256 layers). (Bottom of the rigid foundation, $h/b = 1.0$, $\nu = 0.25$)

Real Part

Imaginary Part
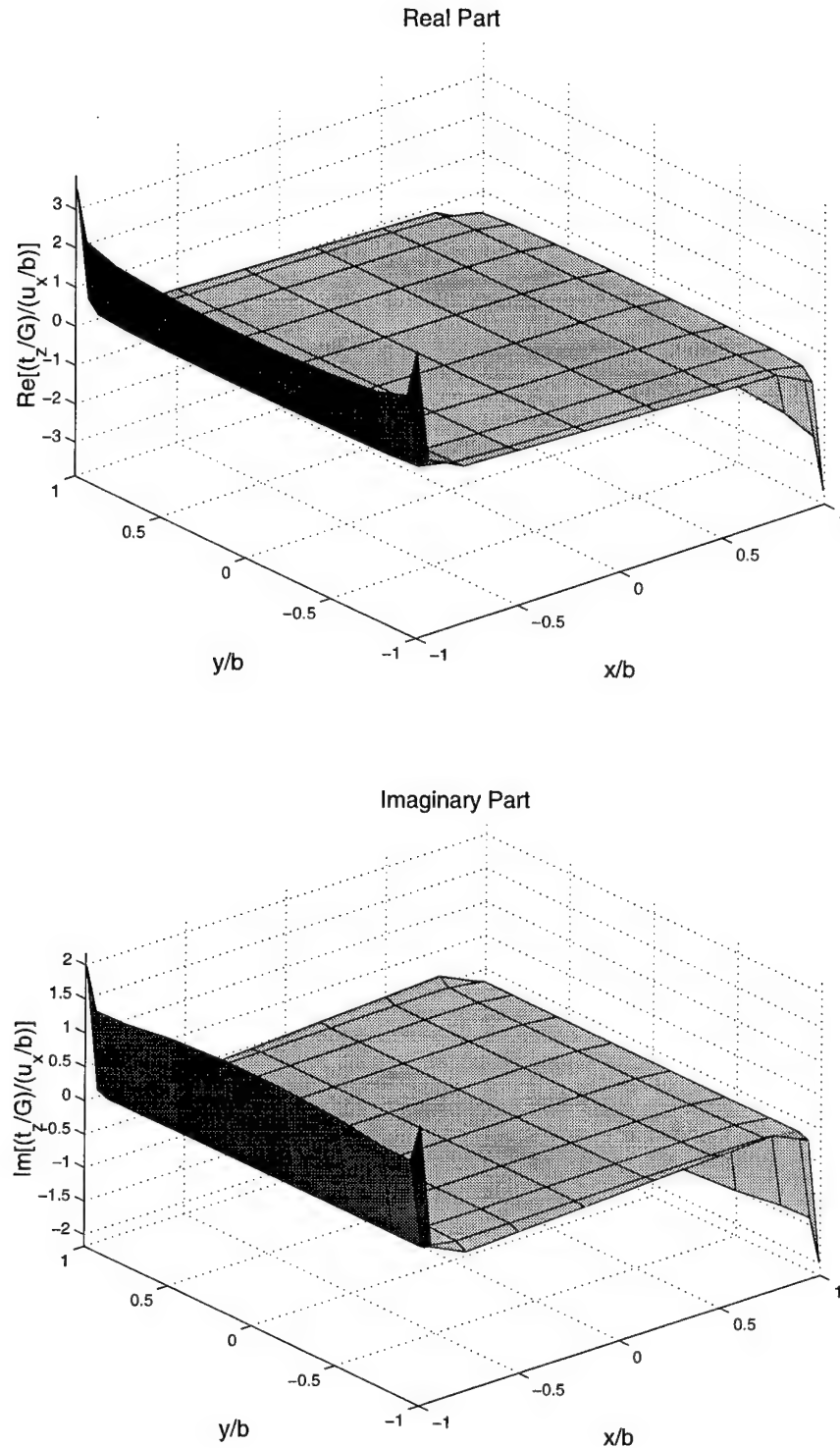
Figure 3.5: Distribution of contact tractions t_z corresponding to dynamic stiffness $K_{mh}(\bar{\omega} = 1.0)$ for the square root profile (256 layers). (Bottom of the rigid foundation, $h/b = 1.0$, $\nu = 0.25$)

Real Part

Imaginary Part
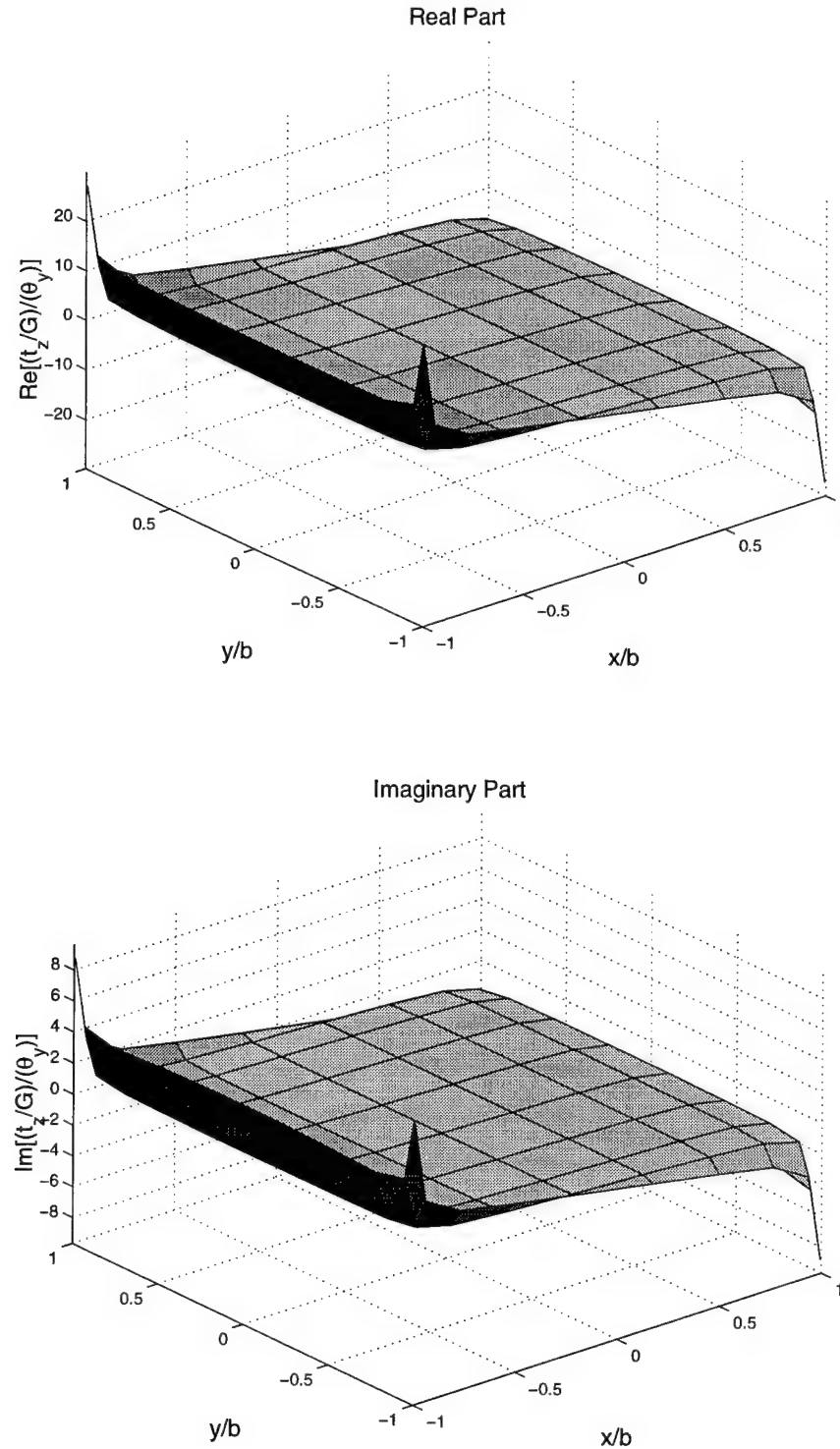
Figure 3.6: Distribution of contact tractions t_z corresponding to dynamic stiffness $K_{mm}(\bar{\omega} = 1.0)$ for the square root profile (256 layers). (Bottom of the rigid foundation, $h/b = 1.0$, $\nu = 0.25$)
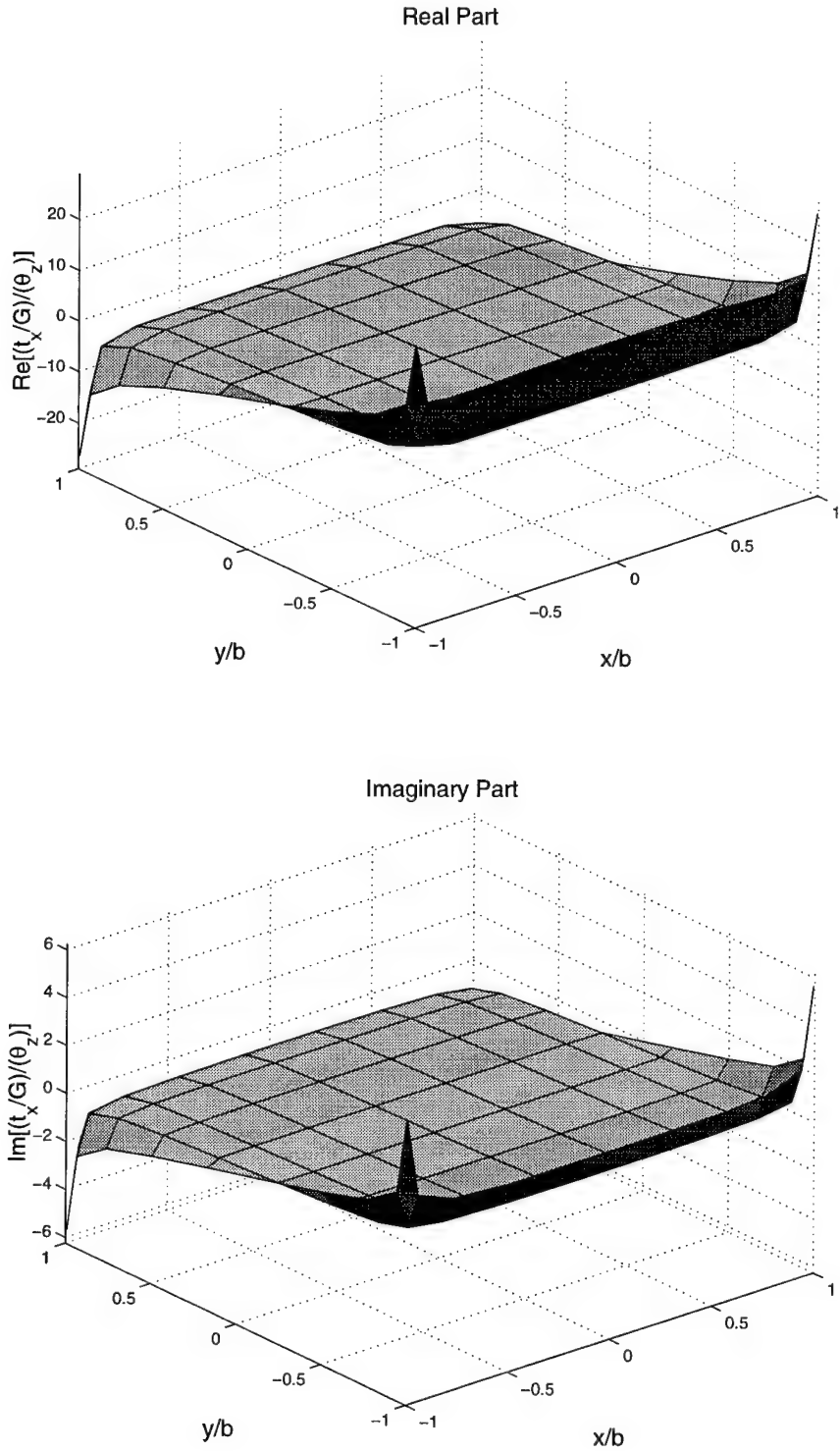
Figure 3.7: Distribution of contact tractions t_x corresponding to dynamic stiffness $K_{tt}(\bar{\omega} = 1.0)$ for the square root profile (256 layers). (Bottom of the rigid foundation, $h/b = 1.0$, $\nu = 0.25$)
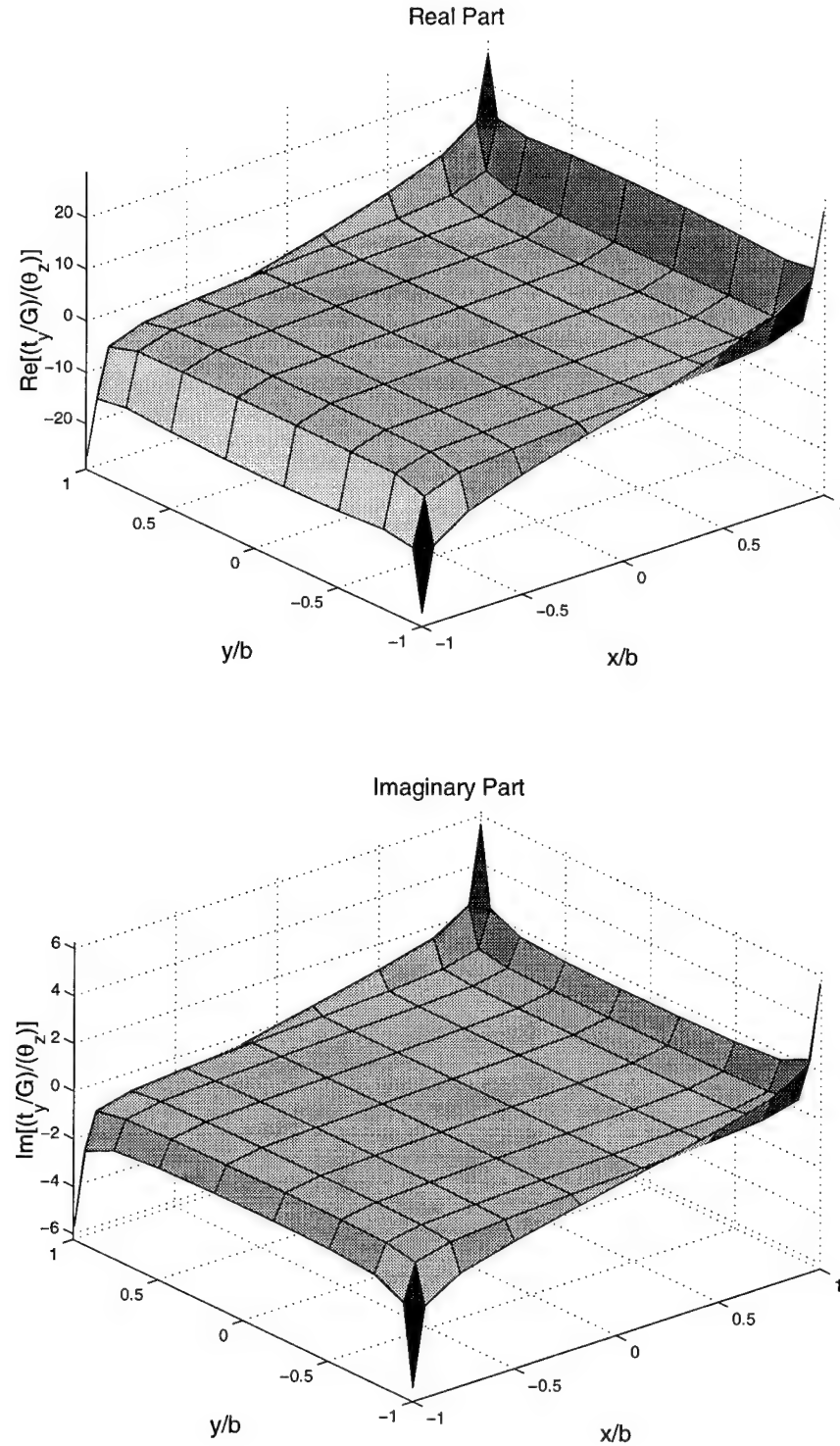
Figure 3.8: Distribution of contact tractions t_y corresponding to dynamic stiffness $K_{tt}(\bar{\omega} = 1.0)$ for the square root profile (256 layers). (Bottom of the rigid foundation, $h/b = 1.0$, $\nu = 0.25$)
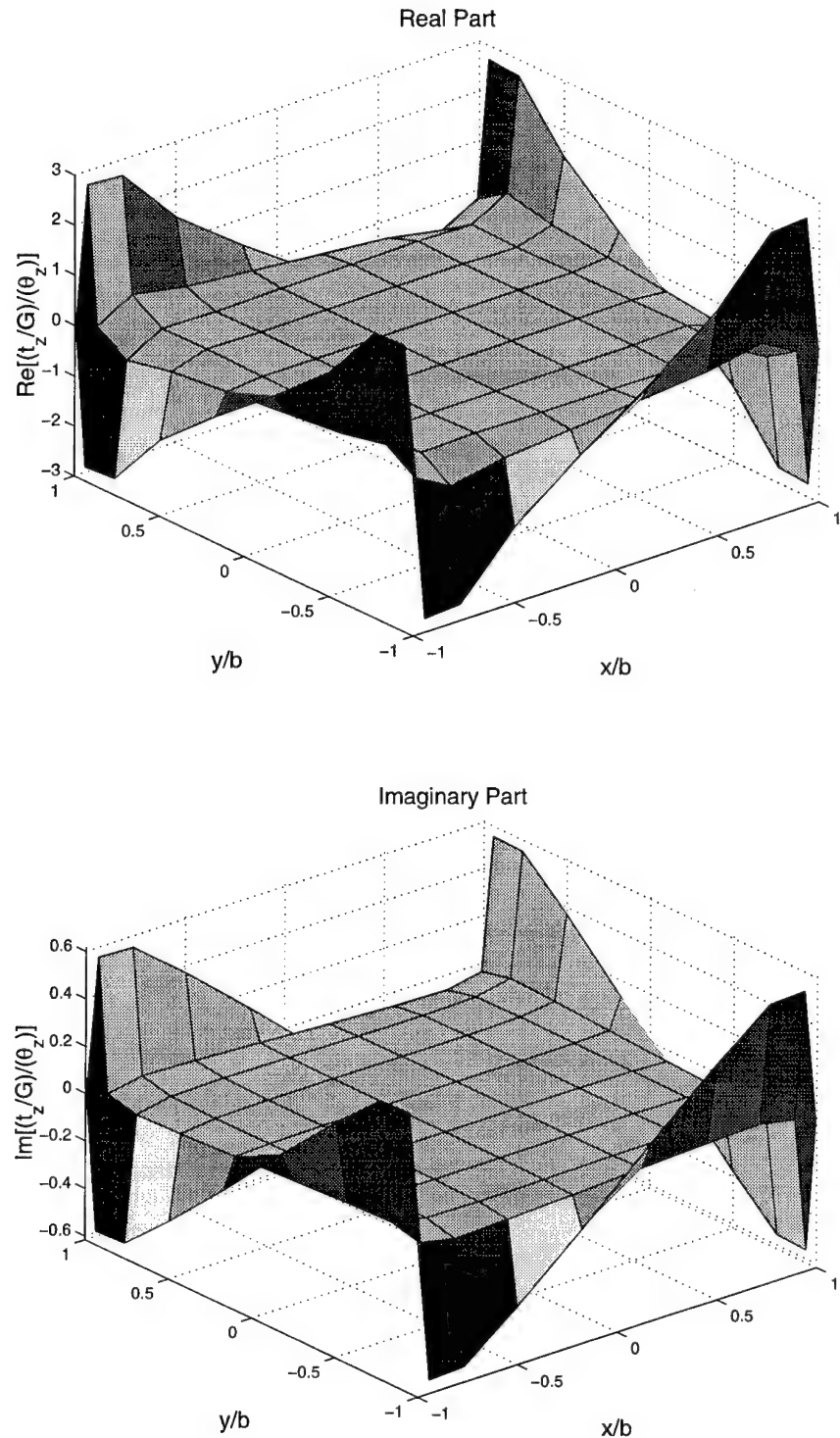
Figure 3.9: Distribution of contact tractions t_z corresponding to dynamic stiffness $K_{tt}(\bar{\omega} = 1.0)$ for the square root profile (256 layers). (Bottom of the rigid foundation, $h/b = 1.0$, $\nu = 0.25$)
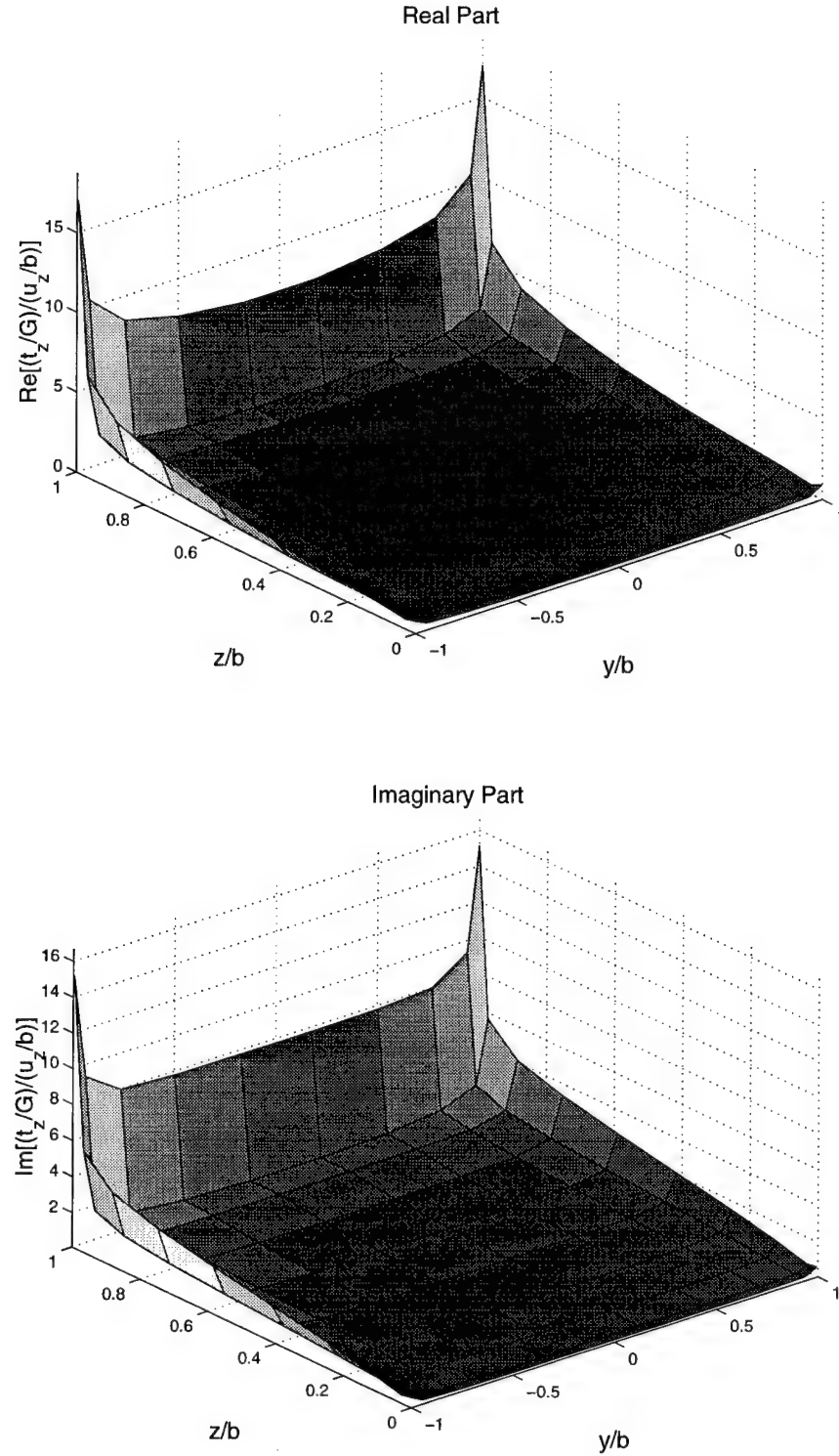
Figure 3.10: Distribution of contact tractions t_z corresponding to dynamic stiffness $K_{vv}(\bar{\omega} = 1.0)$ for the square root profile (256 layers). (Positive X-face of the rigid foundation, $h/b = 1.0$, $\nu = 0.25$)
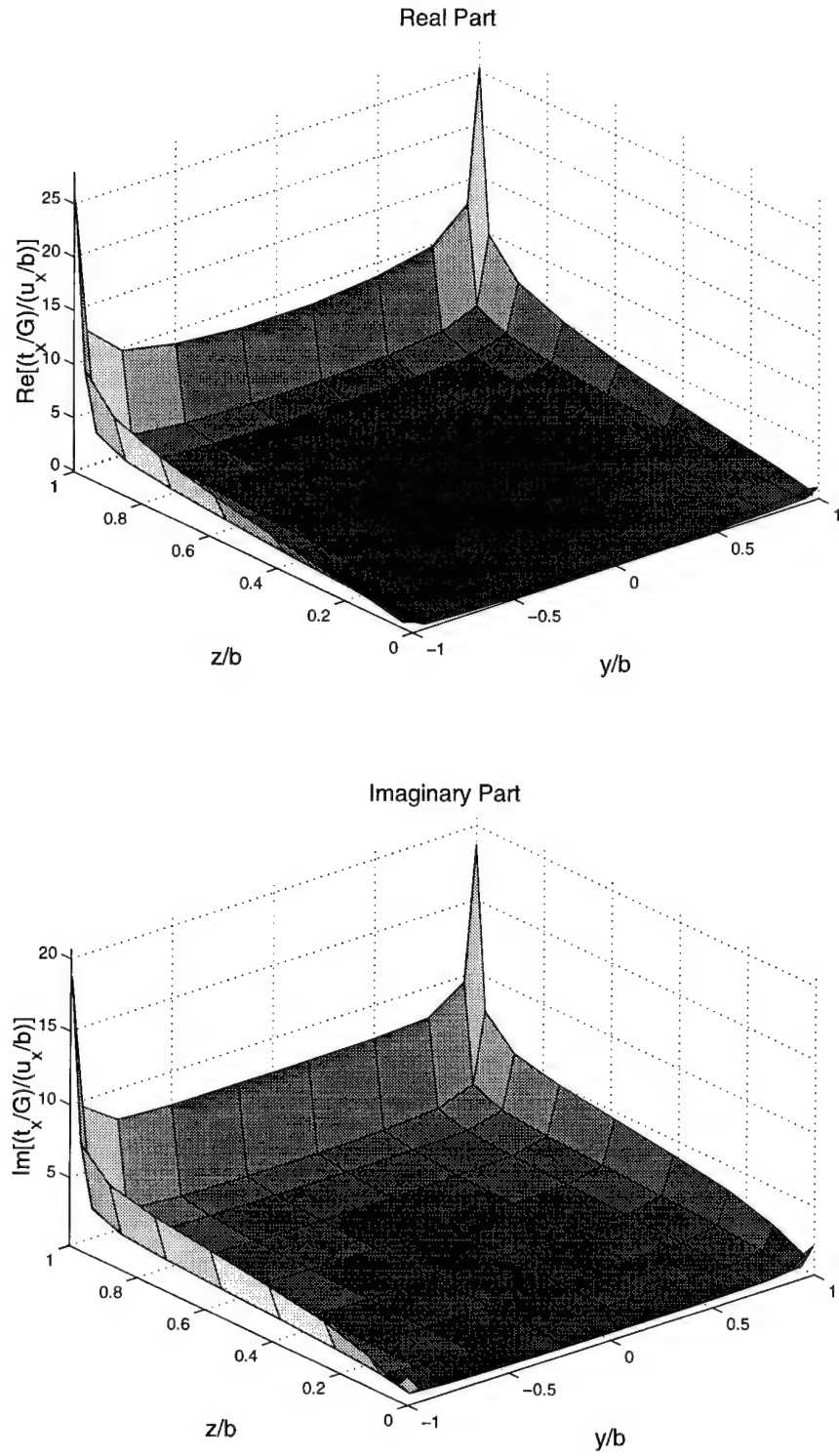
Figure 3.11: Distribution of contact tractions t_x corresponding to dynamic stiffness $K_{hh}(\bar{\omega} = 1.0)$ for the square root profile (256 layers). (Positive X-face of the rigid foundation, $h/b = 1.0$, $\nu = 0.25$)
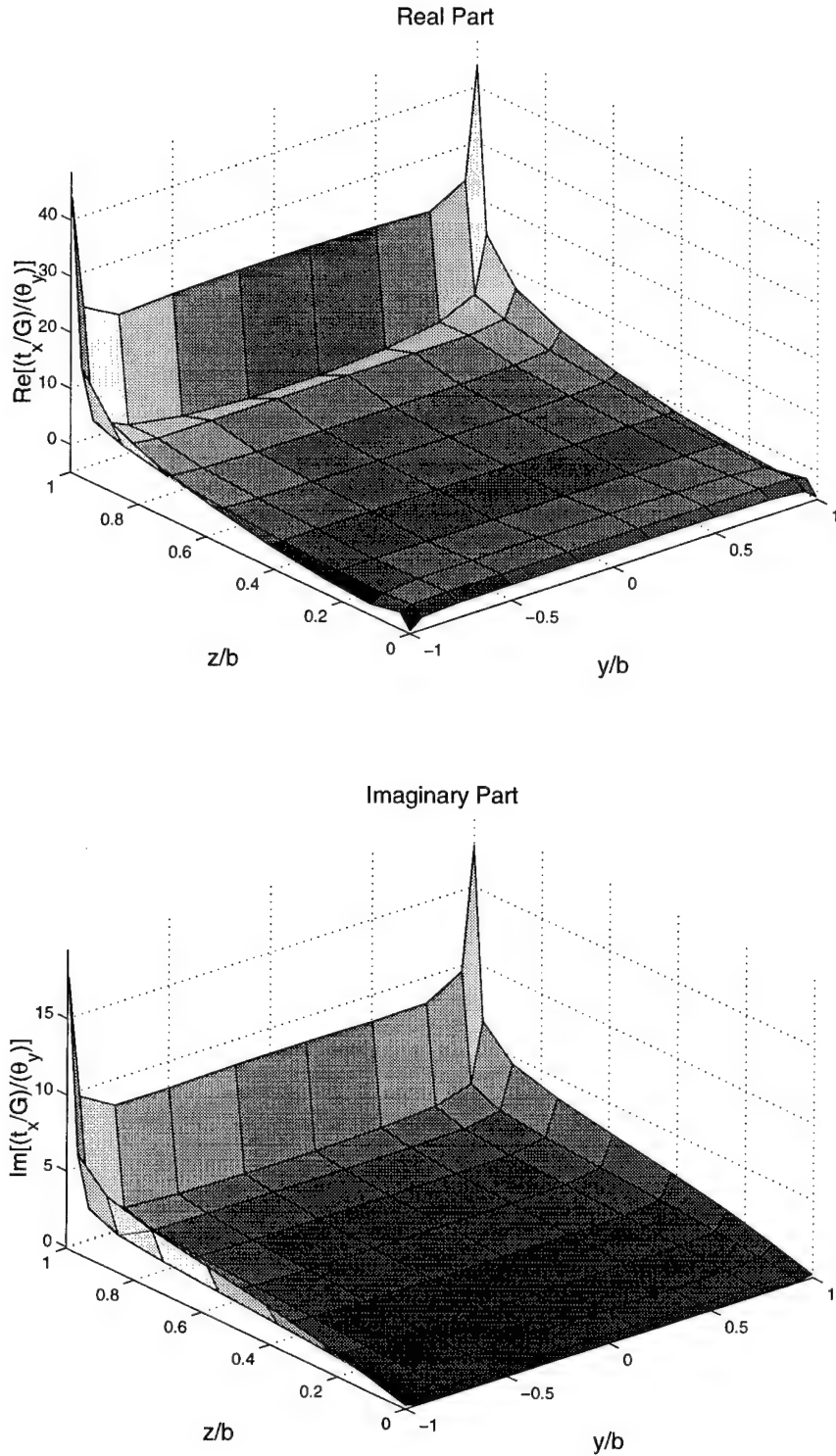
Figure 3.12: Distribution of contact tractions t_x corresponding to dynamic stiffness $K_{mm}(\bar{\omega} = 1.0)$ for the square root profile (256 layers). (Positive X-face of the rigid foundation, $h/b = 1.0$, $\nu = 0.25$)
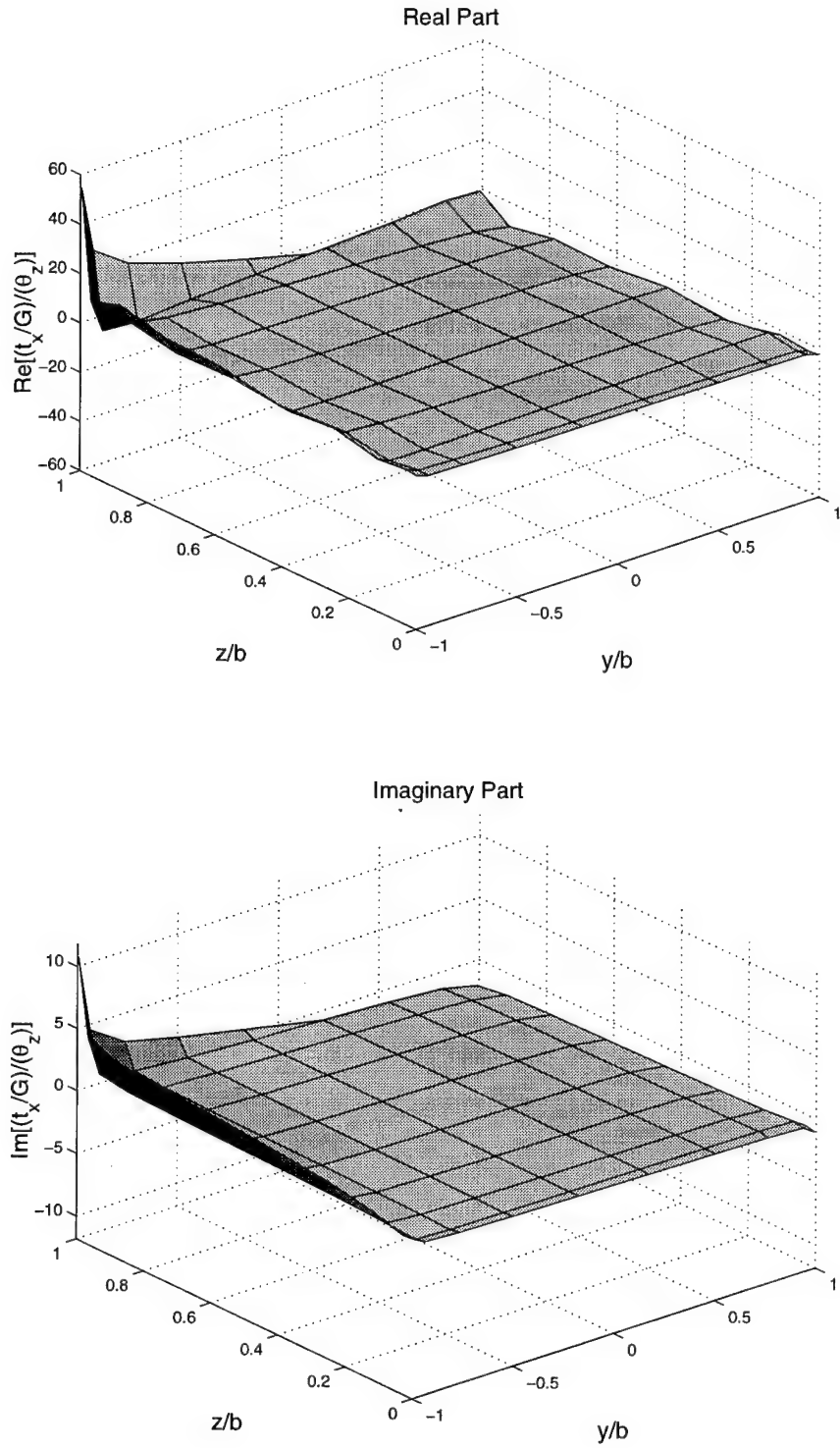
Figure 3.13: Distribution of contact tractions t_x corresponding to dynamic stiffness $K_{tt}(\bar{\omega} = 1.0)$ for the square root profile (256 layers). (Positive X-face of the rigid foundation, $h/b = 1.0$, $\nu = 0.25$)
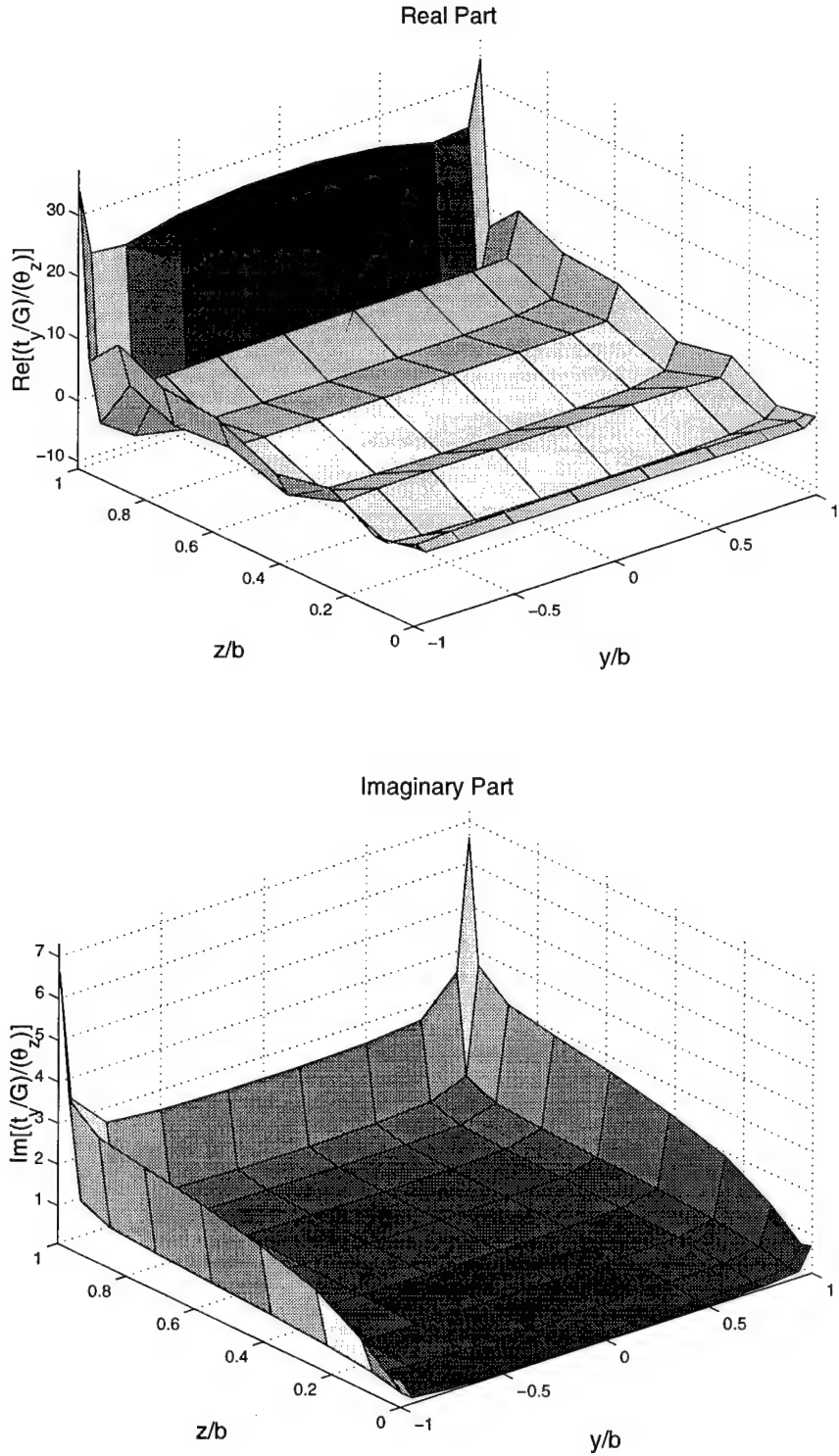
Figure 3.14: Distribution of contact tractions t_y corresponding to dynamic stiffness $K_{tt}(\bar{\omega} = 1.0)$ for the square root profile (256 layers). (Positive X-face of the rigid foundation, $h/b = 1.0$, $\nu = 0.25$)
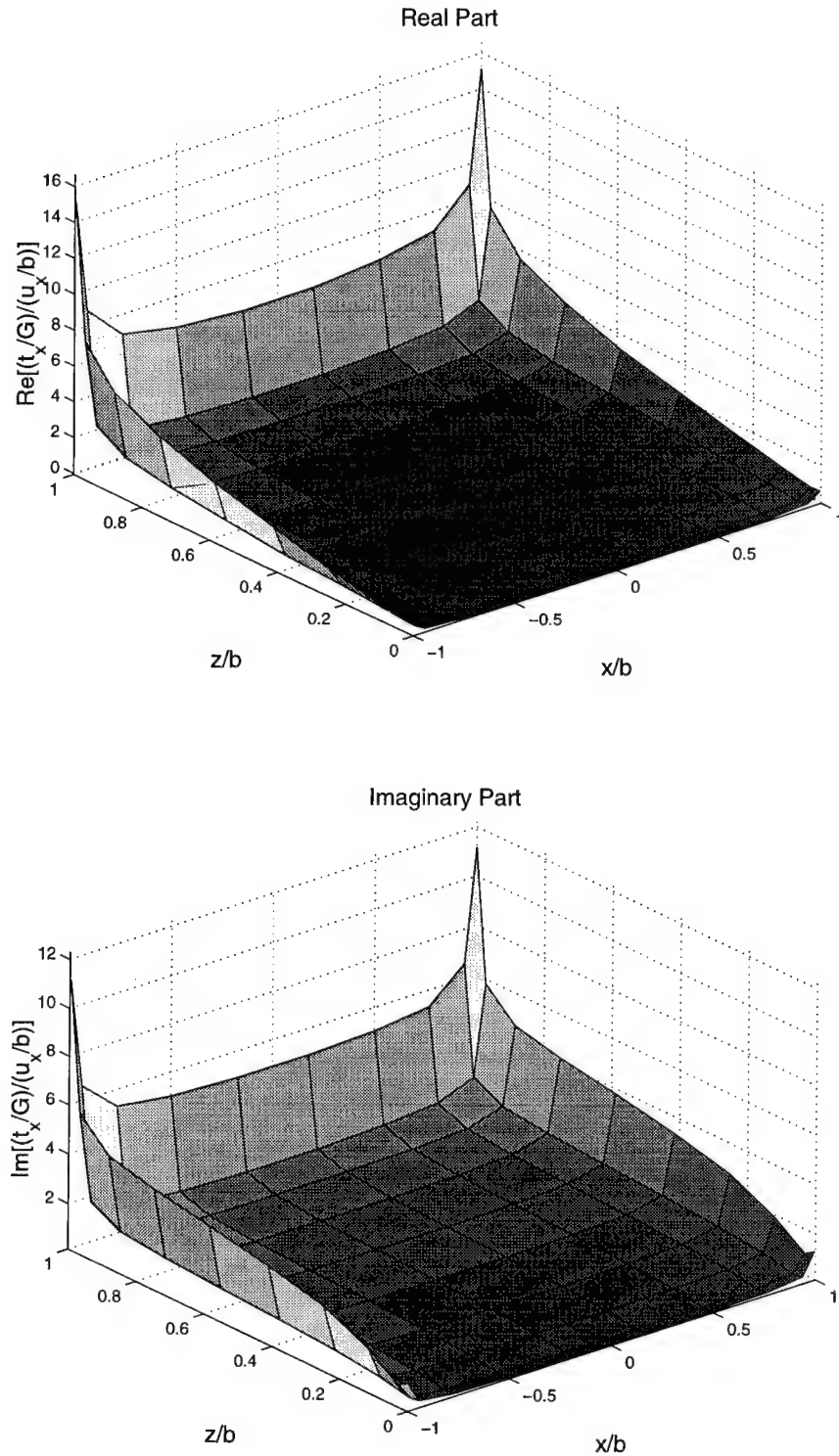
Figure 3.15: Distribution of contact tractions t_x corresponding to dynamic stiffness $K_{hh}(\bar{\omega} = 1.0)$ for the square root profile (256 layers). (Positive Y-face of the rigid foundation, $h/b = 1.0$, $\nu = 0.25$)
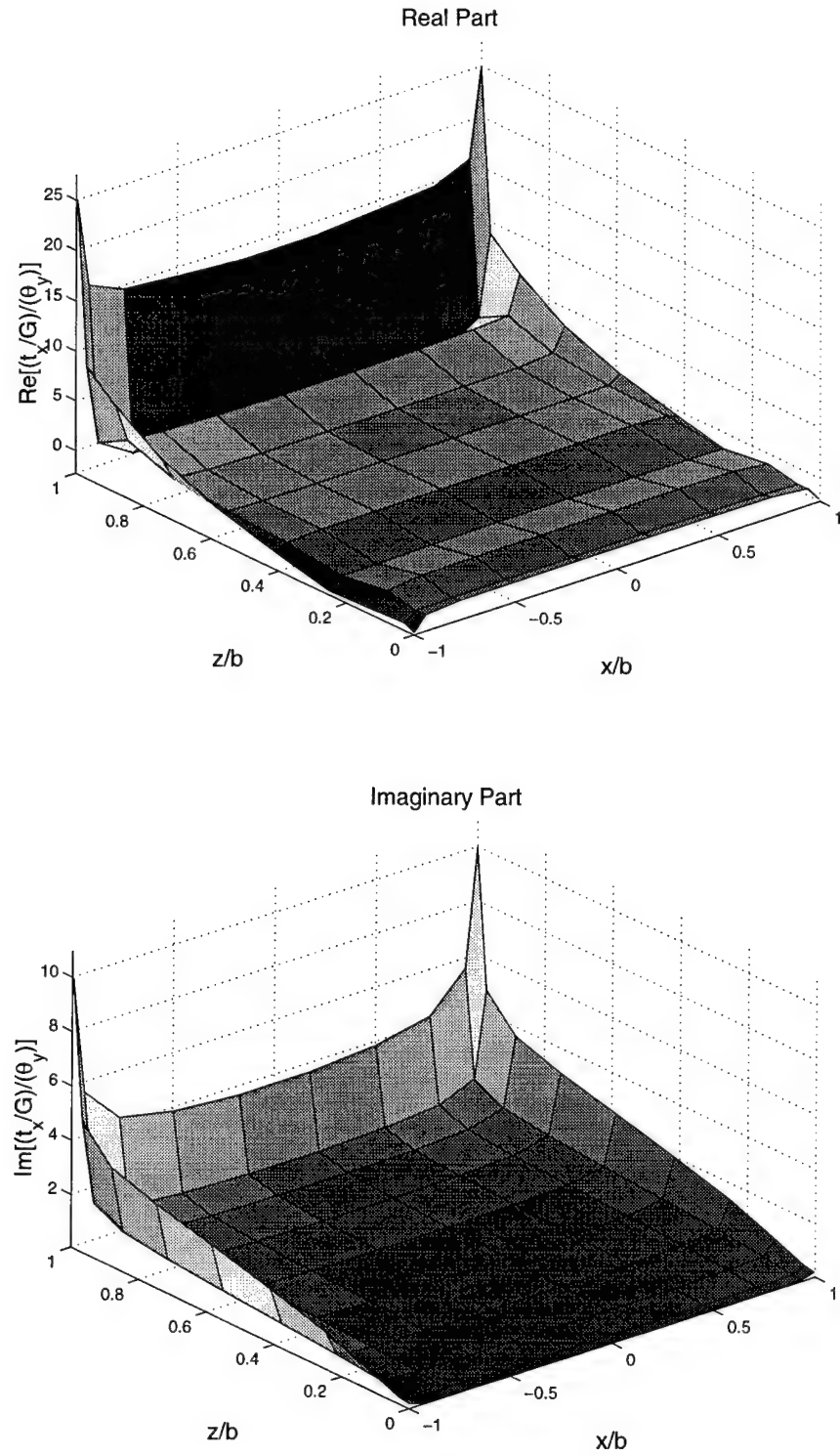
Figure 3.16: Distribution of contact tractions t_x corresponding to dynamic stiffness $K_{mm}(\bar{\omega} = 1.0)$ for the square root profile (256 layers). (Positive Y-face of the rigid foundation, $h/b = 1.0$, $\nu = 0.25$)
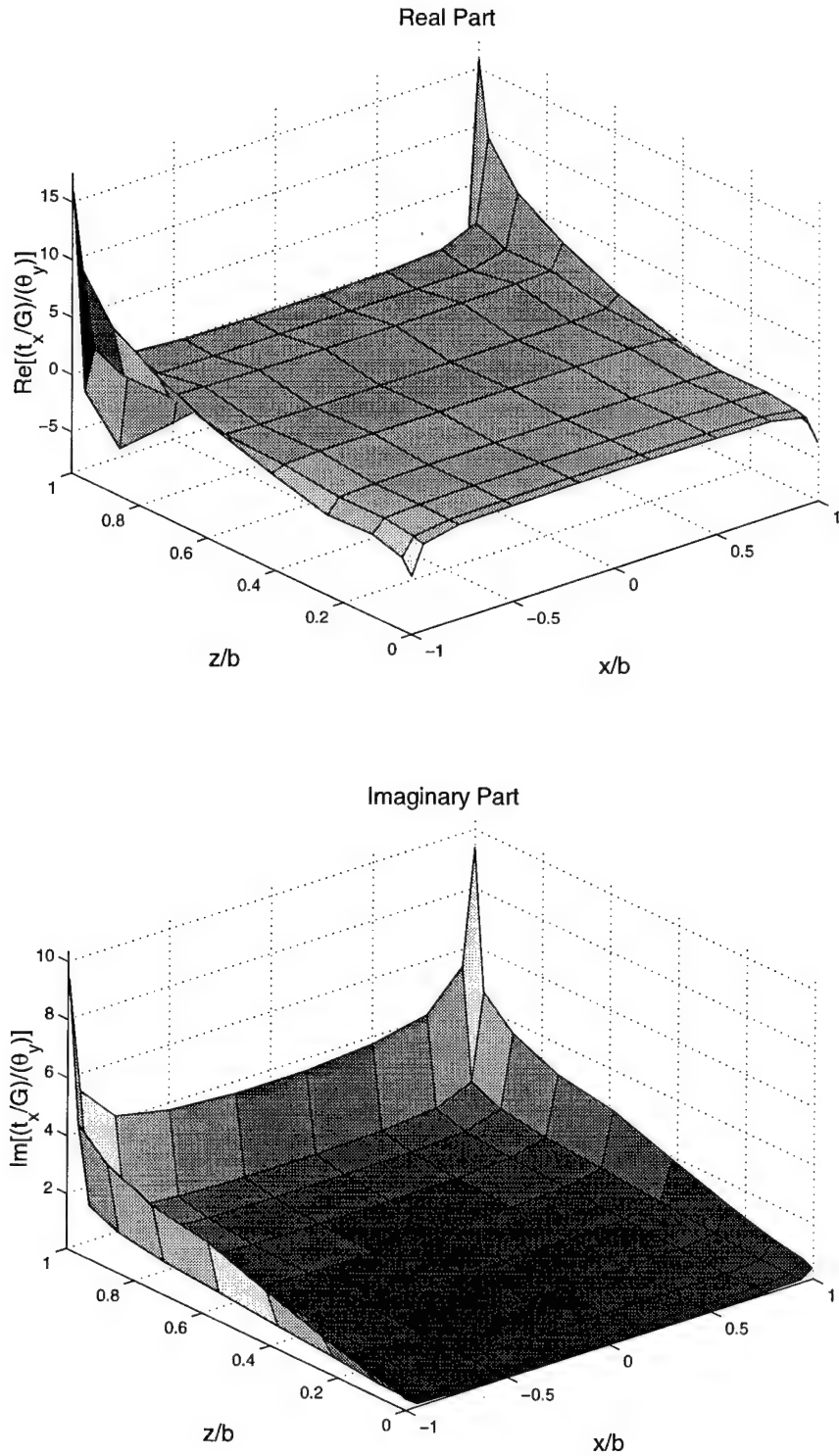
Figure 3.17: Distribution of contact tractions t_x corresponding to dynamic stiffness $K_{mm}(\bar{\omega} = 1.0)$ for the square root profile (64 layers). (Positive Y-face of the rigid foundation, $h/b = 1.0$, $\nu = 0.25$)

3.3   Change in Impedance with Depth of Embedment for the Square-Root Half-Space

Table 3.2 contains the quasi-static impedances at $\mathbf{x}_{ref} = \mathbf{x}_h$ for a square foundation embedded in a layered half-space with a square root profile of 256 layers as discussed previously with a 9×9 mesh on each face of the embedded foundation (see also Figures 3.18 to 3.20). Despite the coarseness of the mesh at deeper embedments and the oscillation in some solutions, the trends of $\bar{K}_{vv}$, $\bar{K}_{hh}$, $\bar{K}_{mm}$, $\bar{K}_{mh}$ and $\bar{K}_{tt}$ with increasing embedment are clearly demonstrated. The impedances in Table 3.2 are the real parts of the quasi-static impedances at $\bar{\omega} = 0.1$ and will be labeled with a superscript [s]. They correspond to Table 2.1 which contains static impedances for the homogeneous half-space. Also shown in Figures 3.21 to 3.25 are the dynamic impedances up to $\bar{\omega} = 4.0$ which are normalized by the quasi-static value at $\bar{\omega} = 0.1$ for the appropriate embedment depth given in Table 3.2. For the square-root profile, the dimensionless frequency $\bar{\omega}$ is defined as

$$\bar{\omega} = \frac{\omega b}{C_{s0}} \tag{3.4}$$

where

$$C_{s0} = \sqrt{\frac{G_0}{\rho}} \tag{3.5}$$

and G_0 is defined in Equation (3.2).

Figures 3.18 to 3.20 show that the impedances for the square-root profile all increase with increasing embedment depth. These figures correspond to Figures 2.21 to 2.23 for the homogeneous half-space. Both the plots from the square-root shear modulus profile and the homogeneous half-space have the same general shape with increasing embedment for each of the five impedances. Like the plot of $\bar{K}_{mh}$ for the homogeneous half-space, the plot of $\bar{K}_{mh}$ with embedment depth for the square-root shear modulus profile in Figure 3.20 reveals that the

coupling terms are positive for shallow embedment depths but become negative as the embedment depth increases.

The plots of the normalized dynamic impedances in Figures 3.21 to 3.25 show that the real parts of each of the five normalized impedances are very similar in shape for $h/b = 0.0$, 1.0, and 2.0. The imaginary parts of the normalized impedances tend towards certain upper limits with increasing embedment depth in a similar manner to the imaginary parts for the homogeneous half-space impedances in Figures 2.24 to 2.28, indicating that embedment enhances radiation damping.

h/b	$\bar{K}^s_{vv}$	$\bar{K}^s_{hh}$	$\bar{K}^s_{mm}$	$\bar{K}^s_{mh}$	$\bar{K}^s_{tt}$
0.00	5.06	2.68	2.73	0.20	2.74
0.25	8.09	5.66	6.08	0.14	8.51
0.50	10.04	7.79	9.22	-0.29	13.69
0.75	11.80	9.79	12.96	-1.02	18.96
1.00	13.49	11.73	17.51	-2.01	24.83
1.25	15.13	13.67	23.21	-3.44	30.19
1.50	16.75	15.56	29.86	-4.89	37.72
1.75	18.34	17.48	38.10	-6.91	42.04
2.00	19.93	19.38	47.56	-8.99	51.12
2.25	21.51	21.32	59.13	-11.59	59.67
2.50	23.08	23.23	72.11	-14.52	60.77
2.75	24.65	25.14	87.42	-17.48	78.44
3.00	26.22	27.08	103.60	-21.19	76.40
3.25	27.80	29.03	123.80	-24.92	77.74
3.50	29.37	31.03	145.50	-29.33	92.30
3.75	30.94	33.00	171.00	-33.60	105.90
4.00	32.52	35.00	195.90	-39.39	101.00

Table 3.2: Quasi-static impedance ($\bar{K}^s_{ij}$) from the square root profile $Re\{K_{ij}(\bar{\omega} = 0.1)\}$, 256 layers to $\bar{z} = 16$, $\nu = 0.25$.
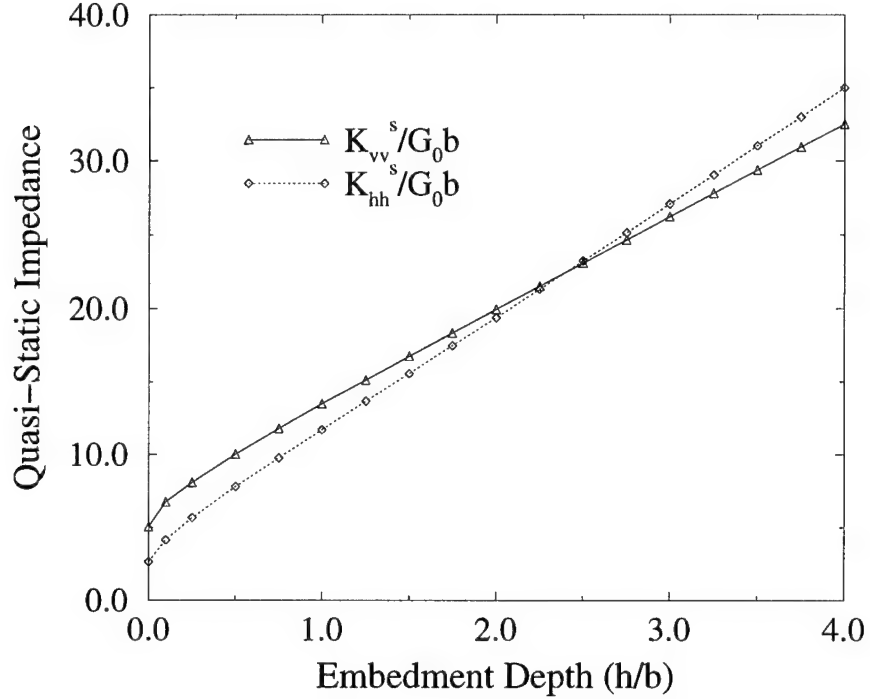
Figure 3.18: Quasi-static vertical $(\bar{K}_{vv}^s)$ and horizontal impedance $(\bar{K}_{hh}^s)$ versus embedment depth (h/b).
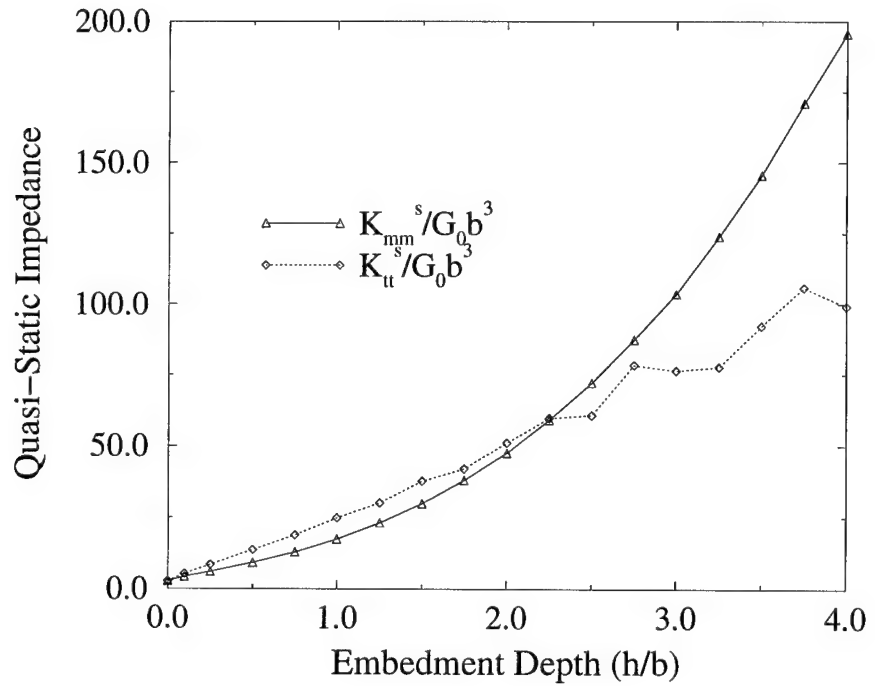
Figure 3.19: Quasi-static rocking $(\bar{K}_{mm}^s)$ and torsional impedance $(\bar{K}_{tt}^s)$ versus embedment depth (h/b).
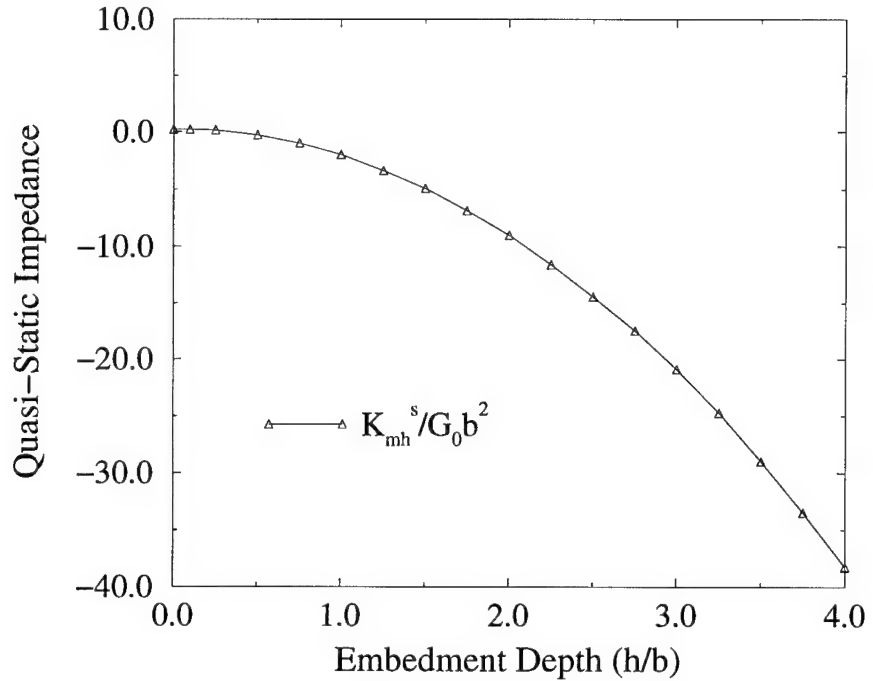
Figure 3.20: Quasi-static coupling impedance ($\bar{K}^s_{mh}$) versus embedment depth (h/b).
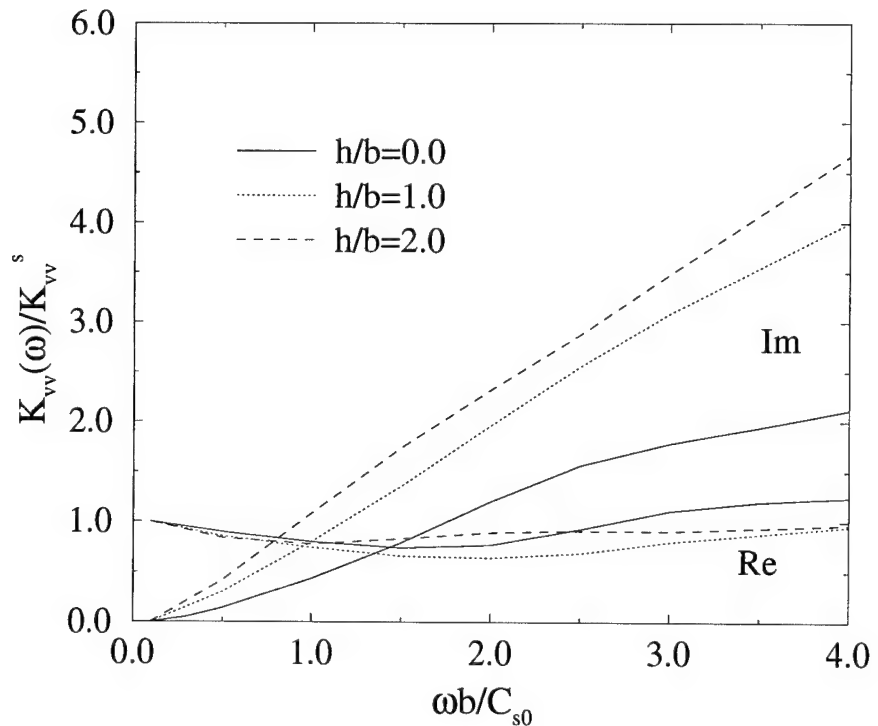
Figure 3.21: Normalized dynamic vertical stiffness ($\bar{K}_{vv}$) for a square foundation embedded in a square-root half-space, $\nu = 0.25$.
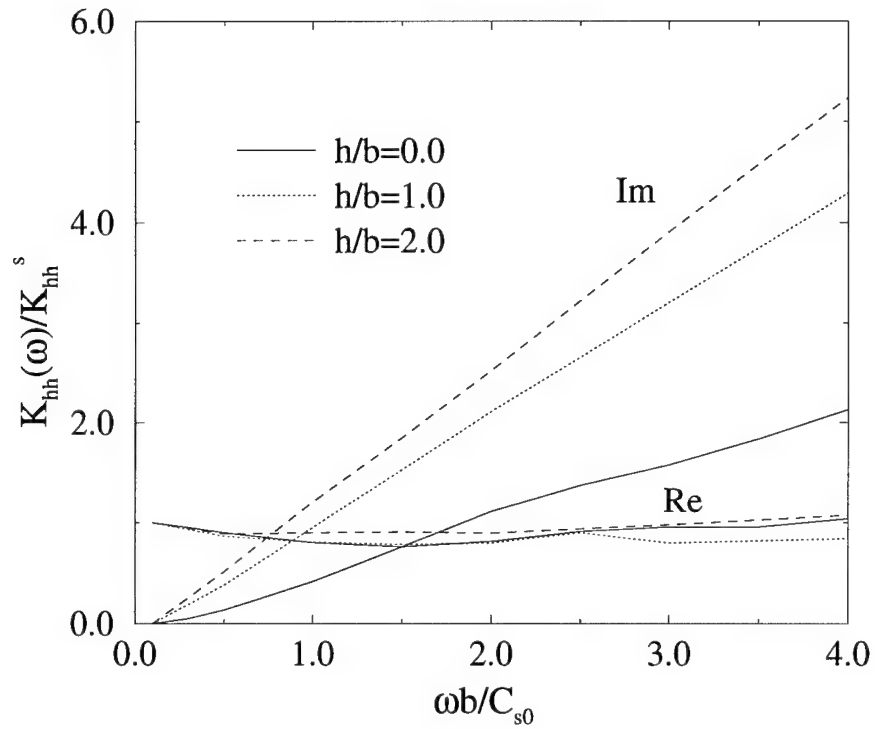
Figure 3.22: Normalized dynamic horizontal stiffness ($\bar{K}_{hh}$) for a square foundation embedded in a square-root half-space, $\nu = 0.25$.
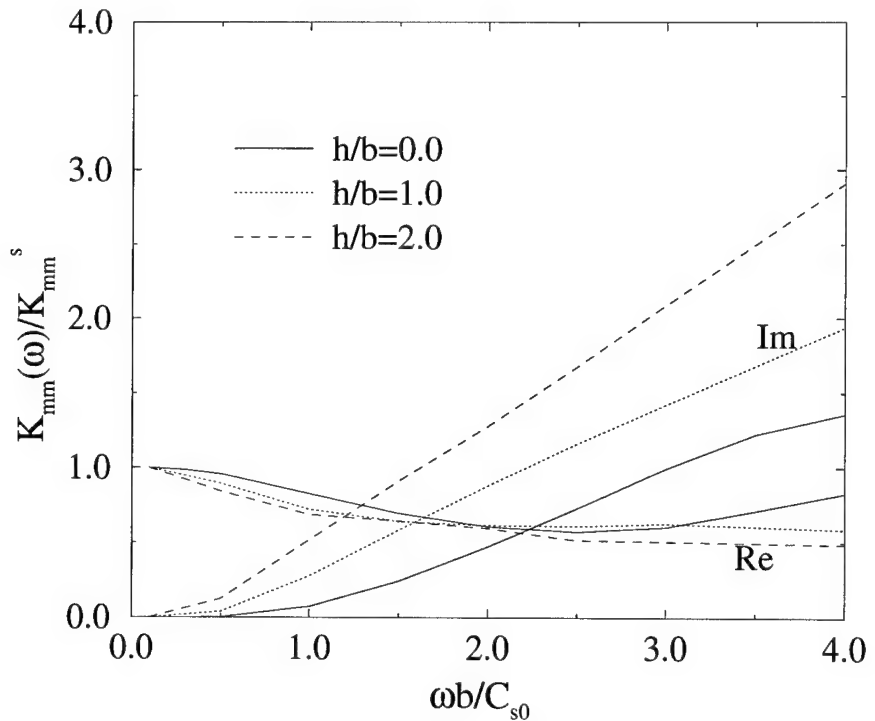
Figure 3.23: Normalized dynamic rocking stiffness ($\bar{K}_{mm}$) for a square foundation embedded in a square-root half-space, $\nu = 0.25$.
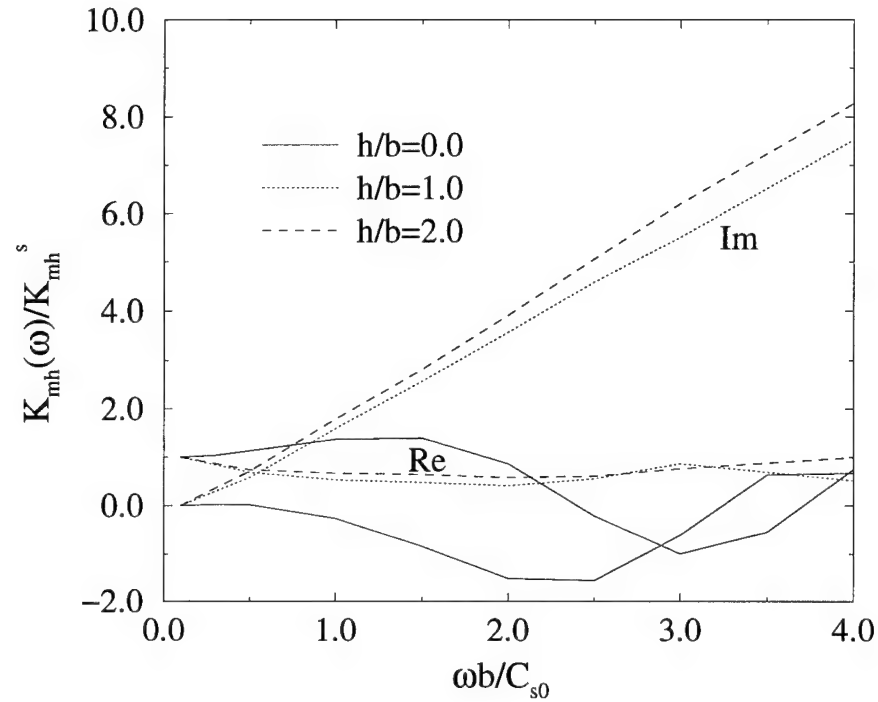
Figure 3.24: Normalized dynamic coupling stiffness $(\bar{K}_{mh})$ for a square foundation embedded in a square-root half-space, $\nu = 0.25$.
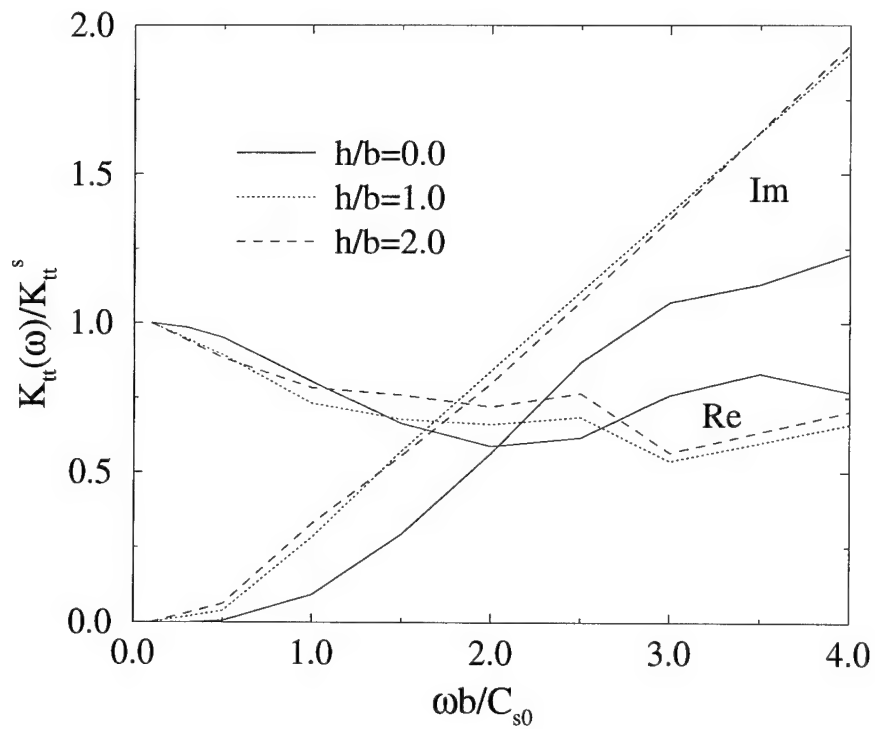
Figure 3.25: Normalized dynamic torsional stiffness $(\bar{K}_{tt})$ for a square foundation embedded in a square-root half-space, $\nu = 0.25$.

3.4 Load Transfer to the Soil

Figures 3.26, 3.27, 3.28 and 3.29 show the contributions from the sides and base of a rigid cavity embedded in a layered half-space with a square-root shear modulus profile under vertical, horizontal, rocking, and torsional loading at both $\mathbf{x}_h = (0, 0, h)$ and $\mathbf{0} = (0, 0, 0)$. Despite the coarseness of the 9×9 mesh on each face, the overall trends of the solution are well illustrated.

In comparison with Figures 2.31, 2.32, 2.33 and 2.34 for the homogeneous half-space, Figures 3.26, 3.27, 3.28 and 3.29 reveal that the point at which the sides and base carry an equal percentage of the load is deeper for the square-root profile than for the homogeneous half-space. This is not surprising given the small shear modulus near the surface for the square-root modulus profile. Additionally, Figure 3.28 reveals that the majority of the load is still transferred through the base of the foundation for a pure moment applied at (0,0,0) for the range of embedment depths plotted.
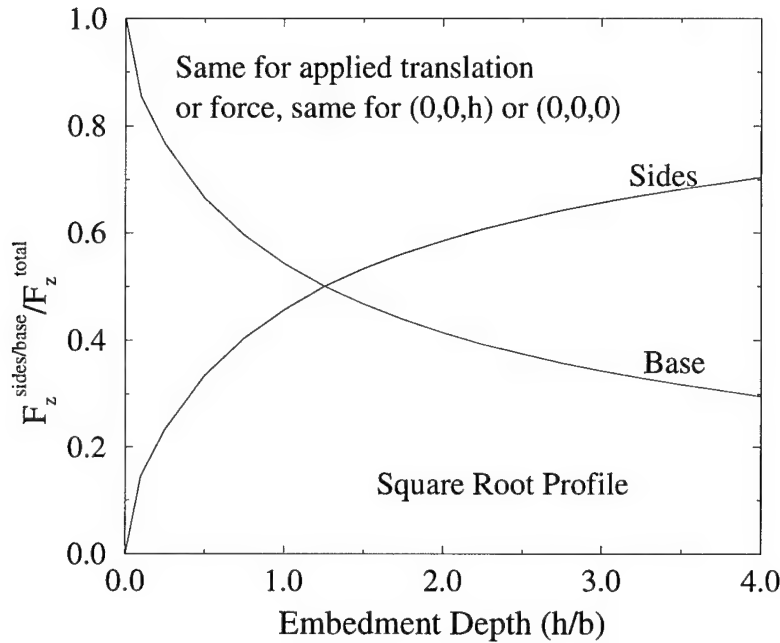
Figure 3.26: Components of vertical resistance vs. embedment depth for the square root profile.
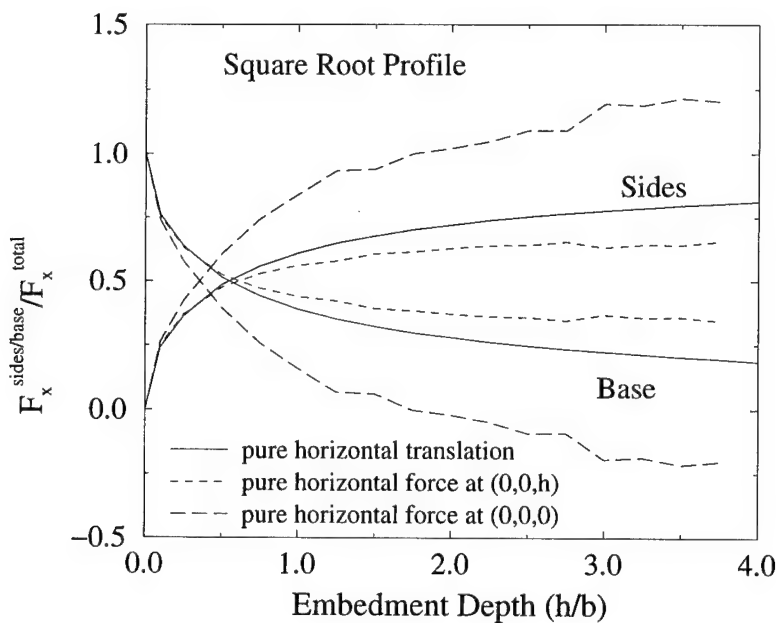
Figure 3.27: Components of horizontal resistance vs. embedment depth for the square root profile.
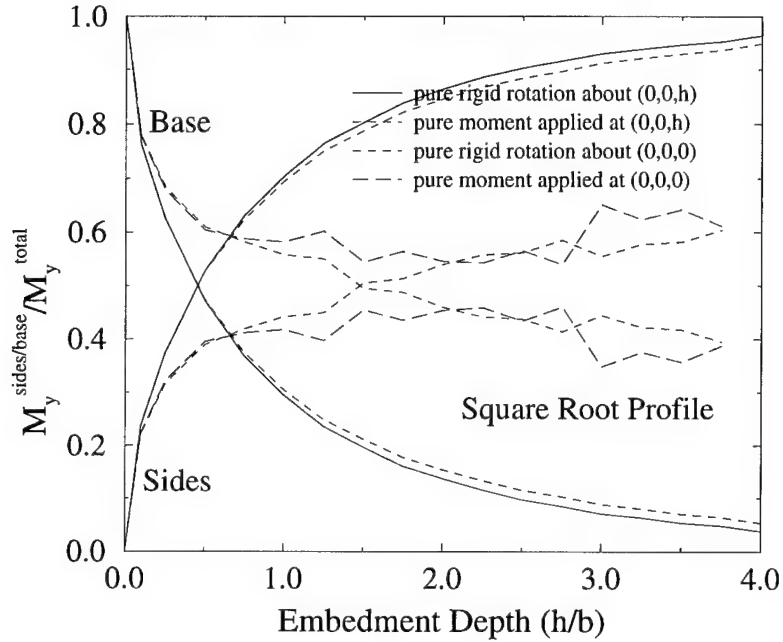
Figure 3.28: Components of rotational resistance vs. embedment depth for the square root profile.
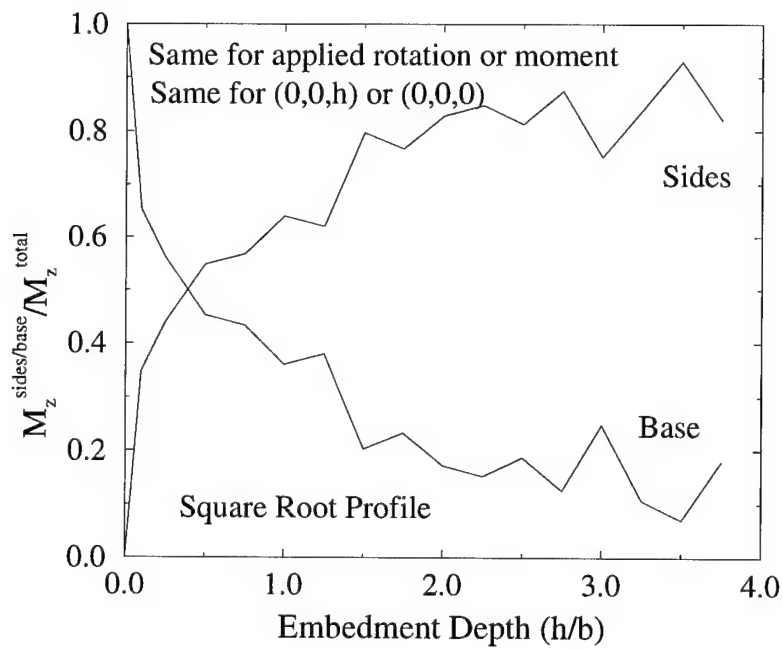
Figure 3.29: Components of torsional resistance vs. embedment depth for the square root profile.

3.5   Impedance Modification Factors

To compare the impedance results for the square-root profile to the homogeneous half-space, the concept of "Impedance Modification Factors" (IMF's) is a convenient vehicle (Pak and Ashlock [31]). The Impedance Modification Factors are defined by

$$\alpha_{ij}(\bar{\omega}) = \frac{\left(\frac{\bar{K}_{ij}(\bar{\omega})}{K_{vv}(\bar{\omega})}\right)^{model}}{\left(\frac{\bar{K}_{ij}(\bar{\omega})}{K_{vv}(\bar{\omega})}\right)^{ref.}} \tag{3.6}$$

where $i, j = h, m$. The superscript "model" refers to either an experimental model or an analytical model and "ref." refers to a chosen reference or benchmark solution. If the vertical impedances are from the model and reference solutions are set to be the same, then Equation (3.6) degenerates to

$$\alpha_{ij}(\bar{\omega}) = \frac{\bar{K}_{ij}^{model}}{\bar{K}_{ij}^{ref.}} \tag{3.7}$$

which is a direct comparison of the rocking, horizontal, and coupling impedance coefficients from the model and the reference solutions. Taking the square-root theoretical solution as the "model" and the homogeneous half-space as the "reference," one can determine the static values of α_{hh}, α_{mm}, and α_{mh} as they vary with embedment depth (see Table 3.3 and Figure 3.31). The ratio of the dimensionless static vertical stiffnesses is shown in Figure 3.30 which is derived from Tables 2.1 and 3.2. At zero embedment, the homogeneous half-space has a higher vertical stiffness than the square-root profile for $G = G_0$, whereas the square-root profile is more than twice as stiff as the homogeneous half-space at an embedment depth of $h/b = 4.0$.

In order to plot the dynamic α_{ij} meaningfully, it is useful to set the quasi-static vertical impedances of the model and reference solutions to be equal. For this purpose, one can define the ratio of quasi-static vertical stiffnesses as given

in Table 3.3 and Figure 3.30 as

$$\alpha_v = \frac{\frac{K_{vv}^{sqrt}}{G_0 b}}{\frac{K_{vv}^{homog}}{G b}}. \tag{3.8}$$

If $K_{vv}^{sqrt} = K_{vv}^{homog}$, then

$$\alpha_v = \frac{G}{G_0} \tag{3.9}$$

which affects the dimensionless frequencies. For a comparison of the square-root shear modulus profile to the homogeneous half-space, the ratio of the dimensionless frequencies is

$$\frac{\bar{\omega}_{sqrt}}{\bar{\omega}_{homog}} = \frac{\frac{\omega b}{C_{s0}}}{\frac{\omega b}{C_s}} \tag{3.10}$$

For a comparison at the same actual frequency ω with the same footing half-width b

$$\frac{\bar{\omega}_{sqrt}}{\bar{\omega}_{homog}} = \frac{C_s}{C_{s0}} = \sqrt{\frac{G}{G_0}} = \sqrt{\alpha_v} \tag{3.11}$$

which yields

$$\bar{\omega}_{sqrt} = \bar{\omega}_{homog}\sqrt{\alpha_v} \tag{3.12}$$

where α_v is given in Table 3.3 and Figure 3.30. For example, at embedment depths of 1.0 and 2.0,

$$\begin{aligned} h/b = 1.0 &\longrightarrow \bar{\omega}_{sqrt} = 1.20 * \bar{\omega}_{homog}, \\ h/b = 2.0 &\longrightarrow \bar{\omega}_{sqrt} = 1.31 * \bar{\omega}_{homog}. \end{aligned} \tag{3.13}$$

Figures 3.32 and Figures 3.33 show the magnitudes of the α_{ij} as a function of frequency at embedments of $h/b = 1.0$ and $h/b = 2.0$, while Figures 3.34 and 3.35 show the real and imaginary parts. Both curves show the same general shape for each α_{ij}.

Figures 3.31, 3.32 and 3.33 reveal that both statically and dynamically, all three α_{ij} are less than one, indicating that the homogeneous half-space provides a stiffer response in the rocking, horizontal, and coupling modes of vibration than the square-root half-space for shallow embedments when the K_{vv}'s from each

solution are set to be equal. This behavior can be attributed to the low value of the shear modulus near the surface in the square-root profile that gives weaker force and moment resistance to the foundation. The erratic behavior of α_{mh} at shallow embedment depths in Figure 3.31 may be related to the lower shear modulus near the surface for the square root profile as well as the small values of the off-diagonal terms for shallow embedment depths.

One of the most important aspects of the static α_{ij}^s versus embedment depth curves in Figure 3.31 and Table 3.3 is the trend with increasing embedment. At deeper embedments, one would expect that the square-root profile might come closer to modeling an actual foundation on sand, since the local increase in shear modulus caused by the foundation contact pressure would have a less significant effect on the soil at deeper embedment depths. From Table 3.3, at $h/b = 4.0$, α_{hh} has a magnitude of 0.84, α_{mm} has a magnitude of 0.57, and α_{mh} has a magnitude of 0.62. Knowledge of these variations of α_{ij}^s with embedment depth is helpful in analyzing the experimental data as will be discussed in Chapter 6.
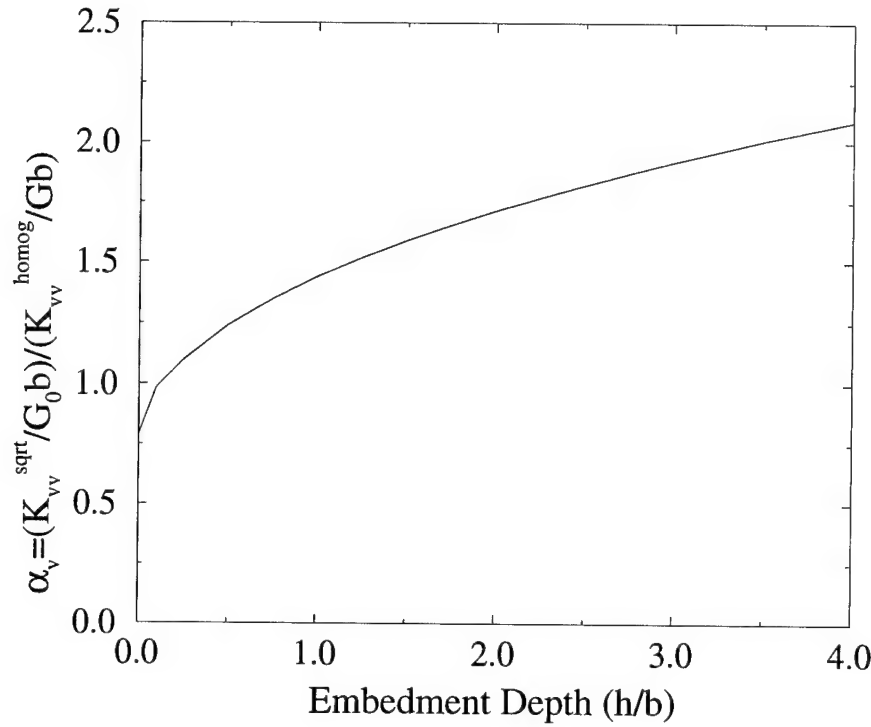
Figure 3.30: Ratio of vertical stiffnesses for the square-root ($\bar{\omega} = 0.1$) and homogeneous ($\bar{\omega} = 0.0$) profiles, $\nu = 0.25$.
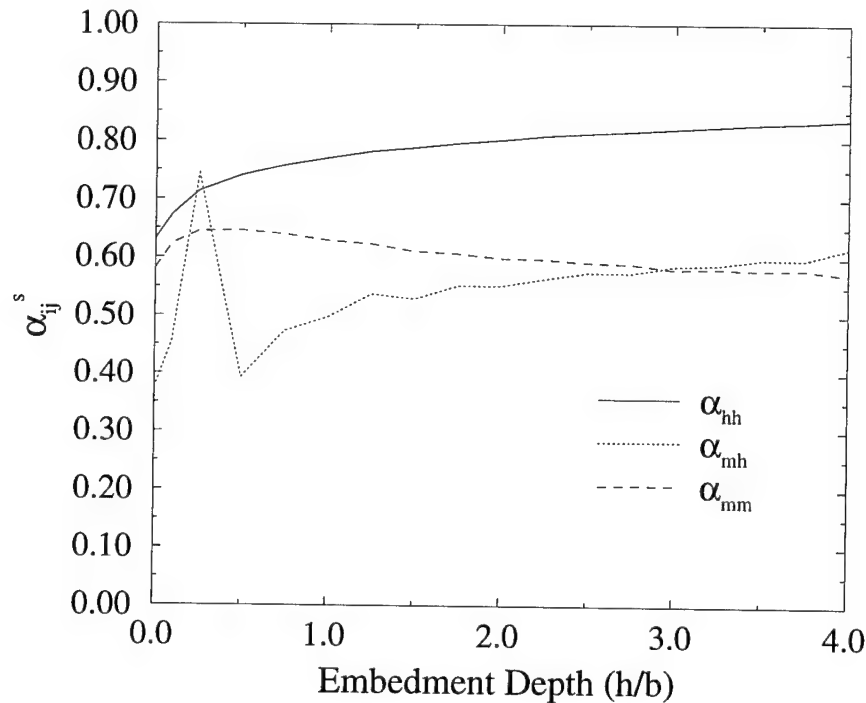
Figure 3.31: Theoretical quasi-static α_{ij}^s for the square-root profile as the model and the homogeneous half-space as the reference, $\nu = 0.25$.
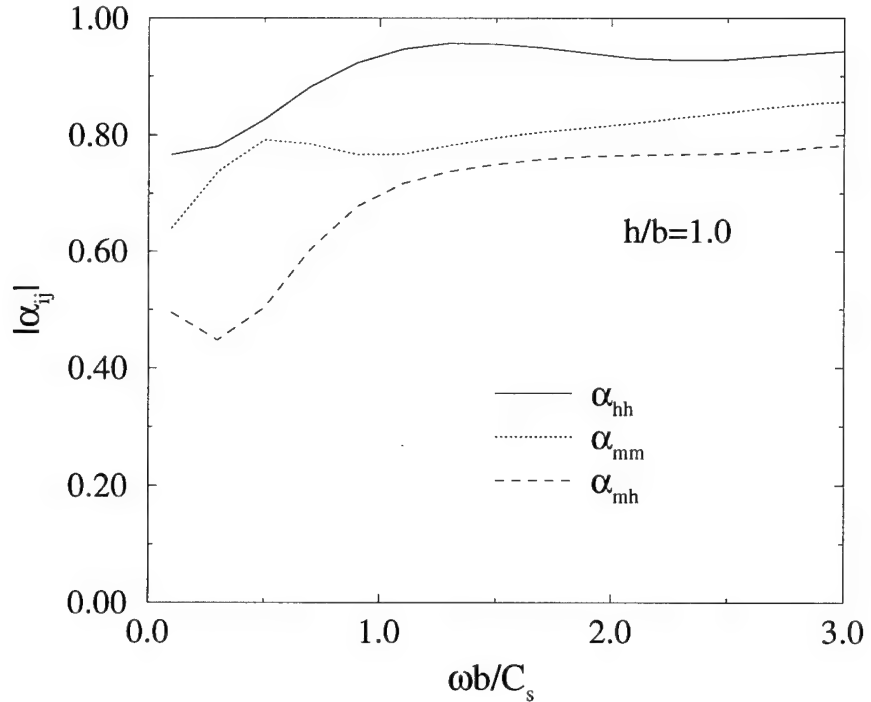
Figure 3.32: Theoretical $|\alpha_{ij}|$ versus frequency for $h/b = 1.0$ for the square-root half-space as the model and the homogeneous half-space as the reference, $\nu = 0.25$.
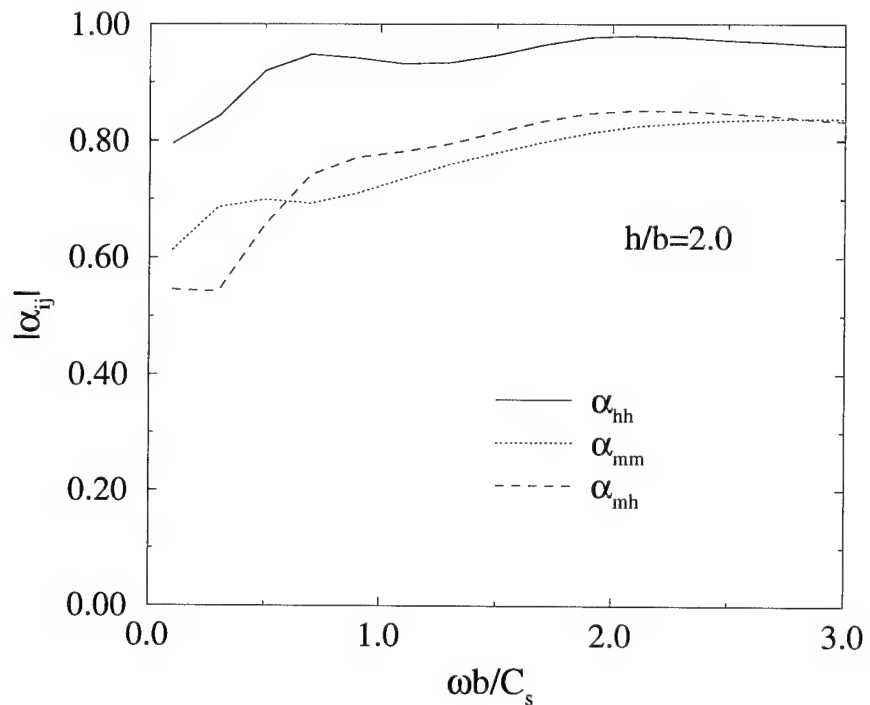
Figure 3.33: Theoretical $|\alpha_{ij}|$ versus frequency for $h/b = 2.0$ for the square-root half-space as the model and the homogeneous half-space as the reference, $\nu = 0.25$.
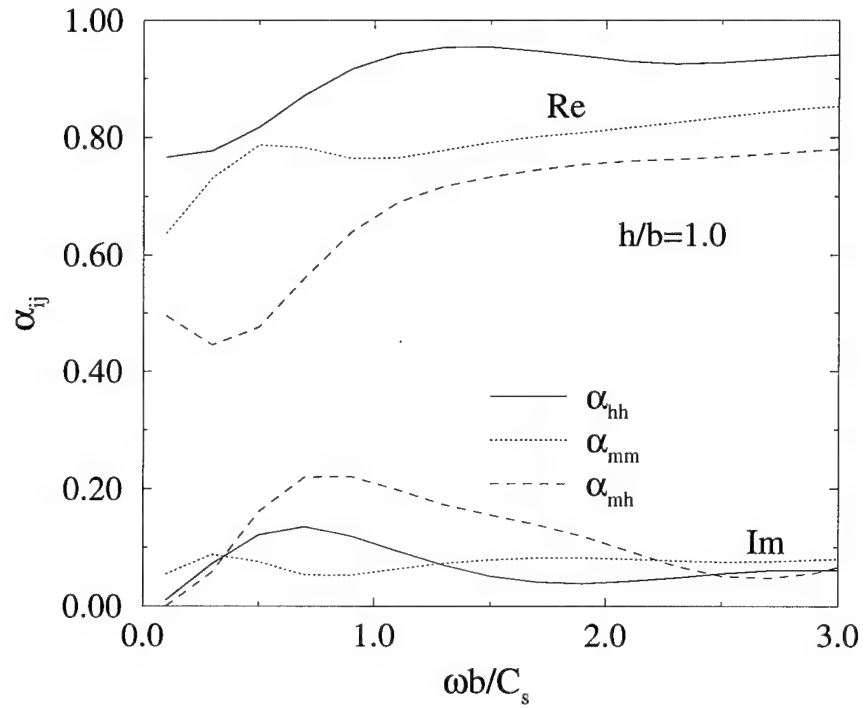
Figure 3.34: Real and imaginary parts of theoretical α_{ij} versus frequency for $h/b = 1.0$, $\nu = 0.25$.
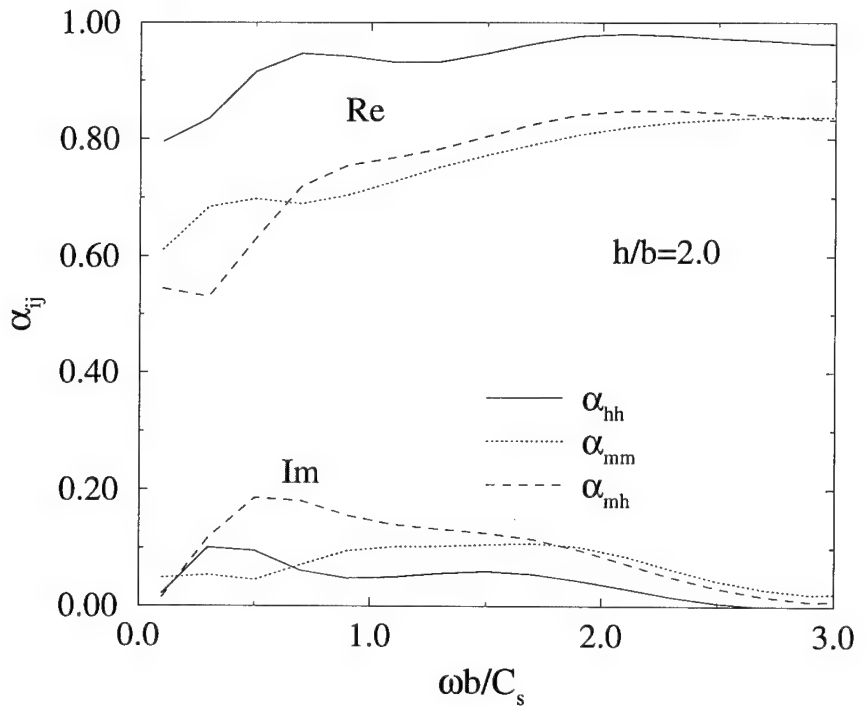
Figure 3.35: Real and imaginary parts of theoretical α_{ij} versus frequency for $h/b = 2.0$, $\nu = 0.25$.

h/b	α_v	α_{hh}	α_{mm}	α_{mh}
0.00	0.79	0.63	0.58	0.37
0.10	0.98	0.67	0.62	0.45
0.25	1.10	0.71	0.64	0.74
0.50	1.24	0.74	0.65	0.39
0.75	1.35	0.76	0.64	0.47
1.00	1.44	0.77	0.63	0.50
1.25	1.52	0.78	0.62	0.54
1.50	1.59	0.79	0.61	0.53
1.75	1.65	0.80	0.61	0.55
2.00	1.71	0.80	0.60	0.55
2.25	1.77	0.81	0.60	0.57
2.50	1.82	0.81	0.59	0.58
2.75	1.87	0.82	0.59	0.57
3.00	1.92	0.82	0.59	0.59
3.25	1.96	0.82	0.58	0.59
3.50	2.01	0.83	0.58	0.60
3.75	2.05	0.83	0.58	0.60
4.00	2.09	0.84	0.57	0.62

Table 3.3: Table of quasi-static α_{ij}^s versus embedment depth with the square-root profile as the model and the homogeneous half-space as the reference, $\nu = 0.25$.

Chapter 4

Experimental Setup and Procedure

4.1 Centrifuge Modeling

As demonstrated in Pak and Guzina [32] and Pak and Ashlock [31] for surface footings, theoretical continuum solutions are usually useful only if they are suitably calibrated with physical observations and experimental results. For the embedded foundation problem of interest, issues such as the effects of bearing pressure and foundation size are also likely to be critical to the dynamic responses. To obtain the experimental data and insight necessary to evaluate the applicability of the results in Chapters 2 and 3 to real soils, the geotechnical centrifuge modeling method is employed for its economy, flexibility, and capacity for accurately controlling the testing environment.

In geotechnical engineering, centrifuge scaled modeling is one of the most powerful experimental techniques to model prototype soil behavior due to its ability to represent various gravity-induced responses of soil. In a geotechnical centrifuge, the induced gravity field resulting from the applied centrifugal force enables the accurate modeling of the gravity effects due to the self-weight of the soil and maintains the critical stress similitude with the prototype configuration. Scaling relations for different applications can be derived from dimensional analysis or the governing differential equations. A table of scaling relations corresponding to the parameters used in the centrifuge experiments in this investigation appears in Table 4.1.

Quantity	Prototype	Model at n g
Length	1	$1/n$
Area	1	$1/n^2$
Volume	1	$1/n^3$
Mass Density	1	1
Mass	1	$1/n^3$
Strain	1	1
Displacement	1	$1/n$
Velocity	1	1
Acceleration	1	n
Stress	1	1
Force	1	$1/n^2$
Time (dynamics)	1	$1/n$

Table 4.1: Centrifuge scaling relations.

All the experiments in this study were conducted on the 440g-ton centrifuge at the University of Colorado at Boulder. A schematic of the centrifuge appears in Figure 4.1. The centrifuge is powered by a General Electric 684 kW DC electric motor and is capable of spinning a payload of up to 2000kg (2.2 tons) to 200g's. The rotor arm is asymmetric, with a $4ft \times 4ft \times 3ft$ platform on one end, and three counterweight loading tanks on the other. The centrifuge is equipped with a set of slip-rings which provide a means of sending electrical data signals from the arm of the centrifuge to the data acquisition system in the centrifuge control room. A detailed description of the University of Colorado's centrifuge facilities appears in Ko [21].

4.2   Model Footing, Exciter, and Instrumentation

With the focus being on the embedment effects, the experimental study will employ model footing "B" which has a square base with a half-width $b = 0.0275m$
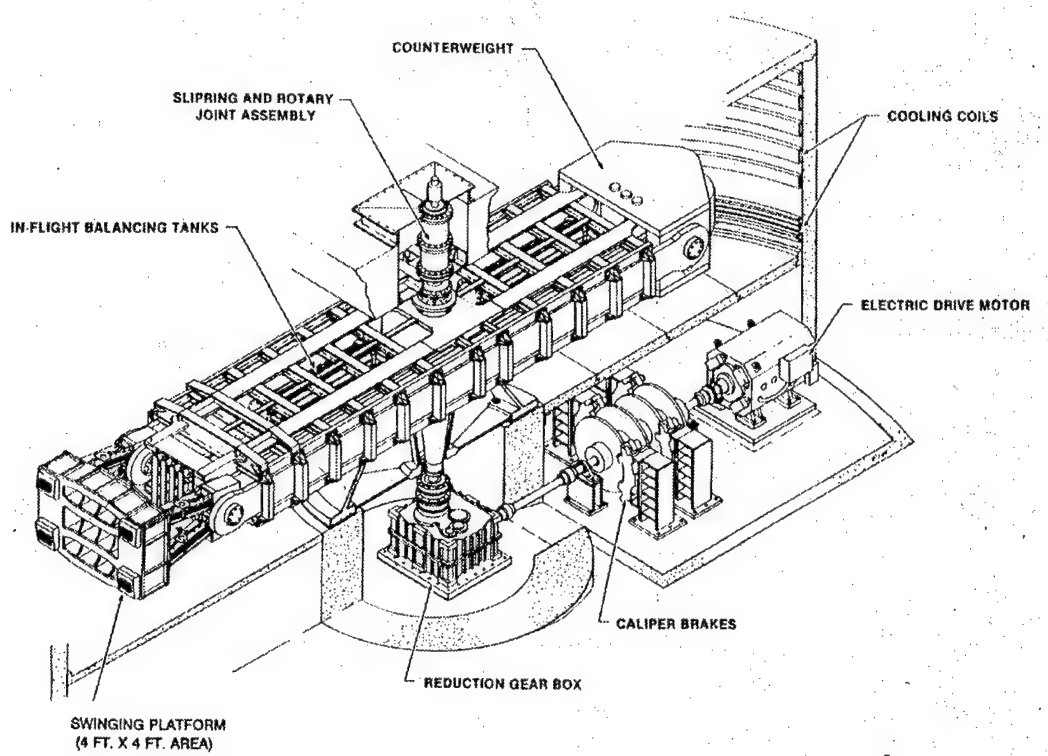
Figure 4.1: Schematic of the 440g-ton centrifuge at the University of Colorado at Boulder.

and a height of $0.1375m$ (see Gillmor [11] and Ashlock [1]). Footing B is made of high-strength 7075-T6 aluminum and has 13 holes tapped in it for the attachment of load cells and accelerometers. Both vertical and lateral vibration tests were performed on Footing B. The exciter used for the application of a vertical load is a Bruel and Kjaer model 4809 vibration exciter. This exciter is shown in Figure 4.2 in the configuration used for vertical vibration loading. A steel bolt is attached to the exciter armature and the head of this bolt makes contact with the footing attachments. Together with the armature mass of the 4809 exciter, the total extra mass of $66g$ adds to the bearing pressure of the footing when vertical vibration tests are conducted. Two different means of distributing a vertical or horizontal dynamic load to the load cell were tried in this investigation. The first

method is via a "stinger" which has a conical shape and is described in Brown [3]. The second method is via a hemispherical "button" described in Ashlock [1]. A diagram of both the stinger and button appear in Figure 4.3. The exciter
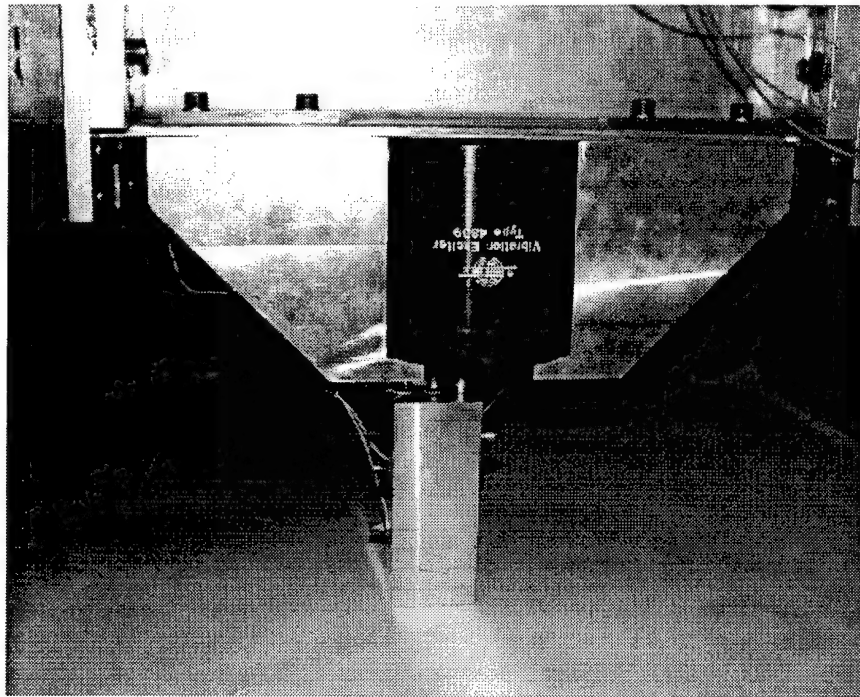
Figure 4.2: Vertical vibration testing configuration.

used for lateral loading is a Bruel and Kjaer model 4810 mini-shaker. The exciter armature has a smooth steel bar bolted to it (see Figure 4.4), through which the lateral dynamic load is applied to the footing. Generally, only one exciter is used on the centrifuge at a given time, since the vertical and lateral tests are conducted separately. In the centrifuge control room, a Tektronix PS280 DC power supply provides a DC current which controls the in-and-out movement of the exciter armature. Consequently, the DC current can be used to control the static prestress that the exciter armature applies to the footing. A random AC current is supplied by a Tektronix 2630 Fourier analyzer which controls the actual vibration of the exciter. The random AC current enables the sampling of data at

Stinger   Hemispherical Button
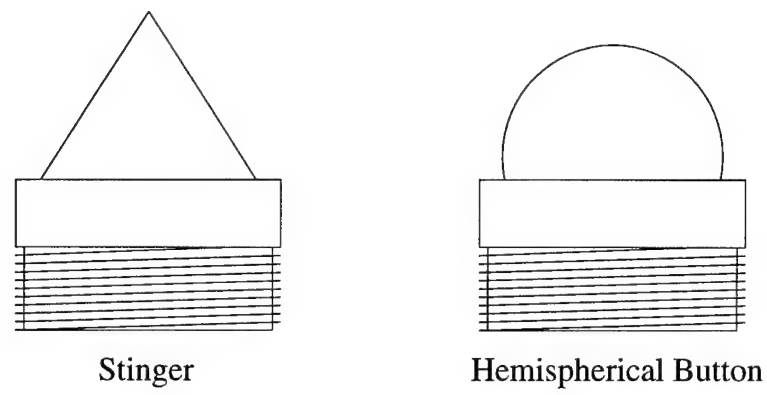
Figure 4.3: Stinger and hemispherical button used to distribute load to the load cell.
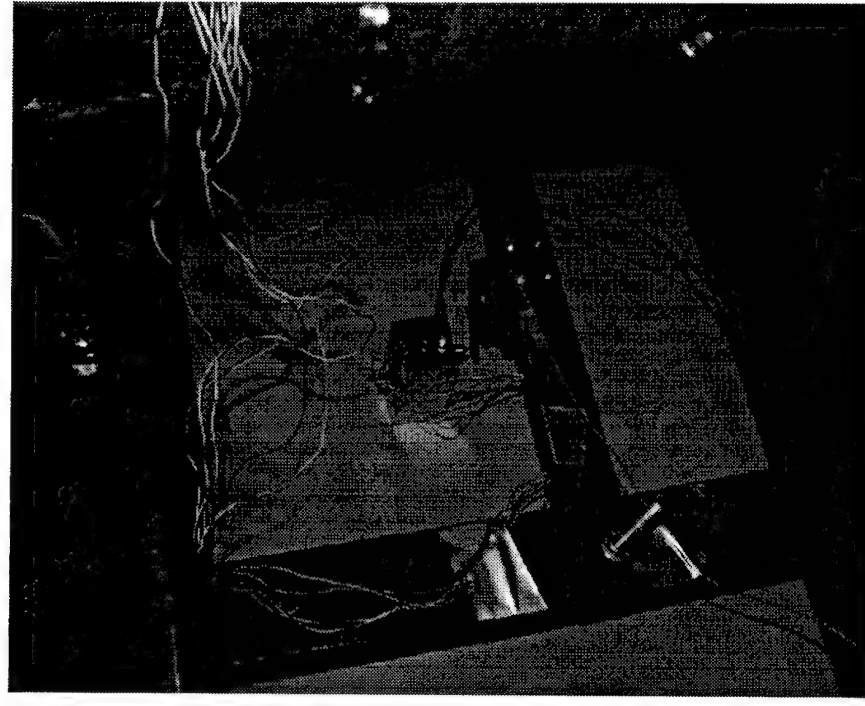
Figure 4.4: Lateral vibration testing configuration.

approximately 1600 frequency points in the frequency range of interest. A signal adder combines the AC and DC signals which are sent though the centrifuge slip rings to the exciter.

The dynamic load applied by the exciter is measured by one of two quartz load cells. Both are Kistler washer type load cells. One is a model 9001 quartz load washer and the other is a model 9001A quartz load washer. The load washers are piezo-electric force transducers which convert a force into an electric charge. This charge is then converted into a voltage by a charge amplifier on the arm of the centrifuge. The charge amplifiers used in the experiments are Kistler type 5010 and type 5004 dual mode amplifiers. The voltage from the charge amplifier is then sent through the centrifuge slip-rings to the Tektronix 2630 Fourier analyzer in the centrifuge control room.

Accelerometers attached to the footing measure the acceleration of the footing at their given location. The accelerometers used are PCB Piezotronics model 352B67 ICP accelerometers. The accelerometer signals are conditioned by a PCB Piezotronics model 483A signal conditioner and the signals are amplified by a Krohn-Hite Model 3905A multichannel filter. Then the accelerometer signals are sent though the slip-rings to the Fourier analyzer in the centrifuge control room.

In the centrifuge control room, the Fourier analyzer gathers the input from the accelerometers and the load cell and converts the data to the frequency domain via the Fast-Fourier Transform (FFT). An instrument program on a personal computer is used to view the data from the Fourier analyzer and to write the data to an output file. The most important pieces of information are the frequency response function (FRF), the coherence function, and the auto-spectral density function. The frequency response function employed in this study is the acceleration at a given point divided by the force applied at another point as a function of frequency. This FRF is referred to as the accelerance function, or simply **accel-**

erance. To account for the inertial and stiffness effects of various attachments, it is essential to determine the dynamic mass transfer function $M(\omega)$ by performing a dynamic vibration test on the model footing at $1g$ (see Ashlock [1]).

4.3   Soil and Sample Preparation

The soil used in all of the experiments is dry F-75 silica sand. According to tests performed at the U.S. Bureau of Reclamation, the maximum and minimum mass densities of F-75 silica sand are

$$\rho_{d,min} = 1469\frac{kg}{m^3}, \quad \rho_{d,max} = 1781\frac{kg}{m^3}, \tag{4.1}$$

and the corresponding maximum and minimum void ratios are

$$e_{d,max} = \frac{G_s\rho_w}{\rho_{d,min}} - 1 = 0.8039, \quad e_{d,min} = \frac{G_s\rho_w}{\rho_{d,max}} - 1 = 0.4879, \tag{4.2}$$

where G_s is the specific gravity of the sand (2.65) and ρ_w is the mass density of water ($1000\frac{kg}{m^3}$). The soil in all of the experiments conducted in this investigation had a density of $1730\frac{kg}{m^3}$ which yields a void ratio of $e = 0.5318$ and a relative density of $D_r = 86.1\%$.

A rectangular container with dimensions given in Figure 4.2 was used for all of the experiments. The rectangular geometry minimizes the concentration of waves reflected off of the boundaries of the container. Additionally, a layer of duxseal was placed on all four sides of the container to mitigate wave reflection. Duxseal is a clay-like material used for sealing air ducts. Previous studies (e.g. Coe et. al. [4] and Lenke et. al. [22]) have shown that duxseal is useful for absorbing the wave intensity and mitigating reflections. The duxseal in this investigation is placed on a grid around the sides of the container to give it support, and covered with plastic wrap to keep it separated from the soil. A picture of the empty container with the duxseal boundary is given in Figure 4.5.

Container Dimensions			Duxseal	Soil Sample Dimensions		
Length [m]	Width [m]	Depth [m]	Thickness [m]	Length [m]	Width [m]	Depth [m]
1.20	1.00	0.61	≈0.035	1.13	0.93	0.46

Table 4.2: Centrifuge container and soil sample dimensions (Guzina [12]).
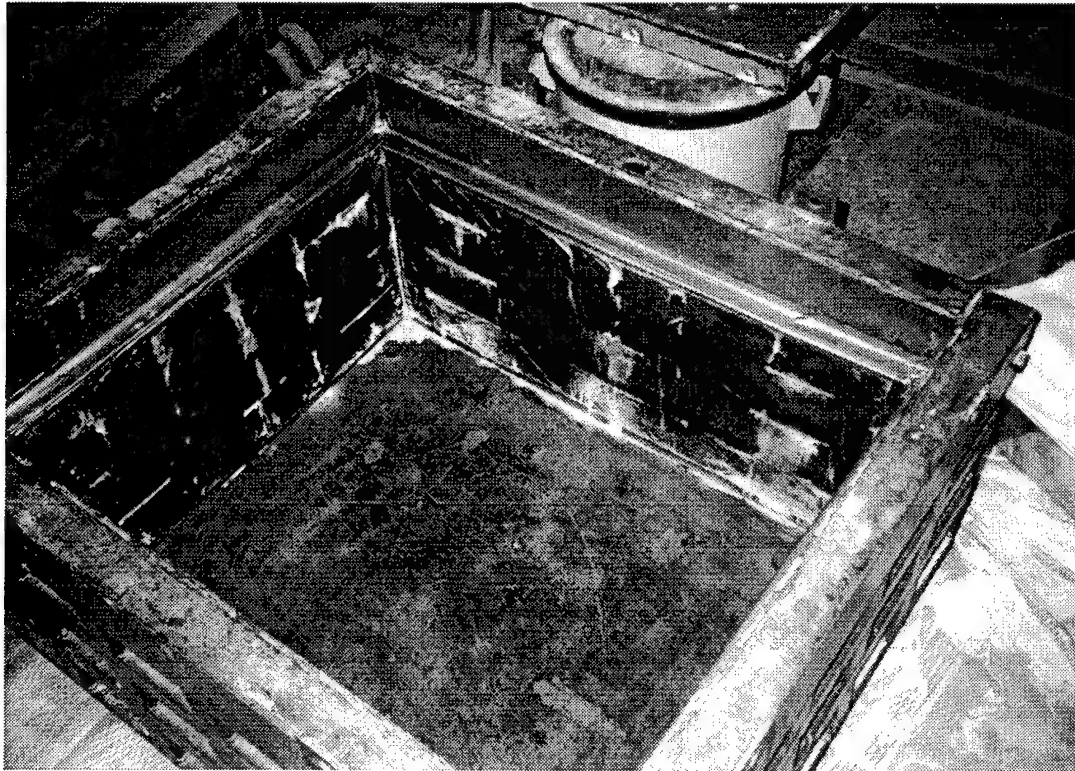
Figure 4.5: Rectangular container with duxseal walls used for centrifuge experiments.

In order to obtain the desired soil density, the method of pluviation through air or "raining" was employed. Two different pluviation methods were used to prepare the soil sample. The first method utilizes a wedge-shaped hopper with a slotted plate at the base to control the flux of soil. The slot is approximately $0.476cm$ wide by $51.44cm$ long. When the soil is rained from a height of $1.37m$, the desired relative density of 86% is obtained. Figure 4.6 shows a picture of this
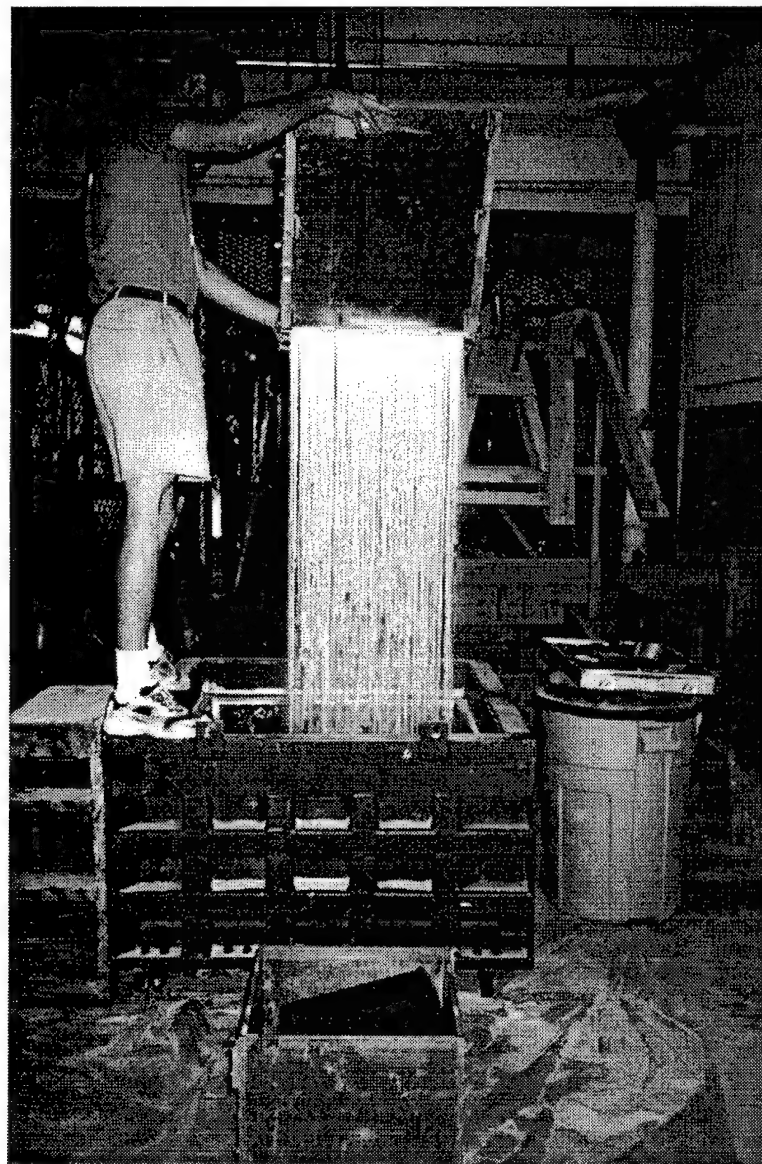
Figure 4.6: Soil pluviation with the wedge-shaped hopper.

raining method. The second method used involves a washer and a "vacuum hose" to control the flux of soil. The washer has an outer diameter of $3.5cm$ and an inner diameter of $1.43cm$, while the vacuum hose has a diameter of $3.81cm$. The washer and vacuum hose are attached to a cylindrical bucket with a conical base which feeds the soil through the washer and hose. The length of the hose is $1.14m$, and when the distance from the end of the hose to the base of the soil is $0.74m$, then

the desired relative density of 86% is obtained. A picture of this raining method is shown in Figure 4.7, while Figure 4.8 shows a diagram illustrating the relevant dimensions used in both pluviation methods.
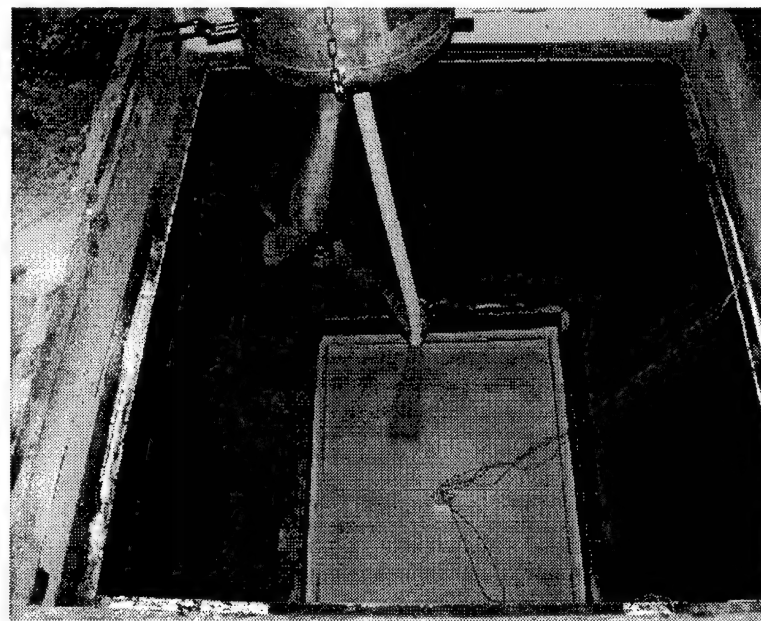
Figure 4.7: Soil pluviation with the cylinder and vacuum hose.

When preparing a sample for testing, the hopper method is used to rain the soil into the bucket up to the desired level at which the footing will be placed. The soil is then scraped off and vacuumed out to provide a level surface for the place-ment of the footing on the sand. The footing is placed with the accelerometers and load cells already attached so as to minimize the sample disturbance if this is done later. However, this did create the need to monitor the instrumentation wires during the raining process to ensure that they did not pull on the footing and cause further disturbance. Figure 4.7 shows the location of the footing and in-strumentation wires as the soil is rained around them. After the footing is placed on the level surface, the hose method is employed to raise the soil level to achieve the intended depth of embedment, since the vacuum hose provides more precise
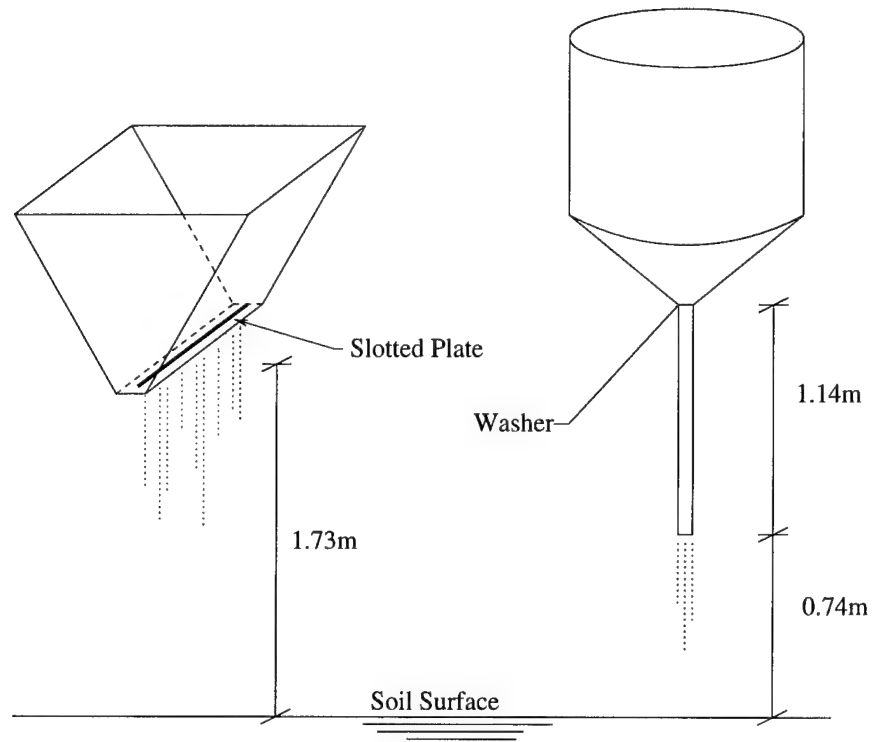
Figure 4.8: Diagram of soil preparation methods.

control of the soil placement around the footing and transducer wires. After the raining of soil around the footing, the soil is scraped and leveled to the precise embedment depth.

Figure 4.9 shows footing B after the soil was placed to an embedment depth of $h/b = 2.0$. In most cases, the soil was rained to a depth of $h/b = 2.0$ and then tests were conducted at this embedment depth. The soil was then scraped off and vacuumed out to a shallower depth, e.g. $h/b = 1.5$, and tests were conducted at this embedment depth. This procedure was then repeated progressively for embedment depths of 1.0, 0.5, and 0.25. This sequential procedure was adopted since the motion of the foundation will be the least at the deepest embedment depth. Thus, sample disturbance due to the application of a dynamic load was minimized by performing the tests at $h/b = 2.0$ first. Surface tests were conducted
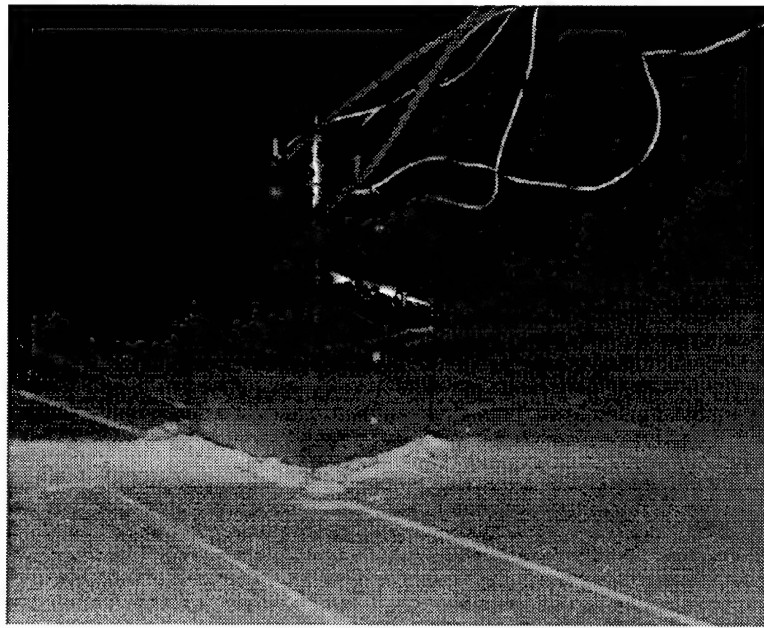
Figure 4.9: Footing B after soil placement to $h/b = 2.0$.

at entirely new locations on the sample after the embedded tests were completed. Thus, including the surface case, a typical testing sequence in this investigation includes tests for six different embedment depths.

Chapter 5

Foundation Accelerance in Forced Vibration Tests

5.1   Accelerance Matching Approach

As mentioned in Chapter 4, the centrifuge model tests will provide data in the form of experimental accelerance functions. However, it is well-known from previous analytical and experimental studies ([1], [3], [12]) that a direct inversion of experimental accelerance to obtain the interfacial impedance matrix is difficult due to the analytical properties of the matrix system (see Guzina and Pak [15]) and the presence of experimental noise (see Ashlock [1]). To circumvent this problem, the theoretical interfacial impedances discussed in the previous chapters are employed to generate a set of theoretical accelerances to match with the experimentally measured ones. In this method, the accelerances can be left in their pristine condition. In order to lay the theoretical groundwork for this approach, the derivation for the accelerance function by rigid-body dynamics is given in this chapter. Accelerance as a frequency response function from an experimental standpoint will be discussed in the following chapter.

The method of accelerance matching involves varying the elastic parameters (G and ν) of the soil medium in an appropriate continuum model (such as a homogeneous half-space or a square-root half-space) in order to find the theoretical accelerance which most closely matches the experimental measurements. Usually, this approach involves calculating the difference between the theory and the experiment in a least squares error sense and selecting the best-fit shear modulus

and Poisson's ratio based on the theoretical curve with the least error. Generally, this initial fit is done for vertical concentric loading since this loading case is the simplest. The best-fit shear wave speed and Poisson's ratio can then be used to match the lateral accelerances. Using the homogeneous half-space model, however, it was found ([1], [11]) that "Impedance Modification Factors" or IMF's were needed to achieve satisfactory agreement with the experiments (see Chapter 3 where IMF's are introduced for this investigation). To appreciate the essence of the experimental data, a good understanding of the chosen theoretical framework is a prerequisite. An overview of the issues is presented in the following sections.

5.2   Derivation of the Theoretical Accelerance Function

A rigid embedded footing for the basis of the accelerance derivation is shown in Figure 5.1. In rigid-body dynamics, all forces and moments that are applied to the footing can be transferred and condensed to the centroid of the footing as shown. By summing the forces according to Newton's Second Law in the x- and z-directions and by summing the moments about the y-axis, one can state the following equations of planar motion for the footing in the time domain:

$$\Sigma f_z^C = m\ddot{u}_z^C(\omega) = q_V(\omega) - f_z^0(\omega),$$

$$\Sigma f_x^C = m\ddot{u}_x^C(\omega) = q_H(\omega) - f_x^0(\omega),$$ (5.1)

$$\Sigma m_y^C = J_y^C \ddot{\theta}_y^C(\omega) = q_M(\omega) - m_y^0(\omega) - f_z^0(\omega)e_c - f_x^0(\omega)h_C,$$

where m is the mass of the footing, J_y^C is the polar moment of inertia about the centroid, $(q_V,\ q_H,\ q_M)$ are the applied external loads and moment, $(f_z^0,\ f_x^0,\ m_y^0)$ and $(u_z^0,\ u_x^0,\ \theta_y^0)$ are the resultant forces and displacements at the control point '0' on the bottom of the rigid body, $(f_z^c,\ f_x^c,\ m_y^c)$ and $(u_z^c,\ u_x^c,\ \theta_y^c)$ are the forces and displacements at the centroid of the footing, and e_C and h_C are the eccentricity and height of the centroid respectively. In their current state, the equations of motion
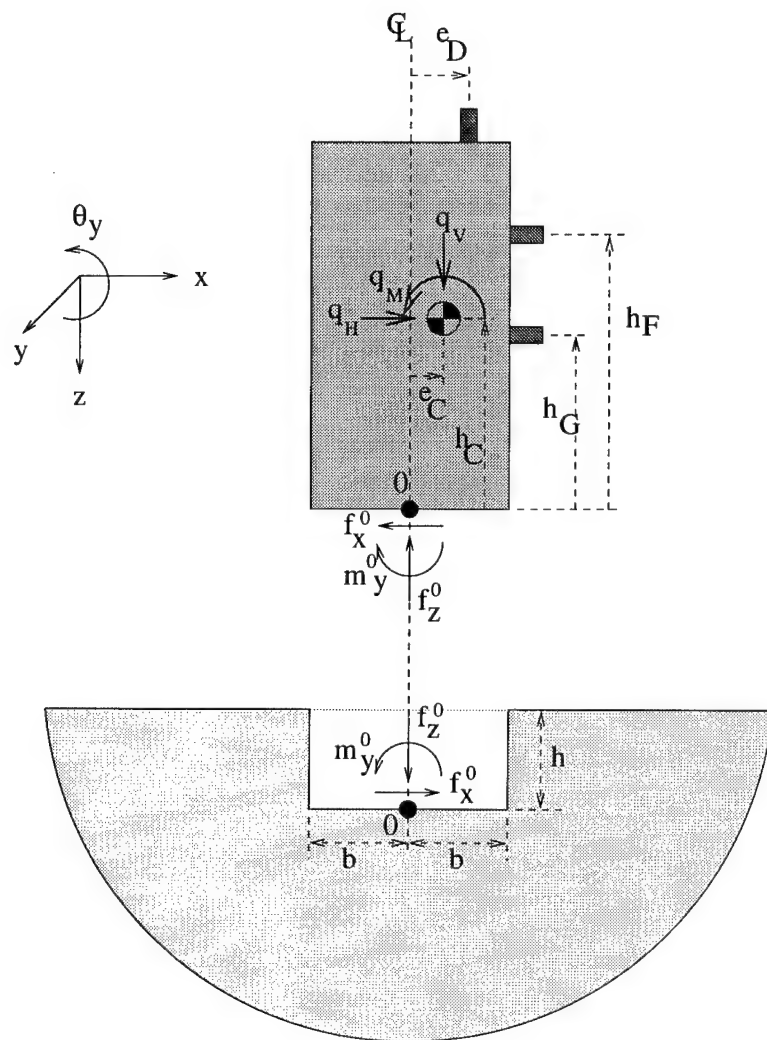
Figure 5.1: Free-body diagram of a square footing on a half-space.

above are ordinary differential equations of the second order. However, taking the Fourier transform of these equations yields the following algebraic equations:

$$Q_V(\omega) - F_z^0(\omega) + \omega^2 m U_z^C(\omega) = 0,$$

$$Q_H(\omega) - F_x^0(\omega) + \omega^2 m U_x^C(\omega) = 0, \qquad (5.2)$$

$$Q_M(\omega) - M_y^0(\omega) - F_z^0(\omega)e_C - F_x^0(\omega)h_C + \omega^2 J_y^C \Theta_y^C(\omega) = 0,$$

where the Fourier transform is defined as,

$$F(\omega) = \int_{-\infty}^{\infty} f(t)e^{-i\omega t}dt. \qquad (5.3)$$

The translational and rotational accelerations $\ddot{u}_z^c(\omega)$, $\ddot{u}_x^c(\omega)$, and $\ddot{\theta}_z^c(\omega)$ become $-\omega^2 U_z^c(\omega)$, $-\omega^2 U_x^c(\omega)$, and $-\omega^2 \Theta_z^c(\omega)$ respectively. All other dynamic components of the equations of motion can be transformed similarly. In dimensionless form, the equations of motion can be stated as

$$\bar{Q}_V(\bar{\omega}) - \bar{F}_z^0(\bar{\omega}) + \bar{\omega}^2 \bar{m} \bar{U}_z^C(\bar{\omega}) = 0,$$

$$\bar{Q}_H(\bar{\omega}) - \bar{F}_x^0(\bar{\omega}) + \bar{\omega}^2 \bar{m} \bar{U}_x^C(\bar{\omega}) = 0, \qquad (5.4)$$

$$\bar{Q}_\theta(\bar{\omega}) - \bar{M}_y^0(\bar{\omega}) - \bar{F}_z^0(\bar{\omega})\bar{e}_C - \bar{F}_x^0(\bar{\omega})\bar{h}_C + \bar{\omega}^2 \bar{J}_y^C \bar{\Theta}_y^C(\bar{\omega}) = 0,$$

where the dimensionless quantities are defined as

$$\begin{aligned}
\bar{Q}_V &= \tfrac{Q_V}{Gb^2}, \quad \bar{Q}_H = \tfrac{Q_H}{Gb^2}, \quad \bar{Q}_M = \tfrac{Q_M}{Gb^2}, \quad \bar{F}_z = \tfrac{F_z}{Gb^2}, \\
\bar{F}_z &= \tfrac{F_z}{Gb^2}, \quad \bar{M}_y = \tfrac{M_y}{Gb^3}, \quad \bar{U}_z^C = \tfrac{U_z}{b}, \quad \bar{U}_x^C = \tfrac{U_x}{b}, \\
\bar{\Theta}_y^C &= \Theta_y, \quad \bar{\omega} = \tfrac{\omega b}{C_s}, \quad \bar{m} = \tfrac{m}{\rho a^3}, \quad \bar{J}_y^C = \tfrac{J_y^C}{\rho a^5}, \\
\bar{e}_C &= \tfrac{e_c}{b}, \quad \bar{h}_C = \tfrac{h_C}{b}.
\end{aligned} \qquad (5.5)$$

The accelerance function of the footing at a point j in the ith direction can be defined as

$$\rho a^3 A_i^j(\omega) = \bar{A}_i^j(\bar{\omega}) = \frac{\ddot{\bar{u}}_i^j(\bar{\omega})}{\bar{Q}_N(\bar{\omega})} = -\frac{\bar{\omega}^2 \bar{U}_i^j(\bar{\omega})}{\bar{Q}_N(\bar{\omega})}, \qquad (5.6)$$

where $i = z,\ x$ and $j = D,\ F,\ G$. Taking accelerance measurements at three non-colinear locations (D, F, G) on the x-z plane will allow the definitive determination of the rigid body motion of the footing in 2-D.

The impedance functions at the soil-foundation interface defined in Equation (2.11) can be re-stated as,

$$\bar{\mathbf{F}}^0(\bar{\omega}) = \bar{\mathbf{K}}(\bar{\omega})\bar{\mathbf{U}}^0(\bar{\omega}), \quad or \quad \left\{ \begin{array}{c} \bar{F}_z^0(\bar{\omega}) \\ \bar{F}_x^0(\bar{\omega}) \\ \bar{M}_y^0(\bar{\omega}) \end{array} \right\} = \left[\begin{array}{ccc} \bar{K}_{vv} & 0 & 0 \\ 0 & \bar{K}_{hh} & \bar{K}_{hm} \\ 0 & \bar{K}_{mh} & \bar{K}_{mm} \end{array} \right] \left\{ \begin{array}{c} \bar{U}_z^0(\bar{\omega}) \\ \bar{U}_x^0(\bar{\omega}) \\ \bar{\Theta}_z^0(\bar{\omega}) \end{array} \right\}.$$

$$(5.7)$$

where $\bar{K}_{ij}$ are defined at $\mathbf{x}_{ref} = \mathbf{x}_h$ of the soil medium. The kinematic relationships between the displacements at various points of interest on the footing will be needed to derive the accelerance function. For a rigid body, the rotation is the same at all points. Accordingly, one may obtain the rotation of the footing from

$$\bar{\Theta}_y(\bar{\omega}) = \frac{\bar{U}_x^G(\bar{\omega}) - \bar{U}_x^F(\bar{\omega})}{\bar{h}_F - \bar{h}_G}$$

$$\bar{h}_F = \frac{h_F}{b}, \quad \bar{h}_F = \frac{h_F}{b}.$$

$$(5.8)$$

where U_x^g and U_x^f are the transformed displacements in the x-direction at points G and F respectively, and h_f and h_g are the heights of points G and F measured from the base of the footing as shown in Figure 5.1. It will also be helpful to deduce from the translation at the measurement locations (D, F, G) the translation at point 0 of the bottom of the soil-foundation interface which is used to define the impedances. By kinematics, the translations in the x direction at point 0 and point F are related according to:

$$\bar{U}_x^0(\bar{\omega}) = \bar{U}_x^F(\bar{\omega}) + \bar{h}_F \Theta_y(\bar{\omega}).$$

$$(5.9)$$

Likewise, the translation U_z^D in the z-direction at point D can be related to the

translation U_z^0 at point 0 by virtue of

$$\bar{U}_z^0(\bar{\omega}) = \bar{U}_z^D(\bar{\omega}) + \bar{e}_D \bar{\Theta}_y(\bar{\omega}), \quad \bar{e}_D = \frac{e_D}{b}. \tag{5.10}$$

Using the equations of motion, the impedance functions, and the rigid body mechanics equations given above, the accelerance functions at points D, F, and G can be defined as,

$$\left\{ \begin{array}{c} \bar{A}_z^D(\bar{\omega}) \\ \\ \bar{A}_x^F(\bar{\omega}) \\ \\ \bar{A}_x^G(\bar{\omega}) \end{array} \right\} = -\bar{\omega}^2 \left[\mathbf{G}_1 \bar{\mathbf{K}} \mathbf{G}_2 - \bar{m}\bar{\omega}^2 \mathbf{G}_3 \right]^{-1} \left\{ \begin{array}{c} \frac{\bar{Q}_V}{Q_N} \\ \\ \frac{\bar{Q}_H}{Q_N} \\ \\ \frac{\bar{Q}_M}{Q_N} \end{array} \right\} \tag{5.11}$$

where $\bar{\mathbf{K}}$ is the impedance matrix and

$$\mathbf{G}_1 = \begin{bmatrix} 1 & 0 & 0 \\ 0 & 1 & 0 \\ \bar{e}_C & \bar{h}_C & 1 \end{bmatrix}, \tag{5.12}$$

$$\mathbf{G}_2 = \begin{bmatrix} 1 & -\frac{\bar{e}_D}{\bar{h}_F - \bar{h}_G} & \frac{\bar{e}_D}{\bar{h}_F - \bar{h}_G} \\ 0 & 1 - \frac{\bar{h}_F}{\bar{h}_G - \bar{h}_G} & \frac{\bar{h}_F}{\bar{h}_F - \bar{h}_G} \\ 0 & -\frac{1}{\bar{h}_F - \bar{h}_G} & \frac{1}{\bar{h}_F - \bar{h}_G} \end{bmatrix}, \tag{5.13}$$

$$\mathbf{G}_3 = \begin{bmatrix} 1 & -\frac{\bar{e}_D - \bar{e}_C}{\bar{h}_F - \bar{h}_G} & \frac{\bar{e}_D - \bar{e}_C}{\bar{h}_F - \bar{h}_G} \\ 0 & 1 - \frac{\bar{h}_F - \bar{h}_C}{\bar{h}_F - \bar{h}_G} & \frac{\bar{h}_F - \bar{h}_C}{\bar{h}_F - \bar{h}_G} \\ 0 & -\frac{\bar{J}_y^C}{\bar{m}(\bar{h}_F - \bar{h}_G)} & \frac{\bar{J}_y^C}{\bar{m}(\bar{h}_F - \bar{h}_G)} \end{bmatrix}. \tag{5.14}$$

5.3   Theoretical Accelerances Computed (Homogeneous Half-Space Impedances)

The theoretical accelerances can now be computed by inserting the dynamic impedance functions from Chapters 2 or 3 into Equations 5.11, 5.12, 5.13,

5.14 above. Accelerances based on the homogeneous half-space impedances from Chapter 2 will be discussed in this section, while accelerances computed from square-root profile impedances from Chapter 3 will be discussed in Section 5.4. There are three types of loading which will be investigated in this study: a vertical concentric load, an eccentric vertical load, and a lateral load. Vertical loading on circular footings has been studied in-depth (see Guzina [12] and Pak and Guzina [32]). Lateral loading has been studied by Brown [3] and Gillmor [11]. Vertical eccentric and lateral loading have been studied by Ashlock [1]. All of these studies are, however, for surface foundations. In this thesis, the effects of these three types of loading on embedded foundations will be examined.

A diagram of the footing used for the theoretical accelerance calculations is shown in Figure 5.2. This diagram shows the actual dimensions of the footing used in the experiments which is discussed in Chapter 4. Without any attachments, the footing has a mass of $m = 1.173kg$ and a mass-moment of inertia $J_0 = 0.002146721kg * m^2$. With reference to the hole numbering scheme shown in Figure 5.2, the accelerance at a particular hole will be denoted as $A_i^j(\omega)$, where i refers to the direction of the measurement (either x or z), and j is the hole number at which the theoretical accelerance is computed (i.e. 1, 2, 3, ..., 13) which correspond to the locations D, F, and G mentioned earlier. Additionally, the accelerance can be made dimensionless by multiplying by ρb^3. In all of the theoretical accelerance calculations, the Poisson's ratio used is $\nu = 0.25$ unless otherwise noted and the mass density of the soil is $\rho = 1730.0kg/m^3$.

5.3.1 Vertical Concentric (VC) Vibration

The simplest of the three loading cases is the vertical concentric case. Consequently, this theoretical case will be discussed first. Since the loading in this case is concentric, there is theoretically no lateral movement. Thus, the only
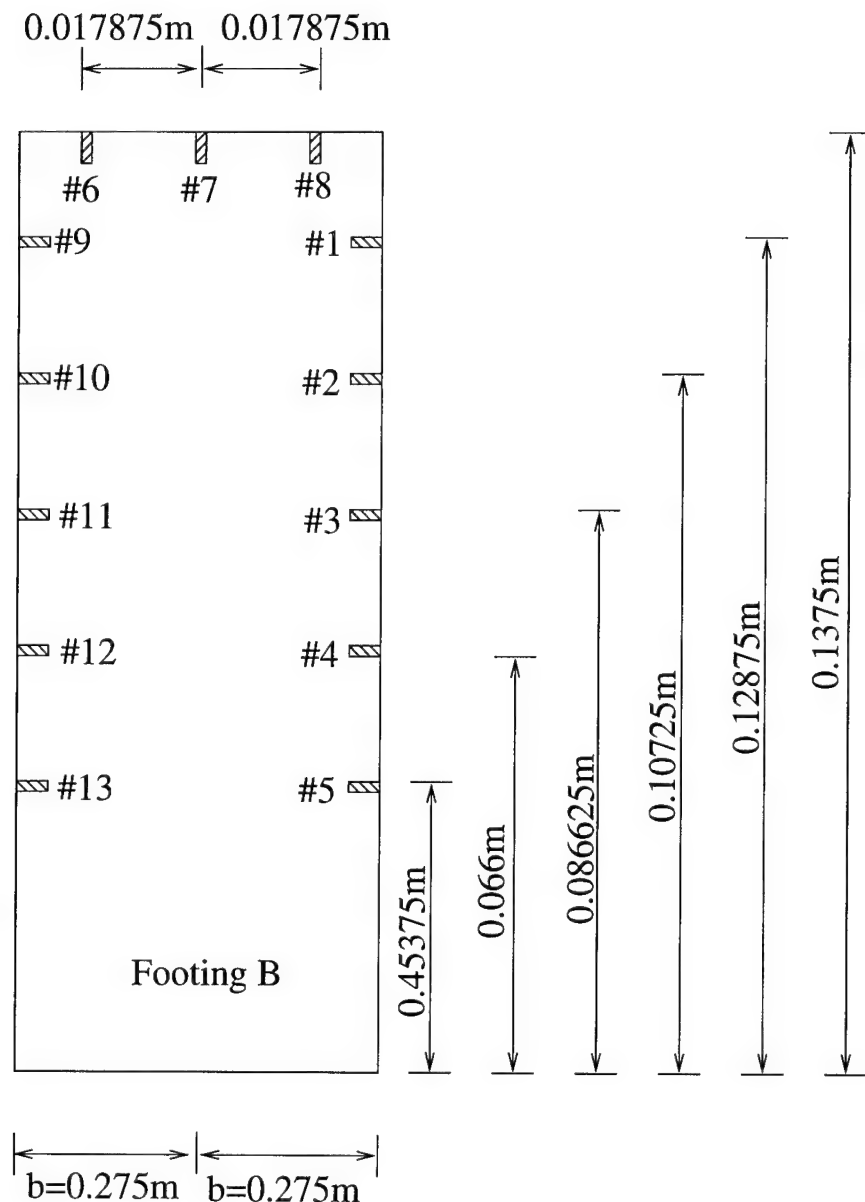
Figure 5.2: Diagram of model Footing "B" used in theoretical accelerance calculations and experiments.

accelerance to be measured is in the vertical direction. Additionally the vertical accelerance will be the same at any point on the footing since the footing is modeled as a rigid body.

5.3.1.1 Theoretical Variation of Vertical Concentric Accelerance with Embedment Depth

Using the impedances for a rigid foundation embedded in a homogeneous half-space, Figure 5.3 shows how the dimensionless vertical centroidal accelerance changes with embedment depth. The primary characteristic which changes with embedment for the vertical concentric loading case is the decrease in the magnitude of the resonant frequency peak. The frequency peak is also shifted slightly to higher frequencies with embedment and virtually disappears by an embedment ratio of 2.0. This effect is expected according to the discussion in the previous chapters regarding the stiffening of the footing's response with increasing embedment. It should be noted that the three curves are essentially the same after $\bar{\omega} = 2.0$. This is due to the fact that the accelerance curve is dominated by inertial effects at high frequencies, and the same mass was used for all three cases.

5.3.1.2 Theoretical Variation of Vertical Concentric Accelerance with Shear Wave Speed

Recall that a homogeneous half-space is fully characterized by the elastic parameters G, ρ, and ν. For a given soil, the mass density ρ is easily measured. Therefore, the primary parameters which can be varied to obtain a satisfactory accelerance match are G and ν. The shear modulus is related to the shear wave speed according to

$$C_s = \sqrt{\frac{G}{\rho}}. \tag{5.15}$$
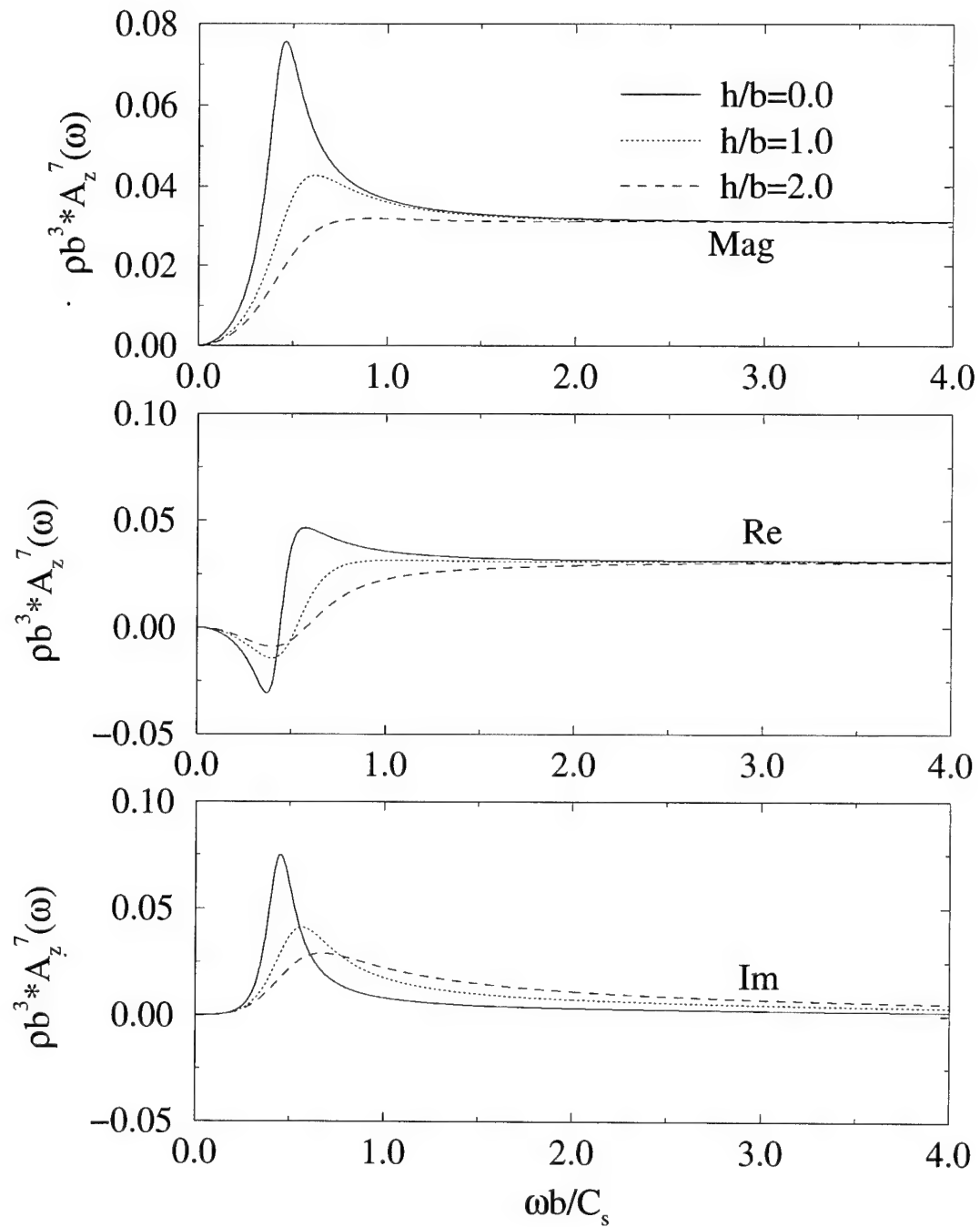
Figure 5.3: Effect of embedment on vertical centroidal accelerance for homogeneous half-space impedances ($h/b = 0.0, 1.0, 2.0$, $\nu = 0.25$).

Since the rotational frequency ω is made dimensionless by utilizing the shear wave speed, accelerance for different shear wave speeds can be plotted versus the frequency to illustrate the effects of different shear wave speeds. In this manner, the rotational frequency ω is related to the frequency in Hz according to

$$f = \frac{\omega}{2\pi}. \tag{5.16}$$

For the configuration of the model footing employed, Figure 5.4 shows plots of the vertical centroidal accelerance versus frequency (Hz) for an embedment ratio of 1.0 and three different shear wave speeds, $200m/s$, $225m/s$, and $250m/s$ which correspond to shear moduli of $69.2MPa$, $87.6MPa$, and $108.1MPa$ respectively. From these curves, it is apparent that the increase in shear modulus increases the resonant frequency.

5.3.1.3   Theoretical Variation of Vertical Concentric Accelerance with Poisson's Ratio

Figure 5.5 shows the dimensionless vertical centroidal accelerance at $h/b = 1.0$ for Poisson's ratios of 0.10, 0.25, and 0.40. As the Poisson's ratio increases, one can see from Figure 5.5 that the resonant frequency increases slightly also.

The curves also illustrate that the effect of Poisson's ratio is not as significant as the effect of the shear wave speed in determining the characteristics of the curve. The accelerance curves for $\nu = 0.10$ and $\nu = 0.25$ contain only very small differences, whereas the curve for $\nu = 0.40$ begins to become noticeably different from the other two.

In Pak and Guzina [32], it was found that the best approach in accelerance matching was to fix the Poisson's ratio and choose the best-fit shear modulus. In three series of tests, they found that the average of the best-fit Poisson's ratios were 0.277, 0.229, and 0.277 respectively. For simplicity, a constant Poisson's
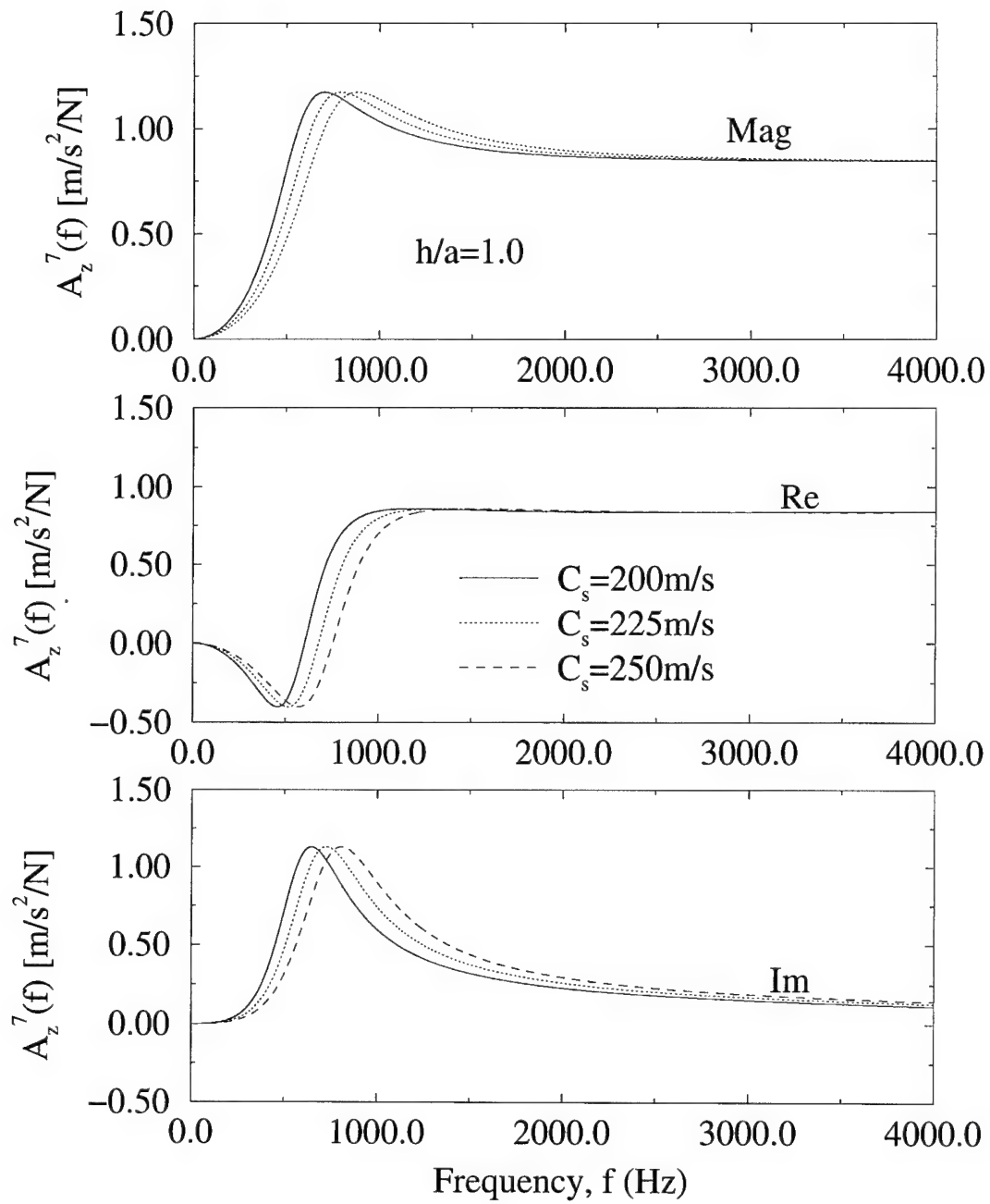
Figure 5.4: Effect of shear wave speed on vertical centroidal accelerance at h/b=1.0 for homogeneous half-space impedances ($\nu = 0.25$).
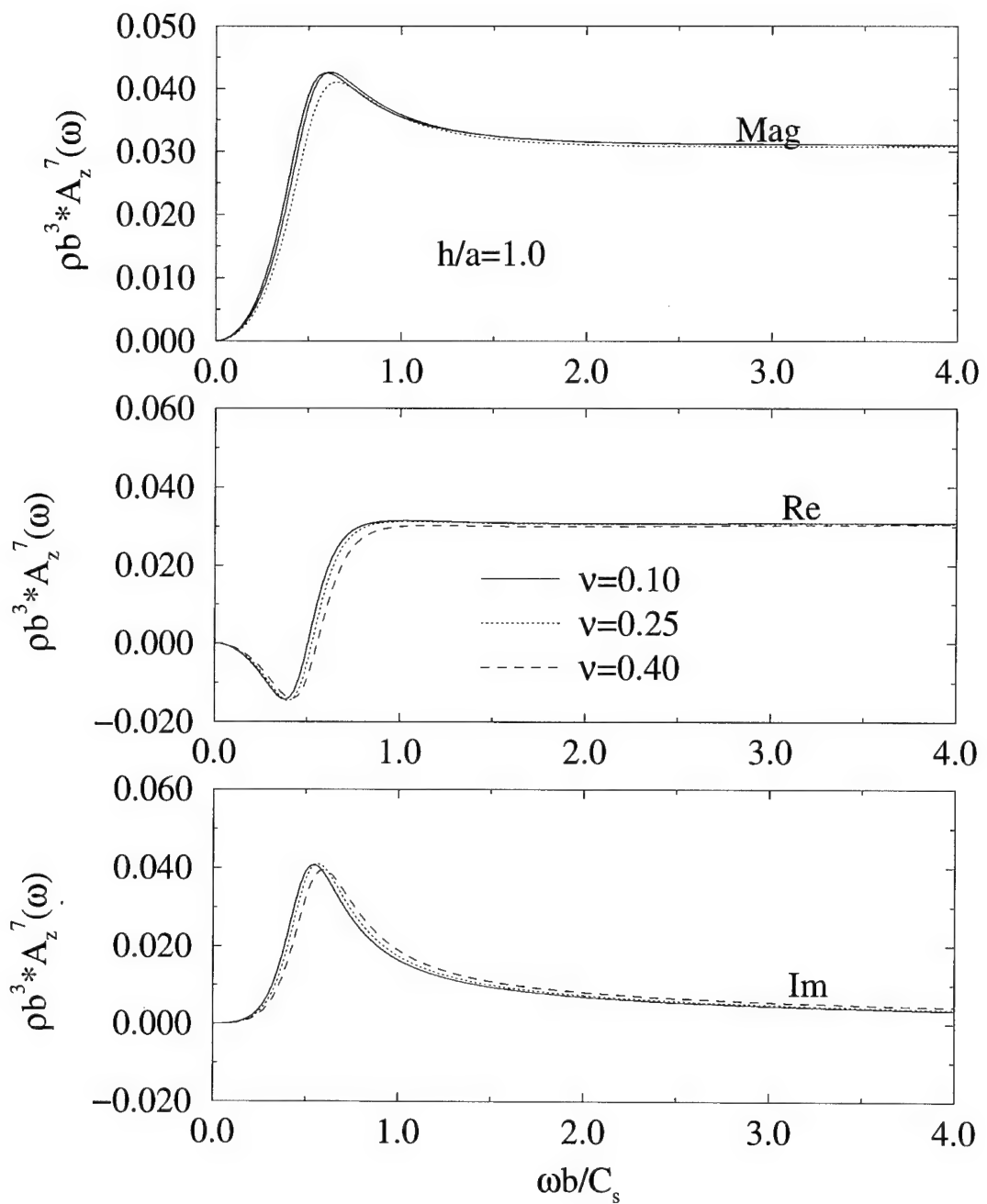
Figure 5.5: Effect of Poisson's ratio on vertical centroidal accelerance at h/b=1.0 ($\nu = 0.10, 0.25, 0.40$) for homogeneous half-space impedances.

ratio of 0.25 was adopted which will also be used in this study for all comparisons between theory and experiment.

5.3.2 Vertical Eccentric (VE) Vibration

The vertical eccentric case is similar in many ways to the vertical concentric case. Theoretically, the vertical vibration at the centroid of the footing is the same as in the vertical concentric case. Consequently, this accelerance measurement location does not need further discussion. However, since the loading is eccentric, there is lateral motion and the vertical accelerance across a horizontal plane of the footing will vary depending on the eccentricity of the load and the eccentricity of the measurement location. Thus, it is important to examine the off-center vertical accelerance and the lateral accelerance.

5.3.2.1 Vertical Accelerance from Vertical Eccentric Loading

Figure 5.6 shows the theoretical off-center vertical accelerance under vertical eccentric loading at three embedment depths. With reference to Figure 5.2, the footing is loaded at hole #6 and the accelerance is measured at hole #8 in this simulation. The dimensionless eccentricity of the load is $\bar{e}_{load} = \frac{e_{load}}{b} = -0.65$ and the eccentricity of the accelerance measurement location is $\bar{e}_{measure} = \frac{e_{measure}}{b} = 0.65$. In addition to the primary peak revealed in the vertical concentric loading case, there is now an additional peak caused by the eccentricity of the loading which occurs at a lower frequency than the primary vertical vibration peak. This peak is extremely sharp and decreases in magnitude with embedment.

5.3.2.2 Lateral Accelerance from Vertical Eccentric Loading

Figure 5.7 shows the lateral accelerance from footing "B" with a vertical eccentric load. The footing is loaded at hole #6 and the theoretical accelerance is
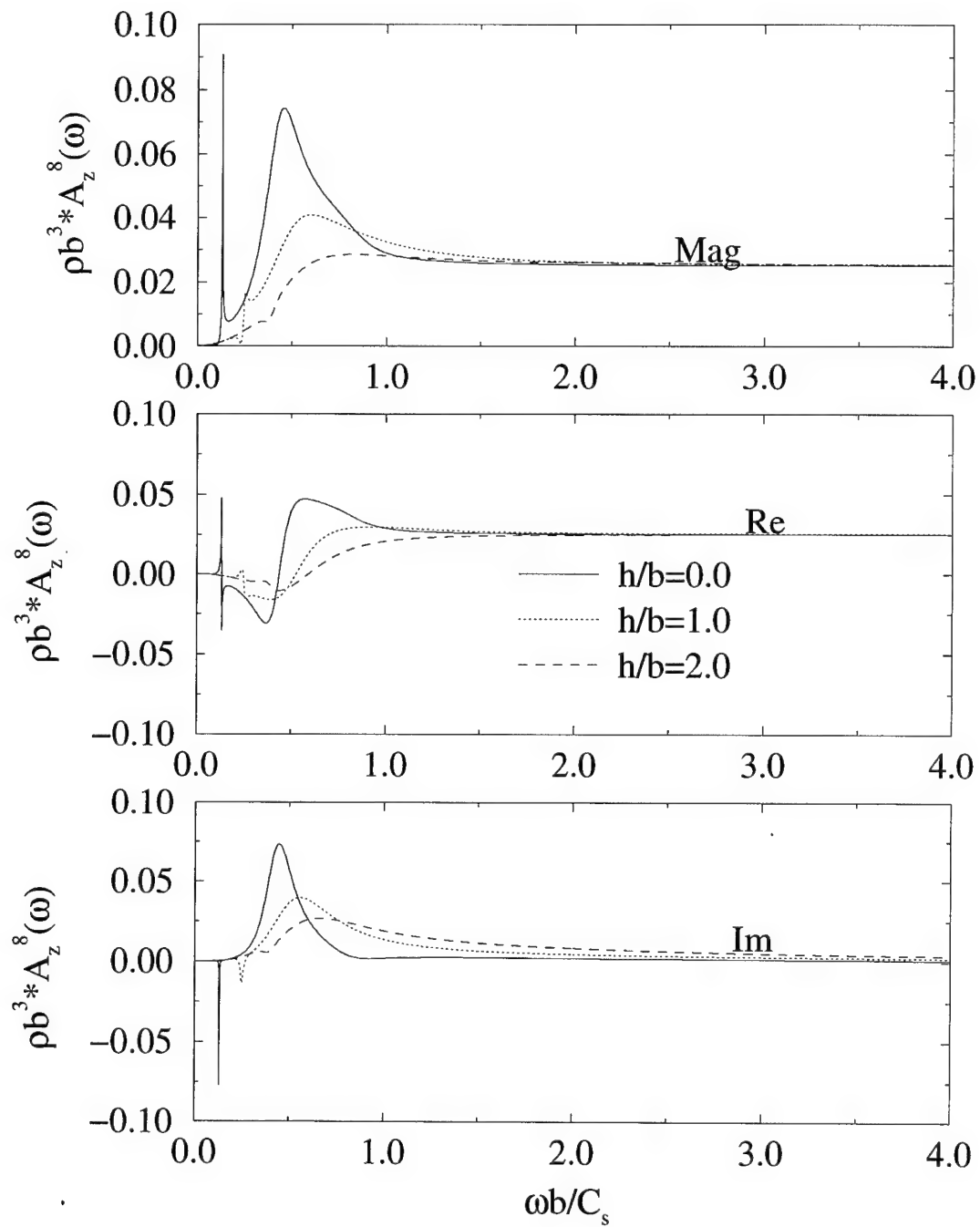
Figure 5.6: Effect of embedment on off-center vertical accelerance at hole #8 from vertical eccentric loading at hole #6 ($h/b = 0.0, 1.0, 2.0$) for homogeneous half-space impedances ($\nu = 0.25$).
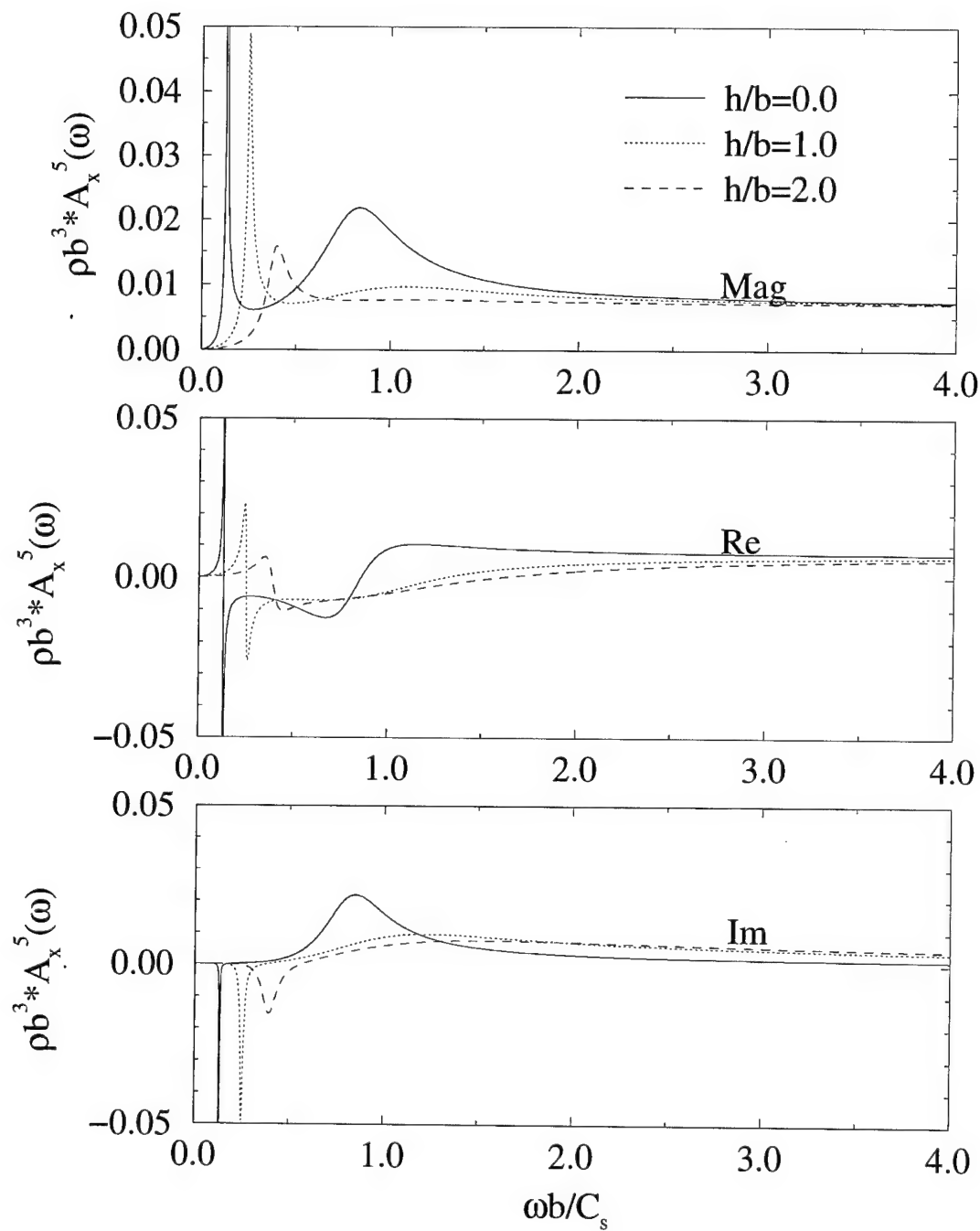
Figure 5.7: Effect of embedment on lateral accelerance at hole #5 from vertical eccentric loading at hole #6 ($h/b = 0.0, 1.0, 2.0$) for homogeneous half-space impedances ($\nu = 0.25$).

calculated for hole #5 at each embedment depth. The eccentricity of the load is $\bar{e}_{load} = -0.65$, the same as that for the vertical accelerance shown in Figure 5.6.

One can see that for the case of $h/b = 0.0$, there are two resonance peaks. The first peak is very sharp and has a large magnitude, while the second peak is much wider and lower in magnitude. Previous studies have shown that the first peak is primarily related to resonance in the rocking mode of vibration, while the second peak is due to resonance in the horizontal mode of vibration. The first peak decreases in magnitude and gradually increases in width with embedment. The frequency at which this peak is found also increases with embedment. Another important characteristic to note is that the second, but more gradual, peak on the accelerance curve is noticeable at $h/b = 0.0$, but diminishes as h/b increases. This observation is relevant to the experimental synthesis to be discussed in Chapter 6.

5.3.3   Lateral Horizontal (LH) Vibration

The third type of loading to be discussed in this study is lateral loading. Under lateral loading, there is some asymmetric vertical vibration due to the rocking of the foundation. However, the magnitude of this vertical acceleration is too small to be measured reliably for the vibration levels and footing width used in this investigation. Therefore, it is best to analyze just the lateral accelerances under lateral loading.

Figure 5.8 shows the lateral accelerance at hole #3 for a load applied at hole #10 for three different embedment depths. At this measurement location, only the resonance peak due to rocking is noticeable, even for a surface footing. Generally speaking, the closer the measurement location is to the soil surface, the more prominent the second resonance peak is since it is primarily related to the horizontal translation mode of vibration. The closer the accelerance measurement is to the soil-foundation interface, the more dominant the horizontal translation
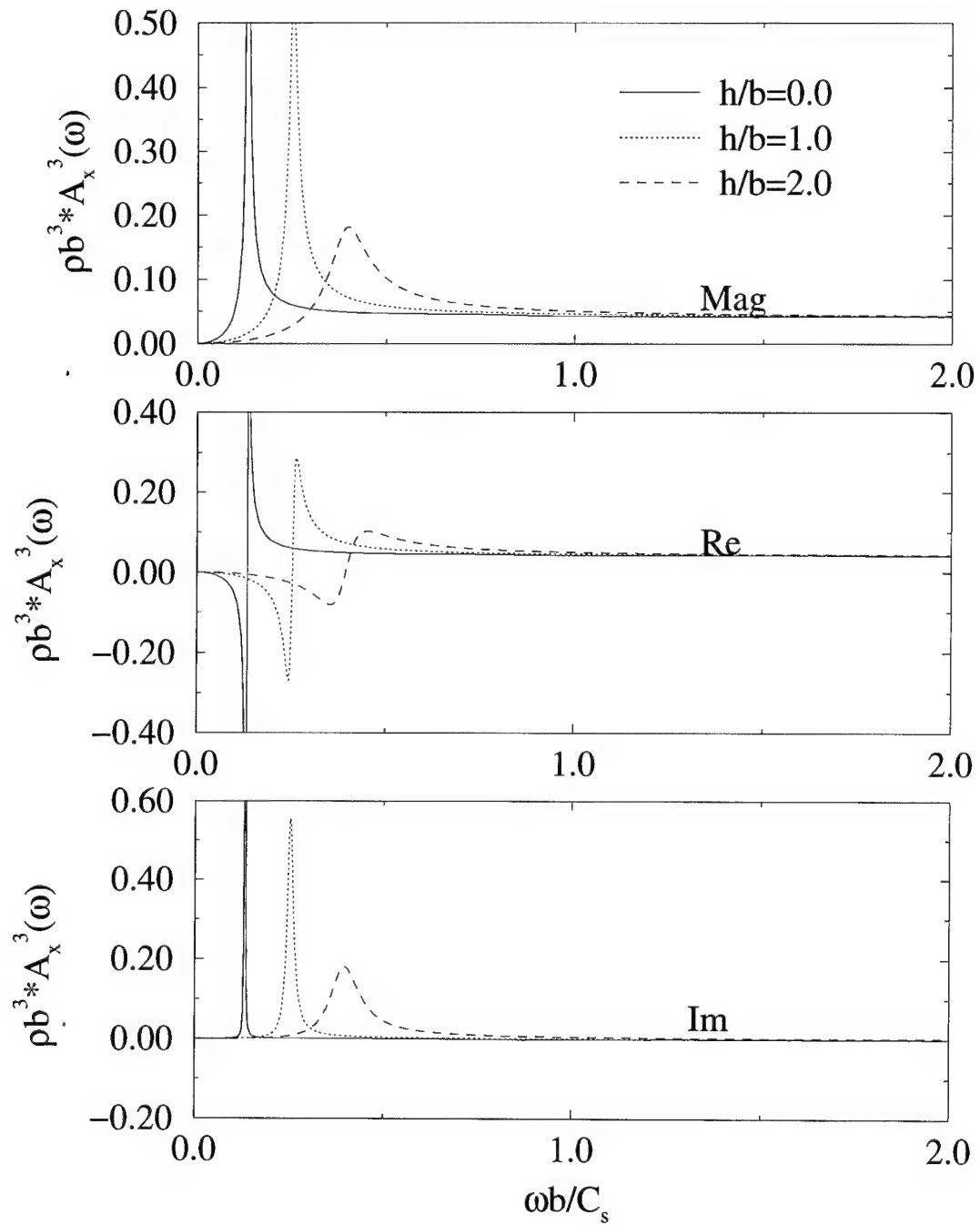
Figure 5.8: Effect of embedment on lateral accelerance at hole #3 from lateral loading at hole #10 ($h/b = 0.0, 1.0, 2.0$) for homogeneous half-space impedances ($\nu = 0.25$).

mode of vibration will be when compared to the rocking mode. Conversely, the rocking mode of vibration will be more prominent the farther the measurement location is from the soil-foundation interface. For accelerance at hole #3, the second peak is practically non-existent due to the location of the theoretical accelerance measurement. As embedment depth increases, the magnitude of the resonance peak decreases and the width of the peak increases gradually as the system increases in stiffness.

Figure 5.9 shows the lateral accelerance at hole #5 for the same horizontal load applied at hole #10. For a surface foundation, the second resonance peak, while still small, is more pronounced than in the accelerance of hole #3 in Figure 5.8. This is because the measurement location (hole #5) is much closer to the soil-foundation interface where the horizontal mode of vibration is more prominent than at other measurement locations. Additionally, the magnitude of the rocking peak is much lower for hole #5 than for hole #3 since the contribution by the rocking mode of vibration is less at this location. As the embedment depth increases, the magnitude of both peaks decrease. As the embedment gets to $h/b = 1.0$, the second peak is already difficult to distinguish.
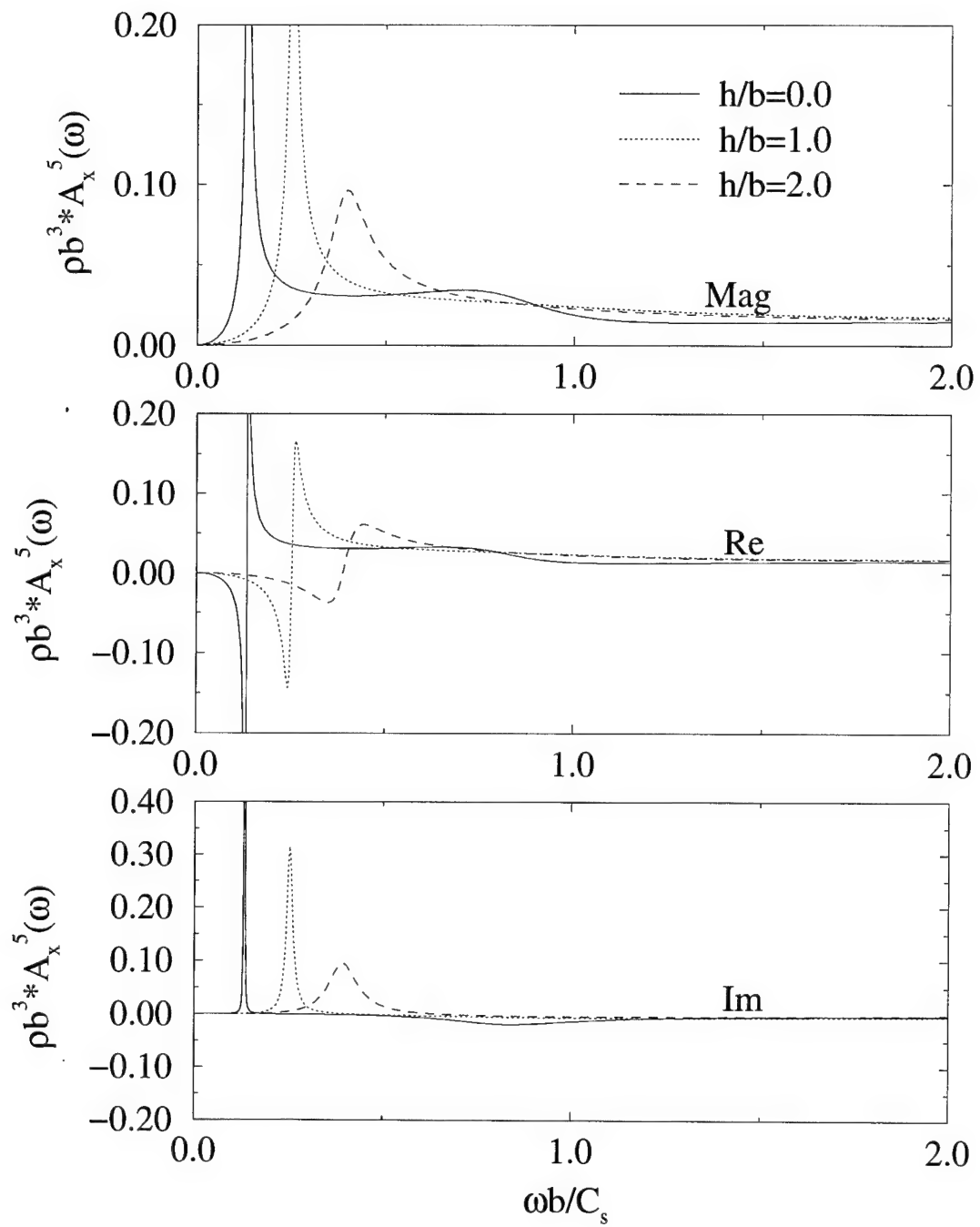
Figure 5.9: Effect of embedment on lateral accelerance at hole #5 from lateral loading at hole #10(h/b = 0.0, 1.0, 2.0) for homogeneous half-space impedances ($\nu = 0.25$).

5.4 Theoretical Accelerances Computed (Square-Root Half-Space Impedances)

·The accelerances computed in this section are for the dynamic impedance functions for a rigid embedded square foundation in a square-root modulus half-space as given in Section 3.3. Recall that the square-root profile was chosen in order to model the variation in shear modulus due to the self-weight of the soil according to Hardin and Drnevich [17]. This type of profile should accurately capture the far-field effects, but may still require modifications to account for the local stiffening due to the presence of a massive footing on the soil.

5.4.1 Vertical Concentric Vibration

Figures 5.10 shows the vertical centroidal accelerance based on the square-root profile impedances for embedment depths of $h/b = 0.0$, 1.0, and 2.0, with the dimensionless frequency defined to be $\bar{\omega} = \frac{\omega b}{C_{s0}}$ where $C_{s0} = \sqrt{\frac{G_0}{\rho}}$. All three curves have a higher magnitude at resonance than the curves generated by the homogeneous half-space impedances in Figure 5.3. For a surface footing on a square-root modulus half-space, the response is particularly soft which yields a very narrow resonance peak with a large magnitude. Such a soft behavior is not observed in physical surface footing experiments on sand by Ashlock [1], who has explored the addition of a stiffened zone under a surface foundation in conjunction with a square-root profile in order to account for both the increase in stiffness due to the weight of the footing and the far-field variation in shear modulus.

Figure 5.11 shows the vertical centroidal accelerances for three different shear wave speeds at $h/b = 1.0$ based on the square-root profile impedances. The effect of the shear wave speed on the square-root profile accelerances is similar to the effects shown in Figure 5.4 for the homogeneous half-space.
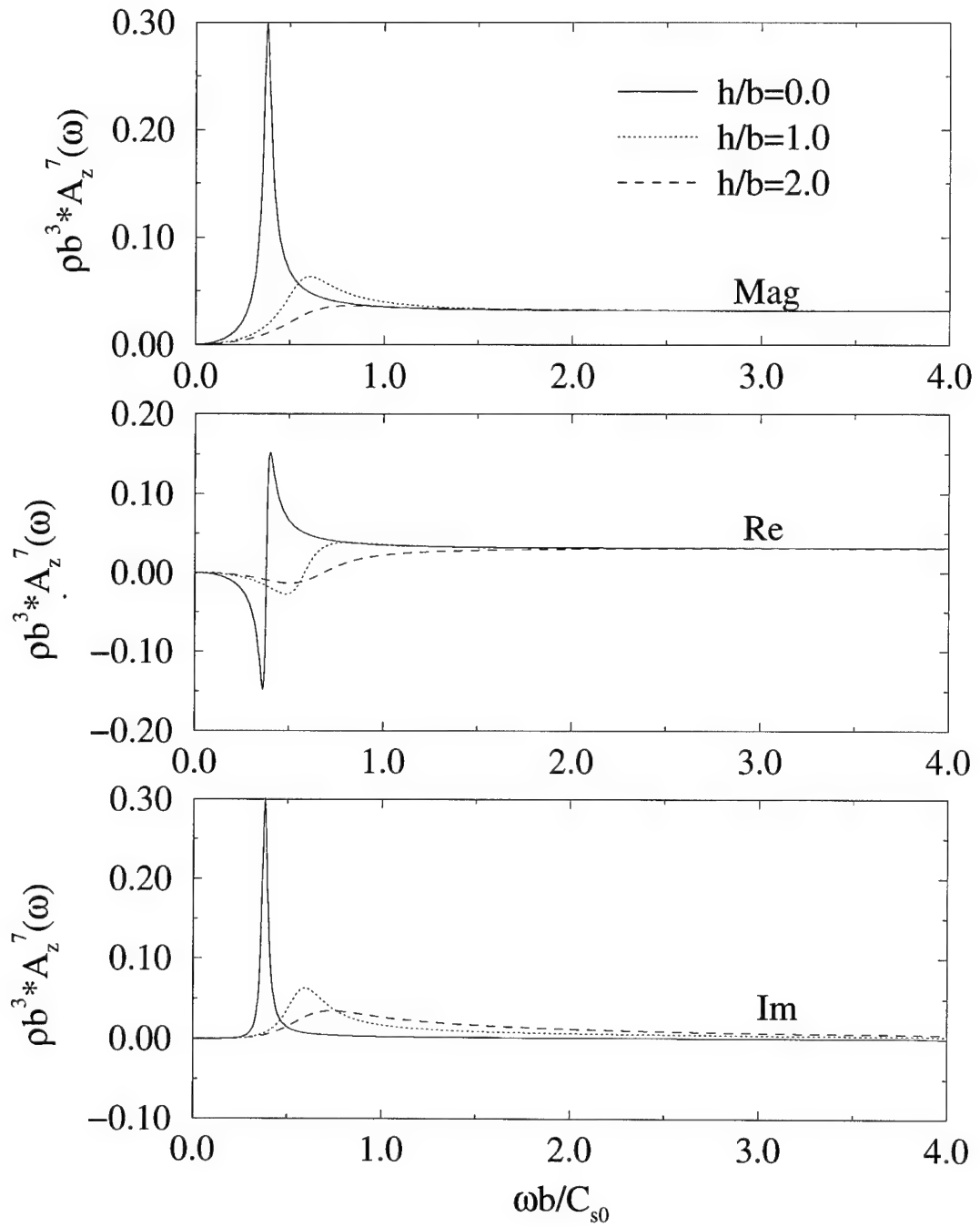
Figure 5.10: Effect of embedment on vertical centroidal accelerance for square-root profile impedances ($h/b = 0.0, 1.0, 2.0$, $\nu = 0.25$).
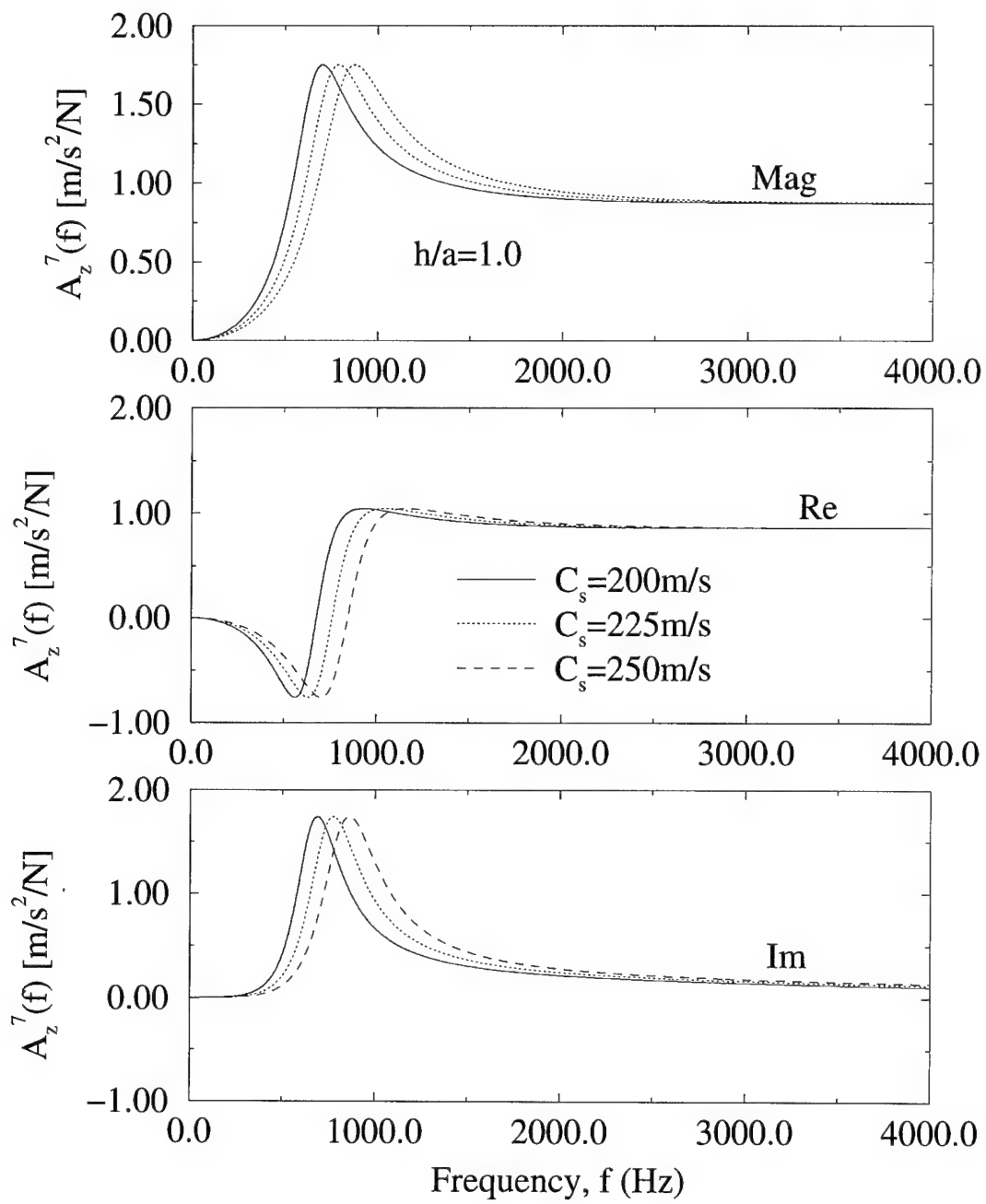
Figure 5.11: Effect of shear wave speed on vertical centroidal accelerance at h/b=1.0 for square-root profile impedances ($\nu = 0.25$).

5.4.2   Vertical Eccentric Vibration

Figure 5.12 shows the accelerance at hole #5 for vertical eccentric loading at hole #6 for square-root profile impedances. Due to the lower shear modulus near the surface for the square-root profile, the horizontal vibration peak for $h/b = 0.0$ is large compared to Figure 5.7 for the homogeneous case. As in the case of vertical concentric loading, Ashlock [1] has shown that experimental accelerance of surface foundations on sand are less dramatic than the theoretical behavior of the square-root shear modulus accelerances. However, for embedment depths of $h/b = 1.0$ and 2.0, the square-root profile may provide a more favorable accelerance match than the surface footing case.

5.4.3   Lateral Horizontal Vibration

Figures 5.13 and 5.14 show the lateral accelerances at holes #3 and #5 respectively for lateral loading at hole #10 for impedances from the square-root profile. The accelerances shown in Figures 5.13 and 5.14 are very similar in shape to the accelerances in Figures 5.8 and 5.9 for homogeneous half-space impedances, although the magnitudes are higher due to the lower shear modulus near the surface for the square-root profile.
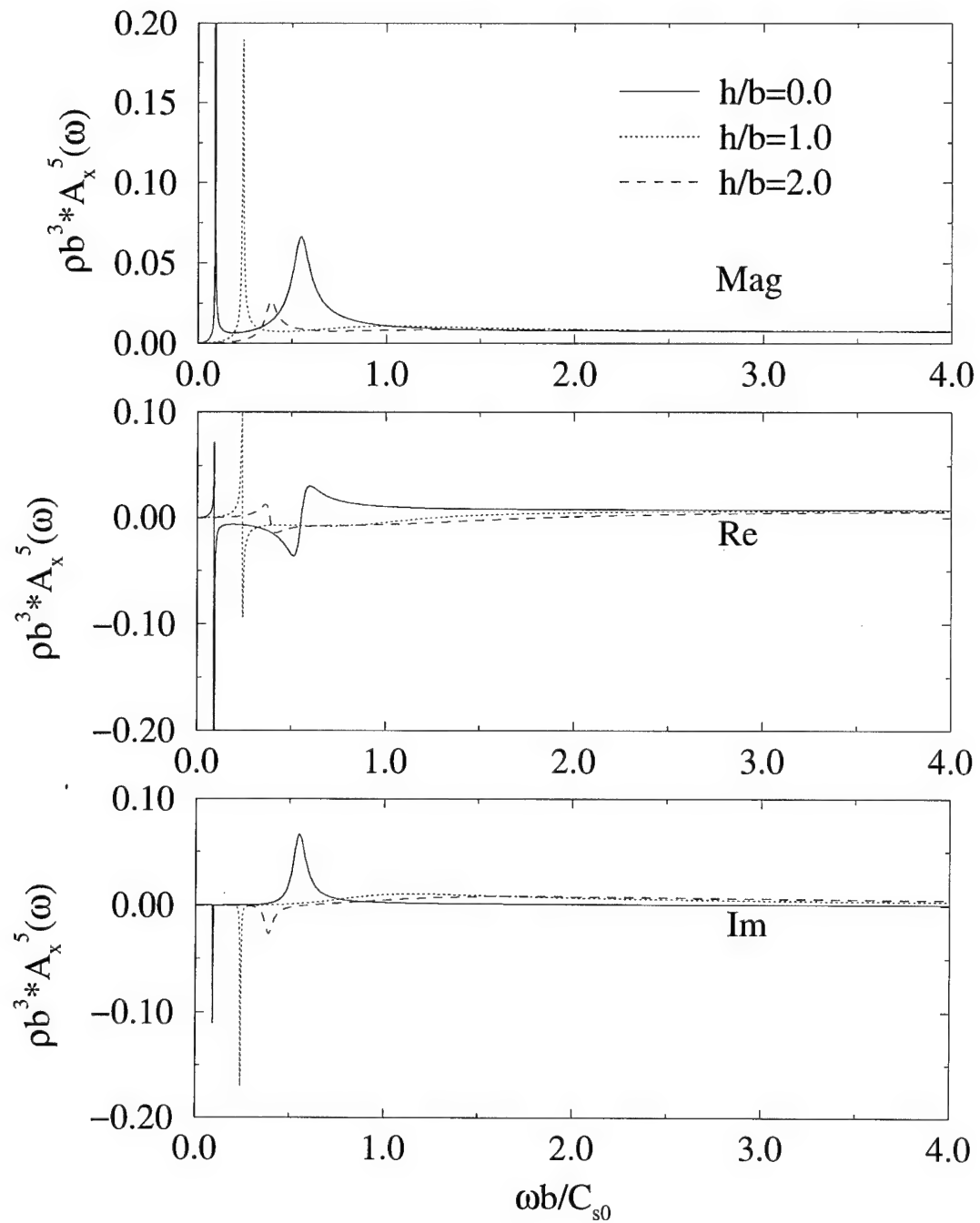
Figure 5.12: Effect of embedment on lateral accelerance at hole #5 from vertical eccentric loading at hole #6 ($h/b = 0.0, 1.0, 2.0$) for square-root profile impedances ($\nu = 0.25$).
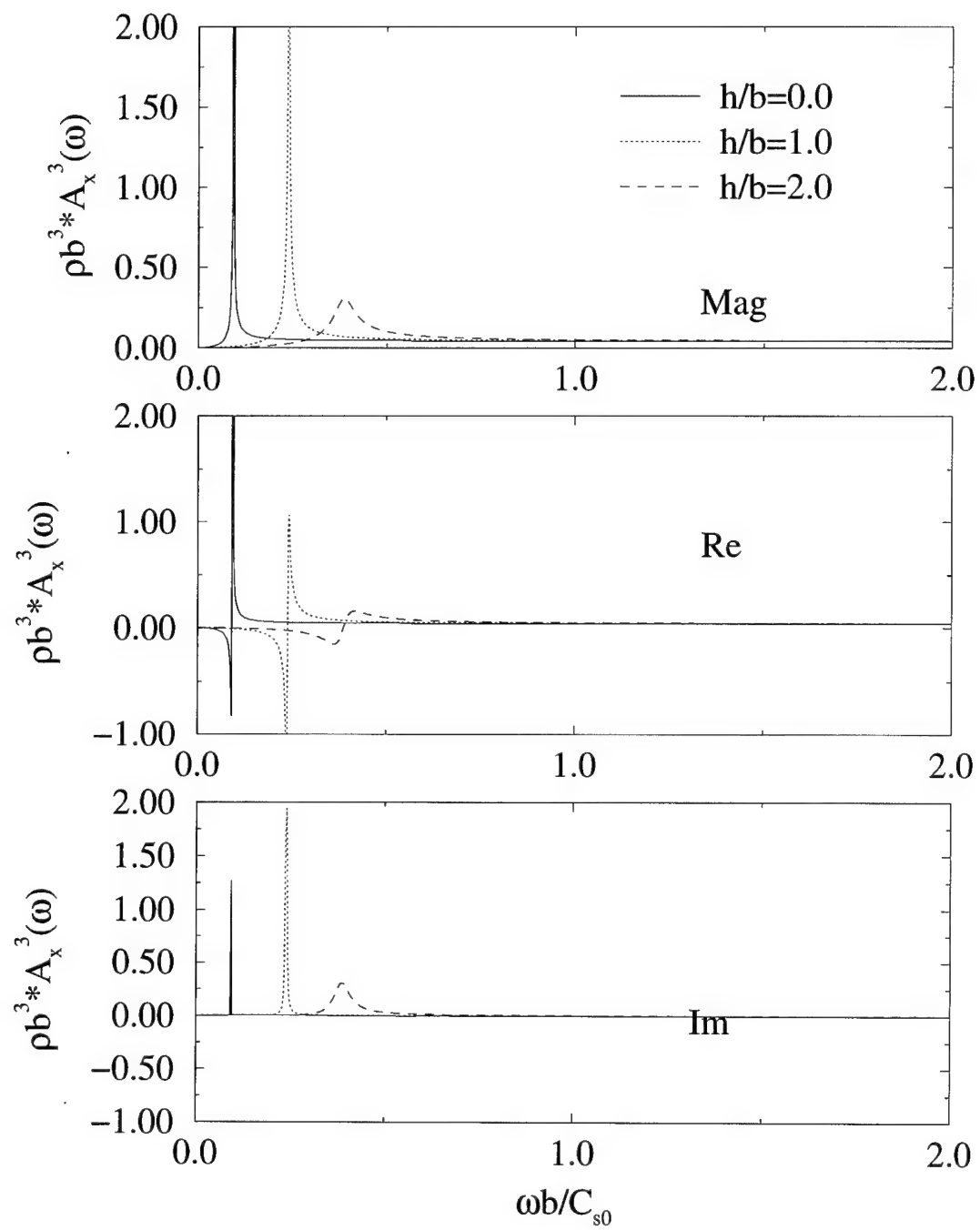
Figure 5.13: Effect of embedment on lateral accelerance at hole #3 from lateral loading at hole #10 ($h/b = 0.0, 1.0, 2.0$) square-root profile impedances ($\nu = 0.25$).
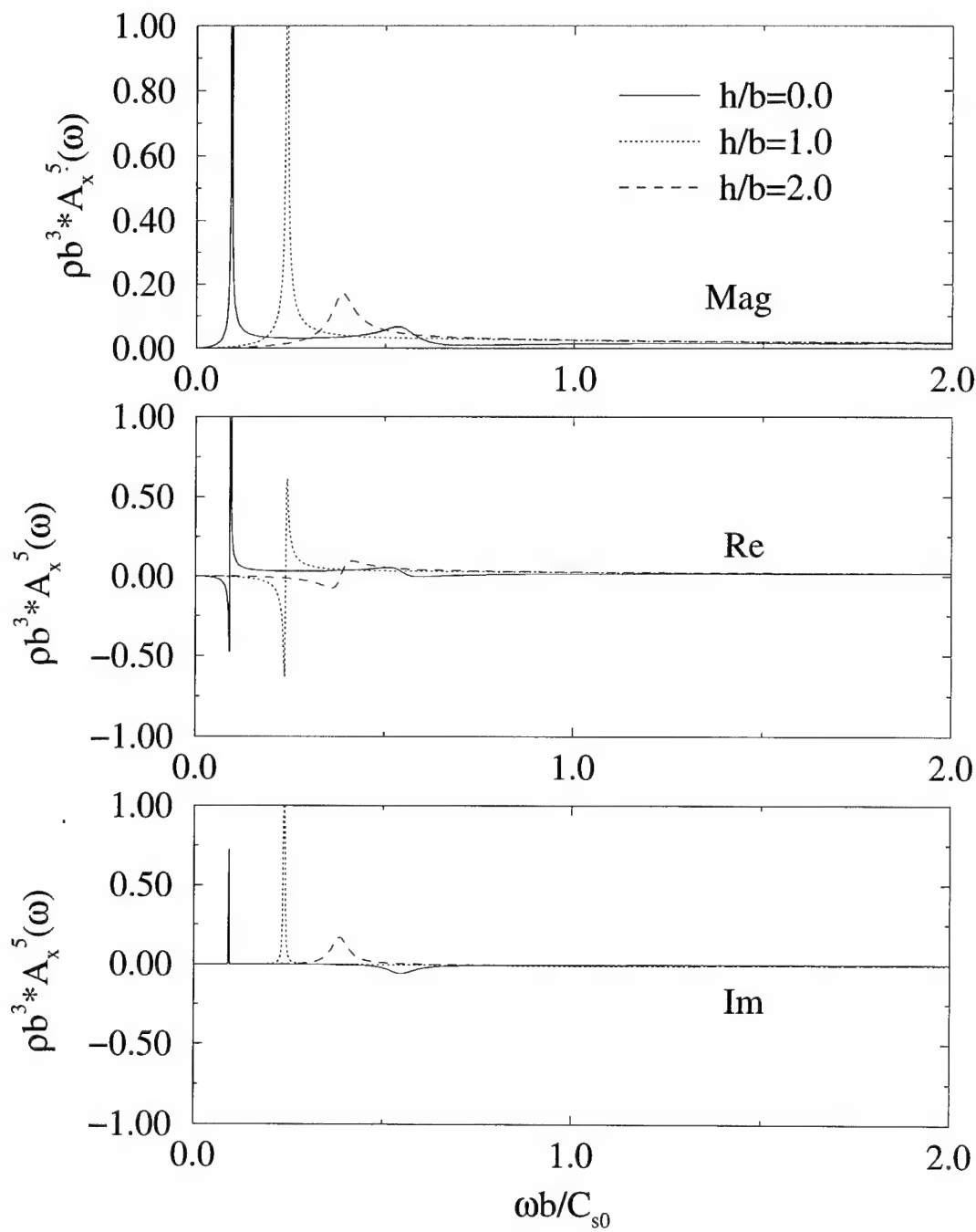
Figure 5.14: Effect of embedment on lateral accelerance at hole #5 from lateral loading at hole #10 ($h/b = 0.0, 1.0, 2.0$) for square-root profile impedances ($\nu = 0.25$).

5.5   Impedance Modification Factors α_{hh}, α_{mm}, and α_{mh}.

To capture the essence of the dynamic behavior of foundations on cohesionless soil, Pak and Ashlock [31] introduced the concept of "Impedance Modification Factors" (IMF's) defined in Equation 3.6. The IMF's were used in Chapter 3 to compare the square-root profile impedances with the reference homogeneous half-space impedances as in Table 3.3 and Figure 3.31. In terms of the impedance modification factors (α_{ij}), the impedance matrix can be written as

$$\mathbf{K}^{model}(\omega) = \begin{bmatrix} K_{vv}^{ref} & 0 & 0 \\ 0 & \alpha_{hh}K_{hh}^{ref}(\omega) & \alpha_{hm}K_{hm}^{ref}(\omega) \\ 0 & \alpha_{mh}K_{mh}^{ref}(\omega) & \alpha_{mm}K_{mm}^{ref}(\omega) \end{bmatrix} \qquad (5.17)$$

where $\mathbf{K}^{ref}$ are the impedance functions for a reference theoretical solution. Due to its simplicity and popularity in practice, the solution for a rigid foundation embedded in a homogeneous half-space will be used as the theoretical reference in defining the α_{ij}. For a rigid surface foundation, Ashlock [1] found that the modification factors α_{mm} and α_{hh} were needed in order to produce a satisfactory accelerance match, while α_{mh} and α_{hm} could be set to 1.0 since the theoretical accelerance is insensitive to the value of K_{mh} and K_{hm}. For embedded foundations, however, the coupling terms K_{mh} and K_{hm} are considerably larger than in the surface case and are likely to influence the theoretical accelerances as embedment depth increases. From Table 2.1 for a surface footing, the magnitude of the dimensionless coupling terms $\bar{K}_{mh}$ is only 0.68, which is about 10% of $\bar{K}_{vv}$ (which is 6.39 for zero embedment). However, at $h/b = 1.0$, $\bar{K}_{mh}$ is over 30% of $\bar{K}_{vv}$, and at $h/b = 2.0$, the magnitude of $\bar{K}_{mh}$ is over 80% of $\bar{K}_{vv}$.

To illustrate the effects of α_{mm}, α_{hh}, and α_{mh} on the theoretical accelerances, Figures 5.15, 5.16, and 5.17 show the consequences of varying α_{mm}, α_{hh}, and α_{mh}

at embedment depths of 0.00, 1.00, and 2.00 respectively. At each embedment depth, each of the modification factors is varied from 0.50 to 0.75 to 1.00, while the other two modification factors are kept constant at 0.75. The accelerances shown are for vertical eccentric loading at hole #6 while the theoretical accelerance is computed at hole #5.

At each embedment depth, it is clear that α_{mm} primarily affects the frequency of the resonance peak associated with the rocking mode of vibration. Physically, this is easy to understand since α_{mm} modifies the rocking impedance K_{mm}. As α_{mm} decreases, the frequency of the resonant peak due to rocking also decreases, and vice versa. For each embedment depth, the horizontal translation peak is not affected greatly by a change in α_{mm} (see Figures 5.15, 5.16, 5.17).

The primary effect that α_{hh} has is on the second resonance peak associated with the horizontal mode of vibration. As α_{hh} is reduced, the frequency of the horizontal translation peak is reduced while the magnitude of the peak increases. Conversely, an increase in α_{hh} tends to flatten the peak and increase the frequency at which the peak occurs. As α_{hh} increases, the frequency of the rocking peak also increases slightly at $h/b = 0.0$ and $h/b = 1.0$, although, this influence is relatively small, especially considering the larger effect that α_{mm} has on this peak. At $h/b = 2.0$, an increase in α_{hh} tends to decrease the frequency of the rocking peak, but this influence is also very small compared to the effect of α_{mm} at the same embedment depth (see Figure 5.17).

At $h/b = 0.0$, α_{mh} has very little effect on accelerance. A slight change is noticeable in both the rocking and horizontal peaks; however, this influence is relatively insignificant when compared to the effects of modifying α_{mm} and α_{hh}. At deeper embedment depths, however, the change in the acceleration due to α_{mh} becomes more noticeable, for example at $h/b = 2.0$ (see Figure 5.17). Decreasing α_{mh} tends to increase the frequency of the rocking peak while decreasing the

frequency of the horizontal vibration peak. This effect is apparent at $h/b = 1.0$ and is even more pronounced at $h/b = 2.0$. At $h/b = 2.0$, α_{mh} has nearly as much effect on the accelerance produced as α_{hh}. The specific values of the α_{ij} will be discussed as the data is presented in Chapter 6.
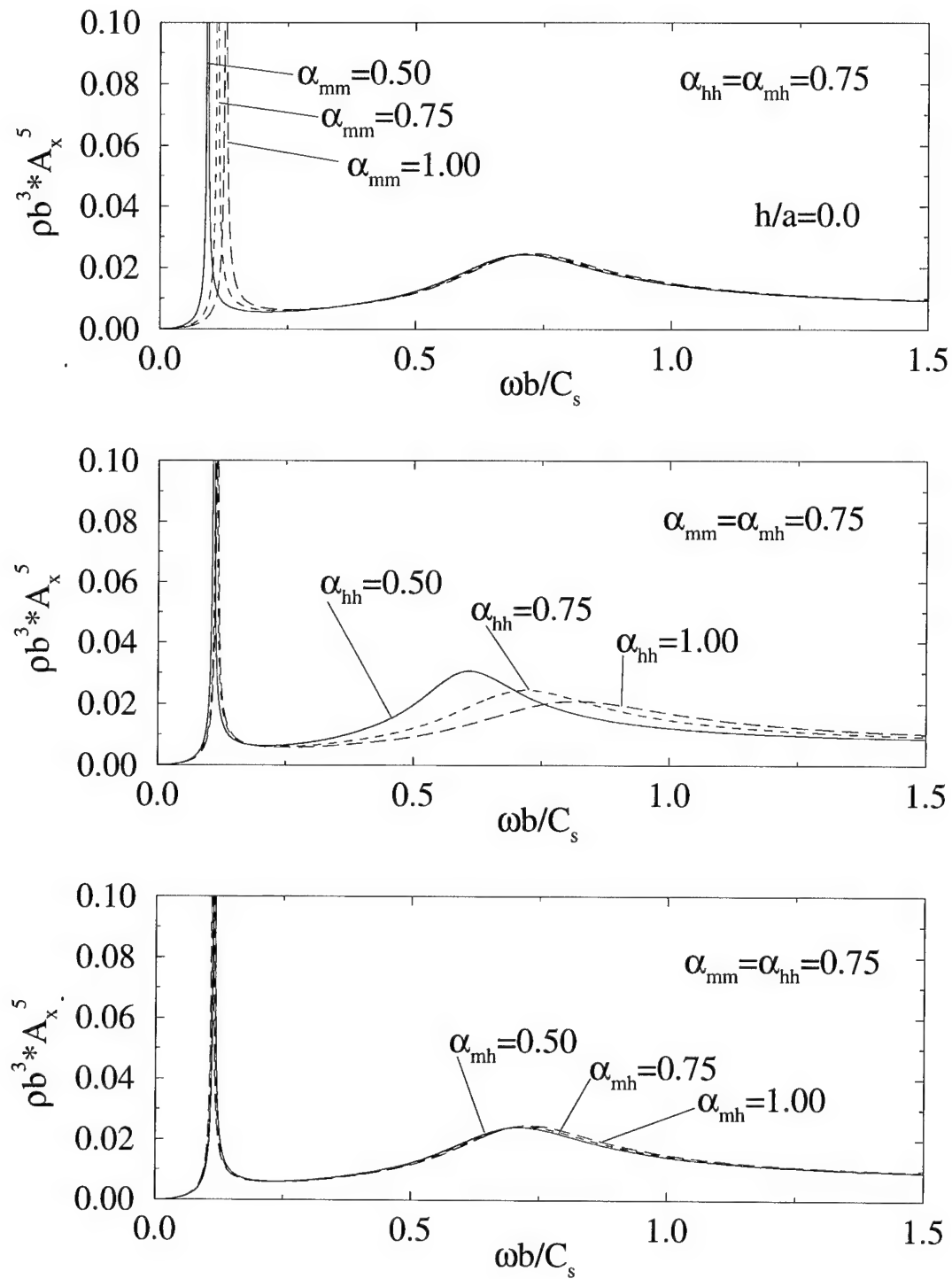
Figure 5.15: Effects of α_{mm}, α_{hh}, and α_{mh} at $h/b = 0.0$ (homogeneous half-space, $\nu = 0.25$).
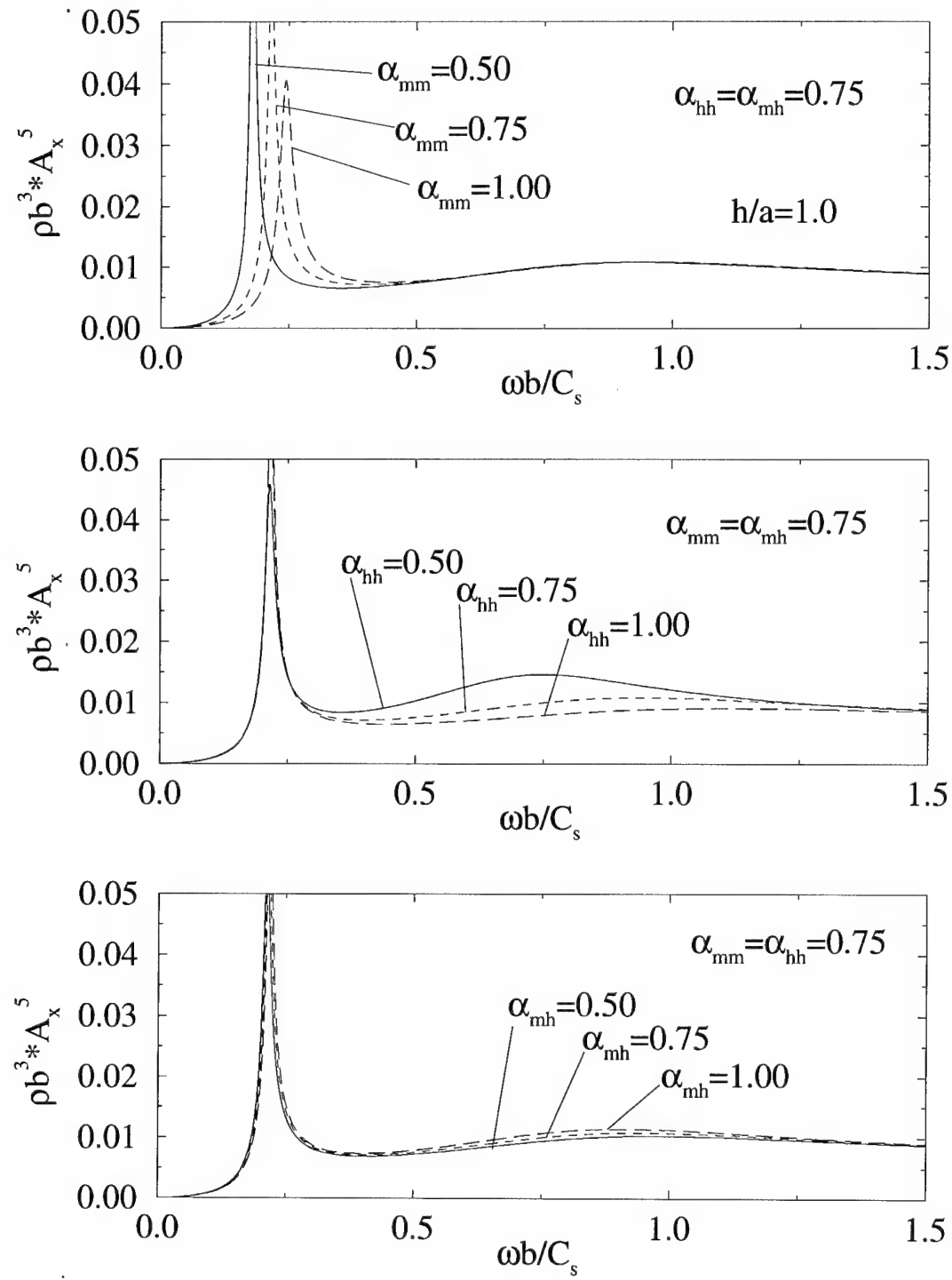
Figure 5.16: Effects of α_{mm}, α_{hh}, and α_{mh} at $h/b = 1.0$ (homogeneous half-space, $\nu = 0.25$).
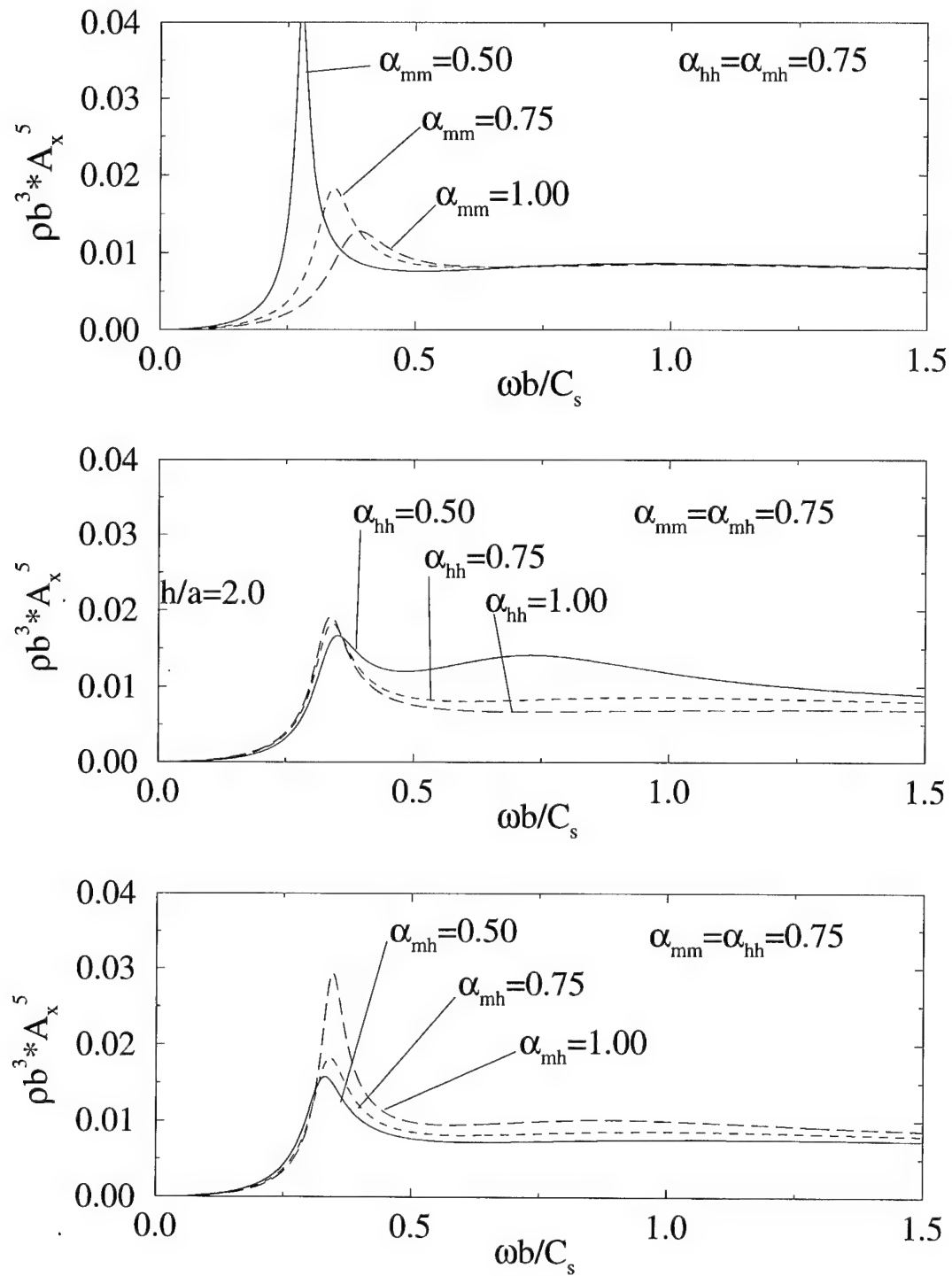
Figure 5.17: Effects of α_{mm}, α_{hh}, and α_{mh} at $h/b = 2.0$ (homogeneous half-space, $\nu = 0.25$).

Chapter 6

Experimental Results

6.1   Introduction

Pak and Guzina [32] have found that the equivalent homogeneous shear modulus for vertical vibration of circular footings on sand can be related to the prototype footing radius and bearing pressure by a power law according to

$$G = 1.64 MPa \frac{(2.97 - e)^2}{1 + e} \left(\frac{a_{pr}}{1\ m}\right)^{0.1} \left(\frac{p_{pr}}{1\ kPa}\right)^{0.5} \tag{6.1}$$

where e is the void ratio of the soil, a_{pr} is the prototype footing radius for a circular footing, and p_{pr} is the static foundation bearing pressure. Research for the case of a square surface footing (Ashlock [1]) also supports the power law format

$$G = G'_{avg} \left(\frac{b_{pr}}{1\ m}\right)^{0.1} \left(\frac{p_{pr}}{1\ kPa}\right)^{0.5}. \tag{6.2}$$

Additionally, Ashlock [1] found that a single shear modulus could be used to accurately capture the response of a square surface footing on sand under vertical eccentric and lateral loading with the use of impedance modification factors (α_{ij}). Up to this point, however, very little research has been conducted on embedded foundations.

To examine the corresponding case of embedded foundations, over 500 embedded model footing tests and nearly 100 surface ones were performed on three different soil samples. At most, two embedded footing spots were used on each sample (although only one footing was embedded at any one time to avoid any

possible interaction effects between two footings embedded in the same sample) with two or three surface testing locations per sample. For each embedment depth, tests were conducted at four different g-levels which translate to four different prototype foundations. To maximize the number of tests that can be conducted in one spin, tests were conducted beginning with the highest g-level, working down to the lowest g-level, since the confining pressure, and thus the soil's strength, is greatest at the highest g-level. The footing was fitted with two load cells before placement so that both vertical and lateral tests could be conducted at a single location without removing the footing or disturbing the footing by adding and removing load cells and accelerometers after the initial footing placement. Generally, vertical vibration tests were performed before the lateral vibration tests and in many cases, two sets each of vertical and lateral tests at the same location were repeated on successive centrifuge spins in order to check the degree of repeatability from test to test.

6.2   Results from Preliminary Tests

The first set of experiments conducted in this investigation included vertical centric (VC), vertical eccentric (VE), and lateral-horizontal (LH) loading tests using the conical stinger to distribute the load from the exciter to the load cell. The vertical eccentric and lateral tests from these preliminary results, however, indicate that the transverse frictional force at the stinger was too significant. With an innovative hemispherical button along with a lubricating cushion to reduce friction, high quality results were achieved as will be illustrated in Section 6.4.

6.2.1   Sample 1, Series A

The first series (Series A) in this investigation was conducted on a single soil sample and includes surface footing tests to confirm the results by Ashlock [1], as

well as embedded tests at $h/b = 1.0$ to explore the versatility of the homogeneous half-space solution in fitting experimental accelerances for embedded foundations.

6.2.1.1   Surface Footing Tests

Table 6.1 contains results of the best-fit shear modulus match between the homogeneous half-space theory and experimental results from this investigation for two different prototype bearing pressures at each g-level. An example file name in Table 6.1 is ACB68G66.MA9, where the first digit is the series (A), the second digit refers to the type of loading (C for vertical concentric, E for vertical eccentric, and L for lateral), the third digit refers to the footing letter (footing B), the fourth and fifth digits refer to the acceleration locations with reference to the hole numbering system in Figure 5.2, the sixth, seventh, and eighth digits refer to the g-level at the top of the soil ($66 \rightarrow 66.45$, $55 \rightarrow 54.55$, $44 \rightarrow 43.64$, $33 \rightarrow 32.73$), and the final three digits refer to the test number (MA1, MA2, MA3, etc). One p_{pr} is with the exciter armature in the "Up" position where a DC current is applied to lift up the exciter armature in order to reduce the static prestress applied by the exciter (which reduces the average contact pressure also). The higher p_{pr} is when the exciter is in the "Down" position and the bearing pressure includes the weight of the exciter armature (for further discussion, see Ashlock [1]). As the table reveals, the correspondence between Ashlock's formula and the results in this investigation is quite good. The maximum difference between the two is 5.57%, but a majority of the results are within 3%.

Since the footing is loaded at hole #7, the vertical accelerance is found by averaging the accelerance from holes #6 and #8 and is denoted $\frac{A_z^6 + A_z^8}{2}$ (see Figure 6.1). The best-fit vertical accelerance is chosen by varying the shear wave speed of the equivalent homogeneous half-space solution across a specified range, and selecting the shear wave speed which provides the smallest error in a least

squares sense. The error is given a weighting according to

$$w = \left\{ \begin{array}{ll} 2.0; & \bar{\omega} \leq 1.5 \\ \\ 1.0; & \bar{\omega} > 1.5 \end{array} \right\} \tag{6.3}$$

since the lower frequencies of the vertical accelerance depend on the properties of the soil, while the higher frequencies depend primarily on the inertial properties of the footing.

g-level	Test Name	b_{pr}	p_{pr}	$G_{equivhomog}$	$G_{Ashlock}$	% diff.
65.45	ACB68G66.MA9	1.800	256.1	106.4	107.6	1.12
65.45	ACB68G66.M10	1.800	256.1	108.1	107.6	0.46
65.45	ACB68G66.M11	1.800	270.1	109.0	110.5	1.34
65.45	ACB68G66.M12	1.800	270.1	108.1	110.5	2.17
54.55	ACB68G55.MA7	1.500	213.5	98.0	96.5	1.55
54.55	ACB68G55.MA8	1.500	213.5	98.8	96.5	2.38
54.55	ACB68G55.MA9	1.500	225.1	99.6	99.1	0.50
54.55	ACB68G55.M10	1.500	225.1	98.8	99.1	0.30
43.64	ACB68G44.MA7	1.200	170.8	88.4	84.4	4.74
43.64	ACB68G44.MA8	1.200	170.8	89.1	84.4	5.57
43.64	ACB68G44.MA9	1.200	180.1	89.9	86.7	3.69
43.64	ACB68G44.M10	1.200	180.1	89.9	86.7	3.69
32.73	ACB68G33.MA8	0.900	128.1	73.4	71.0	3.38
32.73	ACB68G33.MA9	0.900	128.1	72.7	71.0	2.39
32.73	ACB68G33.M10	0.900	135.1	74.1	72.9	1.65
32.73	ACB68G33.M11	0.900	135.1	74.1	72.9	1.65

Table 6.1: Surface footing results for Series A.

Figure 6.1 shows a typical accelerance match between the surface footing test results in Series A and the homogeneous half-space. As one can see, the homogeneous half-space impedances with an equivalent homogeneous shear modulus fit the experimental data quite well for the vertical centric loading case.
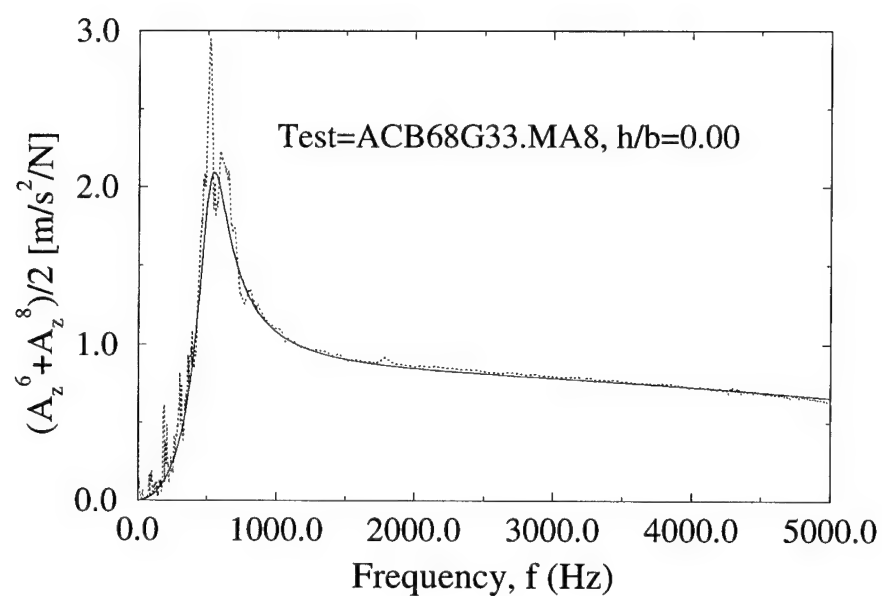
Figure 6.1: Typical results from surface footing tests in Series A.

6.2.1.2   Embedded Footing Tests for $h/b = 1.00$

Since the homogeneous half-space solution for vertical vibrations of surface foundations on sand has been extensively validated by Ashlock [1] and confirmed in this investigation, the next step is to find out whether a model as convenient as the homogeneous half-space will accurately model vertical vibrations of embedded foundations in sand as well. Embedded footing tests in Series A were conducted at $h/b = 1.00$. Table 6.2 contains the best-fit shear moduli obtained from a fit between the experimental data and the impedances for a rigid cavity embedded to $h/b = 1.00$ in a homogeneous half-space. All of the experiments at this embedment depth were conducted with the exciter down, and the double line in Table 6.2 denotes successive spins in the centrifuge.

As far as embedded footings are concerned, it is difficult to assign a specific "average contact pressure" for a particular footing since not all of the load is transferred through the base of the footing. However, for the purposes of this investigation on shallowly embedded foundations, the average contact pressure (p_{pr}) will be used as an index parameter and will be computed in the same manner as for surface footings,

$$p_{pr} = \frac{n * m}{4b_{pr}^2} \qquad (6.4)$$

where n is the centrifuge g-level, m is the mass of the footing and attachments, and b_{pr} is the half-width of the square footing. Although this may not be the true average contact pressure at the base of the footing, it is helpful to have an index relating the weight of the footing to the area of the base.

The data in Table 6.2 can be grouped into three different sets, since three consecutive spins in the centrifuge were conducted with tests at each of the four g-levels on each spin. The difference between the best-fit shear moduli for each spin provides an indication of the repeatability of the test results. The maximum

Test Name	g-level	b_{pr}	p_{pr}	$G_{equivhomog}$
ACB68G66.MAT	65.45	1.800	270.1	104.69
ACB68G66.MA2	65.45	1.800	270.1	104.69
ACB68G66.MA3	65.45	1.800	270.1	104.69
ACB68G55.MAT	54.55	1.500	225.1	96.35
ACB68G55.MA2	54.55	1.500	225.1	96.35
ACB68G44.MAT	43.64	1.200	180.1	86.03
ACB68G44.MA2	43.64	1.200	180.1	86.03
ACB68G33.MA2	32.73	0.900	135.1	73.41
ACB68G66.MA4	65.45	1.800	270.1	106.40
ACB68G66.MA5	65.45	1.800	270.1	106.40
ACB68G55.MA3	54.55	1.500	225.1	97.17
ACB68G55.MA4	54.55	1.500	225.1	97.99
ACB68G44.MA3	43.64	1.200	180.1	85.26
ACB68G44.MA4	43.64	1.200	180.1	85.26
ACB68G33.MA3	32.73	0.900	135.1	74.13
ACB68G33.MA4	32.73	0.900	135.1	74.85
ACB68G33.MA5	32.73	0.900	135.1	73.41
ACB68G66.MA6	65.45	1.800	270.1	106.40
ACB68G66.MA7	65.45	1.800	270.1	107.26
ACB68G66.MA8	65.45	1.800	270.1	107.26
ACB68G55.MA5	54.55	1.500	225.1	97.99
ACB68G55.MA6	54.55	1.500	225.1	97.99
ACB68G44.MA5	43.64	1.200	180.1	86.03
ACB68G44.MA6	43.64	1.200	180.1	86.80
ACB68G33.MA6	32.73	0.900	135.1	75.57
ACB68G33.MA7	32.73	0.900	135.1	74.13

Table 6.2: Embedded footing results for Series A ($h/b = 1.0$).

increase in shear modulus for each of the four g-levels in descending order is 2.45%, 1.70%, 1.81%, and 2.94% respectively. Such a small increase in G from three consecutive spins illustrates the repeatability of the tests and provides confidence that each test disturbs the sample minimally.

Figure 6.2 shows a typical accelerance match between experimental data and the embedded foundation homogeneous half-space impedances. As the plot reveals, the match is quite good, illustrating the versatility of the homogeneous half-space model to accurately fit embedded footing accelerances in addition to the surface case.
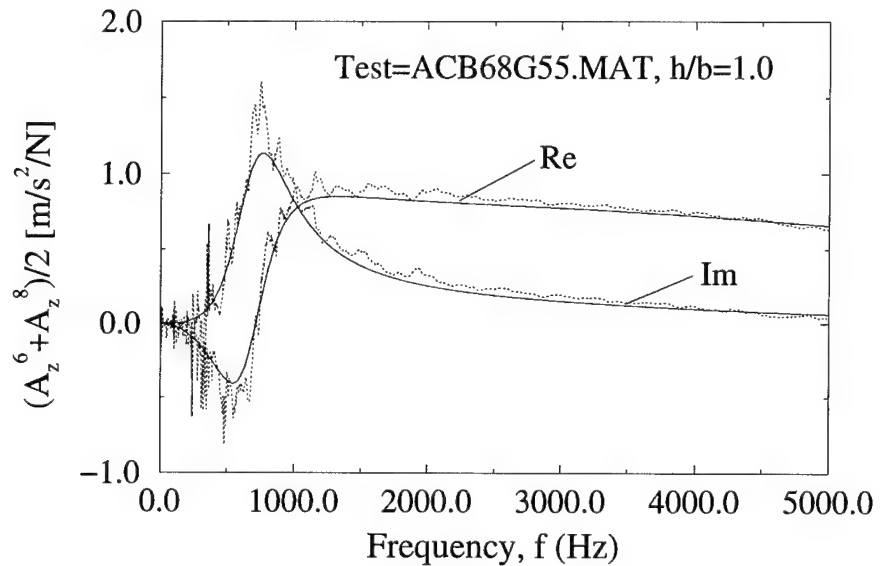
Figure 6.2: Typical results from embedded footing ($h/b = 1.0$) tests in Series A.

Table 6.2 reveals that the best-fit shear modulus at $h/b = 1.00$ is slightly lower than the best-fit shear modulus for a surface footing with a corresponding bearing pressure (as in Table 6.1). However, it is difficult to draw firm conclusions on how the shear modulus might vary with depth without conducting more tests at a variety of embedment depths as will be discussed next.

6.2.2 Vertical Tests from Series B, C, D, E, F, G

Since the homogeneous half-space has been shown to provide a good vertical accelerance match for a single embedment depth ($h/b = 1.0$), the next step was to conduct tests for a variety of embedment depths. Several series of tests were performed at a single location on a second soil sample. Tests were conducted at embedment depths of $h/b = 2.00$, 1.50, 1.00, 0.50, 0.25, and 0.00, and denoted as Series B, C, D, E, F, and G respectively. Tests were first conducted at $h/b = 2.0$, after which the soil was scraped and vacuumed away as described in Section 4.3 to obtain the successive embedment depths. The results of the best-fit shear moduli in these tests are contained in Tables 6.3 and 6.4. Additionally, Figures 6.3 and 6.4 contain typical results from the vertical centric accelerance matches in Series B, C, D, E, F, and G. As one can see, these figures show a good accelerance match between theory and experiment for all of the embedment depths tested.

Figure 6.5 shows the change in the best-fit equivalent homogeneous shear modulus from the vertical concentric tests with embedment depth for Series B to G. Included in the plots are the individual best-fit G's from each test, along with a line which represents the average best-fit G for a given g-level at a given embedment depth. It is important to remember that the accelerance match to find the best-fit G is performed using the **embedded** homogeneous half-space solution. Many solution methods simply try to introduce depth modification factors for the surface footing solution [8]. However, in this investigation, each embedment depth has its own set of square foundation impedances which are generated by a rigorous boundary element method. Figure 6.5 shows that there is not much change in the best-fit equivalent homogeneous shear modulus with depth of embedment. Although the trend is not monotonic, there is a mild decrease in the best-fit G with increasing embedment depth.

h/b	Filename	g-level	b_{pr}	p_{pr}	$G_{equivhomog}$
2.00	BCB68G66.MAT	65.45	1.800	270.1	100.48
2.00	BCB68G66.MA2	65.45	1.800	270.1	99.65
2.00	BCB68G55.MAT	54.55	1.500	225.1	94.73
2.00	BCB68G55.MA2	54.55	1.500	225.1	92.31
2.00	BCB68G44.MAT	43.64	1.200	180.1	81.46
2.00	BCB68G44.MA3	43.64	1.200	180.1	82.97
2.00	BCB68G33.MAT	32.73	0.900	135.1	72.70
2.00	BCB68G33.MA2	32.73	0.900	135.1	68.51
1.50	CCB68G66.MAT	65.45	1.800	270.1	103.84
1.50	CCB68G66.MA2	65.45	1.800	270.1	105.55
1.50	CCB68G55.MAT	54.55	1.500	225.1	97.99
1.50	CCB68G55.MA2	54.55	1.500	225.1	97.17
1.50	CCB68G44.MAT	43.64	1.200	180.1	84.49
1.50	CCB68G44.MA2	43.64	1.200	180.1	85.26
1.50	CCB68G33.MAT	32.73	0.900	135.1	71.29
1.50	CCB68G33.MA2	32.73	0.900	135.1	69.20
1.00	DCB68G66.MAT	65.45	1.800	270.1	97.99
1.00	DCB68G66.MA2	65.45	1.800	270.1	98.82
1.00	DCB68G55.MAT	54.55	1.500	225.1	90.72
1.00	DCB68G44.MAT	43.64	1.200	180.1	80.71
1.00	DCB68G44.MA2	43.64	1.200	180.1	80.71
1.00	DCB68G33.MAT	32.73	0.900	135.1	68.51
1.00	DCB68G33.MA2	32.73	0.900	135.1	67.82

Table 6.3: Best-fit shear moduli for Series B - D.

h/b	Filename	g-level	b_{pr}	p_{pr}	$G_{equivhomog}$
0.50	ECB68G66.MAT	65.45	1.800	270.1	105.55
0.50	ECB68G66.MA2	65.45	1.800	270.1	107.26
0.50	ECB68G55.MAT	54.55	1.500	225.1	97.17
0.50	ECB68G55.MA2	54.55	1.500	225.1	97.99
0.50	ECB68G44.MAT	43.64	1.200	180.1	88.36
0.50	ECB68G44.MA2	43.64	1.200	180.1	88.36
0.50	ECB68G33.MAT	32.73	0.900	135.1	76.29
0.50	ECB68G33.MA2	32.73	0.900	135.1	75.57
0.25	FCB68G66.MAT	65.45	1.800	270.1	110.74
0.25	FCB68G66.MA2	65.45	1.800	270.1	110.74
0.25	FCB68G55.MAT	54.55	1.500	225.1	99.65
0.25	FCB68G55.MA2	54.55	1.500	225.1	100.48
0.25	FCB68G44.MAT	43.64	1.200	180.1	86.80
0.25	FCB68G44.MA2	43.64	1.200	180.1	87.58
0.25	FCB68G33.MAT	32.73	0.900	135.1	79.23
0.25	FCB68G33.MA2	32.73	0.900	135.1	78.49
0.00	GCB68G66.MAT	65.45	1.800	270.1	107.26
0.00	GCB68G66.MA2	65.45	1.800	270.1	108.12
0.00	GCB68G55.MAT	54.55	1.500	225.1	98.82
0.00	GCB68G55.MA2	54.55	1.500	225.1	99.65
0.00	GCB68G44.MAT	43.64	1.200	180.1	86.80
0.00	GCB68G44.MA2	43.64	1.200	180.1	88.36
0.00	GCB68G33.MAT	32.73	0.900	135.1	72.70
0.00	GCB68G33.MA2	32.73	0.900	135.1	72.00

Table 6.4: Best-fit shear moduli for Series E - G.
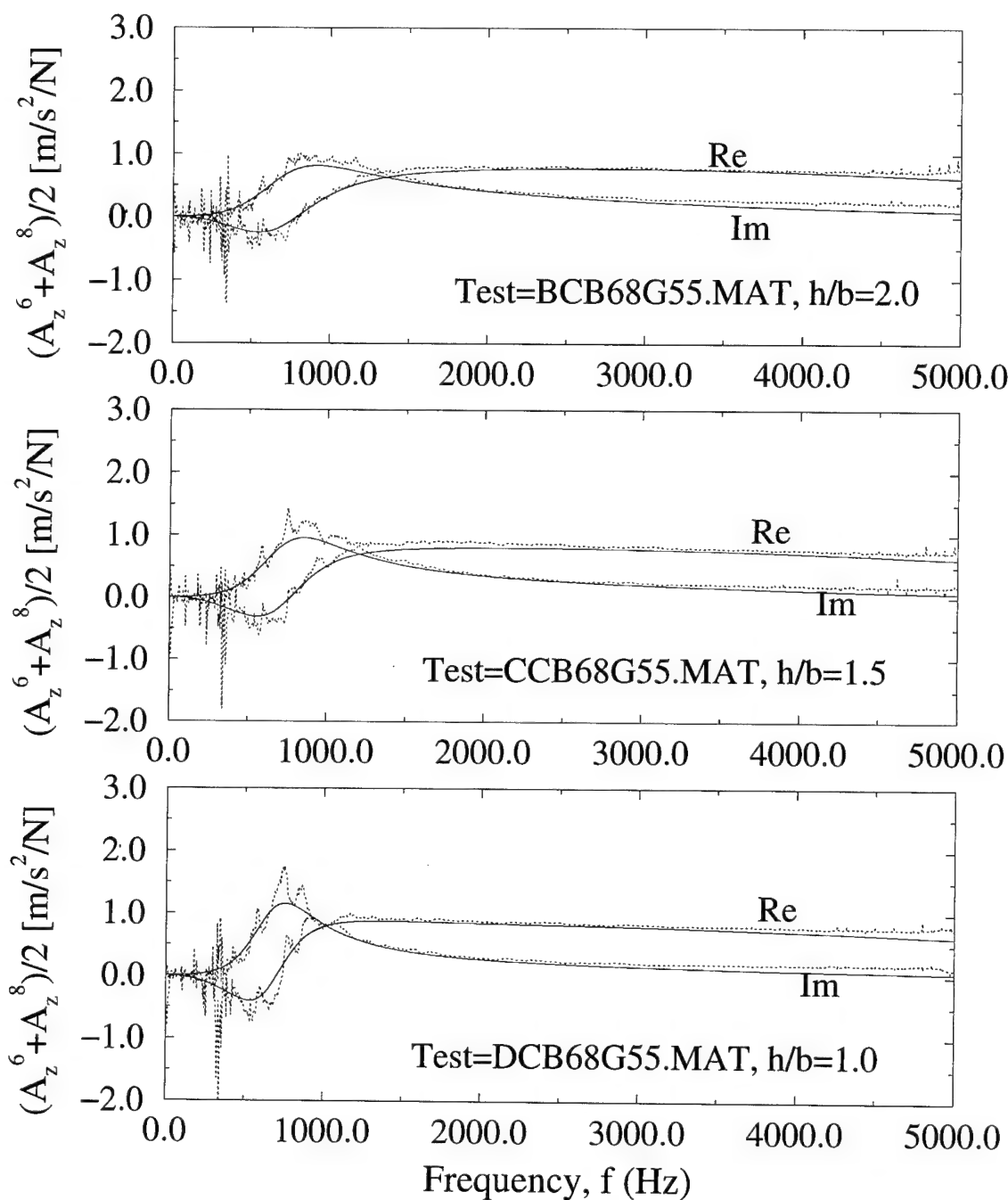
Figure 6.3: Typical results from vertical concentric tests on embedded footings in Series B, C, and D.
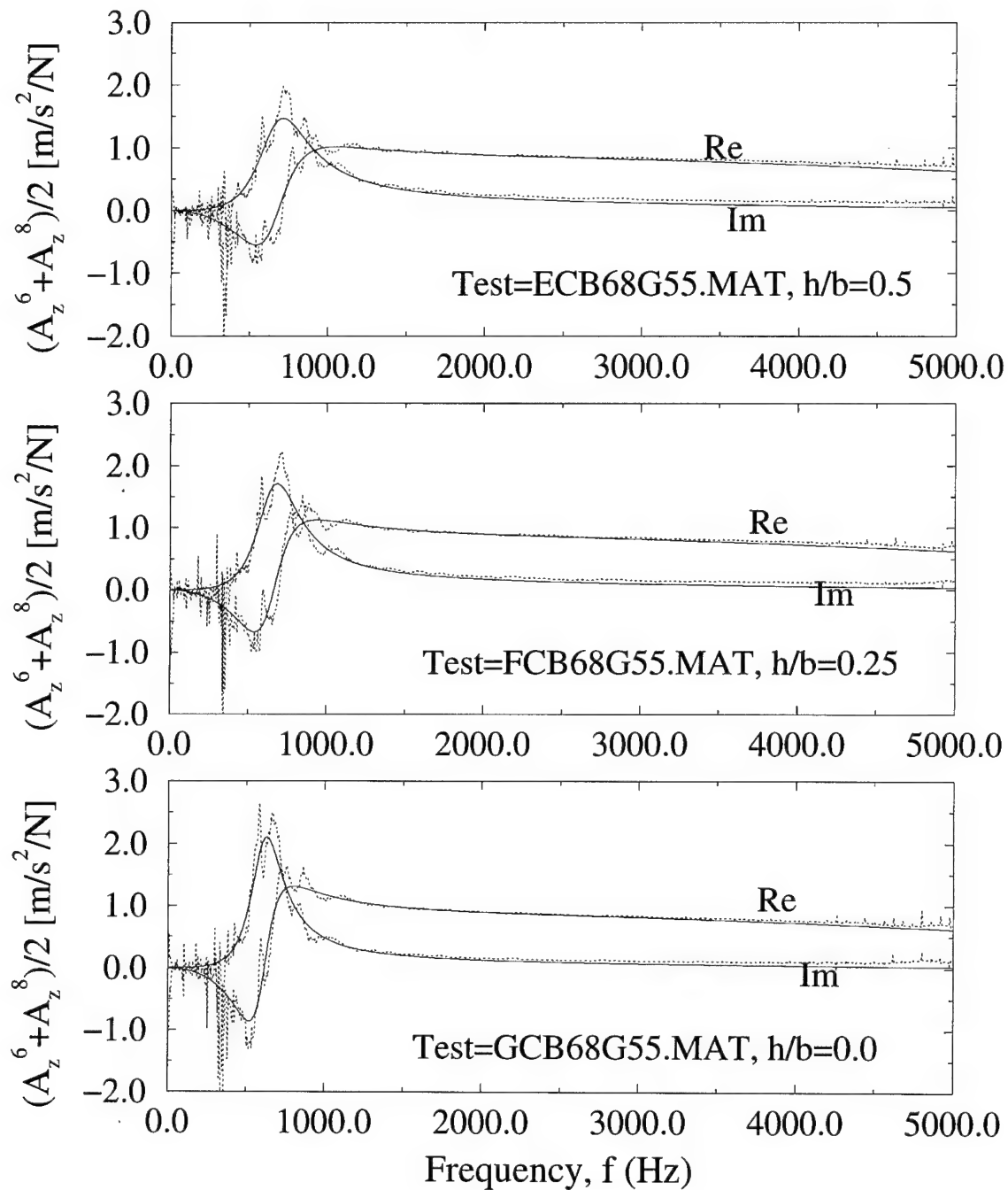
Figure 6.4: Typical results from vertical concentric tests on embedded footings in Series E, F, and G.
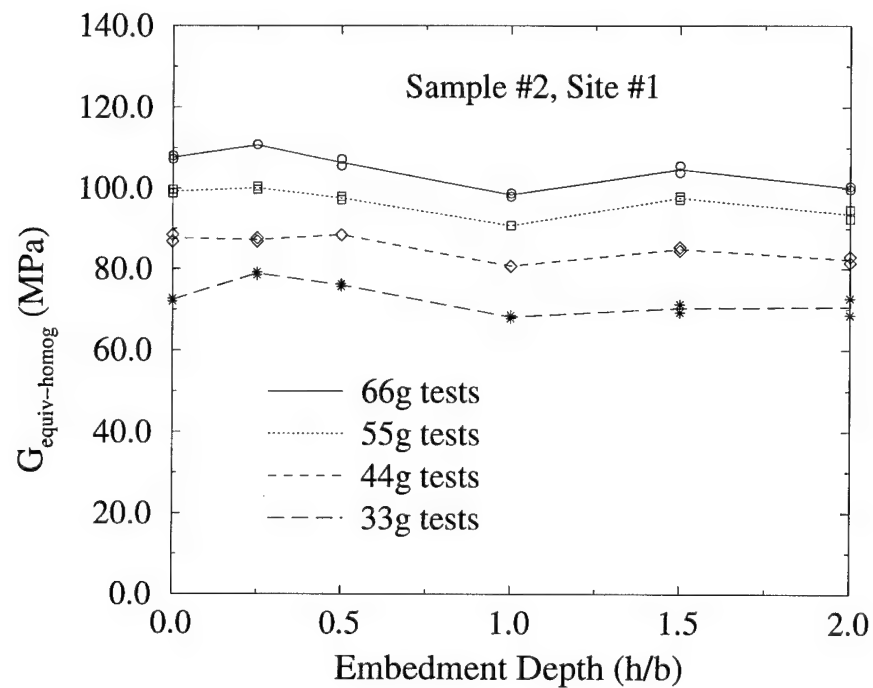
Figure 6.5: Change in best-fit equivalent homogeneous shear modulus with embedment depth (Series B, C, D, E, F, G).

6.2.3   Vertical Tests from Series H, I, J, K, L, M

Series H, I, J, K, L, and M included vertical eccentric tests using the stinger at embedment depths of $h/b = 2.0$, 1.5, 1.0, 0.5, 0.25, and 0.0 respectively. Although the problem of the transverse frictional force is present due to the use of the stinger, it is helpful to look at the vertical centroidal accelerance from these tests. Figure 6.6 shows the best-fit equivalent homogeneous shear moduli for Series H, I, J, K, L, M as a function of embedment depth. Although the trend is not monotonic except for the $33g$ tests, the overall trend is that $G_{equivhomog}$ decreases with increasing embedment.
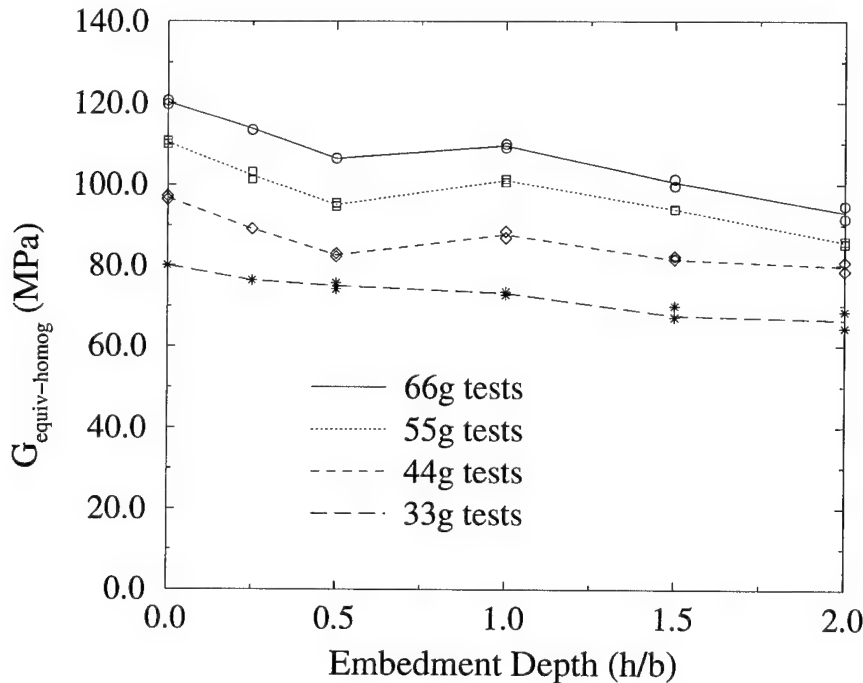
Figure 6.6: Change in best-fit equivalent homogeneous shear modulus with embedment depth (Series H, I, J, K, L, M).

6.3   Computing G_{lat} from G_{vert}

Recall that the skew-symmetric vertical motion in a lateral-load test is very small and cannot be accurately measured. Therefore, a vertical accelerance match

cannot be used to determine the best-fit shear modulus for tests with lateral loading. However, the shear modulus can be varied in order to fit the lateral accelerances. Previous studies have shown that the best-fit shear modulus from lateral loading is significantly lower than the best-fit shear modulus from vertical loading for the surface case (Gillmor [11]). Furthermore, Hushmand [19] reported that the resonant frequencies predicted by Lysmer's analog were 15 to 55% higher than experimentally measured resonant frequencies for lateral excitation. Rather than using a different shear modulus for different types of loading (which is unphysical and counter-intuitive), Impedance Modification Factors were employed by Gillmor [11] and Ashlock [1] to fit lateral-load accelerances based on the shear modulus found in vertical loading. However, due to the mass of the exciter armature, there is a slight difference in contact pressure between the vertical and lateral loading cases. To resolve this issue, Ashlock employed the power law format in Equation (6.2) to calculate G_{lat} from G_{vert}. Based on Equation (6.2), one can define,

$$G_{lat} = f(e, b_{pr}) \left(\frac{p_{pr}^{lat}}{1kPa} \right)^{0.5}, \quad G_{vert} = f(e, b_{pr}) \left(\frac{p_{pr}^{vert}}{1kPa} \right)^{0.5}, \tag{6.5}$$

from which

$$G_{lat} = G_{vert} \left(\frac{p_{pr}^{lat}}{p_{pr}^{vert}} \right)^{0.5}. \tag{6.6}$$

The power law format in Equations (6.1) and (6.2) has only been validated for surface foundations. Since tests in this investigation were conducted on a single footing, there is only one combination of b_{pr} and the embedded foundation pressure parameter p_{pr} at each g-level, and a validation of the $b_{pr}^{0.1}$ and $p_{pr}^{0.5}$ exponents cannot be done individually by a regression analysis. However, it is possible to investigate the experimental support for this power law format which can be stated as,

$$G = G' b_{pr}^{0.1} p_{pr}^{0.5}. \tag{6.7}$$

In centrifuge modeling, b_{pr} and p_{pr} are related to the g-level according to

$$b_{pr} = nb_m, \quad p_{pr} = np_m, \tag{6.8}$$

where b_m is the half-width of the scaled model, p_m is the contact pressure of the model at $1g$, and n is the g-level. Substituting (6.8) into (6.7) and taking the log of each term yields,

$$log(G) = log(G') + 0.1log(b_m) + 0.5log(p_m) + 0.6log(n) \tag{6.9}$$

where $log(G')$, $0.1log(b_m)$, and $0.5log(p_m)$ are constants. Therefore, performing a linear regression in the form of

$$log(G) = \alpha + \beta log(n) \tag{6.10}$$

could show support for the power law format if $\beta \approx 0.6$. Table 6.5 shows the results from such a regression performed on the average G at each g-level from each series of tests in this investigation. The average β is 0.54 for all embedment depths considered. Figure 6.7 shows the resulting β's plotted versus embedment depth. Results for the regression analysis by Guzina for the original $a_{pr}^{0.1}$ and $p_{pr}^{0.5}$ format for circular foundations yielded exponent pairs of (0.10, 0.51), (0.11, 0.47), and (0.09, 0.47), which yield sums of 0.61, 0.58, and 0.56. Thus, the average β and its degree of variation for different embedment depths are very close to Guzina's result. Since the difference between the bearing pressure with and without the mass of the exciter armature is only about 5%, and the G should be reduced by some factor for the lateral tests with a lower p_{pr}, it was chosen to adopt the $p_{pr}^{0.5}$ format for calculating the corresponding G for the lateral case as in Equation (6.6).

6.4 Lateral and Vertical Eccentric Test Results with Button and Dumpling System

Subsequent to the excellent matching of vertical accelerances, several additional series of experiments were conducted to explore the vertical eccentric and

h/b	VC-stinger B,C,D,E,F,G	VE-stinger H,I,J,K,L,M	VE-button N,O,P,Q	VE-button R,S,T,U
0.00	0.566127	0.579618	—	0.569032
0.25	0.487814	0.567457	—	0.618098
0.50	0.474990	0.503990	0.575184	0.568922
1.00	0.522451	0.581139	0.512108	0.560797
1.50	0.573963	0.574247	0.539262	—
2.00	0.502987	0.467341	0.502326	—

Table 6.5: Linear regression results of vertical tests for "β".
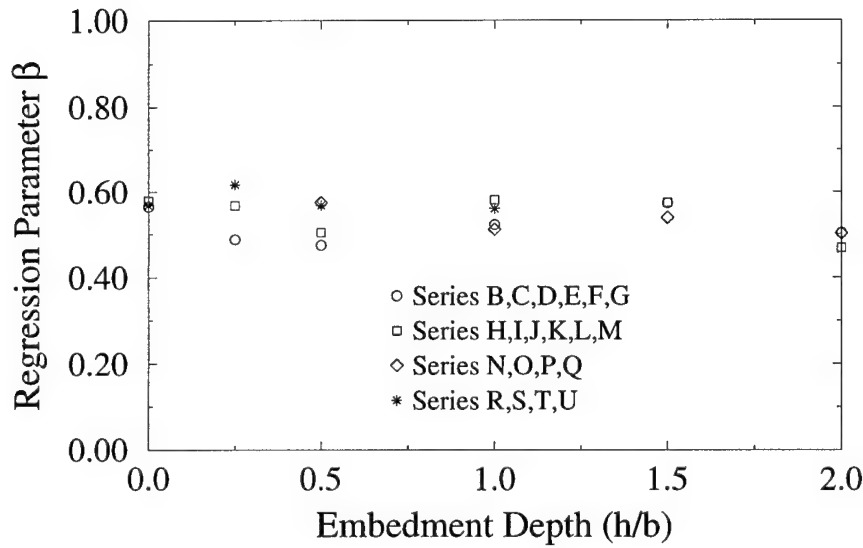
Figure 6.7: Regression parameter β versus embedment depth.

lateral loading cases. Lateral tests were conducted in Series A, B, C, D, E, F, and G, and vertical eccentric and lateral tests were conducted on a second location on sample #2 from $h/b = 2.0$ to 0.0 and denoted as Series H, I, J, K, L, and M respectively. However, all of these tests were performed using the conical stinger shown in Figure 4.3. As shown in Ashlock [1], the conical shape of the stinger is conducive to the transmitting of a transverse force at the tip of the cone since the pointed stinger cannot slide very easily across the exciter bolt. Therefore, in

the application of an eccentric load, there is an additional friction force caused by the contact between the exciter and the stinger. This friction causes a poor correlation between the peak frequencies in the lateral accelerances from the vertical eccentric and lateral loading cases as discussed in Aslock [1].

A solution to the friction problem in the form of hemispherical "button" with an oil-filled dumpling is also presented in Ashlock [1] (see Figure 4.3 for a diagram of the button). The rounded shape of the button is less conducive to the transmitting of a frictional force in the application of both vertical and lateral loads. Additionally, the oil-filled pocket provided by the dumpling allows each side of the latex membrane to slide relatively frictionlessly over one another with lubrication provided by the oil contained inside. The only drawback to the dumpling design is that the latex rubber may prevent the transmission of high frequency vibrations applied by the exciter. Ashlock [1] found that this was not a problem in the vertical case since the mass of the exciter armature provided enough prestress to transmit the vibrations for frequencies up to $2kHz$. However, the use of the dumpling in the lateral case yielded poor coherence at frequencies above 500 to $1,000Hz$ and was found unsuitable for use in the lateral loading tests (Ashlock [1]).

As a possible improvement on the latex membrane dumpling, a thinner latex bag (made from a medical glove) filled with oil and tied off in order to provide a closed lubrication system similar to the dumpling was used. Latex gloves are thinner than the membrane used in the dumpling and this method was employed with the hope that the glove would yield better coherence at higher frequencies in both the vertical and lateral cases. Consequently a series of tests was conducted using an oil-filled latex glove for lubrication between the hemispherical button and the exciter.

6.4.1   Results from the Thin Oil-filled Latex Membrane (Series N, O, P, Q)

Series N, O, P, and Q include both vertical eccentric and lateral tests at embedment depths of 2.0, 1.5, 1.0, and 0.5 respectively. These tests were conducted on a single location on sample #3. Vertical eccentric loading was applied at hole #6 and lateral loading was applied at hole #10, while accelerance was measured at holes #7, #3, and #4 for both types of loading. These tests will be discussed in the order in which they were performed, beginning with Series N.

6.4.1.1   Series N ($h/b = 2.0$)

Tables 6.6 and 6.7 contain results from the best fit vertical accelerance match, as well as the best-fit α_{ij}. The best-fit α_{ij} are chosen according to the error function defined as $E(\alpha_{ij}) = E_1 + E_2$ similar to Ashlock [1], where

$$E_1 = (f_{pk}^{th} - f_{pk}^{meas})^2 \tag{6.11}$$

$$E_2 = \left\{ \begin{array}{cc} \sum_{i=1}^{N} \left[\left\{ Re(A_i^{th}) - Re(A_i^{meas}) \right\}^2 + \left\{ Im(A_i^{th}) - Im(A_i^{meas}) \right\}^2 \right]; & f_1 < f < f_2 \\ 0; & otherwise \end{array} \right\}$$

where f_{pk}^{th} and f_{pk}^{meas} are the peak frequencies from the theoretical and experimentally measured accelerance curves and A_i^{th} and A_i^{meas} are the individual data points. The frequencies f_1 and f_2 constitute a frequency range desired for the least squares fit. For all of the tests in this investigation, $f_1 = 500Hz$ and $f_2 = 2000Hz$ which constitutes the range in which the horizontal translation accelerance peak is generally found.

The use of the thin latex membrane in Series N yielded good results for vertical eccentric loading. The accelerance had a coherence of nearly 1 for a ma-

jority of the frequency range. A typical lateral accelerance from vertical eccentric loading is shown in Figure 6.8a. However, for lateral loading, the thin membrane was not nearly as successful. Lateral tests with the thin membrane showed very poor coherence. A typical lateral accelerance curve with the thin latex membrane appears in Figure 6.8b. The test in Figure 6.8b is only a $1kHz$ test, but, tests beyond $1kHz$ showed even worse results at higher frequencies than those shown in Figure 6.8b. This conclusion is similar to that of Ashlock, where the latex membrane dumpling yielded good coherence for the vertical case (due to the added prestress of the exciter armature), but poor test results in the lateral case. As an alternative to the thin latex membrane or the latex membrane dumpling used by Ashlock [1], a commercially available synthetic oil called Tri-Flow was then used to lubricate the contact between the exciter and the hemispherical button in all remaining lateral tests which were conducted in Series N to U. A typical lateral accelerance from lateral loading with the Tri-Flow lubrication in Series N is shown in Figure 6.8c. Noting the large amount of noise in Figure 6.8b with the thin membrane when compared to Figure 6.8c with Tri-Flow shows the significance of the improvements made.

For Series N with an embedment depth of $h/b = 2.0$, the results of the initial accelerance match yielded widely varying values of α_{hh} and α_{mh}. The fact that a precise α_{hh} or α_{mh} cannot be pinpointed at this embedment depth is not surprising given the lack of defining characteristics (other than the primary rocking peak) in the accelerance curves as shown in Figures 5.7 and 5.9 for the vertical eccentric and lateral loading cases respectively. Figure 6.9 shows a contour plot of the error surface as a function of α_{mm} and α_{hh} for a typical test in Series N with $\alpha_{mh}=0.60$, while Figure 6.10 shows a contour plot of the error as a function of α_{mm} and α_{mh} for the same test with $\alpha_{hh}=0.80$. One can see that although α_{mm} is very well defined, there is a large longitudinal trench for both α_{hh} and α_{mh}, signifying that

the precise best-fit α_{hh} and α_{mh} are not well defined. While Figures 6.9 and 6.10 show two perpendicular planes in a three-dimensional space, Figure 6.11 shows the complete three-dimensional $\alpha_{mm} - \alpha_{hh} - \alpha_{mh}$ space with isosurfaces for normalized error values of 400, 1000, and 5000. Each of the isosurfaces has the shape of a "pancake" in the $\alpha_{hh} - \alpha_{mh}$ plane with the thickness of the pancake increasing slightly as the value of normalized error increases. This shape signifies that α_{mm} is very well-defined, but α_{hh} and α_{mh} can be any value lying within the pancake and still yield a reasonable accelerance match. Table 3.3 revealed that α_{hh} and α_{mh} when comparing the square root profile to the homogeneous half-space at $h/b = 2.0$ are 0.80 and 0.55 respectively. Since Figure 6.11 reveals that there is not a specific trend in the best-fit α_{hh} and α_{mh}, the best approach may be to set α_{hh} and α_{mh} to the values specified in Figure 3.3. The α_{ij} shown in Tables 6.6 and 6.7 are for α_{hh} set to 0.80, α_{mh} set to 0.55, and the best-fit α_{mm} computed from Equation (6.11) with the other two α's specified. The best-fit α_{mm} will be plotted versus centrifuge g-level in Section 6.5.2.

To illustrate the lack of sensitivity to the specific values of α_{hh} and α_{mh}, Figure 6.12 shows a typical lateral accelerance (hole #4) from a vertical eccentric test in Series N. Also shown are two theoretical accelerances. The first theoretical accelerance is for a fixed α_{hh} and α_{mh} of 0.80 and 0.55 respectively, with the best-fit α_{mm} of 0.54 under these conditions. The second theoretical accelerance is for the best-fit α_{ij} according to Equation (6.11) when each α_{ij} is varied from 0.30 to 1.00. The latter approach yields $\alpha_{mm}=0.59$, $\alpha_{hh}=0.54$, $\alpha_{mh}=0.30$. One can see that the difference in the two theoretical accelerance curves is very small, and that the curve where α_{hh} and α_{mh} are specified may even produce a better overall visual accelerance match in the frequency range of interest.
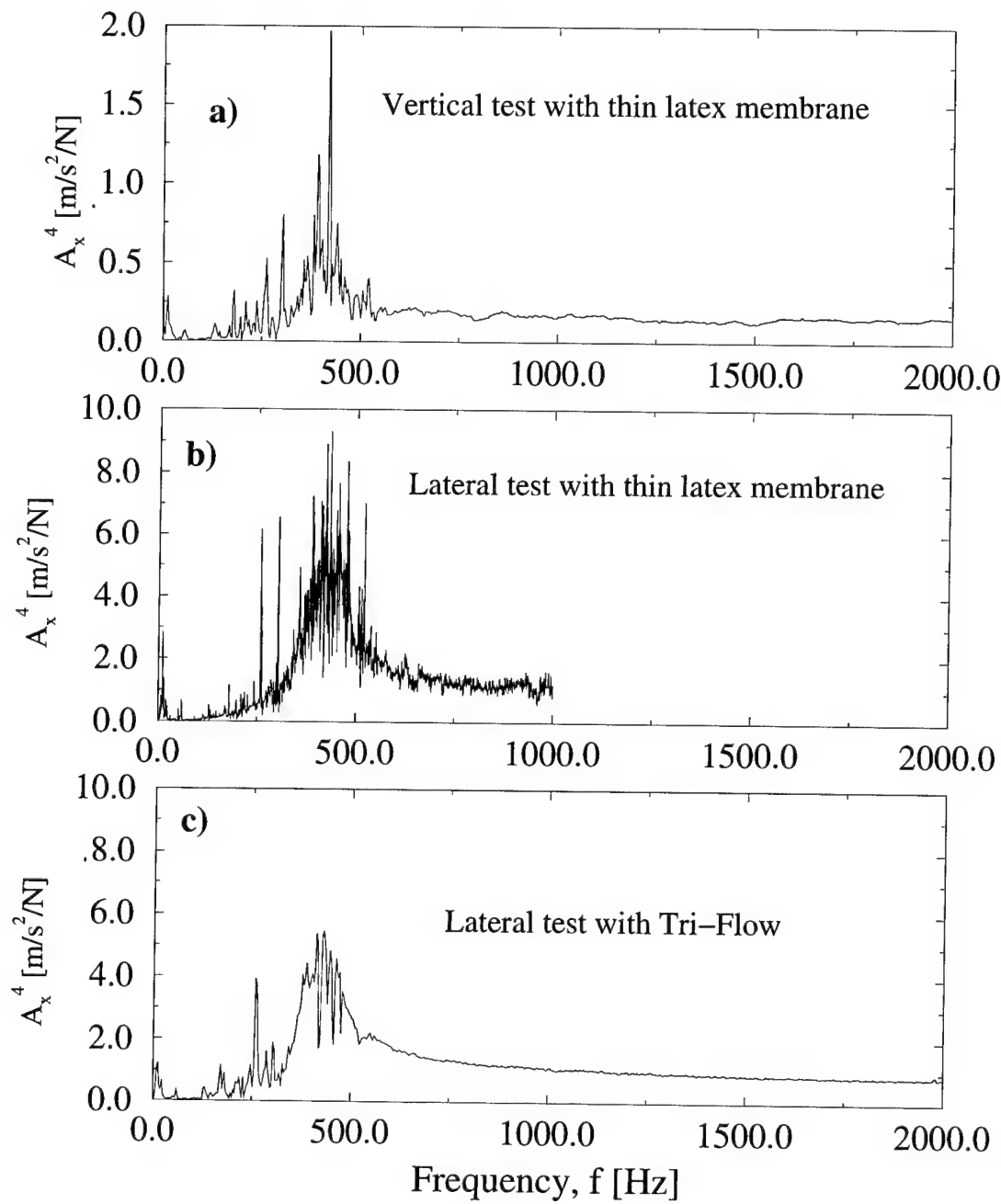
Figure 6.8: Experimental accelerance (hole #4) from Series N: a) vertical eccentric loading with thin membrane, b) lateral loading with thin membrane, c) lateral loading with Tri-Flow.

Filename	g-level	b_{pr}	p_{pr}	$G_{equivhomog}$	α_{mm}	α_{hh}	α_{mh}
NEB34G66.MAT	65.45	1.800	269.6	113.38	0.54	0.80	0.55
NEB34G66.MA2	65.45	1.800	269.6	112.49	0.55	0.80	0.55
NEB34G55.MAT	54.55	1.500	224.7	108.12	0.52	0.80	0.55
NEB34G55.MA2	54.55	1.500	224.7	106.40	0.57	0.80	0.55
NEB34G44.MAT	43.64	1.200	179.8	96.35	0.54	0.80	0.55
NEB34G44.MA2	43.64	1.200	179.8	96.35	0.55	0.80	0.55
NEB34G44.MA3	43.64	1.200	179.8	94.73	0.56	0.80	0.55
NEB34G33.MAT	32.73	0.900	134.8	81.46	0.60	0.80	0.55
NEB34G33.MA2	32.73	0.900	134.8	79.23	0.50	0.80	0.55
NEB34G33.MA3	32.73	0.900	134.8	78.49	0.50	0.80	0.55
NEB34G33.MA4	32.73	0.900	134.8	79.23	0.62	0.80	0.55
NLB34G66.MA8	65.45	1.800	255.6	110.03	0.59	0.80	0.55
NLB34G66.MA9	65.45	1.800	255.6	110.03	0.50	0.80	0.55
NLB34G66.M10	65.45	1.800	255.6	110.03	0.56	0.80	0.55
NLB34G55.MA2	54.55	1.500	213.0	104.48	0.57	0.80	0.55
NLB34G55.MA3	54.55	1.500	213.0	104.48	0.57	0.80	0.55
NLB34G44.MA2	43.64	1.200	170.4	93.28	0.59	0.80	0.55
NLB34G44.MA3	43.64	1.200	170.4	93.28	0.50	0.80	0.55
NLB34G44.MA4	43.64	1.200	170.4	93.28	0.56	0.80	0.55
NLB34G33.MA2	32.73	0.900	127.8	77.50	0.51	0.80	0.55
NLB34G33.MA3	32.73	0.900	127.8	77.50	0.52	0.80	0.55
NLB34G33.MA4	32.73	0.900	127.8	77.50	0.51	0.80	0.55

Table 6.6: Table of results from Series N, $h/b = 2.0$.

Filename	g-level	b_{pr}	p_{pr}	$G_{equivhomog}$	α_{mm}	α_{hh}	α_{mh}
NEB34G66.MA3	65.45	1.800	269.6	118.75	0.50	0.80	0.55
NEB34G66.MA4	65.45	1.800	269.6	119.66	0.53	0.80	0.55
NEB34G66.MA5	65.45	1.800	255.6	118.75	0.53	0.80	0.55
NEB34G66.MA6	65.45	1.800	269.6	119.66	0.51	0.80	0.55
NEB34G66.MA7	65.45	1.800	269.6	119.66	0.51	0.80	0.55
NEB34G55.MA3	54.55	1.500	224.7	113.38	0.50	0.80	0.55
NEB34G55.MA4	54.55	1.500	224.7	114.26	0.50	0.80	0.55
NEB34G55.MA5	54.55	1.500	213.0	111.61	0.53	0.80	0.55
NEB34G55.MA6	54.55	1.500	224.7	111.61	0.55	0.80	0.55
NEB34G55.MA7	54.55	1.500	224.7	112.49	0.52	0.80	0.55
NEB34G55.MA8	54.55	1.500	224.7	112.49	0.52	0.80	0.55
NEB34G55.MA9	54.55	1.500	224.7	111.61	0.54	0.80	0.55
NEB34G44.MA4	43.64	1.200	179.8	102.15	0.55	0.80	0.55
NEB34G44.MA5	43.64	1.200	179.8	99.65	0.55	0.80	0.55
NEB34G33.MA5	32.73	0.900	134.8	83.73	0.50	0.80	0.55
NEB34G33.MA6	32.73	0.900	134.8	83.73	0.50	0.80	0.55
NLB34G66.M11	65.45	1.800	255.6	116.35	0.50	0.80	0.55
NLB34G55.MA4	54.55	1.500	213.0	109.54	0.53	0.80	0.55
NLB34G44.MA5	43.64	1.200	170.4	98.24	0.56	0.80	0.55
NLB34G33.MA5	32.73	0.900	127.8	81.50	0.50	0.80	0.55

Table 6.7: Table of results from Series N, $h/b = 2.0$.
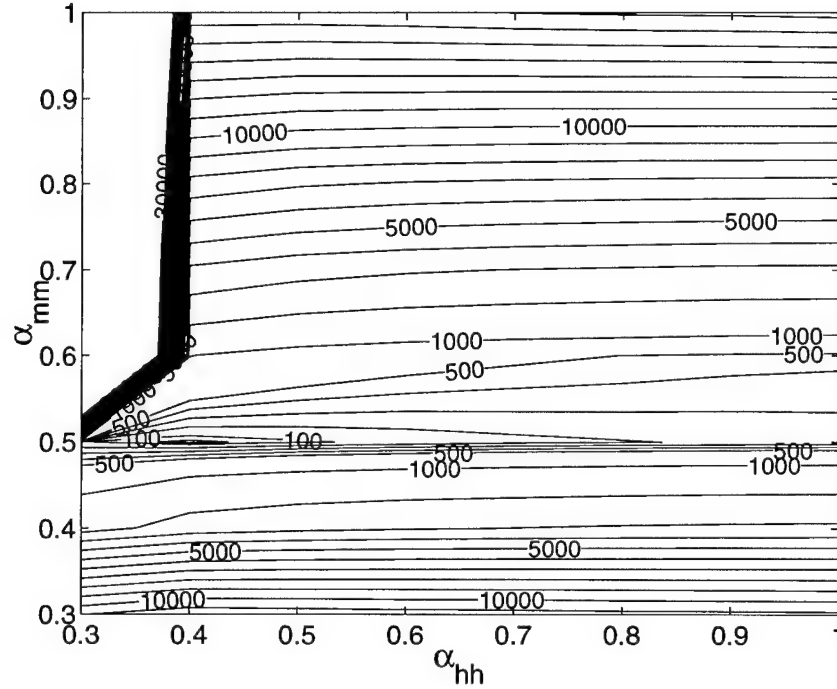
Figure 6.9: α_{mm} vs. α_{hh} error contour plot for accelerance at hole #4 from test NEB34G66.MAT with $\alpha_{mh} = 0.60$, $h/b = 2.0$.
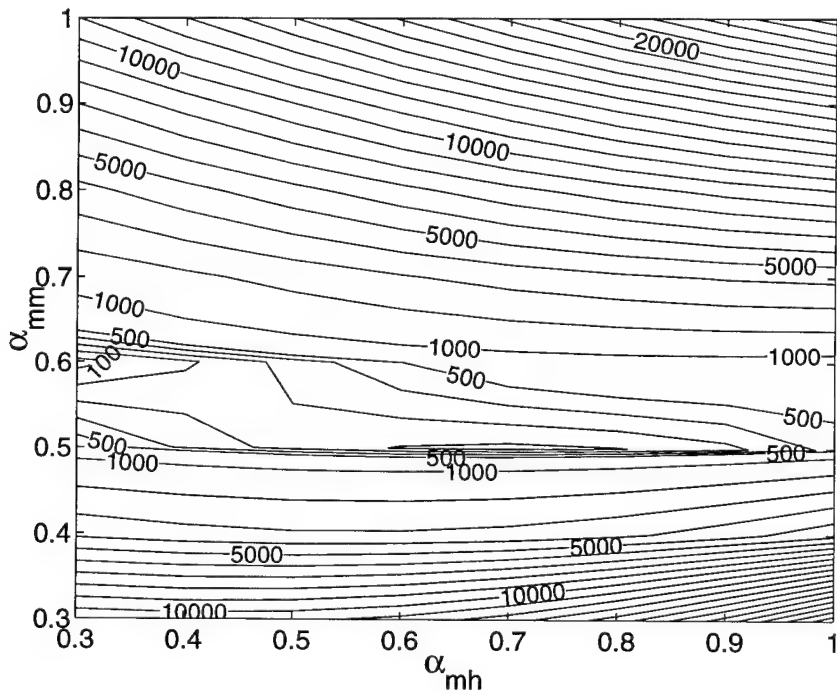
Figure 6.10: α_{mm} vs. α_{mh} error contour plot for accelerance at hole #4 from test NEB34G66.MAT with $\alpha_{hh} = 0.80$, $h/b = 2.0$.
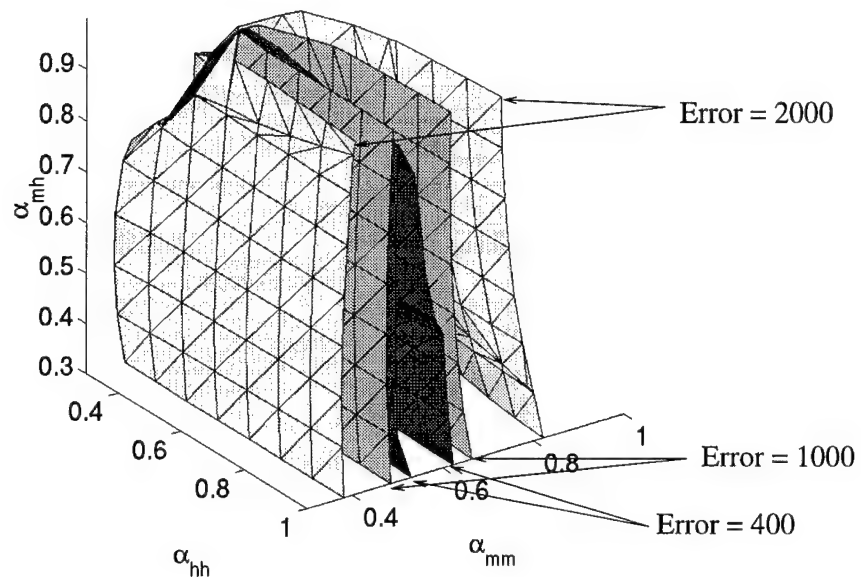
Figure 6.11: Three-dimensional error surface plot in $\alpha_{mm} - \alpha_{hh} - \alpha_{mh}$ space for normalized error=400, 1000, 5000 (test NEB34G66.MAT, accelerance of hole #4, $h/b = 2.0$).
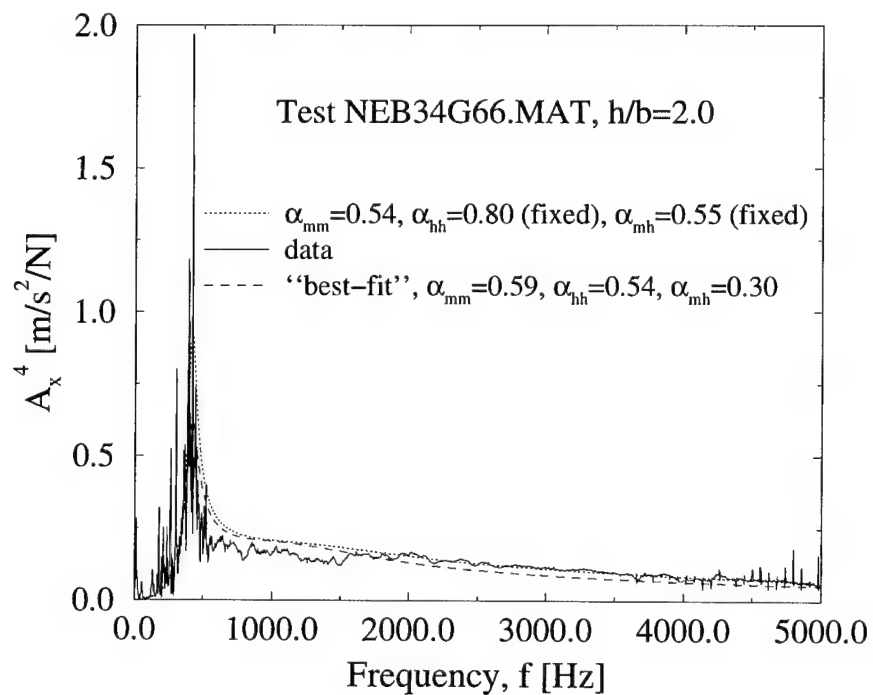
Figure 6.12: Theoretical accelerance with specified α_{hh} and α_{mh} ($\alpha_{mm} = 0.54$, $\alpha_{hh} = 0.80$, $\alpha_{mh} = 0.55$), experimental data, and "best-fit" accelerance ($\alpha_{mm} = 0.59$, $\alpha_{hh} = 0.54$, $\alpha_{mh} = 0.30$).

6.4.1.2   Series O $(h/b = 1.5)$

Series O included tests at $h/b = 1.5$ at the same location as Series N. One set of vertical eccentric tests with the thin latex membrane and one set of lateral tests with Tri-Flow were conducted in Series O on consecutive spins in the centrifuge. Table 6.8 contains the tabulated results from this series of tests. Figure 6.13 shows the three-dimensional α_{ij} space with three isosurfaces drawn for normalized error values of 100, 500, and 2000. The error surfaces have the same "pancake" shape as in Series N where the optimal α_{mm} is well-defined and α_{hh} and α_{mh} can be any value lying within the thinnest pancake. The specific values of α_{hh} and α_{mh} were fixed to 0.79 and 0.53 respectively in accordance with Table 3.3 for a comparison of the square-root profile and homogeneous half-space. Figures 6.14 and 6.15 show typical accelerance matches from the vertical eccentric and lateral loading cases respectively in Series O.

Filename	g-level	b_{pr}	p_{pr}	$G_{equivhomog}$	α_{mm}	α_{hh}	α_{mh}
OEB34G66.MAT	65.45	1.800	269.6	117.85	0.59	0.79	0.53
OEB34G66.MA2	65.45	1.800	269.6	117.85	0.58	0.79	0.53
OEB34G55.MAT	54.55	1.500	224.7	110.74	0.58	0.79	0.53
OEB34G55.MA2	54.55	1.500	224.7	110.74	0.62	0.79	0.53
OEB34G44.MAT	43.64	1.200	179.8	97.17	0.64	0.79	0.53
OEB34G44.MA2	43.64	1.200	179.8	96.35	0.66	0.79	0.53
OEB34G33.MAT	32.73	0.900	134.8	81.46	0.59	0.79	0.53
OEB34G33.MA2	32.73	0.900	134.8	80.71	0.60	0.79	0.53
OLB34G66.MAT	65.45	1.800	255.6	114.70	0.60	0.79	0.53
OLB34G66.MA2	65.45	1.800	255.6	114.70	0.59	0.79	0.53
OLB34G55.MAT	54.55	1.500	213.0	107.79	0.60	0.79	0.53
OLB34G55.MA2	54.55	1.500	213.0	107.79	0.62	0.79	0.53
OLB34G44.MAT	43.64	1.200	170.4	94.25	0.56	0.79	0.53
OLB34G44.MA2	43.64	1.200	170.4	94.25	0.60	0.79	0.53
OLB34G33.MAT	32.73	0.900	127.8	78.97	0.63	0.79	0.53
OLB34G33.MA2	32.73	0.900	127.8	78.97	0.58	0.79	0.53

Table 6.8: Table of results from Series O, $h/b = 1.5$.
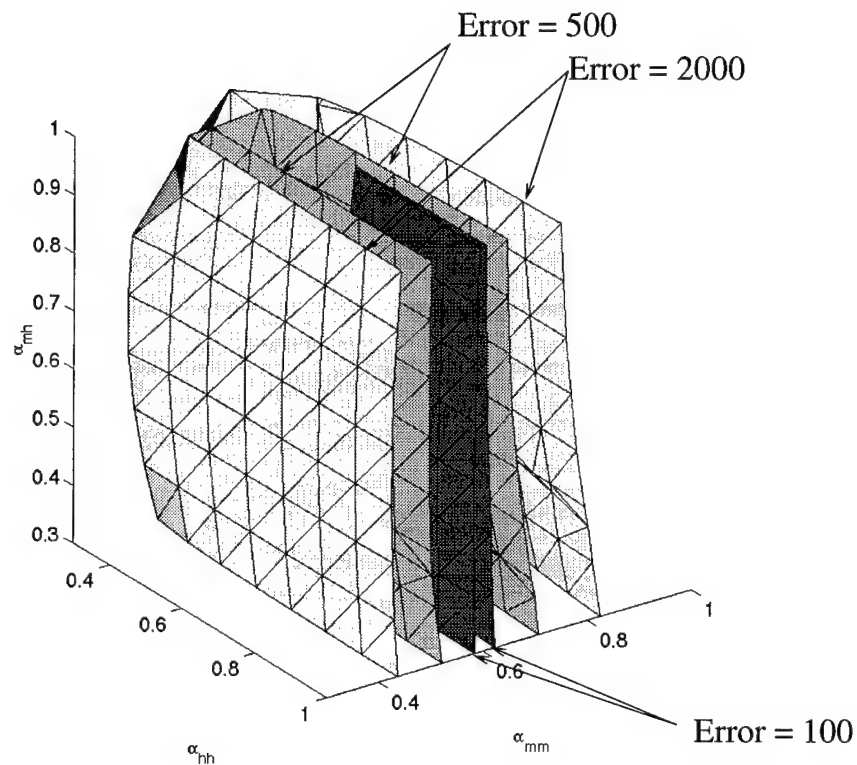
Figure 6.13: Three-dimensional error surface plot in $\alpha_{mm} - \alpha_{hh} - \alpha_{mh}$ space for normalized error=100, 500, 2000 (test OEB34G66.DAT, accelerance of hole #4, $h/b = 1.5$).
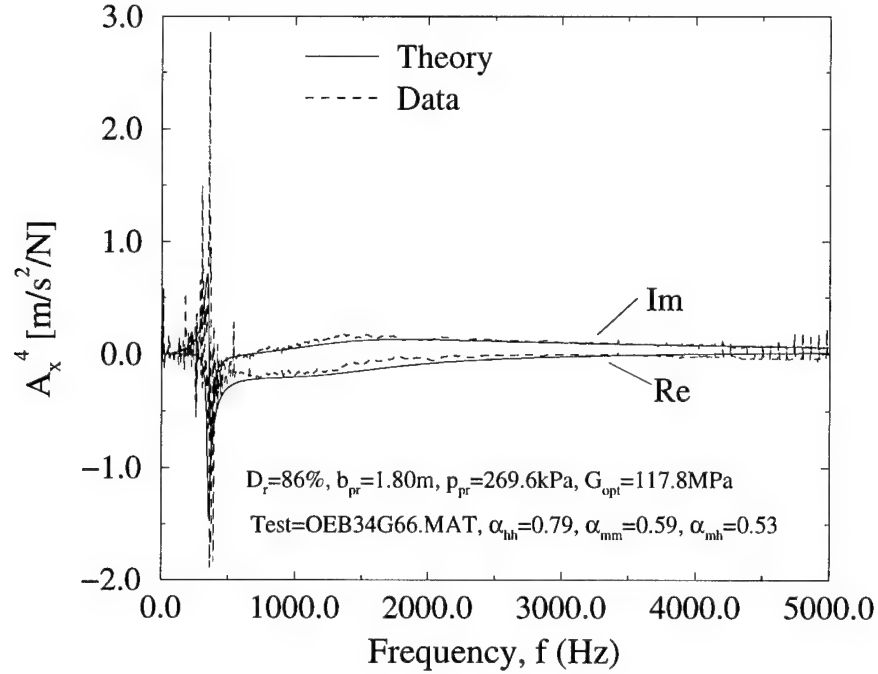
Figure 6.14: Theoretical and experimental accelerance from typical vertical eccentric test in Series O, thin latex membrane, $h/b = 1.5$.
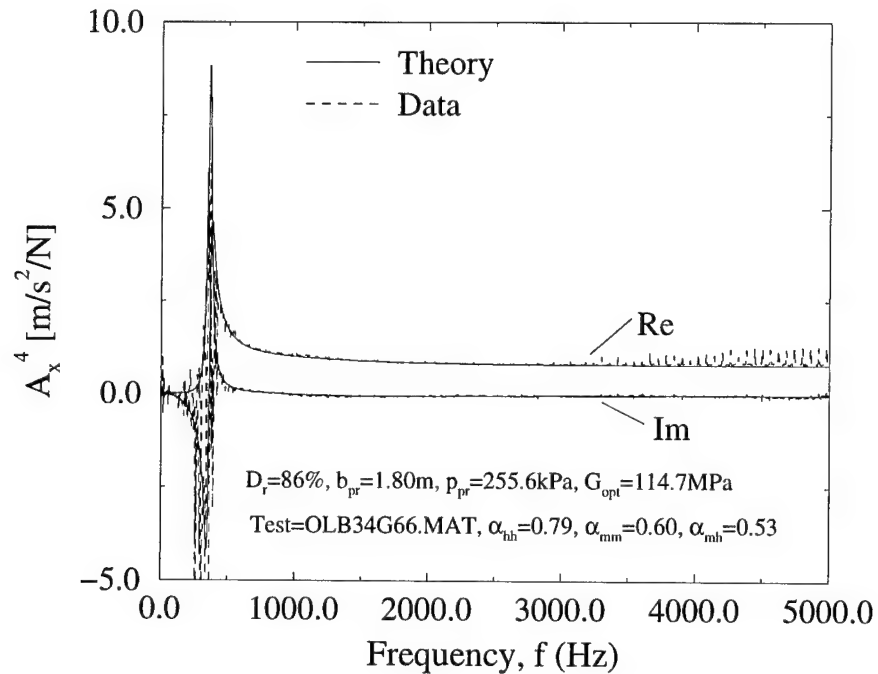
Figure 6.15: Theoretical and experimental accelerance from typical lateral test in Series O, thin latex membrane, $h/b = 1.5$.

6.4.1.3   Series P $(h/b = 1.0)$

Series P was conducted at $h/b = 1.0$ at the same location as Series N and O. The thin latex membrane was used in the vertical eccentric loading and Tri-flow was used in the lateral loading just as in Series O. Five spins were conducted in Series P, consisting of VE, VE, LH, LH, and VE tests in the five successive spins. Table 6.9 contains the results of the tests performed in Series P. Based on Table 3.3, α_{hh} and α_{mh} were set to 0.77 and 0.50 respectively.

Figure 6.16 shows the best-fit α_{mm} versus g-level for Spins 2 and 3 in Series P which consisted of vertical eccentric and lateral tests respectively. Clearly, there is a difference in the best-fit α_{mm} from these two types of loading. Since the α_{mm}'s from vertical eccentric tests are higher, it would appear that the latex glove does not offer sufficient lubrication to reduce the friction between the exciter and the button. The added frictional force would cause an increase in the resonance frequency peak due to the rocking mode of vibration in the vertical eccentric tests, and thus an increase in α_{mm} over the lateral vibration case, as shown in Figure 6.16. Support for this belief is given in Series Q at $h/b = 0.5$, which means that the vertical eccentric tests from Series P and Series Q should be ignored.

Filename	g-level	b_{pr}	p_{pr}	$G_{equivhomog}$	α_{mm}	α_{hh}	α_{mh}
PEB34G66.MAT	65.45	1.800	269.6	107.26	0.77	0.77	0.50
PEB34G66.MA2	65.45	1.800	269.6	107.26	0.77	0.77	0.50
PEB34G55.MAT	54.55	1.500	224.7	99.65	0.74	0.77	0.50
PEB34G55.MA2	54.55	1.500	224.7	99.65	0.67	0.77	0.50
PEB34G44.MAT	43.64	1.200	179.8	87.58	0.72	0.77	0.50
PEB34G44.MA2	43.64	1.200	179.8	88.36	0.72	0.77	0.50
PEB34G33.MAT	32.73	0.900	134.8	74.13	0.76	0.77	0.50
PEB34G33.MA2	32.73	0.900	134.8	74.85	0.83	0.77	0.50
PEB34G33.MA3	32.73	0.900	134.8	76.29	0.86	0.77	0.50
PEB34G66.MA3	65.45	1.800	268.4	110.74	0.72	0.77	0.50
PEB34G55.MA3	54.55	1.500	223.7	102.15	0.70	0.77	0.50
PEB34G44.MA3	43.64	1.200	179.0	89.93	0.69	0.77	0.50
PEB34G33.MA4	32.73	0.900	134.2	76.29	0.69	0.77	0.50
PLB34G66.MAT	65.45	1.800	254.4	104.46	0.54	0.77	0.50
PLB34G66.MA2	65.45	1.800	254.4	104.46	0.61	0.77	0.50
PLB34G66.MA3	65.45	1.800	254.4	104.46	0.62	0.77	0.50
PLB34G55.MAT	54.55	1.500	212.0	96.97	0.60	0.77	0.50
PLB34G55.MA2	54.55	1.500	212.0	96.97	0.61	0.77	0.50
PLB34G44.MAT	43.64	1.200	169.6	85.67	0.61	0.77	0.50
PLB34G44.MA2	43.64	1.200	169.6	85.67	0.58	0.77	0.50
PLB34G33.MAT	32.73	0.900	127.2	73.11	0.57	0.77	0.50
PLB34G33.MA2	32.73	0.900	127.2	73.11	0.54	0.77	0.50
PLB34G66.MA4	65.45	1.800	254.4	104.46	0.62	0.77	0.50
PLB34G55.MA3	54.55	1.500	212.0	96.97	0.67	0.77	0.50
PLB34G55.MA4	54.55	1.500	212.0	96.97	0.63	0.77	0.50
PLB34G44.MA3	43.64	1.200	169.6	85.67	0.59	0.77	0.50
PLB34G33.MA3	32.73	0.900	127.2	73.50	0.57	0.77	0.50
PLB34G66.MA5	65.45	1.800	254.4	104.46	0.60	0.77	0.50
PEB34G66.MA4	65.45	1.800	269.6	111.61	0.72	0.77	0.50
PEB34G55.MA4	54.55	1.500	224.7	103.84	0.63	0.77	0.50
PEB34G44.MA4	43.64	1.200	179.8	91.52	0.70	0.77	0.50
PEB34G33.MA5	32.73	0.900	134.8	76.29	0.75	0.77	0.50

Table 6.9: Table of results from Series P, $h/b = 1.0$.
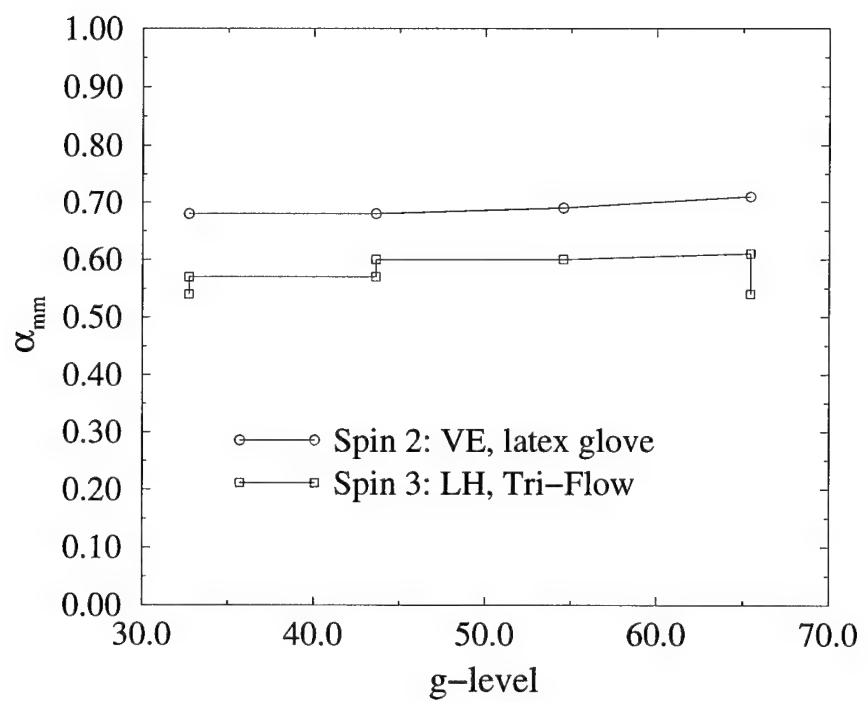
Figure 6.16: α_{mm} vs. g-level for Series P ($h/b = 1.0$), with α_{hh}=0.80, α_{mh}=0.60.

6.4.1.4   Series Q ($h/b = 0.5$)

Series Q was conducted at $h/b = 0.5$, subsequent to Series P, with the thin latex membrane employed in the vertical eccentric tests and Tri-Flow in the lateral tests. Table 6.10 shows the tabular results from Series Q for α_{hh}=0.74, α_{mh}=0.39 in accordance with Table 3.3. Like Series P, Series Q showed a difference in the peak frequencies (and thus, differences in the best-fit α_{mm}) between the vertical eccentric and lateral loading cases. Figure 6.17 shows the clear difference in the best-fit α_{mm} for the thin membrane vertical eccentric and Tri-Flow lateral loading cases. Having the results in Series Q which show the same trend as Series P lends support for the fact that the difference between the best-fit α_{mm} in the two loading cases is due to the increased importance of the residual frictional force at the button. However, from Figures 6.16 and 6.17, it is clear that there is still a difference between the vertical eccentric tests with the latex glove and the lateral tests with the Tri-Flow. Thus, vertical eccentric test results from Series P and Series Q should be ignored. Since Ashlock [1] found good correlation between the two loading cases using the thicker latex membrane dumpling, a similar latex membrane dumpling was used in Series R, S, T, and U in place of the latex glove.

The use of the latex glove for lubrication in the vertical eccentric loading case yielded similar results (α_{mm}) as those lateral tests with the Tri-Flow at embedment depths of $h/b = 2.0$ and $h/b = 1.5$. It was not until tests were conducted at $h/b = 1.0$ and $h/b = 0.5$ that the problem arose. This is most likely due to the fact that the added stiffness due to the extra embedment at $h/b = 2.0$ and $h/b = 1.5$ rendered the frictional force of less importance than at embedments of $h/b = 1.0$ and $h/b = 0.5$ where the reduced embedment provides a softer response. Additionally, the difference in the best-fit α_{mm} between the vertical eccentric and lateral loading is larger at $h/b = 0.5$ than at $h/b = 1.0$, which shows the increasing

effect that the frictional force plays with decreasing embedment.

Figure 6.18 shows the change in the best-fit equivalent homogeneous shear moduli versus embedment depth for Series N, O, P, and Q. In contrast to Figures 6.5 and 6.6 which show a slight downward trend in the best-fit G with increasing embedment, the best-fit G in Figure 6.18 are relatively constant from embedment depths of 0.5 to 2.0.

Filename	g-level	b_{pr}	p_{pr}	$G_{equivhomog}$	α_{mm}	α_{hh}	α_{mh}
QEB34G66.MAT	65.45	1.800	268.4	113.38	0.91	0.74	0.39
QEB34G66.MA2	65.45	1.800	268.4	114.26	0.90	0.74	0.39
QEB34G55.MAT	54.55	1.500	223.7	103.84	0.95	0.74	0.39
QEB34G55.MA2	54.55	1.500	223.7	104.69	0.92	0.74	0.39
QEB34G44.MAT	43.64	1.200	179.0	91.52	0.97	0.74	0.39
QEB34G44.MA2	43.64	1.200	179.0	92.31	0.94	0.74	0.39
QEB34G33.MAT	32.73	0.900	134.2	76.29	0.79	0.74	0.39
QEB34G33.MA2	32.73	0.900	134.2	75.57	0.86	0.74	0.39
QLB34G66.MAT	65.45	1.800	254.4	110.89	0.68	0.74	0.39
QLB34G66.MA2	65.45	1.800	254.4	110.89	0.72	0.74	0.39
QLB34G55.MAT	54.55	1.500	212.0	101.54	0.75	0.74	0.39
QLB34G55.MA2	54.55	1.500	212.0	101.54	0.73	0.74	0.39
QLB34G44.MAT	43.64	1.200	169.6	89.47	0.69	0.74	0.39
QLB34G44.MA2	43.64	1.200	169.6	89.47	0.68	0.74	0.39
QLB34G33.MAT	32.73	0.900	127.2	73.99	0.71	0.74	0.39
QLB34G33.MA2	32.73	0.900	127.2	73.99	0.69	0.74	0.39

Table 6.10: Table of results from Series Q, $h/b = 0.5$.
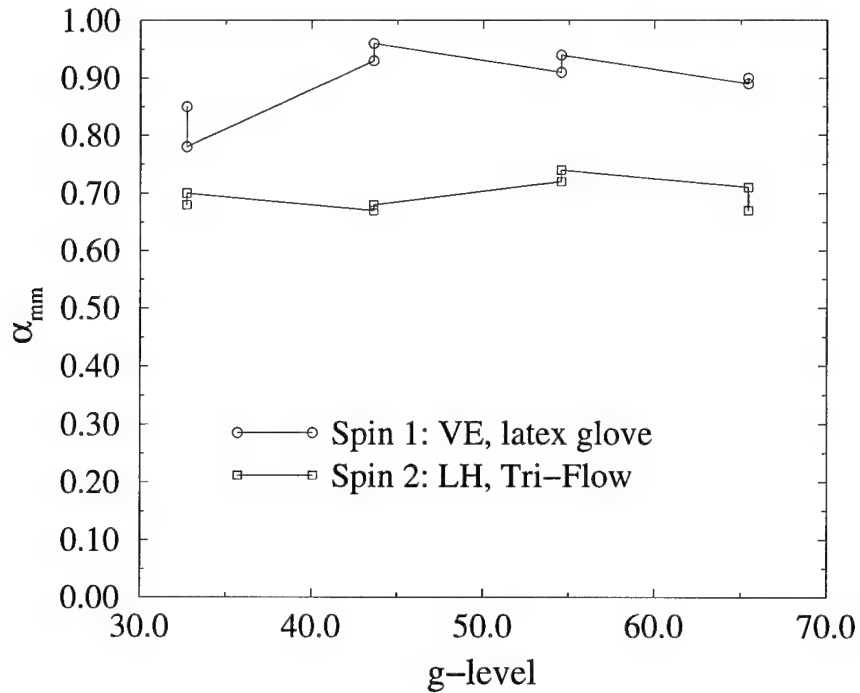
Figure 6.17: α_{mm} vs. g-level for Series Q ($h/b = 0.5$), with α_{hh}=0.74, α_{mh}=0.39.
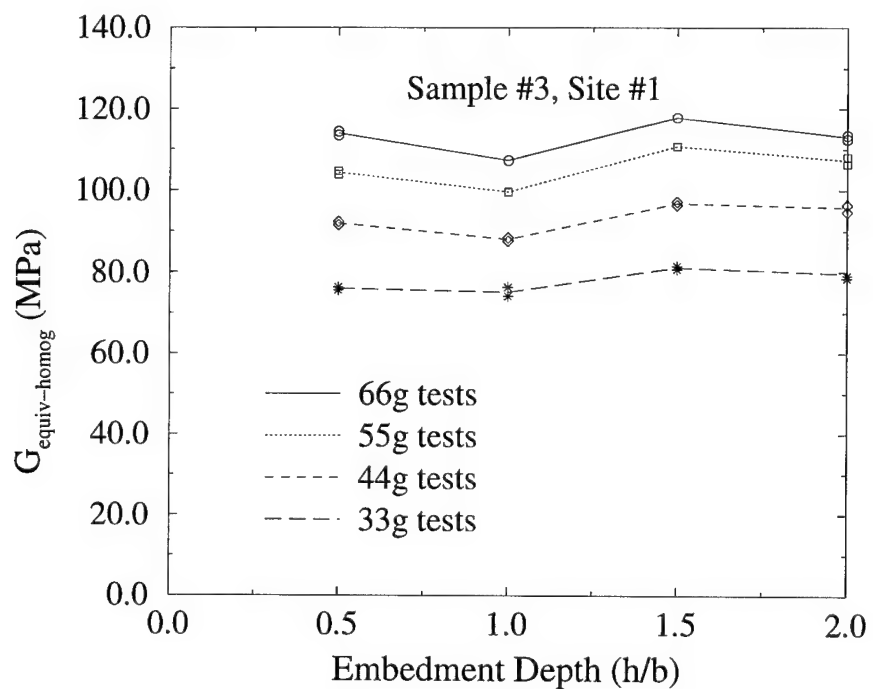
Figure 6.18: Change in best-fit equivalent homogeneous shear modulus with embedment depth for vertical eccentric tests with the thin latex membrane (Series N, O, P, Q).

6.4.2 Results from the Thicker Oil-filled Latex Dumpling (Series R, S, T, U)

Since the latex glove was shown to be inadequate as a lubricating device at shallower embedments (as in Series P and Q), the oil filled latex dumpling was used in the remainder of the test series in this study (R, S, T, U). Vertical eccentric tests with the thicker latex dumpling and lateral tests with Tri-Flow were conducted in Series R, S, and T at a single location on sample #3 with embedment depths of 1.0, 0.5, and 0.25 respectively. Series U is comprised of vertical eccentric and lateral tests at two different locations on the same sample at $h/b = 0.0$. These tests will be discussed in the order in which they were performed, beginning with Series R.

6.4.2.1 Series R $(h/b = 1.0)$

Series R was conducted at an embedment depth of $h/b = 1.0$ at a new location on the same sample as Series N to Q. Vertical eccentric tests with the hemispherical button and latex membrane dumpling, as well as lateral tests with the button and Tri-Flow, were conducted. Table 6.11 contains the tabulated results from Series R. Figures 6.20 and 6.21 show typical results from Series R with the corresponding best-fit parameters for vertical eccentric and lateral tests respectively. From Table 6.11, the α_{mm} from the vertical eccentric and lateral tests show good agreement, indicating that the transverse frictional force was reduced by employing the thicker latex dumpling. As in Series N and O, there was not a clear trend as to the best-fit α_{hh} due to the lack of defining characteristics in the accelerance curves at this embedment depth. Figure 6.19 shows the error isosurfaces in $\alpha_{mm} - \alpha_{hh} - \alpha_{mh}$ space for normalized error values of 50, 100, and 500. The best-fit α_{mm} versus g-level will be shown in Section 6.5.2.

Filename	g-level	b_{pr}	p_{pr}	$G_{equivhomog}$	α_{mm}	α_{hh}	α_{mh}
RLB35G66.MAT	65.45	1.800	255.6	106.13	0.60	0.77	0.50
RLB35G66.MA2	65.45	1.800	255.6	106.13	0.60	0.77	0.50
RLB35G55.MAT	54.55	1.500	213.0	98.63	0.54	0.77	0.50
RLB35G55.MA2	54.55	1.500	213.0	98.63	0.60	0.77	0.50
RLB35G55.MA3	54.55	1.500	213.0	98.63	0.56	0.77	0.50
RLB35G44.MAT	43.64	1.200	170.4	86.07	0.55	0.77	0.50
RLB35G44.MA2	43.64	1.200	170.4	86.07	0.57	0.77	0.50
RLB35G33.MAT	32.73	0.900	127.8	72.15	0.56	0.77	0.50
RLB35G33.MA2	32.73	0.900	127.8	72.15	0.56	0.77	0.50
REB35G66.MA4	65.45	1.800	269.6	108.12	0.63	0.77	0.50
REB35G66.MA5	65.45	1.800	269.6	108.99	0.63	0.77	0.50
REB35G55.MA4	54.55	1.500	224.7	100.48	0.60	0.77	0.50
REB35G55.MA5	54.55	1.500	224.7	100.48	0.61	0.77	0.50
REB35G44.MA4	43.64	1.200	179.8	88.36	0.59	0.77	0.50
REB35G44.MA5	43.64	1.200	179.8	87.58	0.59	0.77	0.50
REB35G33.MA4	32.73	0.900	134.8	73.41	0.55	0.77	0.50
REB35G33.MA5	32.73	0.900	134.8	73.41	0.55	0.77	0.50
REB35G66.MA6	65.45	1.800	269.6	109.86	0.59	0.77	0.50
REB35G55.MA6	54.55	1.500	224.7	103.00	0.61	0.77	0.50
REB35G44.MA6	43.64	1.200	179.8	89.15	0.62	0.77	0.50
REB35G33.MA6	32.73	0.900	134.8	75.57	0.54	0.77	0.50

Table 6.11: Table of results from Series R, $h/b = 1.0$.
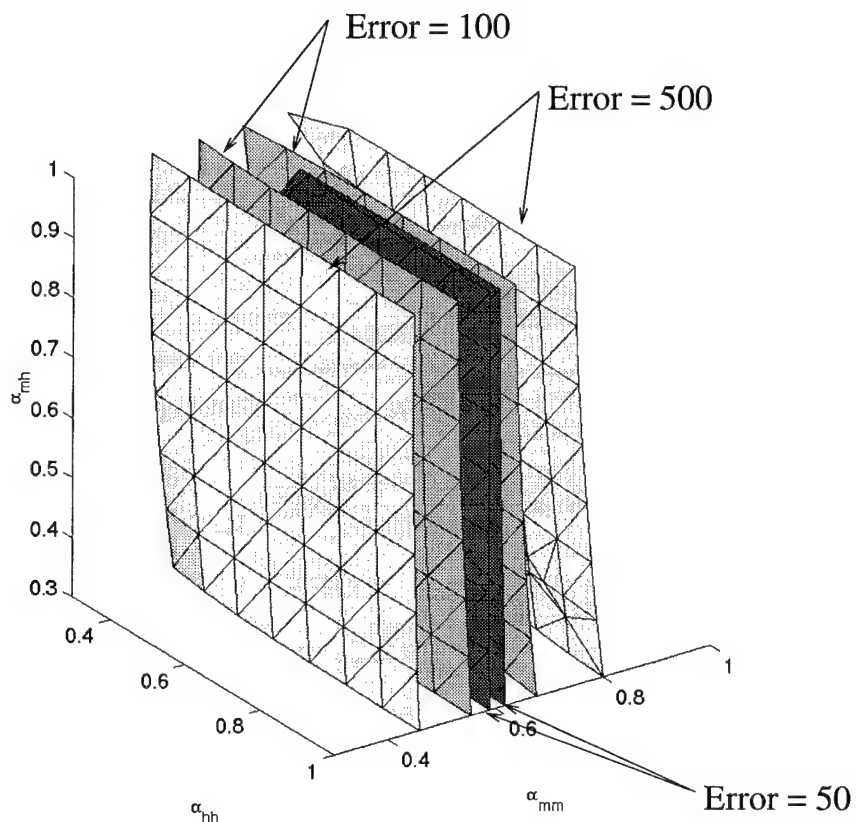
Figure 6.19: Three-dimensional error surface plot in $\alpha_{mm} - \alpha_{hh} - \alpha_{mh}$ space for normalized error=50, 100, 500 (test REB35G55.DA4, accelerance of hole #5, $h/b = 1.0$).

Figure 6.20: Theoretical and experimental accelerance from typical vertical eccentric test in Series R.

Figure 6.21: Theoretical and experimental accelerance from typical lateral test in Series R.
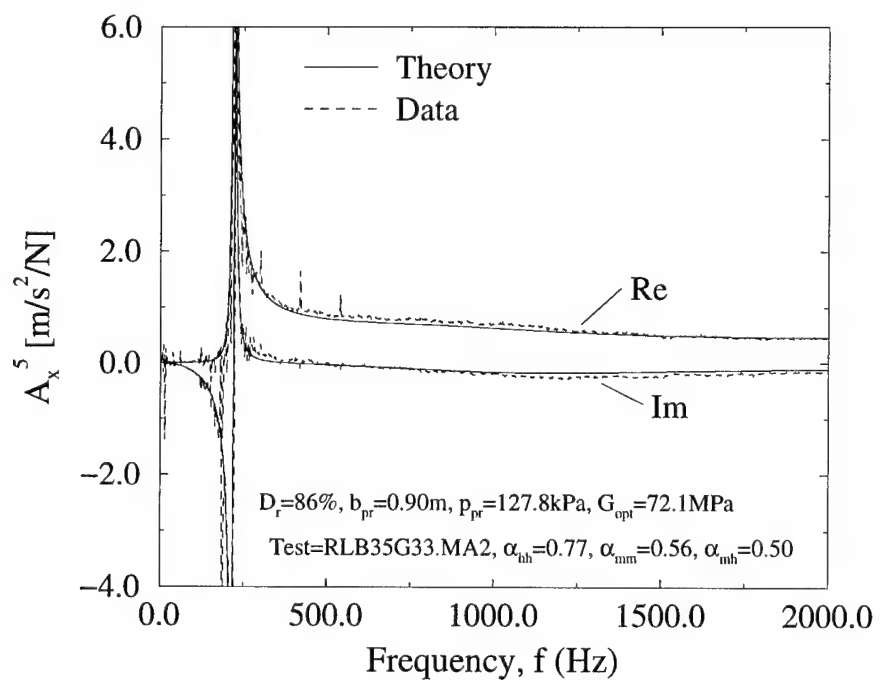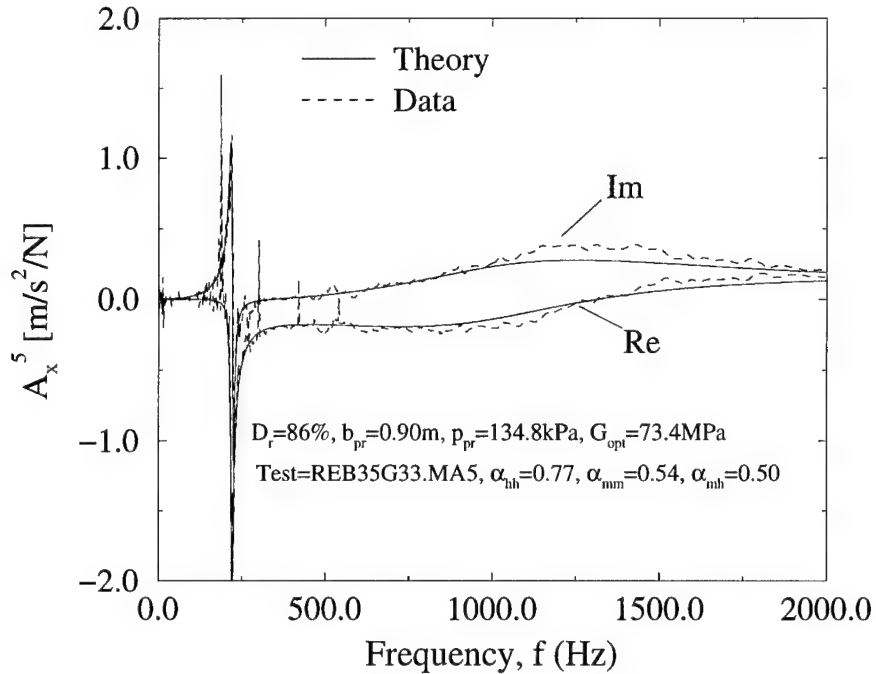
6.4.2.2 Series S ($h/b = 0.50$)

Series S contains results using the oil-filled dumpling for the vertical eccentric tests and Tri-Flow as a lubricant in the lateral tests. Series S was conducted at $h/b = 0.5$ on the same location as Series R. In contrast to the preceding tests which were discussed, the error function as defined in Equation (6.11) yielded a decisive trend in the best-fit α_{hh} for this shallow embedment depth. Figure 6.22 shows a contour plot of the error function which shows a definite minimum for the pinpointing of both α_{mm} and α_{hh}. Notice also that the normalized error is very small (≈ 1.5) compared to the error contours shown for Series N, O, and R (see Figures 6.11, 6.13, and 6.19 where the error of the best-fit curve is ≈ 400, ≈ 100, and ≈ 50 respectively). Table 6.12 contains the best-fit α_{mm} and α_{hh} for Series S, while Figures 6.23 and 6.24 show typical accelerance results for vertical eccentric and lateral loading respectively.

At this embedment depth, α_{mh} has very little affect on the accelerance. Statically, K_{mh} at $h/b = 0.5$ has about the same magnitude as K_{mh} for a surface footing (see Table 2.1), while K_{vv}, K_{hh}, and K_{mm} are larger at $h/b = 0.5$ than at the surface. Consequently, α_{mh} has less effect on accelerance at $h/b = 0.5$ than at $h/b = 0.0$ (see Figure 5.15). For this reason, α_{mh} was set to 1.00 as in Ashlock [1] for surface footings. Figure 6.25 shows the best-fit α_{hh} and α_{mm} pairs for each test with $\alpha_{mh} = 1.0$.

The average best-fit α_{hh} for these tests is 0.82 which is very close to the theoretical α_{hh} given in Table 3.3 from a comparison of the square-root and homogeneous shear modulus profiles. The static α_{hh} and α_{mh} predicted in Table 3.3 for an embedment depth of $h/b = 0.5$ are 0.74 and 0.39 respectively.

Filename	g-level	b_{pr}	p_{pr}	$G_{equivhomog}$	α_{mm}	α_{hh}	α_{mh}
SEB35G66.MAT	65.45	1.800	269.6	111.61	0.60	0.83	1.00
SEB35G66.MA2	65.45	1.800	269.6	111.61	0.67	0.80	1.00
SEB35G66.MA3	65.45	1.800	269.6	111.61	0.67	0.80	1.00
SEB35G55.MAT	54.55	1.500	224.7	102.15	0.61	0.84	1.00
SEB35G55.MA2	54.55	1.500	224.7	102.15	0.62	0.84	1.00
SEB35G55.MA3	54.55	1.500	224.7	103.00	0.62	0.82	1.00
SEB35G44.MA2	43.64	1.200	179.8	89.93	0.59	0.82	1.00
SEB35G44.MA3	43.64	1.200	179.8	89.93	0.59	0.84	1.00
SEB35G33.MA2	32.73	0.900	134.8	74.85	0.57	0.80	1.00
SEB35G33.MA3	32.73	0.900	134.8	74.85	0.59	0.81	1.00
SLB35G66.MAT	65.45	1.800	255.6	108.66	0.68	0.80	1.00
SLB35G66.MA2	65.45	1.800	255.6	108.66	0.70	0.81	1.00
SLB35G55.MAT	54.55	1.500	213.0	99.80	0.66	0.81	1.00
SLB35G55.MA2	54.55	1.500	213.0	99.80	0.68	0.80	1.00
SLB35G44.MAT	43.64	1.200	170.4	87.53	0.62	0.82	1.00
SLB35G44.MA2	43.64	1.200	170.4	87.53	0.65	0.79	1.00
SLB35G33.MAT	32.73	0.900	127.8	72.83	0.60	0.80	1.00
SLB35G33.MA2	32.73	0.900	127.8	72.83	0.61	0.82	1.00
SLB35G66.MA3	65.45	1.800	255.6	108.66	0.70	0.81	1.00
SLB35G55.MA3	54.55	1.500	213.0	99.80	0.69	0.80	1.00
SLB35G44.MA3	43.64	1.200	170.4	87.53	0.69	0.82	1.00
SLB35G33.MA3	32.73	0.900	127.8	72.83	0.61	0.84	1.00
SEB35G66.MA5	65.45	1.800	269.6	116.95	0.70	0.81	1.00
SEB35G66.MA6	65.45	1.800	269.6	116.95	0.71	0.83	1.00
SEB35G55.MA5	54.55	1.500	224.7	107.26	0.70	0.84	1.00
SEB35G44.MA5	43.64	1.200	179.8	93.92	0.65	0.84	1.00

Table 6.12: Table of results from Series S, $h/b = 0.5$.
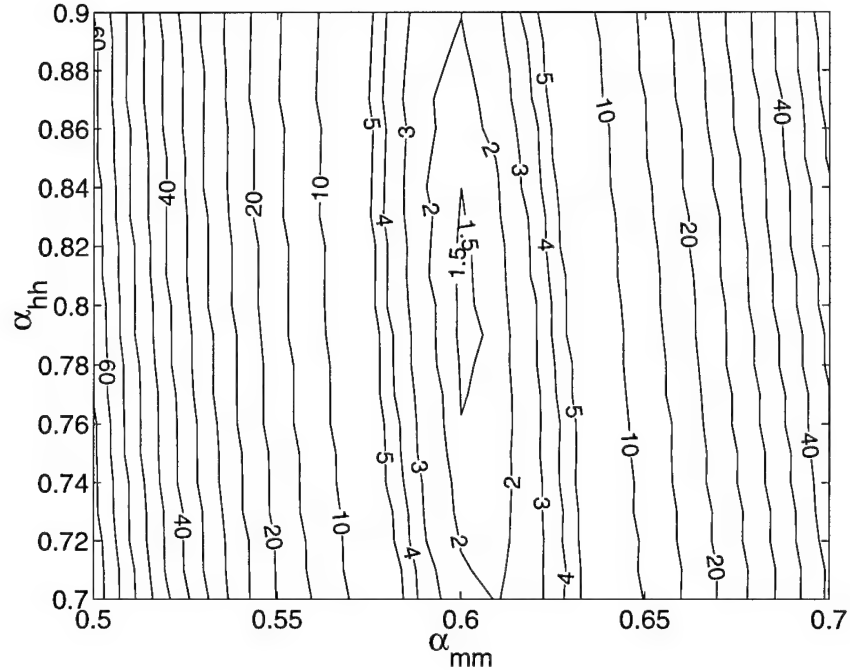
Figure 6.22: α_{mm} vs. α_{hh} error contour plot for accelerance at hole #5 from test SEB35G44.MA3 with $\alpha_{mh} = 1.00$, $h/b = 0.5$.
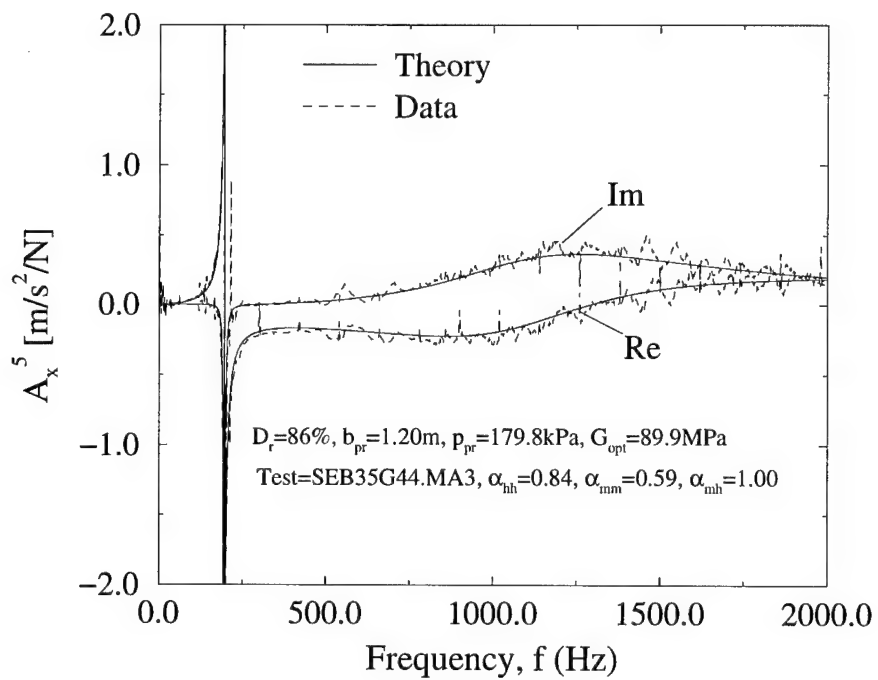
Figure 6.23: Theoretical and experimental accelerance from typical vertical eccentric test in Series S.
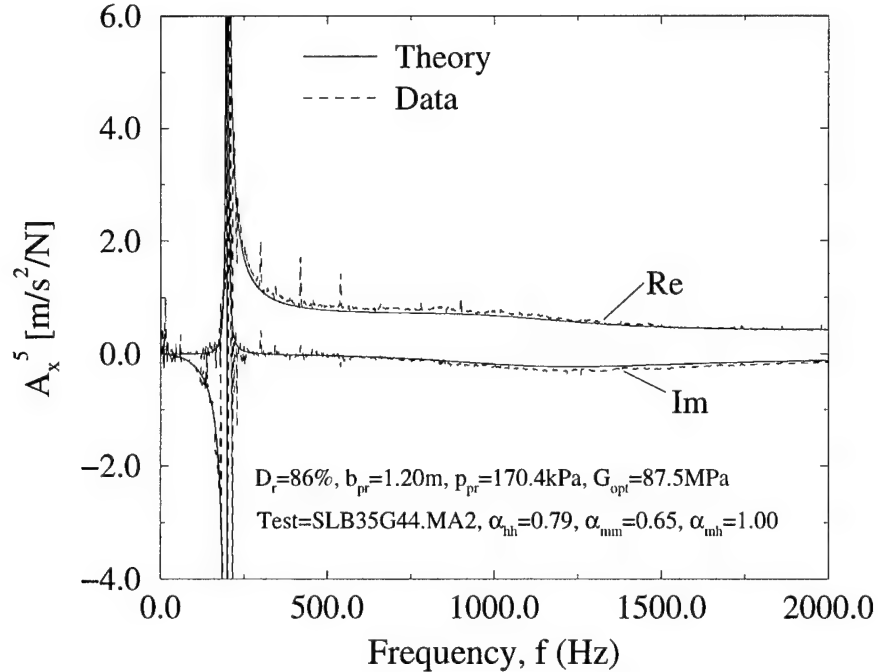
Figure 6.24: Theoretical and experimental accelerance from typical lateral test in Series S.
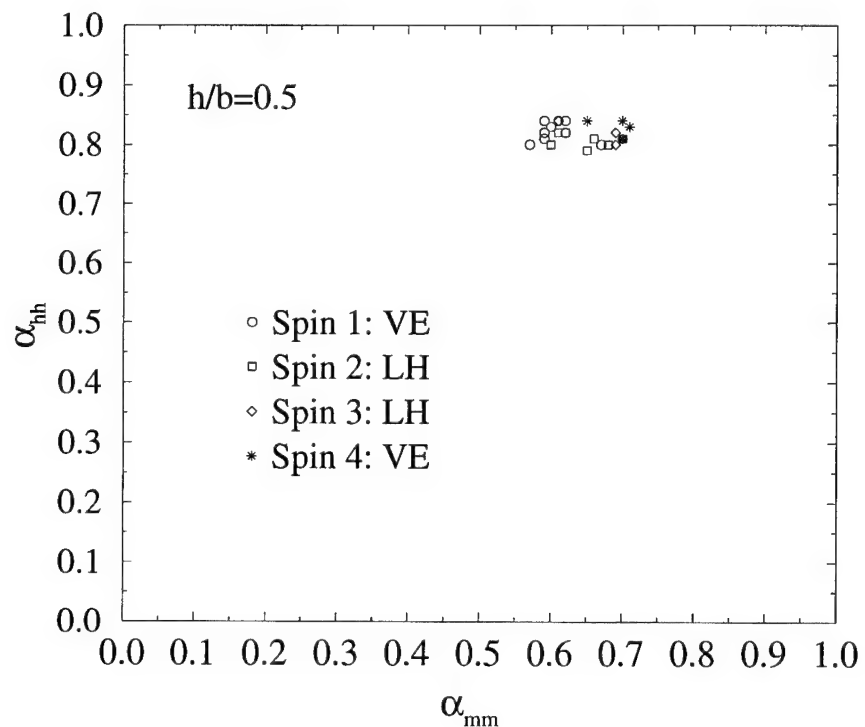
Figure 6.25: α_{hh} vs. α_{mm} for Series S ($\alpha_{mh} = 1.00$, $h/b = 0.50$).

6.4.2.3   Series T ($h/b = 0.25$)

Series T was conducted at $h/b = 0.25$ on the same location as Series R and S. Figure 6.13 contains tabular results for the best-fit G, α_{mm}, and α_{hh} from Series T. Figures 6.26 and 6.27 show typical accelerance matches from the vertical eccentric (button and dumpling) and lateral (button and Tri-Flow) tests respectively. Just as for $h/b = 0.5$ in Series S, the error as defined in Equation 6.11 provides an excellent accelerance match for both the vertical eccentric and lateral loading cases. Furthermore, there is not a great deal of scatter in the values of α_{mm} and α_{hh} in Figure 6.28, which shows the best-fit α_{mm} and α_{hh} pairs from each test in Series T.

In Series T, α_{mh} was set to 1.00. At this embedment depth, K_{mh} is very small across most of the frequency range of interest (see Figure 2.1 for the static value). Consequently, the accelerance shows very little dependence on α_{mh}. Since $h/b = 0.25$ is a very shallow embedment, α_{mh} was set to be 1.00 in order to be consistent with Ashlock [1] who set α_{mh} to 1.0 for surface tests.

Filename	g-level	b_{pr}	p_{pr}	$G_{equivhomog}$	α_{mm}	α_{hh}	α_{mh}
TEB35G66.MAT	65.45	1.800	269.6	116.05	0.69	0.84	1.00
TEB35G66.MA2	65.45	1.800	269.6	117.85	0.71	0.80	1.00
TEB35G55.MAT	54.55	1.500	224.7	106.40	0.69	0.78	1.00
TEB35G55.MA2	54.55	1.500	224.7	107.26	0.69	0.81	1.00
TEB35G44.MAT	43.64	1.200	179.8	93.92	0.70	0.82	1.00
TEB35G44.MA2	43.64	1.200	179.8	93.12	0.68	0.80	1.00
TEB35G33.MAT	32.73	0.900	134.8	75.57	0.71	0.81	1.00
TEB35G33.MA2	32.73	0.900	134.8	78.49	0.68	0.77	1.00
TEB35G55.MA3	54.55	1.500	224.7	107.26	0.74	0.80	1.00
TEB35G44.MA3	43.64	1.200	179.8	93.92	0.68	0.80	1.00
TEB35G33.MA3	32.73	0.900	134.8	78.49	0.69	0.79	1.00
TLB35G66.MAT	65.45	1.800	255.6	114.12	0.72	0.84	1.00
TLB35G66.MA2	65.45	1.800	255.6	114.12	0.71	0.84	1.00
TLB35G55.MAT	54.55	1.500	213.0	104.18	0.70	0.83	1.00
TLB35G55.MA2	54.55	1.500	213.0	104.18	0.69	0.82	1.00
TLB35G44.MAT	43.64	1.200	170.4	91.14	0.69	0.80	1.00
TLB35G44.MA2	43.64	1.200	170.4	91.14	0.70	0.83	1.00
TLB35G33.MAT	32.73	0.900	127.8	75.46	0.69	0.80	1.00
TLB35G33.MA2	32.73	0.900	127.8	75.46	0.69	0.84	1.00
TLB35G66.MA3	65.45	1.800	255.6	114.12	0.77	0.80	1.00
TLB35G55.MA3	54.55	1.500	213.0	104.18	0.71	0.85	1.00
TLB35G44.MA3	43.64	1.200	170.4	91.14	0.69	0.85	1.00
TLB35G33.MA3	32.73	0.900	127.8	75.46	0.69	0.84	1.00

Table 6.13: Table of results from Series T, $h/b = 0.25$.

Figure 6.26: Theoretical and experimental accelerance from typical vertical eccentric test in Series T.

Figure 6.27: Theoretical and experimental accelerance from typical lateral test in Series T.
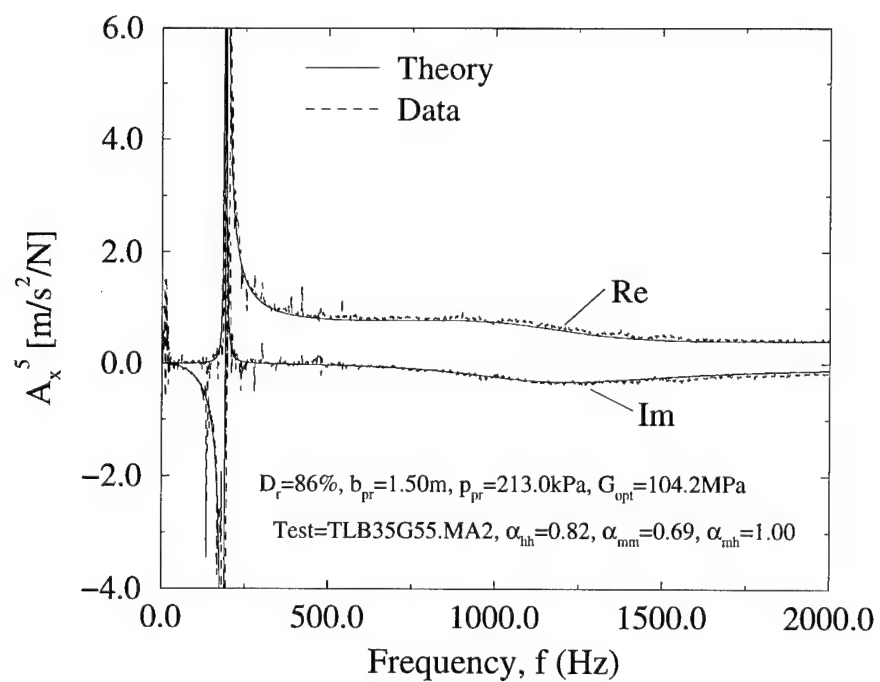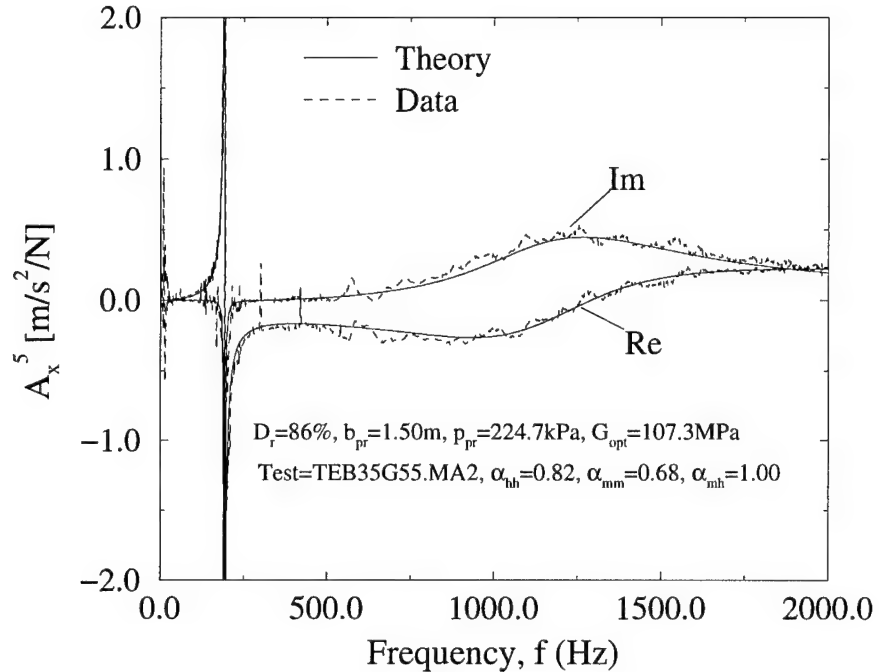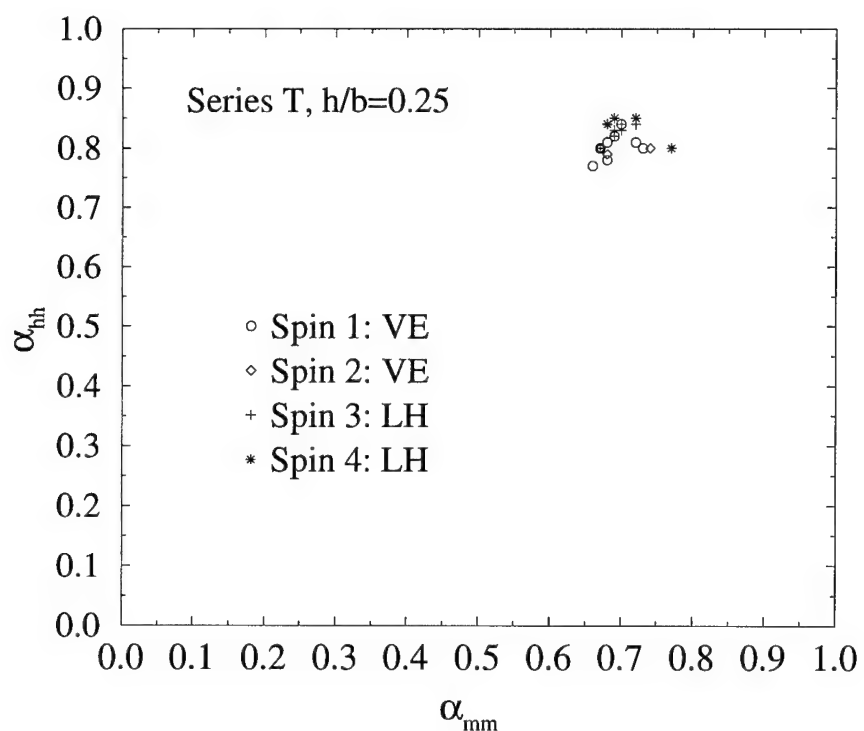
Figure 6.28: α_{hh} vs. α_{mm} for Series T $(\alpha_{mh}=1.00,\ h/b = 0.25)$.

6.4.2.4 Series U $(h/b = 0.00)$

Series U was conducted at $h/b = 0.0$ on two different locations on Sample #3, which are labeled "U1" and "U2." Tables 6.14 and 6.15 shows the tabular results from Series U, while Figures 6.29 and 6.30 show typical results from the vertical eccentric and lateral loading cases respectively. The best-fit shear moduli in Tables 6.14 and 6.15 are higher than those from Series G for $h/b = 0.0$. This is most likely due to the use of Sample #3 for many series of tests (Series N, O, P, Q, R, S, T, U) which may lead to a densification of the soil sample. Previous studies have shown that the scraping and vacuuming off of soil, as well as continued testing, tends to cause a slight densification of the soil and an increase in the best-fit shear modulus (see Guzina [12] and Ashlock [1]).

Figures 6.31 and 6.32 show the resulting α_{mm} and α_{hh} pairs from the two locations tested in Series U. Since the accelerance does not depend heavily on the exact value of α_{mh}, α_{mh} was set to 1.0 for the surface footing tests as in Ashlock [1]. The average α_{hh} from all of the tests in Series U is 0.84.

Figure 6.33 shows the change in the best-fit shear modulus with embedment depth from Series R to Series U. The data from these tests show support for a decreasing shear modulus with increasing embedment depth for shallow foundations. The results from Series B to Series G in Figure 6.5 show the general trend of a decreasing G with increasing embedment, although the trend is not nearly as uniform.

Filename	g-level	b_{pr}	p_{pr}	$G_{equivhomog}$	α_{mm}	α_{hh}	α_{mh}
UEB35G66.MAT	65.45	1.800	269.6	117.85	0.89	0.84	1.00
UEB35G66.MA2	65.45	1.800	269.6	118.75	0.90	0.85	1.00
UEB35G55.MAT	54.55	1.500	224.7	107.26	0.88	0.83	1.00
UEB35G55.MA2	54.55	1.500	224.7	108.12	0.88	0.85	1.00
UEB35G44.MAT	43.64	1.200	179.8	94.73	0.79	0.82	1.00
UEB35G44.MA2	43.64	1.200	179.8	94.73	0.79	0.84	1.00
UEB35G33.MAT	32.73	0.900	134.8	77.75	0.69	0.82	1.00
UEB35G33.MA2	32.73	0.900	134.8	79.97	0.71	0.81	1.00
UEB35G33.MA3	32.73	0.900	134.8	79.97	0.77	0.82	1.00
ULB35G66.MAT	65.45	1.800	255.6	115.19	0.80	0.90	1.00
ULB35G66.MA2	65.45	1.800	255.6	115.19	0.87	0.91	1.00
ULB35G55.MAT	54.55	1.500	213.0	104.87	0.79	0.80	1.00
ULB35G55.MA2	54.55	1.500	213.0	104.87	0.80	0.90	1.00
ULB35G44.MAT	43.64	1.200	170.4	92.21	0.77	0.80	1.00
ULB35G44.MA2	43.64	1.200	170.4	92.21	0.76	0.91	1.00
ULB35G33.MAT	32.73	0.900	127.8	77.21	0.70	0.85	1.00
ULB35G33.MA2	32.73	0.900	127.8	77.21	0.70	0.88	1.00
ULB35G66.MA3	65.45	1.800	255.6	115.19	0.90	0.90	1.00
ULB35G55.MA3	54.55	1.500	213.0	104.87	0.83	0.90	1.00
ULB35G44.MA3	43.64	1.200	170.4	92.21	0.80	0.90	1.00
ULB35G33.MA3	32.73	0.900	127.8	77.21	0.71	0.90	1.00

Table 6.14: Table of results from Series U1, $h/b = 0.0$.

Filename	g-level	b_{pr}	p_{pr}	$G_{equivhomog}$	α_{mm}	α_{hh}	α_{mh}
UEB35G66.MA3	65.45	1.800	269.6	122.41	0.87	0.80	1.00
UEB35G55.MA3	54.55	1.500	224.7	109.86	0.86	0.80	1.00
UEB35G44.MA3	43.64	1.200	179.8	95.54	0.81	0.81	1.00
UEB35G44.MA4	43.64	1.200	179.8	95.54	0.78	0.82	1.00
UEB35G33.MA4	32.73	0.900	134.8	80.71	0.77	0.77	1.00
UEB35G66.MA4	65.45	1.800	269.6	124.26	0.96	0.83	1.00
UEB35G66.MA5	65.45	1.800	269.6	124.26	0.90	0.83	1.00
UEB35G55.MA4	54.55	1.500	224.7	110.74	0.88	0.84	1.00
UEB35G55.MA5	54.55	1.500	224.7	110.74	0.89	0.83	1.00
UEB35G44.MA5	43.64	1.200	179.8	96.35	0.79	0.82	1.00
UEB35G44.MA6	43.64	1.200	179.8	96.35	0.81	0.82	1.00
UEB35G33.MA5	32.73	0.900	134.8	79.97	0.79	0.78	1.00
UEB35G33.MA6	32.73	0.900	134.8	81.46	0.78	0.79	1.00

Table 6.15: Table of results from Series U2, $h/b = 0.0$.
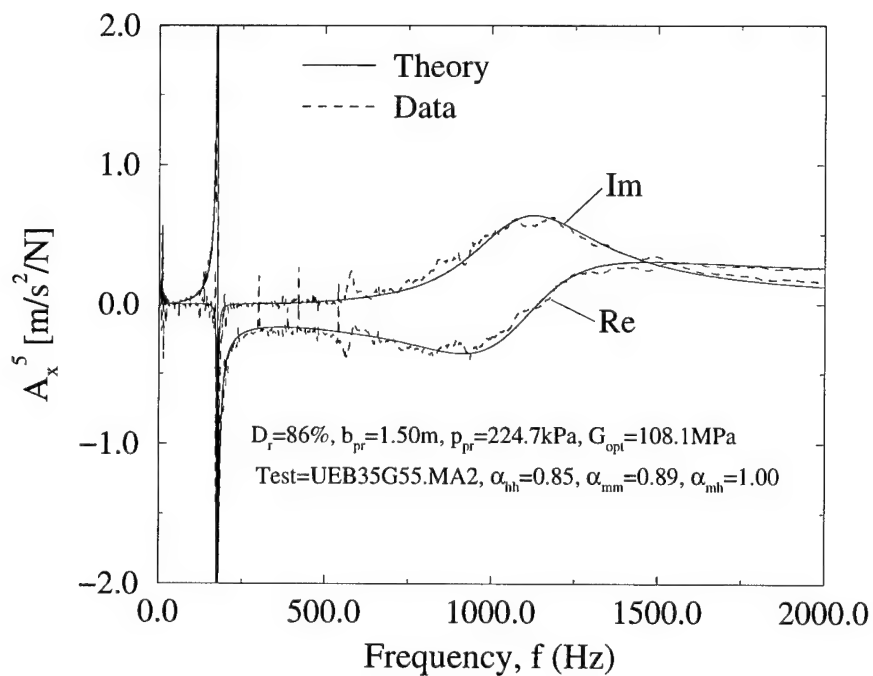
Figure 6.29: Theoretical and experimental accelerance from typical vertical eccentric test in Series U.
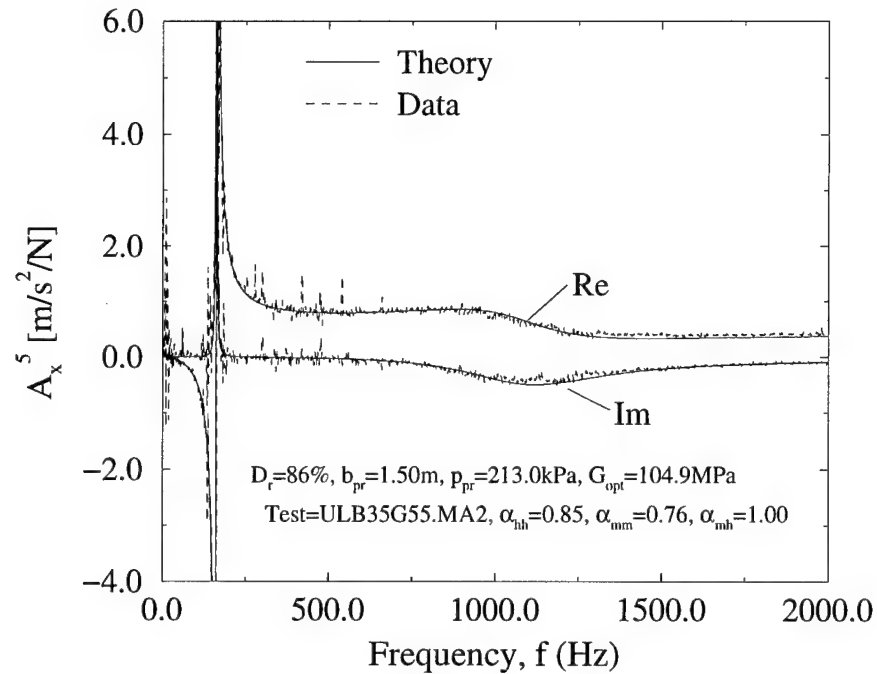
Figure 6.30: Theoretical and experimental accelerance from typical lateral test in Series U.
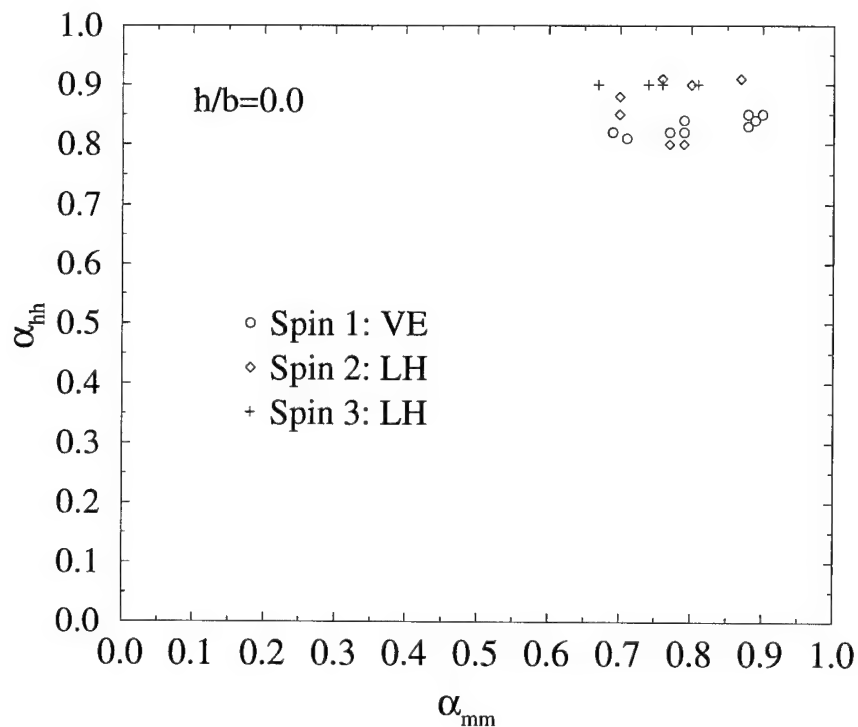
Figure 6.31: α_{hh} vs. α_{mm} for the first testing location in Series U ($\alpha_{mh}=1.00$, $h/b = 0.0$).
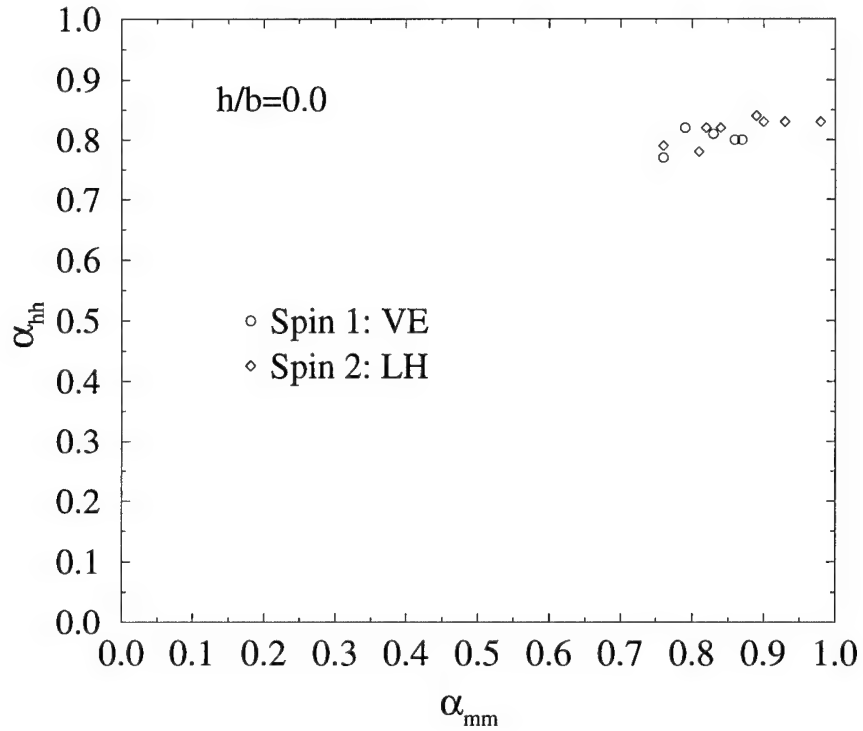
Figure 6.32: α_{hh} vs. α_{mm} for the second testing location in Series U (α_{mh}=1.00, $h/b = 0.0$).
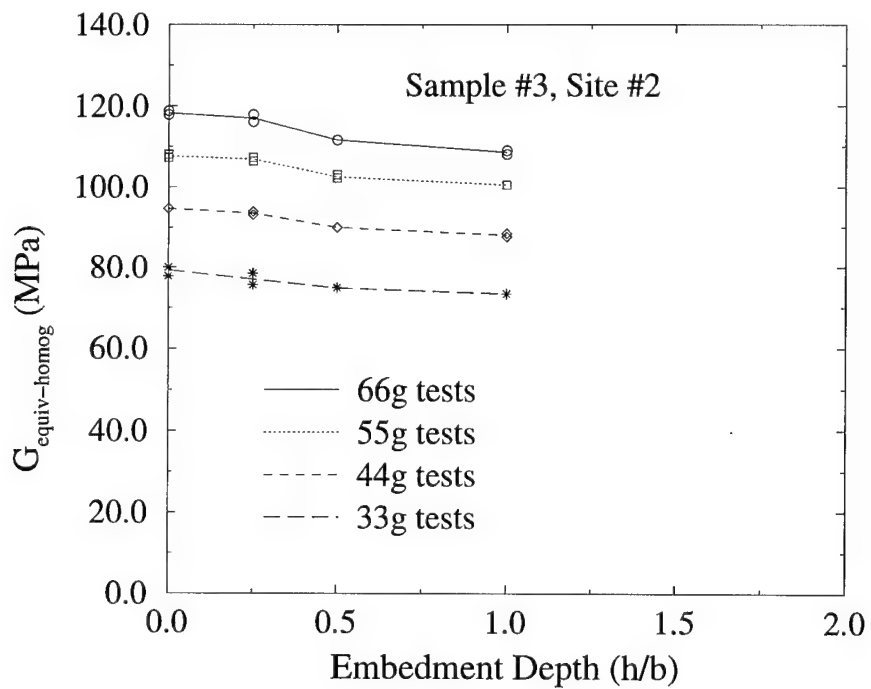
Figure 6.33: Change in best-fit equivalent homogeneous shear modulus with embedment depth (Series R, S, T, U).

6.5 Summary of Results for Accelerance Matching to Homogeneous Half-Space Solution

Table 6.16 contains the best-fit α_{ij} discussed so far for each embedment depth. The α_{hh} and α_{mh} for embedment depths of $h/b = 2.00$, 1.50, and 1.00 are from Table 3.3 which compares the square-root profile to the homogeneous half-space. All of the α_{mm} and the α_{hh} for embedment depths of $h/b = 0.50$, 0.25,

h/b	Series	α_{mm}	α_{hh}	α_{mh}
0.00	U	$0.81^{a,b}$	0.84^b	1.00^d
0.25	T	$0.70^{a,b}$	0.82^b	1.00^d
0.50	S	$0.65^{a,b}$	0.82^b	1.00^d
1.00	R	0.58^b	0.77^c	0.50^c
1.50	O	0.60^b	0.79^c	0.53^c
2.00	N	0.53^b	0.80^c	0.55^c

Table 6.16: Summary table of the best-fit α_{ij} ([a]signifies g-level dependence, [b]signifies average value, [c]signifies a specified value based on theoretical analysis, [d]signifies setting α_{mh} to 1.0 since the accelerance is not sensitive to a specific value).

and 0.00 are averages from the least squares fit conducted on each individual test. For embedment depths of $h/b = 0.50$, 0.25, and 0.00, α_{mh} was set to 1.00 since the accelerance is not sensitive to the specific value of K_{mh}. Table 6.16 reveals that the best-fit α_{mm} decreases with increasing embedment for every test series except Series R, while the best-fit α_{hh} is fairly constant for embedment depths of 0.00, 0.25, and 0.50. Results from Ashlock [1] showed that the average best-fit α_{mm} and α_{hh} from surface footing tests are 0.78 and 0.85 respectively with $\alpha_{mh} = 1.00$, which correspond very well to the α_{mm} and α_{hh} of 0.81 and 0.84 for tests on surface footings in this investigation for $\alpha_{mh}=1.00$. Although the α_{ij} values as a function of h/b given in Table 3.3 have been used in the data analysis so far, some

simplifications can be made to reflect the findings of this investigation.

6.5.1 Summary of Best-Fit α_{ij}

For Series N, O, and R with embedment depths of 2.0, 1.5, and 1.0 respectively, the quality of the accelerance match is insensitive to the precise values of α_{hh} and α_{mh} as shown in the error surface plots in Figures 6.11, 6.13, and 6.19. While keeping in mind that there are still three parameters which can be varied to obtain an acceptable accelerance match (i.e. α_{mm}, α_{hh}, α_{mh}), the values of α_{hh} and α_{mh} can be set to specified values for practical purposes. Additionally, it was shown that the accelerance at $h/b = 0.0$ to 0.50 is very insensitive to the precise value of α_{mh} both by Ashlock [1] and in this study (see Figure 5.15 and Table 2.1). Consequently, α_{mh} can be chosen to be 0.60 for all embedment depths which is an approximate mean value from Figure 3.31 which contains the α_{ij} as a function of embedment depth for a comparison of a square-root half-space and a homogeneous half-space. To illustrate the feasibility of such an approach, Figure 6.34 contains typical accelerance results with $\alpha_{hh} = 0.80$ and $\alpha_{mh} = 0.60$ from vertical eccentric loading in Series N, O, and R, while Figure 6.35 contains typical accelerance matches from Series S, T, and U with $\alpha_{mh}=0.60$. In addition, for Series S, T, and U, α_{hh} has been set to a specified value at each embedment depth which roughly corresponds to the best-fit α_{hh} given in Table 6.16. The resulting α_{ij} are shown in Table 6.17. One can see that the best-fit α_{mm} have changed slightly from Table 6.16 since α_{mh} and α_{hh} are specified. Tables 6.18 to 6.25 show the best-fit α_{ij} from each individual test in Series U to Series N.
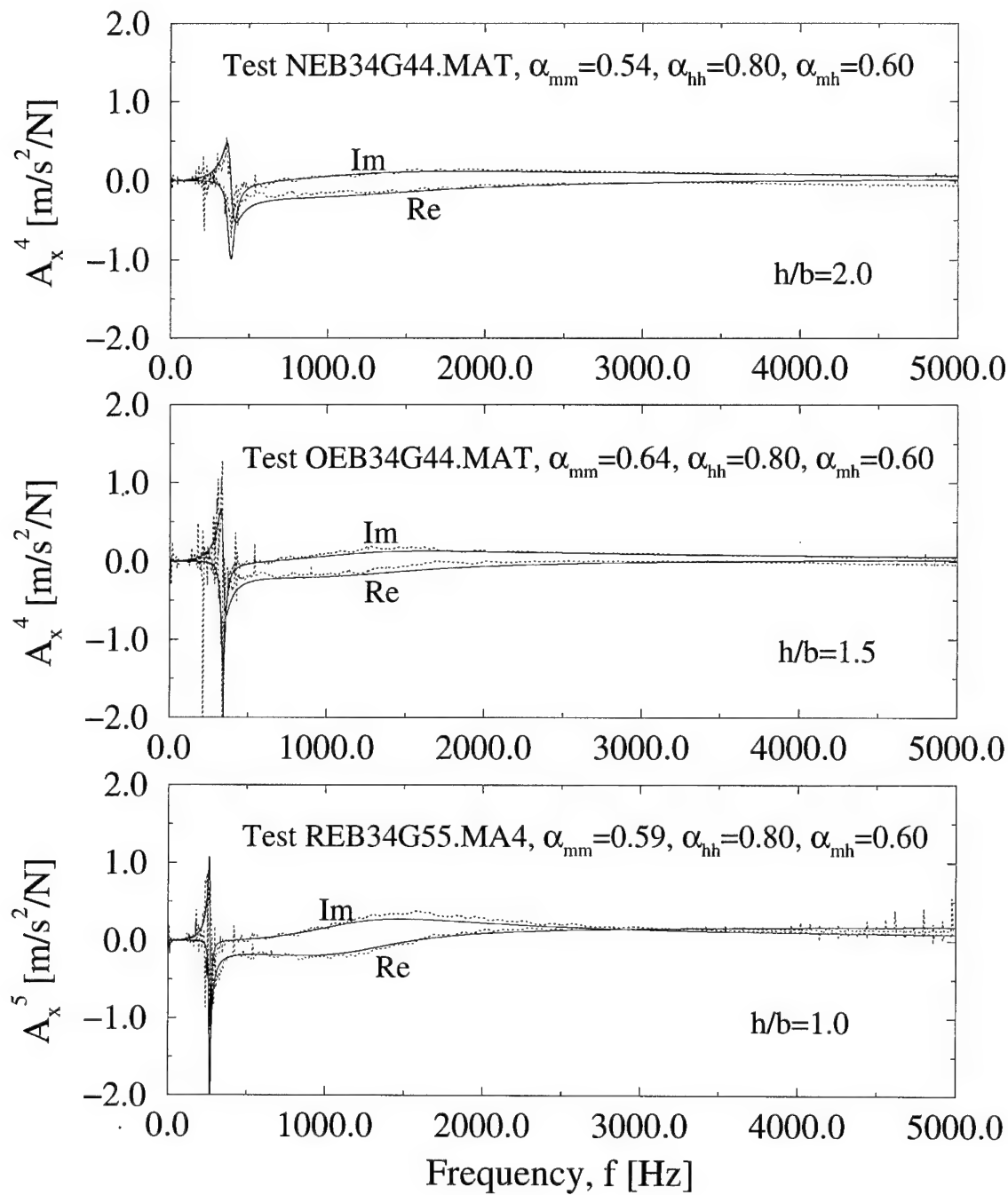
Figure 6.34: Typical accelerance match with homogeneous half-space impedances for Series N, R, and O, with α_{hh} and α_{mh} specified in Table 6.17.
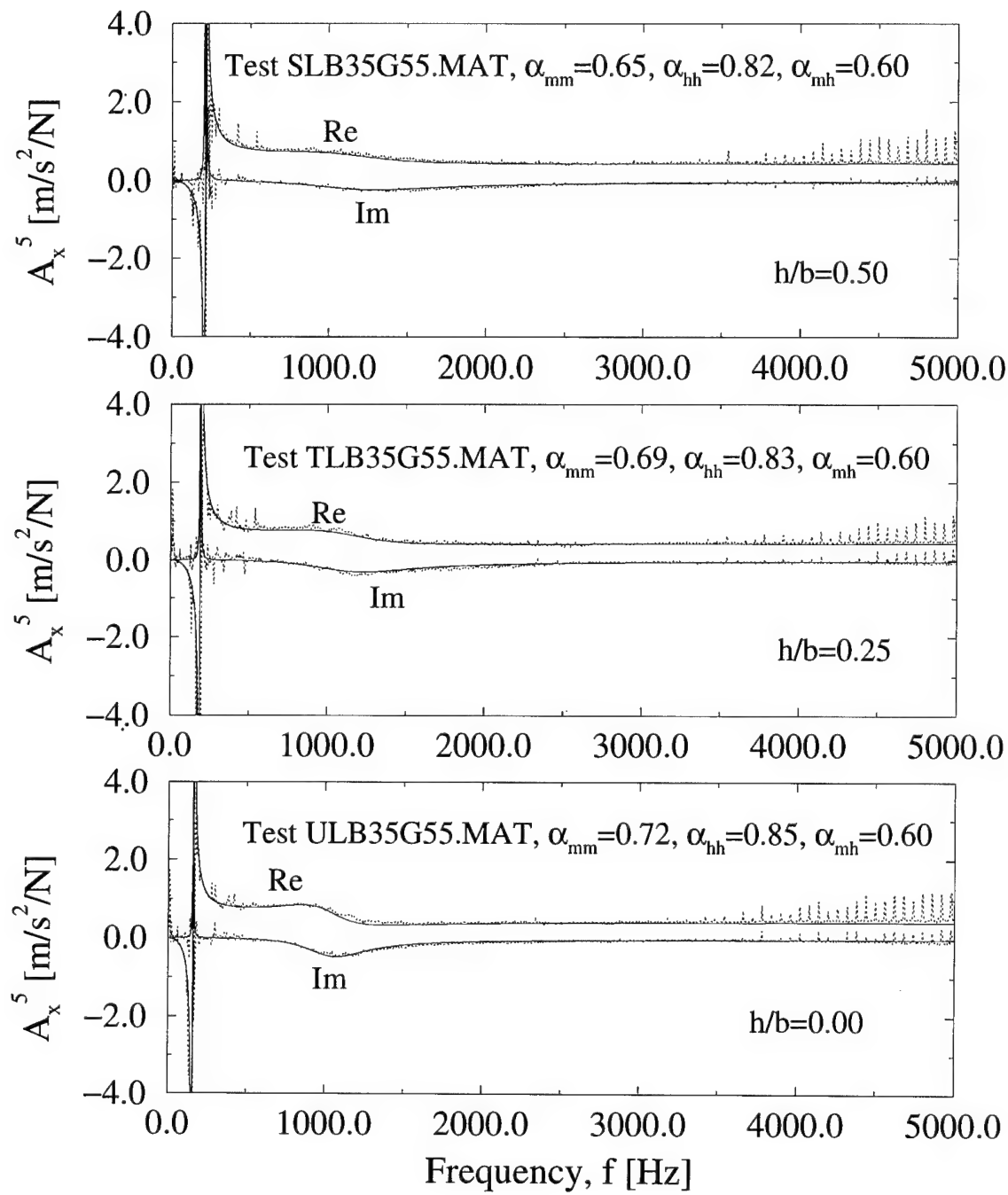
Figure 6.35: Typical accelerance match with homogeneous half-space impedances for Series S, T, and U, with α_{hh} and α_{mh} specified in Table 6.17.

h/b	Series	α_{mm}	α_{hh}	α_{mh}
0.00	U	0.76	0.85	0.60
0.25	T	0.69	0.83	0.60
0.50	S	0.66	0.82	0.60
1.00	R	0.58	0.80	0.60
1.50	O	0.60	0.80	0.60
2.00	N	0.53	0.80	0.60

Table 6.17: Average α_{mm} in Series N, O, and R, for α_{hh}=0.80 and α_{mh}=0.60.

Filename	g-level	b_{pr}	p_{pr}	$G_{equivhomog}$	α_{mm}	α_{hh}	α_{mh}
UEB35G66.MAT	65.45	1.800	269.6	117.85	0.85	0.85	0.60
UEB35G66.MA2	65.45	1.800	269.6	118.75	0.88	0.85	0.60
UEB35G55.MAT	54.55	1.500	224.7	107.26	0.84	0.85	0.60
UEB35G55.MA2	54.55	1.500	224.7	108.12	0.85	0.85	0.60
UEB35G44.MAT	43.64	1.200	179.8	94.73	0.75	0.85	0.60
UEB35G44.MA2	43.64	1.200	179.8	94.73	0.75	0.85	0.60
UEB35G33.MAT	32.73	0.900	134.8	77.75	0.64	0.85	0.60
UEB35G33.MA2	32.73	0.900	134.8	79.97	0.69	0.85	0.60
UEB35G33.MA3	32.73	0.900	134.8	79.97	0.70	0.85	0.60
ULB35G66.MAT	65.45	1.800	255.6	115.19	0.76	0.85	0.60
ULB35G66.MA2	65.45	1.800	255.6	115.19	0.79	0.85	0.60
ULB35G55.MAT	54.55	1.500	213.0	104.87	0.72	0.85	0.60
ULB35G55.MA2	54.55	1.500	213.0	104.87	0.74	0.85	0.60
ULB35G44.MAT	43.64	1.200	170.4	92.21	0.72	0.85	0.60
ULB35G44.MA2	43.64	1.200	170.4	92.21	0.70	0.85	0.60
ULB35G33.MAT	32.73	0.900	127.8	77.21	0.66	0.85	0.60
ULB35G33.MA2	32.73	0.900	127.8	77.21	0.64	0.85	0.60
ULB35G66.MA3	65.45	1.800	255.6	115.19	0.79	0.85	0.60
ULB35G55.MA3	54.55	1.500	213.0	104.87	0.74	0.85	0.60
ULB35G44.MA3	43.64	1.200	170.4	92.21	0.71	0.85	0.60
ULB35G33.MA3	32.73	0.900	127.8	77.21	0.64	0.85	0.60

Table 6.18: Table of results from Series U ($h/b = 0.00$) for $\alpha_{hh} = 0.85$ and $\alpha_{mh} = 0.60$.

Filename	g-level	b_{pr}	p_{pr}	$G_{equivhomog}$	α_{mm}	α_{hh}	α_{mh}
UEB35G66.MA3	65.45	1.800	269.6	122.41	0.82	0.85	0.60
UEB35G55.MA3	54.55	1.500	224.7	109.86	0.81	0.85	0.60
UEB35G44.MA3	43.64	1.200	179.8	95.54	0.79	0.85	0.60
UEB35G44.MA4	43.64	1.200	179.8	95.54	0.75	0.85	0.60
UEB35G33.MA4	32.73	0.900	134.8	80.71	0.71	0.85	0.60
UEB35G66.MA4	65.45	1.800	269.6	124.26	0.93	0.85	0.60
UEB35G66.MA5	65.45	1.800	269.6	124.26	0.88	0.85	0.60
UEB35G55.MA4	54.55	1.500	224.7	110.74	0.85	0.85	0.60
UEB35G55.MA5	54.55	1.500	224.7	110.74	0.85	0.85	0.60
UEB35G44.MA5	43.64	1.200	179.8	96.35	0.77	0.85	0.60
UEB35G44.MA6	43.64	1.200	179.8	96.35	0.79	0.85	0.60
UEB35G33.MA5	32.73	0.900	134.8	79.97	0.76	0.85	0.60
UEB35G33.MA6	32.73	0.900	134.8	81.46	0.71	0.85	0.60

Table 6.19: Table of results from Series U2 ($h/b = 0.00$) for $\alpha_{hh} = 0.85$ and $\alpha_{mh} = 0.60$.

Filename	g-level	b_{pr}	p_{pr}	$G_{equivhomog}$	α_{mm}	α_{hh}	α_{mh}
TEB35G66.MAT	65.45	1.800	269.6	116.05	0.70	0.83	0.60
TEB35G66.MA2	65.45	1.800	269.6	117.85	0.72	0.83	0.60
TEB35G55.MAT	54.55	1.500	224.7	106.40	0.67	0.83	0.60
TEB35G55.MA2	54.55	1.500	224.7	107.26	0.67	0.83	0.60
TEB35G44.MAT	43.64	1.200	179.8	93.92	0.68	0.83	0.60
TEB35G44.MA2	43.64	1.200	179.8	93.12	0.66	0.83	0.60
TEB35G33.MAT	32.73	0.900	134.8	75.57	0.71	0.83	0.60
TEB35G33.MA2	32.73	0.900	134.8	78.49	0.65	0.83	0.60
TEB35G66.MA3	65.45	1.800	269.6	117.85	0.76	0.83	0.60
TEB35G55.MA3	54.55	1.500	224.7	107.26	0.73	0.83	0.60
TEB35G44.MA3	43.64	1.200	179.8	93.92	0.66	0.83	0.60
TEB35G33.MA3	32.73	0.900	134.8	78.49	0.67	0.83	0.60
TLB35G66.MAT	65.45	1.800	255.6	114.12	0.72	0.83	0.60
TLB35G66.MA2	65.45	1.800	255.6	114.12	0.71	0.83	0.60
TLB35G55.MAT	54.55	1.500	213.0	104.18	0.69	0.83	0.60
TLB35G55.MA2	54.55	1.500	213.0	104.18	0.69	0.83	0.60
TLB35G44.MAT	43.64	1.200	170.4	91.14	0.66	0.83	0.60
TLB35G44.MA2	43.64	1.200	170.4	91.14	0.69	0.83	0.60
TLB35G33.MAT	32.73	0.900	127.8	75.46	0.67	0.83	0.60
TLB35G33.MA2	32.73	0.900	127.8	75.46	0.67	0.83	0.60
TLB35G66.MA3	65.45	1.800	255.6	114.12	0.75	0.83	0.60
TLB35G55.MA3	54.55	1.500	213.0	104.18	0.72	0.83	0.60
TLB35G44.MA3	43.64	1.200	170.4	91.14	0.69	0.83	0.60
TLB35G33.MA3	32.73	0.900	127.8	75.46	0.67	0.83	0.60

Table 6.20: Table of results from Series T ($h/b = 0.25$) for $\alpha_{hh} = 0.83$ and $\alpha_{mh} = 0.60$.

Filename	g-level	b_{pr}	p_{pr}	$G_{equivhomog}$	α_{mm}	α_{hh}	α_{mh}
SEB35G66.MAT	65.45	1.800	269.6	111.61	0.61	0.82	0.60
SEB35G66.MA2	65.45	1.800	269.6	111.61	0.67	0.82	0.60
SEB35G66.MA3	65.45	1.800	269.6	111.61	0.67	0.82	0.60
SEB35G55.MAT	54.55	1.500	224.7	102.15	0.63	0.82	0.60
SEB35G55.MA2	54.55	1.500	224.7	102.15	0.64	0.82	0.60
SEB35G55.MA3	54.55	1.500	224.7	103.00	0.64	0.82	0.60
SEB35G44.MA2	43.64	1.200	179.8	89.93	0.61	0.82	0.60
SEB35G44.MA3	43.64	1.200	179.8	89.93	0.60	0.82	0.60
SEB35G33.MA2	32.73	0.900	134.8	74.85	0.57	0.82	0.60
SEB35G33.MA3	32.73	0.900	134.8	74.85	0.59	0.82	0.60
SLB35G66.MAT	65.45	1.800	255.6	108.66	0.67	0.82	0.60
SLB35G66.MA2	65.45	1.800	255.6	108.66	0.71	0.82	0.60
SLB35G55.MAT	54.55	1.500	213.0	99.80	0.65	0.82	0.60
SLB35G55.MA2	54.55	1.500	213.0	99.80	0.68	0.82	0.60
SLB35G44.MAT	43.64	1.200	170.4	87.53	0.64	0.82	0.60
SLB35G44.MA2	43.64	1.200	170.4	87.53	0.65	0.82	0.60
SLB35G33.MAT	32.73	0.900	127.8	72.83	0.60	0.82	0.60
SLB35G33.MA2	32.73	0.900	127.8	72.83	0.62	0.82	0.60
SLB35G66.MA3	65.45	1.800	255.6	108.66	0.71	0.82	0.60
SLB35G55.MA3	54.55	1.500	213.0	99.80	0.69	0.82	0.60
SLB35G44.MA3	43.64	1.200	170.4	87.53	0.70	0.82	0.60
SLB35G33.MA3	32.73	0.900	127.8	72.83	0.62	0.82	0.60
SEB35G66.MA5	65.45	1.800	269.6	116.95	0.71	0.82	0.60
SEB35G66.MA6	65.45	1.800	269.6	116.95	0.73	0.82	0.60
SEB35G55.MA5	54.55	1.500	224.7	107.26	0.72	0.82	0.60
SEB35G44.MA5	43.64	1.200	179.8	93.92	0.65	0.82	0.60

Table 6.21: Table of results from Series S ($h/b = 0.50$) for $\alpha_{hh} = 0.82$ and $\alpha_{mh} = 0.60$.

Filename	g-level	b_{pr}	p_{pr}	$G_{equivhomog}$	α_{mm}	α_{hh}	α_{mh}
RLB35G66.MAT	65.45	1.800	255.6	106.13	0.59	0.80	0.60
RLB35G66.MA2	65.45	1.800	255.6	106.13	0.59	0.80	0.60
RLB35G55.MAT	54.55	1.500	213.0	98.63	0.54	0.80	0.60
RLB35G55.MA2	54.55	1.500	213.0	98.63	0.59	0.80	0.60
RLB35G55.MA3	54.55	1.500	213.0	98.63	0.55	0.80	0.60
RLB35G44.MAT	43.64	1.200	170.4	86.07	0.54	0.80	0.60
RLB35G44.MA2	43.64	1.200	170.4	86.07	0.56	0.80	0.60
RLB35G33.MAT	32.73	0.900	127.8	72.15	0.55	0.80	0.60
RLB35G33.MA2	32.73	0.900	127.8	72.15	0.56	0.80	0.60
REB35G66.MA4	65.45	1.800	269.6	108.12	0.63	0.80	0.60
REB35G66.MA5	65.45	1.800	269.6	108.99	0.63	0.80	0.60
REB35G55.MA4	54.55	1.500	224.7	100.48	0.59	0.80	0.60
REB35G55.MA5	54.55	1.500	224.7	100.48	0.60	0.80	0.60
REB35G44.MA4	43.64	1.200	179.8	88.36	0.58	0.80	0.60
REB35G44.MA5	43.64	1.200	179.8	87.58	0.59	0.80	0.60
REB35G33.MA4	32.73	0.900	134.8	73.41	0.55	0.80	0.60
REB35G33.MA5	32.73	0.900	134.8	73.41	0.55	0.80	0.60
REB35G66.MA6	65.45	1.800	269.6	109.86	0.58	0.80	0.60
REB35G55.MA6	54.55	1.500	224.7	103.00	0.61	0.80	0.60
REB35G44.MA6	43.64	1.200	179.8	89.15	0.61	0.80	0.60
REB35G33.MA6	32.73	0.900	134.8	75.57	0.53	0.80	0.60

Table 6.22: Table of results from Series R ($h/b = 1.00$) for $\alpha_{hh} = 0.80$ and $\alpha_{mh} = 0.60$.

Filename	g-level	b_{pr}	p_{pr}	$G_{equivhomog}$	α_{mm}	α_{hh}	α_{mh}
OEB34G66.MAT	65.45	1.800	269.6	117.85	0.58	0.80	0.60
OEB34G66.MA2	65.45	1.800	269.6	117.85	0.57	0.80	0.60
OEB34G55.MAT	54.55	1.500	224.7	110.74	0.57	0.80	0.60
OEB34G55.MA2	54.55	1.500	224.7	110.74	0.61	0.80	0.60
OEB34G44.MAT	43.64	1.200	179.8	97.17	0.64	0.80	0.60
OEB34G44.MA2	43.64	1.200	179.8	96.35	0.66	0.80	0.60
OEB34G33.MAT	32.73	0.900	134.8	81.46	0.58	0.80	0.60
OEB34G33.MA2	32.73	0.900	134.8	80.71	0.59	0.80	0.60
OLB34G66.MAT	65.45	1.800	255.6	114.70	0.59	0.80	0.60
OLB34G66.MA2	65.45	1.800	255.6	114.70	0.58	0.80	0.60
OLB34G55.MAT	54.55	1.500	213.0	107.79	0.60	0.80	0.60
OLB34G55.MA2	54.55	1.500	213.0	107.79	0.61	0.80	0.60
OLB34G44.MAT	43.64	1.200	170.4	94.25	0.55	0.80	0.60
OLB34G44.MA2	43.64	1.200	170.4	94.25	0.59	0.80	0.60
OLB34G33.MAT	32.73	0.900	127.8	78.97	0.63	0.80	0.60
OLB34G33.MA2	32.73	0.900	127.8	78.97	0.57	0.80	0.60

Table 6.23: Table of results from Series O ($h/b = 1.50$) for $\alpha_{hh} = 0.80$ and $\alpha_{mh} = 0.60$.

Filename	g-level	b_{pr}	p_{pr}	$G_{equivhomog}$	α_{mm}	α_{hh}	α_{mh}
NEB34G66.MAT	65.45	1.800	269.6	113.38	0.54	0.80	0.60
NEB34G66.MA2	65.45	1.800	269.6	112.49	0.54	0.80	0.60
NEB34G55.MAT	54.55	1.500	224.7	108.12	0.52	0.80	0.60
NEB34G55.MA2	54.55	1.500	224.7	106.40	0.57	0.80	0.60
NEB34G44.MAT	43.64	1.200	179.8	96.35	0.54	0.80	0.60
NEB34G44.MA2	43.64	1.200	179.8	96.35	0.55	0.80	0.60
NEB34G44.MA3	43.64	1.200	179.8	94.73	0.56	0.80	0.60
NEB34G33.MAT	32.73	0.900	134.8	81.46	0.52	0.80	0.60
NEB34G33.MA2	32.73	0.900	134.8	79.23	0.51	0.80	0.60
NEB34G33.MA3	32.73	0.900	134.8	78.49	0.50	0.80	0.60
NEB34G33.MA4	32.73	0.900	134.8	79.23	0.52	0.80	0.60
NLB34G66.MA8	65.45	1.800	255.6	110.03	0.58	0.80	0.60
NLB34G66.MA9	65.45	1.800	255.6	110.03	0.50	0.80	0.60
NLB34G66.M10	65.45	1.800	255.6	110.03	0.56	0.80	0.60
NLB34G55.MA2	54.55	1.500	213.0	104.48	0.56	0.80	0.60
NLB34G55.MA3	54.55	1.500	213.0	104.48	0.56	0.80	0.60
NLB34G44.MA2	43.64	1.200	170.4	93.28	0.58	0.80	0.60
NLB34G44.MA3	43.64	1.200	170.4	93.28	0.56	0.80	0.60
NLB34G44.MA4	43.64	1.200	170.4	93.28	0.56	0.80	0.60
NLB34G33.MA2	32.73	0.900	127.8	77.50	0.50	0.80	0.60
NLB34G33.MA3	32.73	0.900	127.8	77.50	0.51	0.80	0.60
NLB34G33.MA4	32.73	0.900	127.8	77.50	0.51	0.80	0.60

Table 6.24: Table of results from Series N (h/b = 2.00) for α_{hh} = 0.80 and α_{mh} = 0.60.

Filename	g-level	b_{pr}	p_{pr}	$G_{equivhomog}$	α_{mm}	α_{hh}	α_{mh}
NEB34G66.MA3	65.45	1.800	269.6	118.75	0.50	0.80	0.60
NEB34G66.MA4	65.45	1.800	269.6	119.66	0.52	0.80	0.60
NEB34G66.MA5	65.45	1.800	255.6	118.75	0.53	0.80	0.60
NEB34G66.MA6	65.45	1.800	269.6	119.66	0.51	0.80	0.60
NEB34G66.MA7	65.45	1.800	269.6	119.66	0.51	0.80	0.60
NEB34G55.MA5	54.55	1.500	213.0	111.61	0.53	0.80	0.60
NEB34G55.MA6	54.55	1.500	224.7	111.61	0.54	0.80	0.60
NEB34G55.MA7	54.55	1.500	224.7	112.49	0.52	0.80	0.60
NEB34G55.MA8	54.55	1.500	224.7	112.49	0.52	0.80	0.60
NEB34G55.MA9	54.55	1.500	224.7	111.61	0.54	0.80	0.60
NEB34G44.MA4	43.64	1.200	179.8	102.15	0.54	0.80	0.60
NEB34G44.MA5	43.64	1.200	179.8	99.65	0.54	0.80	0.60
NEB34G33.MA5	32.73	0.900	134.8	83.73	0.50	0.80	0.60
NEB34G33.MA6	32.73	0.900	134.8	83.73	0.50	0.80	0.60
NLB34G66.M11	65.45	1.800	255.6	116.35	0.51	0.80	0.60
NLB34G55.MA4	54.55	1.500	213.0	109.54	0.53	0.80	0.60
NLB34G44.MA5	43.64	1.200	170.4	98.24	0.56	0.80	0.60
NLB34G33.MA5	32.73	0.900	127.8	81.50	0.50	0.80	0.60

Table 6.25: Table of results from Series N ($h/b = 2.00$) for $\alpha_{hh} = 0.80$ and $\alpha_{mh} = 0.60$.

6.5.2   Best-Fit α_{mm} versus g-level

Figures 6.36 to 6.41 show the resulting α_{mm} from Series U to Series N (for a constant α_{mh} and the specified variation of α_{hh} in Table 6.17) plotted versus the centrifuge g-level. It is important to note that a specific centrifuge g-level also corresponds to a particular prototype footing half-width (b_{pr}) and average contact pressure (p_{pr}) since the same footing was used in all tests. All of the figures show that there is no distinguishable difference between the α_{mm} produced from lateral tests and the α_{mm} produced by vertical eccentric tests. One would expect that this would be the case in the absence of any differences in the response caused by the the two distinct methods of applying vertical or horizontal loads. One such problem was the transverse force caused by friction between the stinger and the exciter which was reduced by the use of the hemispherical button with the oil-filled dumpling in the vertical eccentric case and Tri-Flow in the lateral case. Furthermore, one can see from Figures 6.39, 6.40, and 6.41 that α_{mm} is fairly constant with g-level at embedment depths of $h/b = 1.0$, 1.5, and 2.0 respectively. On the other hand, Figures 6.36, 6.37, and 6.38 show that α_{mm} decreases with decreasing g-level at embedment depths of $h/b = 0.0, 0.25$, and 0.50. The decrease in α_{mm} with decreasing g-level is consistent with Ashlock's [1] observation for surface footings.
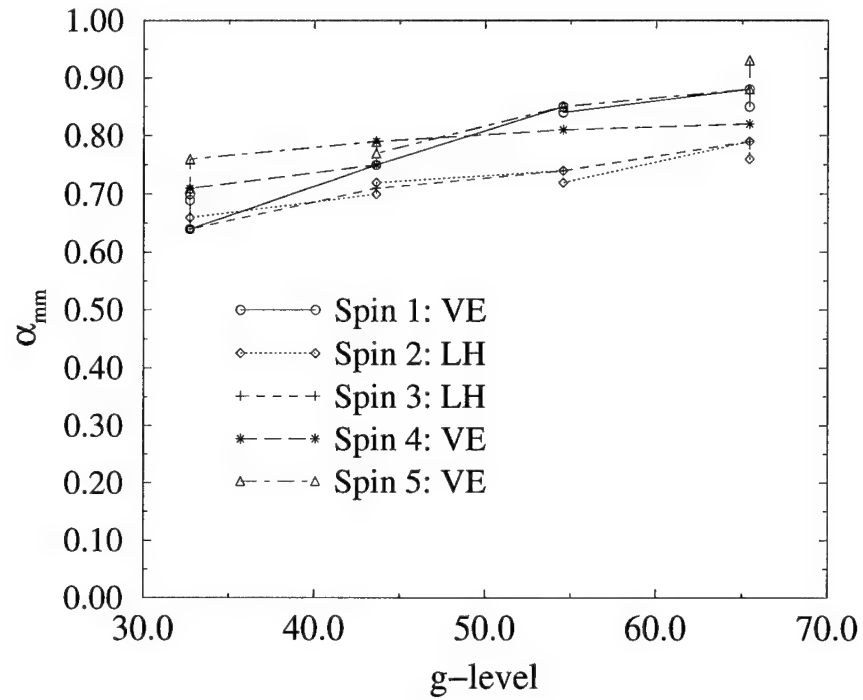
Figure 6.36: α_{mm} vs. g-level for Series U ($h/b = 0.00$), with α_{hh}=0.85, α_{mh}=0.60.
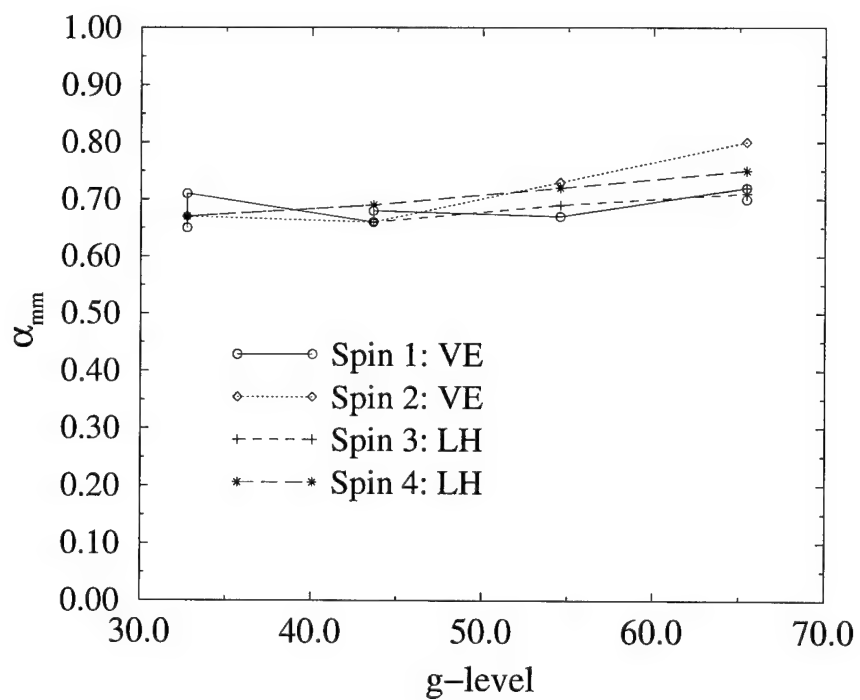
Figure 6.37: α_{mm} vs. g-level for Series T ($h/b = 0.25$), with α_{hh}=0.83, α_{mh}=0.60.
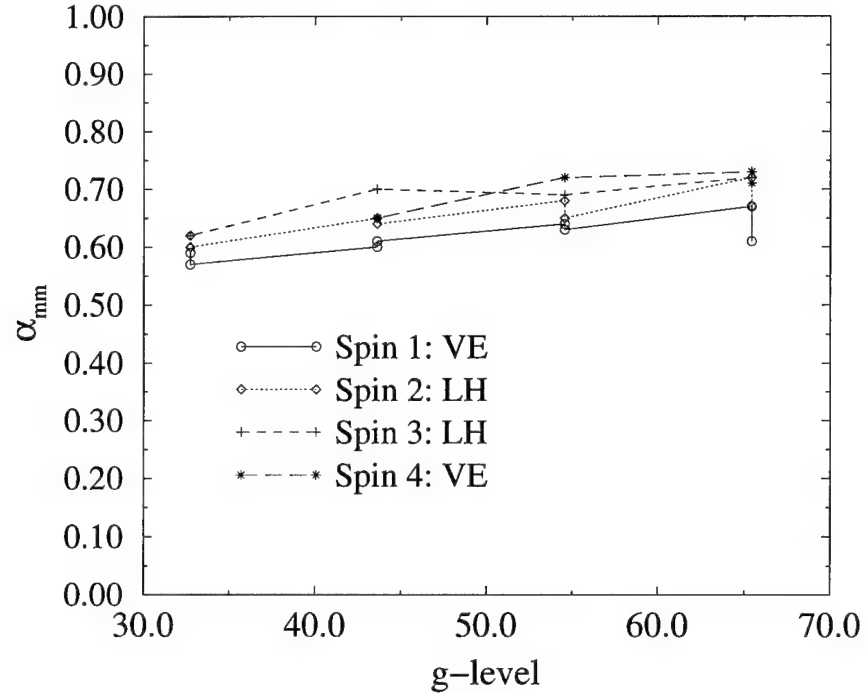
Figure 6.38: α_{mm} vs. g-level for Series S ($h/b = 0.5$), with α_{hh}=0.82, α_{mh}=0.60.
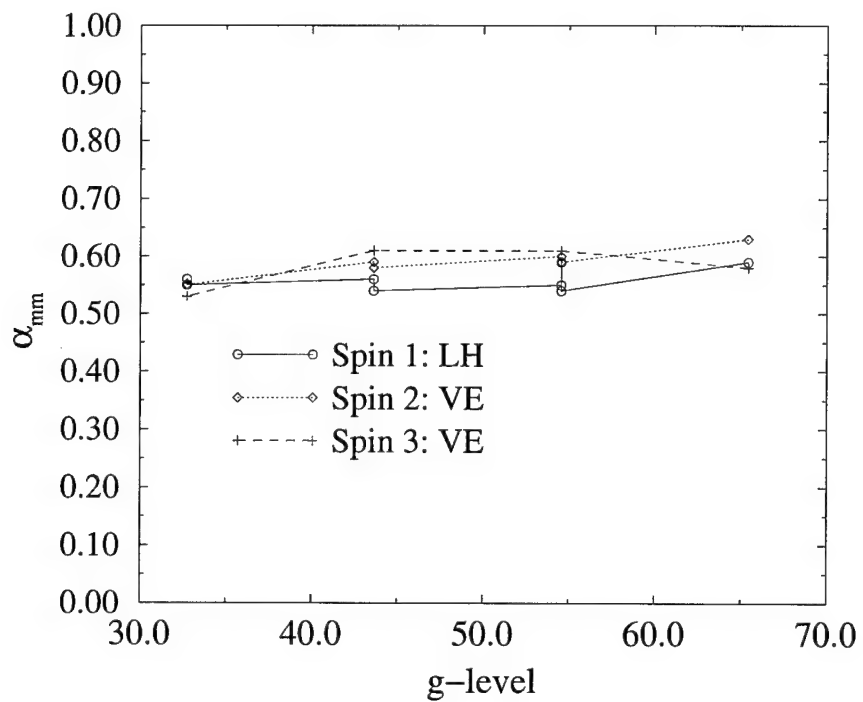
Figure 6.39: α_{mm} vs. g-level for Series R ($h/b = 1.0$), with α_{hh}=0.80, α_{mh}=0.60.
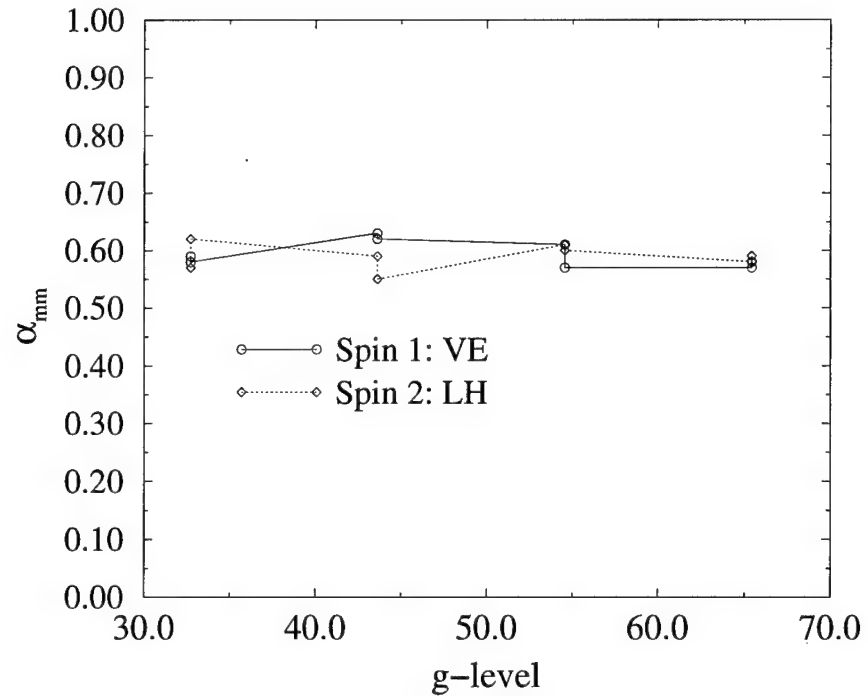
Figure 6.40: α_{mm} vs. g-level for Series O $(h/b = 1.5)$, with α_{hh}=0.80, α_{mh}=0.60.
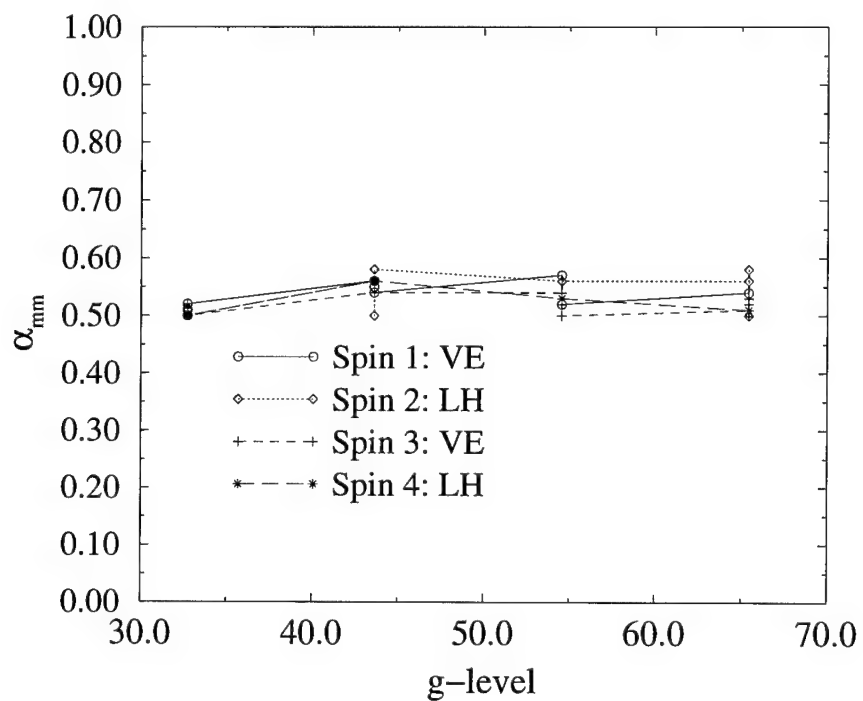
Figure 6.41: α_{mm} vs. g-level for Series N $(h/b = 2.0)$, with α_{hh}=0.80, α_{mh}=0.60.

6.6　Accelerance Match for Square-Root Profile Impedances

The next level of refinement in the data analysis is to compare the experimental results to the accelerances generated by impedances for the square-root profile. For the square-root profile, G_0 was varied across a specified range to find the best-fit G_{0equiv} for a given vertical test. Figures 6.42 and 6.43 show a typical vertical centroidal acceleration match using the square-root shear modulus profile impedances for Series R and Series N respectively. For Series R at $h/b = 1.0$, the equivalent square-root profile slightly overestimates the magnitude of the vertical acceleration at resonance due to the relative softness of the square root profile at shallow depths, while the equivalent homogeneous half-space underestimates the magnitude of accelerance at resonance (see Figure 6.42). However, the square-root profile accelerance prediction for $h/b = 2.0$ fits the experimentally measured accelerance in Series N quite well (see Figure 6.43); the lower shear modulus at the surface for the square-root profile in this case yields a greater magnitude at the resonance frequency which fits the experimental data better than the homogeneous half-space theory at $h/b = 2.0$.

Figure 6.44 shows the lateral acceleration of hole #5 for vertical eccentric loading at hole #6 for Series R ($h/b = 1.0$) when matched with the square-root profile accelerance prediction (all $\alpha_{ij} = 1.0$). The plot reveals that the rocking peak predicted by the square-root profile impedances is only slightly higher than the location of the rocking peak in the experimental measurement without any modification factors. Figure 6.45 shows the lateral acceleration of hole #4 for vertical eccentric loading at hole #6 for Series N ($h/b = 2.0$) along with the square-root profile prediction. The primary difference in the two curves in Figure 6.45 is the location of the main resonance peak. The square-root profile predicts that the peak will occur at a frequency observably higher than that measured in the

experimental results. However, if the theoretical accelerance peak is adjusted by means of an α_{mm} as in the next section, then the two curves will match very well.
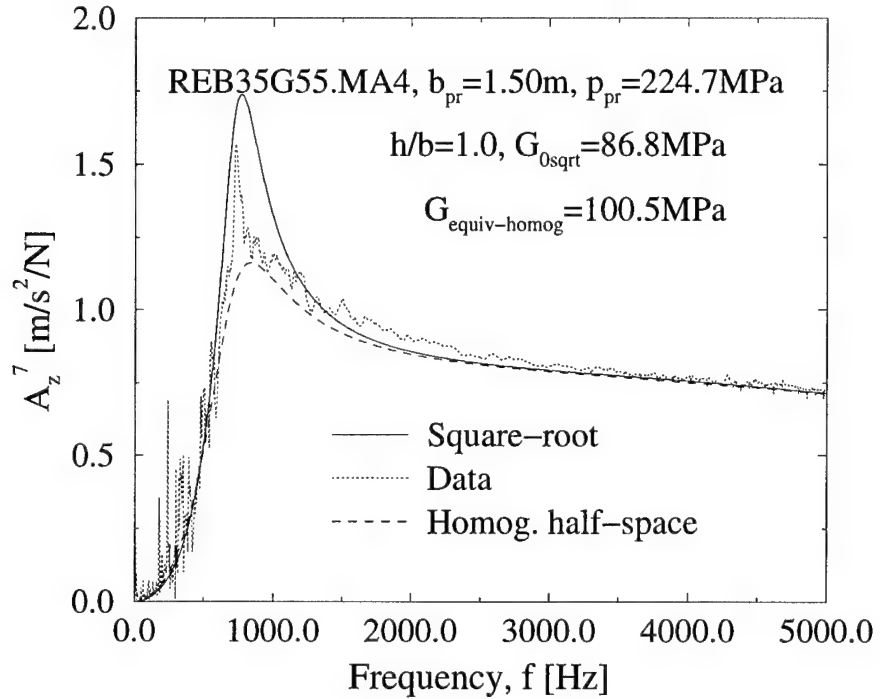
Figure 6.42: Vertical centroidal accelerance match from Series R ($h/b = 1.0$) to square-root profile impedances.
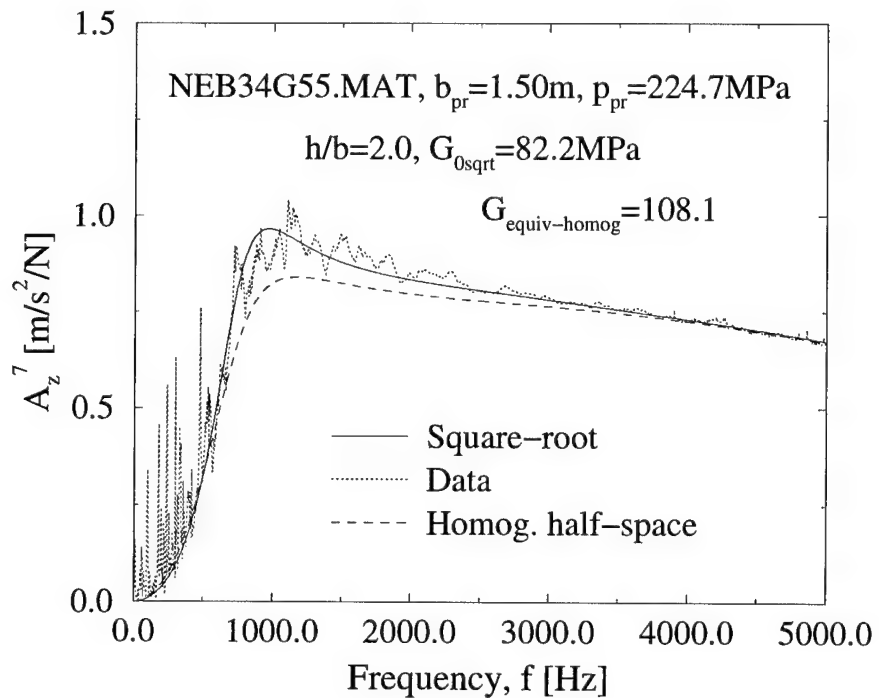
Figure 6.43: Vertical centroidal accelerance match from Series N ($h/b = 2.0$) to square-root profile impedances.
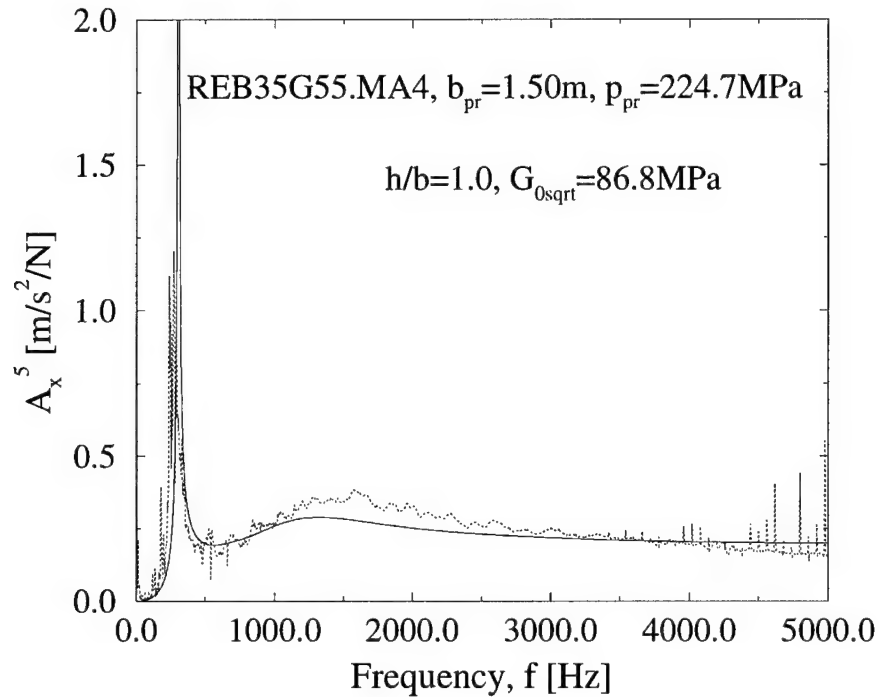
Figure 6.44: Lateral accelerance at hole #5 for vertical eccentric loading at hole #6 from Series R ($h/b = 1.0$) compared with square-root profile accelerance.
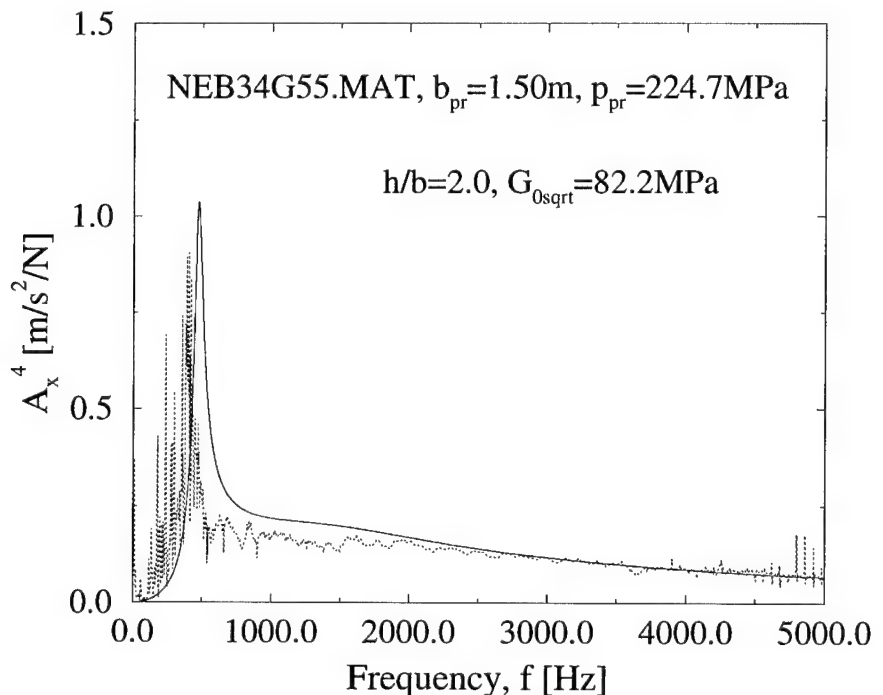
Figure 6.45: Lateral accelerance at hole #4 for vertical eccentric loading at hole #6 from Series N ($h/b = 2.0$) compared with square-root profile accelerance.

6.6.1   Impedance Modification Factors Applied to the Square-Root Half-Space

Since the square-root half-space solution is still inadequate in describing the experimental data, the next step is to apply a set of α_{ij} to the square-root profile impedances to improve the acceleration match. Since Figures 6.42 and 6.43 reveal that the primary difference between the theoretical square-root profile solution is in the location or the rocking peak, α_{hh} and α_{mh} were set to 1.0 while α_{mm} was varied across an appropriate range to find the best acceleration match. Tables 6.27, 6.28 and 6.29 show the best-fit α_{mm} under these conditions for Series R and Series N. Figure 6.46 shows typical vertical eccentric and lateral test results from both Series R and Series N. One can see that the choice of the appropriate α_{mm} with α_{hh} and α_{mh} set to 1.0 yields a satisfactory acceleration match for the square-root profile impedances.

Table 6.26 shows the average Impedance Modification Factors needed to produce a satisfactory acceleration match for Series R and Series N. The average

h/b	Series	α_{mm}	α_{hh}	α_{mh}
1.00	R	0.73	1.00	1.00
2.00	N	0.69	1.00	1.00

Table 6.26: Square-root half-space Impedance Modification Factors.

α_{mm} for square-root profile impedances from Series R is 0.73, compared to 0.58 for homogeneous half-space impedances, while the average α_{mm} for square-root profile impedances from Series N is 0.69, compared to 0.53 for homogeneous half-space impedances. The fact that the α_{mm} are closer to 1.00 shows some improvement over the homogeneous half-space at these embedment depths. However, it is clear that the square-root profile needs some further improvement to obtain an

acceptable accelerance match since Impedance Modification Factors are required. Possible improvements would include a locally stiffened zone at the base and sides of the foundation.
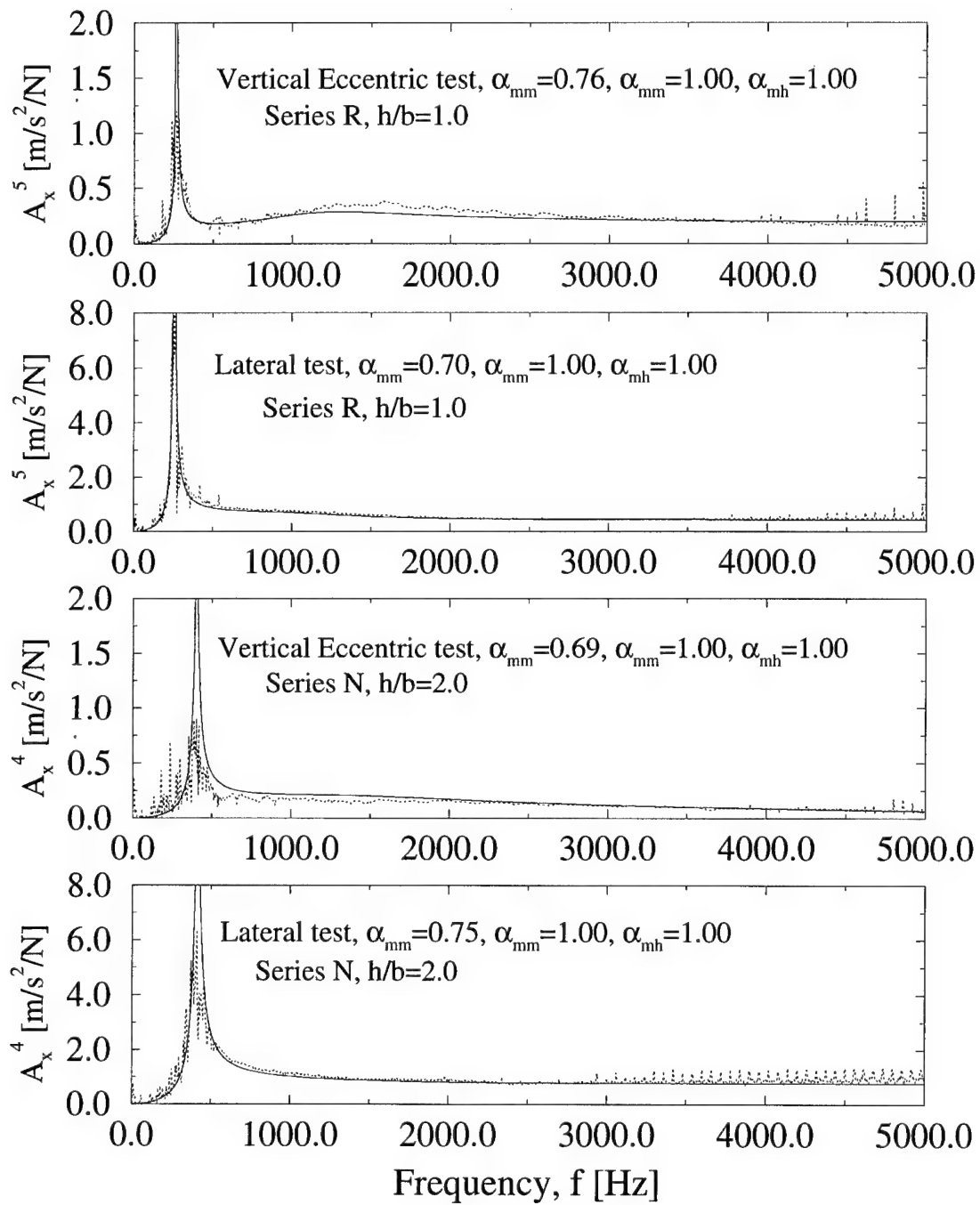
Figure 6.46: Vertical eccentric and lateral accelerance matches for square-root hslf-space impedances from Series R and Series N.

Filename	g-level	b_{pr}	p_{pr}	$G_{equivsqrt}$	α_{mm}	α_{hh}	α_{mh}
RLB35G66.MAT	65.45	1.800	255.6	92.21	0.76	1.00	1.00
RLB35G66.MA2	65.45	1.800	255.6	92.21	0.75	1.00	1.00
RLB35G55.MAT	54.55	1.500	213.0	86.07	0.59	1.00	1.00
RLB35G55.MA2	54.55	1.500	213.0	86.07	0.75	1.00	1.00
RLB35G55.MA3	54.55	1.500	213.0	86.07	0.70	1.00	1.00
RLB35G44.MAT	43.64	1.200	170.4	75.75	0.68	1.00	1.00
RLB35G44.MA2	43.64	1.200	170.4	75.75	0.70	1.00	1.00
RLB35G33.MAT	32.73	0.900	127.8	64.07	0.68	1.00	1.00
RLB35G33.MA2	32.73	0.900	127.8	64.07	0.69	1.00	1.00
REB35G66.MA4	65.45	1.800	269.6	93.92	0.78	1.00	1.00
REB35G66.MA5	65.45	1.800	269.6	93.92	0.78	1.00	1.00
REB35G55.MA4	54.55	1.500	224.7	86.80	0.76	1.00	1.00
REB35G55.MA5	54.55	1.500	224.7	86.80	0.77	1.00	1.00
REB35G44.MA4	43.64	1.200	179.8	76.29	0.75	1.00	1.00
REB35G44.MA5	43.64	1.200	179.8	76.29	0.75	1.00	1.00
REB35G33.MA4	32.73	0.900	134.8	64.44	0.69	1.00	1.00
REB35G33.MA5	32.73	0.900	134.8	63.77	0.69	1.00	1.00
REB35G66.MA6	65.45	1.800	269.6	94.73	0.74	1.00	1.00
REB35G55.MA6	54.55	1.500	224.7	88.36	0.78	1.00	1.00
REB35G44.MA6	43.64	1.200	179.8	77.75	0.77	1.00	1.00
REB35G33.MA6	32.73	0.900	134.8	65.78	0.68	1.00	1.00

Table 6.27: Best-fit α_{mm} for the square-root profile impedances to Series R ($h/b = 1.0$) for α_{hh}=1.00 and α_{mh}=1.00.

Filename	g-level	b_{pr}	p_{pr}	$G_{equivsqrt}$	α_{mm}	α_{hh}	α_{mh}
NEB34G66.MAT	65.45	1.800	269.6	86.80	0.71	1.00	1.00
NEB34G66.MA2	65.45	1.800	269.6	86.03	0.72	1.00	1.00
NEB34G55.MAT	54.55	1.500	224.7	82.22	0.69	1.00	1.00
NEB34G55.MA2	54.55	1.500	224.7	80.71	0.76	1.00	1.00
NEB34G44.MAT	43.64	1.200	179.8	73.41	0.72	1.00	1.00
NEB34G44.MA2	43.64	1.200	179.8	73.41	0.73	1.00	1.00
NEB34G44.MA3	43.64	1.200	179.8	73.41	0.73	1.00	1.00
NEB34G33.MAT	32.73	0.900	134.8	63.11	0.77	1.00	1.00
NEB34G33.MA2	32.73	0.900	134.8	62.45	0.60	1.00	1.00
NEB34G33.MA3	32.73	0.900	134.8	60.50	0.57	1.00	1.00
NEB34G33.MA4	32.73	0.900	134.8	61.15	0.81	1.00	1.00
NLB34G66.MAT	65.45	1.800	255.6	84.13	0.78	1.00	1.00
NLB34G66.MA2	65.45	1.800	255.6	84.13	0.74	1.00	1.00
NLB34G55.MAT	54.55	1.500	213.0	79.35	0.66	1.00	1.00
NLB34G44.MAT	43.64	1.200	170.4	71.47	0.69	1.00	1.00
NLB34G33.MAT	32.73	0.900	127.8	60.17	0.64	1.00	1.00
NLB34G66.MA8	65.45	1.800	255.6	84.13	0.77	1.00	1.00
NLB34G66.MA9	65.45	1.800	255.6	84.13	0.75	1.00	1.00
NLB34G66.M10	65.45	1.800	255.6	84.13	0.74	1.00	1.00
NLB34G55.MA2	54.55	1.500	213.0	79.35	0.75	1.00	1.00
NLB34G55.MA3	54.55	1.500	213.0	79.35	0.75	1.00	1.00
NLB34G44.MA2	43.64	1.200	170.4	71.47	0.77	1.00	1.00
NLB34G44.MA3	43.64	1.200	170.4	71.47	0.63	1.00	1.00
NLB34G44.MA4	43.64	1.200	170.4	71.47	0.74	1.00	1.00
NLB34G33.MA2	32.73	0.900	127.8	60.17	0.65	1.00	1.00
NLB34G33.MA3	32.73	0.900	127.8	60.17	0.67	1.00	1.00
NLB34G33.MA4	32.73	0.900	127.8	60.17	0.66	1.00	1.00

Table 6.28: Best-fit α_{mm} for the square-root profile impedances to Series N ($h/b = 2.0$) for α_{hh}=1.00 and α_{mh}=1.00.

Filename	g-level	b_{pr}	p_{pr}	$G_{equivsqrt}$	α_{mm}	α_{hh}	α_{mh}
NEB34G66.MA3	65.45	1.800	269.6	90.72	0.58	1.00	1.00
NEB34G66.MA4	65.45	1.800	269.6	91.52	0.69	1.00	1.00
NEB34G66.MA5	65.45	1.800	255.6	90.72	0.70	1.00	1.00
NEB34G66.MA6	65.45	1.800	269.6	90.72	0.68	1.00	1.00
NEB34G66.MA7	65.45	1.800	269.6	91.52	0.67	1.00	1.00
NEB34G55.MA3	54.55	1.500	224.7	86.80	0.60	1.00	1.00
NEB34G55.MA4	54.55	1.500	224.7	86.80	0.60	1.00	1.00
NEB34G55.MA5	54.55	1.500	213.0	85.26	0.70	1.00	1.00
NEB34G55.MA6	54.55	1.500	224.7	85.26	0.72	1.00	1.00
NEB34G55.MA7	54.55	1.500	224.7	86.03	0.68	1.00	1.00
NEB34G55.MA8	54.55	1.500	224.7	86.03	0.69	1.00	1.00
NEB34G55.MA9	54.55	1.500	224.7	85.26	0.71	1.00	1.00
NEB34G44.MA4	43.64	1.200	179.8	77.75	0.72	1.00	1.00
NEB34G44.MA5	43.64	1.200	179.8	77.02	0.71	1.00	1.00
NEB34G33.MA5	32.73	0.900	134.8	65.78	0.61	1.00	1.00
NEB34G33.MA6	32.73	0.900	134.8	65.11	0.61	1.00	1.00
NLB34G66.M11	65.45	1.800	255.6	88.60	0.71	1.00	1.00
NLB34G55.MA4	54.55	1.500	213.0	83.64	0.70	1.00	1.00
NLB34G44.MA5	43.64	1.200	170.4	75.36	0.73	1.00	1.00
NLB34G33.MA5	32.73	0.900	127.8	63.68	0.62	1.00	1.00

Table 6.29: Best-fit α_{mm} for the square-root half-space impedances to Series N ($h/b = 2.0$) for α_{hh}=1.00 and α_{mh}=1.00.

6.6.2   Experimental $G_{equivsqrt}$ Compared with Hardin and Drnevich Prediction

.The formula proposed by Hardin and Drnevich [17] for computing G_{max} was given in Equation (3.1) and is repeated here

$$G_{max} = 1230\frac{(2.973 - e)^2}{(1 + e)}(OCR)^K\bar{\sigma}_o^{1/2}. \tag{6.12}$$

Using this formula, one can compute the G_{max} due to the self-weight of the soil, which would represent the far-field shear modulus and will be labeled G^{site}. The mean principal effective stress for the soil model at a depth z can be written as

$$\bar{\sigma}_o = \frac{(1 + 2K_0)zng\rho}{3} \tag{6.13}$$

where K_0 is the coefficient of lateral earth pressure at rest, n is the centrifuge g-level, g is the acceleration due to gravity, and ρ is the mass density of the soil. If $\phi' = 40^o$ for a uniform fine sand as in Bardet [2], and if

$$K_0 = 1 - \sin \phi' \tag{6.14}$$

as proposed by Jaky, then $K_0 = 0.357$. At a depth of z/b=2.0, the mean principal effective stress is

$$\bar{\sigma}_o = 0.2781\sqrt{n} \ [psi], \tag{6.15}$$

for a footing with a half-width, $b = 0.0275m = 1.0827in.$ as footing "B," which yields

$$G^{site} = 9.172\sqrt{n} \ [MPa] \tag{6.16}$$

for a void ratio $e = 0.5318$ as in the experiments in this investigation, where the profile produced is according to

$$G^{site} = G_{0site}\bar{z}^{1/2}. \tag{6.17}$$

Additionally, one can compute near-field G at the base of the footing, which will be labeled G^{near}, by taking into account the weight of the footing. In this case, the mean principal effective stress at a point directly under the footing is

$$\bar{\sigma}_o = \frac{(1 + 2K_0)\frac{m_f ng}{4b^2}}{3} \tag{6.18}$$

assuming that the total footing mass is transferred to the base of the footing where m_f is the mass of the footing. For a footing mass of $1.1965kg=2.6378lb$, the mean principal effective stress is

$$\bar{\sigma}_o = 0.3214\sqrt{n} \ [psi], \tag{6.19}$$

which yields

$$G^{near} = 18.70\sqrt{n} \ [MPa] \tag{6.20}$$

which is over twice as large as G^{site} in Equation (6.16). Table 6.30 contains G^{site} and G^{near} for an embedment depth of $h/b = 2.0$ along with the average experimental G in MPa (called G^{exp}) from the first set of vertical eccentric tests in Series N at each centrifuge g-level. G^{exp} is computed from $G^{exp} = G_{equivsqrt}\bar{z}^{1/2}$,

g-level	G^{site}	G^{exp}	G^{near}
66	74.5	122.2	151.9
55	68.0	115.2	138.7
44	60.1	103.8	124.0
33	52.8	86.8	107.0

Table 6.30: Near- and Far-field G predicted by Hardin and Drnevich [17] along with G from experimental data (MPa).

where $G_{equivsqrt}$ is given in Table 6.28 and $\bar{z} = 2.0$. Figure 6.47a shows a representation of the three values of G at the depth of the base of the footing along with the proposed shear-modulus profiles described by each G. It is not surprising that the G^{exp} is higher than G^{site} since G^{site} does not account for the local

stiffening due to the self-weight of the footing. Both of the G^{site} and G^{exp} profiles are pure square-root profiles with differing values of G_0 as seen in Figure 6.47a and Figure 6.47b. However, the actual shear modulus profile under the footing most likely extends beyond the experimental shear modulus profiles, since G^{near} is greater than G^{exp}. Under this scenario, G^{exp} is an average approximation of the G^{near} and G^{site} profiles and neither the far-field modulus nor the near-field modulus is represented accurately since the near-field modulus is an approximation of the actual near-field profile (see Figure 6.47a), while the far-field modulus is overestimated due to the presence of the footing in the near-field (see Figure 6.47b). This illustrates the need for a more elaborate continuum model which takes into account the local stiffening effects, and therefore, accurately captures both the near- and far-field shear modulus profiles.
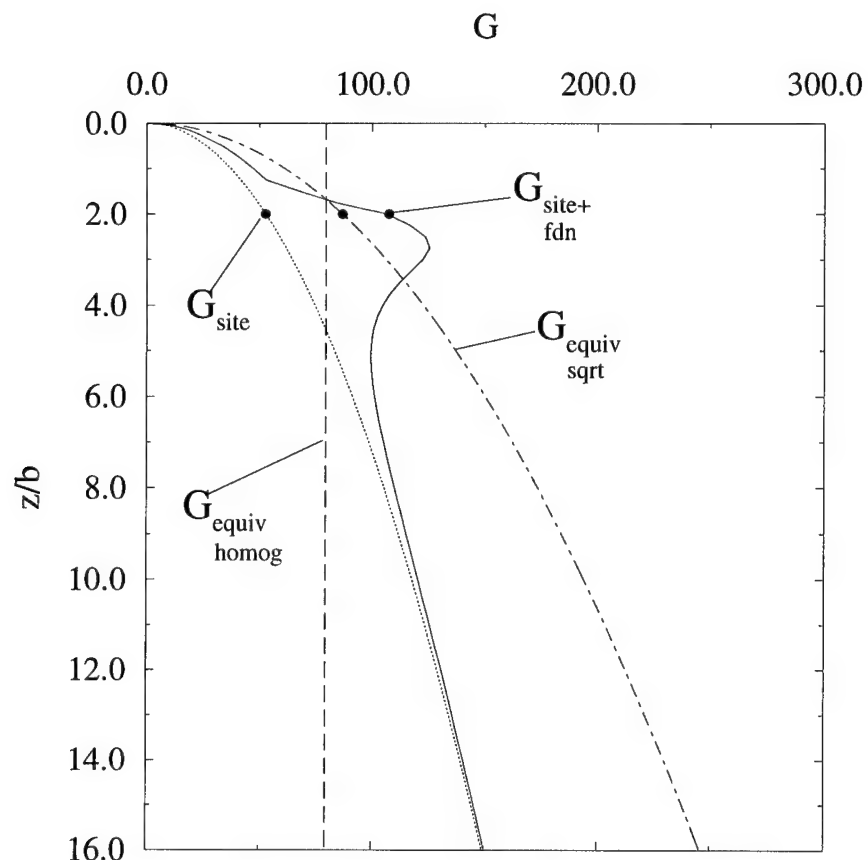
Figure 6.47: Illustration of near- and far-field shear modulus profile predicted by Hardin and Drnevich [17] along with proposed shear modulus profile from 33g experiments in Series N.

Chapter 7

Conclusion

In this investigation, the general behavior of shallow foundations was investigated analytically and experimentally. Theoretical impedances were first presented for a variety of embedment depths for both a homogeneous half-space and a half-space with a square-root shear modulus profile. A parallel experimental investigation was conducted on scale models in a geotechnical centrifuge to explore the behavior of the soil-structure interaction problem on a sandy medium. Comparing the analytical results with the physical data, it was shown that the dynamic vertical stiffness of the embedded foundation using a homogeneous half-space model is satisfactory in describing the dynamic vertical response of the foundations. In the case of lateral or eccentric vertical loading, however, neither the homogeneous half-space nor the square-root modulus profile can capture the dynamic foundation response directly. As a practical resolution to the problem, a set of Impedance Modification Factors were defined for the foundation problem as a function of embedment depth. Additionally, support was shown for the power law dependence of equivalent homogeneous shear modulus on the prototype footing half-width and average contact pressure for embedded footings.

For further study, additional vertical excitation experiments should be conducted to gain a better resolution of the variation of the best-fit equivalent shear modulus with increasing embedment for a variety of prototype half-widths and bearing pressures. Further study could also include the implementation of a more

comprehensive continuum model which can account for the local stiffening of the soil at the base and sides of an embedded foundation.

Bibliography

[1] J. C. Ashlock. Experimental and theoretical modeling of dynamically loaded surface foundations on granular soils. Master's thesis, University of Colorado at Boulder, Department of Civil, Environmental, and Architectural Engineering, 2000.

[2] J.-P. Bardet. Experimental Soil Mechanics. Prentice-Hall, Inc., Upper Saddle River, New Jersey, 1997.

[3] E. C. Brown. Centrifuge modeling of surface foundations subject to dynamic loads. Master's thesis, University of Colorado at Boulder, Department of Civil, Environmental, and Architectural Engineering, 1995.

[4] C. J. Coe, J. H. Prevost, and R. H. Scanlan. Dynamic stress wave reflections/attenuation: Earthquake simulation in centrifuge soil models. Earthquake Engineering and Structural Dynamics, 13:109–128, 1985.

[5] C. B. Crouse, B. Hushmand, J. E. Luco, , and H. L. Wong. Foundation impedance functions: Theory versus experiment. Journal of Geotechnical Engineering, ASCE, 116(3):432–449, March 1990.

[6] J. Dominguez. Dynamic stiffness of rectangular foundations. Technical Report R78-20, MIT, Cambridge, MA, 1978a.

[7] J. Dominguez. Response of embedded foundations to travelling waves. Technical Report R78-24, MIT, Cambridge, MA, 1978b.

[8] G. Gazetas. Foundation vibrations. In H.-Y. Fang, editor, Foundation Engineering Handbook, pages 553–593, Van Nostrand Reinhold, New York, 1991.

[9] G. Gazetas, R. Dobry, and J. L. Tassoulas. Vertical response of arbitrarily shaped embedded foundations. Journal of Geotechnical Engineering, ASCE, 111(6):750–771, June 1985.

[10] G. Gazetas and J. L. Tassoulas. Horizontal stiffness of arbitrarily shaped embedded foundations. Journal of Geotechnical Engineering, ASCE, 113(5):440–457, May 1987.

[11] G. Gillmor. Centrifuge modeling of of surface foundations subject to dynamic loads. Master's thesis, University of Colorado at Boulder, Department of Civil, Environmental, and Architectural Engineering, 1999.

[12] B. B. Guzina. Dynamic behavior of surface foundations on heterogenous soils. Master's thesis, University of Colorado at Boulder, Department of Civil, Environmental, and Architectural Engineering, 1992.

[13] B. B. Guzina. Seismic Response of Foundations and Structures in Multilayered Media. PhD thesis, University of Colorado at Boulder, Department of Civil, Environmental, and Architectural Engineering, 1996.

[14] B. B. Guzina and R. Y. S. Pak. Multi-layer representation of continuous insitu profiles in soil dynamics. In ASCE Geotechnical Special Publication No. 64, pages 1–12, July 1997.

[15] B. B. Guzina and R. Y. S. Pak. Experimental inversion of lateral-rocking impedance matrix. In Geotechnical Earthquake Engineering and Soil Dynamics III, volume 2, pages 1294–1306, Geotechnical Special Publication No. 75, ASCE, 1998.

[16] B. B. Guzina and R. Y. S. Pak. Vertical vibration of a circular footing on a linear-wave-velocity half-space. Geotechnique, 48(2):159–168, 1998.

[17] B. O. Hardin and V. P. Drnevich. Shear modulus and damping in soils: Design equations and curves. Journal of the Soil Mechanics and Foundations Division, ASCE, 98:667–692, 1972.

[18] E. Hatzikonstantinou, J. L. Tassoulas, G. Gazetas, P. Kotsanopoulos, , and M. Fotopoulou. Rocking stiffness of arbitrarily shaped embedded foundations. Journal of Geotechnical Engineering, ASCE, 114(4):457–490, April 1989.

[19] B. Hushmand. Experimental Studies of Dynamic Response of Foundations. PhD thesis, California Institute of Technology, 1983.

[20] D. L. Karabalis and D. E. Beskos. Dynamic response of 3-d embedded foundations by the boundary element method. Computer Methods in Applied Mechanics and Engineering, 56:91–119, 1986.

[21] H. Y. Ko. The colorado centrifuge facility. In Centrifuge 88, pages 73–76, A.A. Balkema, Rotterdam, The Netherlands, 1988.

[22] L. Lenke, R. Y. S. Pak, and H. Y. Ko. Boundary effects in modeling of foundations subjected to vertical excitation. In Centrifuge 91, A.A. Balkema, Rotterdam, The Netherlands, 1991.

[23] J. E. Luco. Linear soil-structure interaction: a review. In S. K. Datta, editor, Earthquake Ground Motion and Its Effects on Structures, pages 1039–1044, ASME, New York, NY, 1982.

[24] J. E. Luco and H. L. Wong. Seismic response of foundations embedded in a layered half-space. Earthquake Engineering and Structural Dynamics, 15:233–247, 1987.

[25] F. Medina and J. Penzien. Infinite elements for elastodynamics. Earthquake Engineering and Structural Dynamics, 10:699–709, 1982.

[26] A. Mita and J. E. Luco. Dynamic response of embedded foundations: A hybrid approach. Computer Methods in Applied Mechanics and Engineering, 63:233–259, 1987.

[27] A. Mita and J. E. Luco. Dynamic response of a square foundation embedded in an elastic half-space. Soil Dynamics and Earthquake Engineering, 8(2):54–67, 1989.

[28] A. Mita and J. E. Luco. Impedance functions and input motions for embedded square foundations. Journal of Geotechnical Engineering, ASCE, 115(4):491–503, April 1989.

[29] M. Novak. Prediction of footing vibrations. Journal of the Soil Mechanics and Foundations Division, 96(SM3):837–861, May 1970.

[30] R. Y. S. Pak. Asymmetric wave propagation in a half-space by a method of potentials. Journal of Applied Mechanics, ASME, 54:121–126, 1987.

[31] R. Y. S. Pak and J. A. Ashlock. Concept of impedance modification factors for foundations on cohesionless soils. In Proceedings of 14th ASCE Engineering Mechanics Conference, Austin, Texas, 2000.

[32] R. Y. S. Pak and B. B. Guzina. Dynamic characterization of vertically loaded foundations on granular soils. Journal of Geotechnical Engineering, ASCE, 121(3):274–286, March 1995.

[33] R. Y. S. Pak and B. B. Guzina. Seismic soil-structure interaction analysis by direct boundary element methods. International Journal of Solids and Structures, 36:4743–4766, 1999.

[34] J. M. Roesset and M. M. Ettouney. Transmitting boundaries: A comparison. International J. Numer. Analyt. Meths. Geomech., 1:151–176, 1977.

[35] H. B. Seed, R. T. Wong, I. M. Idriss, and K. Tokimatsu. Moduli and damping factors for dynamic analyses of cohesionless soils. Journal of Geotechnical Engineering, ASCE, 112(11):1016–1032, November 1986.

[36] K. H. Stokoe and F.E. Richart Jr. Dynamic response of embedded machine foundations. Journal of the Geotechnical Engineering Division, 100(GT4):427–447, April 1974.

[37] M. Tohdo, O. Chiba, and R. Fukuzawa. Impedance functions and effective input motions of embedded rigid foundations. In <u>Proceedings: 7th Japan Earthquake Engineering Symposium</u>, pages 1039–1044, Tokyo, 1986.

[38] K. Yoshida and H. Kawase. Dynamic cross-interaction of embedded foundations. In <u>Proceedings: 7th Japan Earthquake Engineering Symposium</u>, pages 1045–1050, Tokyo, 1986.